

IMPERIAL

Spirals, defects, rolls and bands;
**Transitional Rayleigh-Bénard Poiseuille flows
using spectral/*hp* element methods**

BY

Chi Hin Chan

SUPERVISED BY

Professor Spencer J. Sherwin
&
Professor Yongyun Hwang

at the

DEPARTMENT OF AERONAUTICS
FACULTY OF ENGINEERING
IMPERIAL COLLEGE LONDON

THIS THESIS IS SUBMITTED FOR THE DEGREE OF DOCTOR OF PHILOSOPHY

Declarations

Statement Of Originality

I certify that the content of this thesis is a product of my own work. I have appropriately acknowledged any other material that may have been used through standard referencing practices.

Copyright Declaration

The copyright of this thesis rests with the author. Unless otherwise indicated, its contents are licensed under a Creative Commons Attribution-Non Commercial 4.0 International Licence (CC BY-NC). Under this licence, you may copy and redistribute the material in any medium or format. You may also create and distribute modified versions of the work. This is on the condition that: you credit the author and do not use it, or any derivative works, for a commercial purpose. When reusing or sharing this work, ensure you make the licence terms clear to others by naming the licence and linking to the licence text. Where a work has been adapted, you should indicate that the work has been changed and describe those changes. Please seek permission from the copyright holder for uses of this work that are not included in this licence or permitted under UK Copyright Law.

Abstract

The transitional regimes of Rayleigh-Bénard Poiseuille (RBP) flows and Rayleigh-Bénard convection (RBC) are investigated using direct numerical simulations and linear stability analysis. RBP flows serve as a paradigmatic configuration that describes fluid motion driven by shear and buoyancy forces, a combination of the classical buoyancy-driven RBC and shear-driven plane Poiseuille flow (PPF). While the transitional regime of RBC and PPF have been well studied over the past century, the transitional regime where both forces interact remains largely unexplored beyond linear instability.

Following a review of the relevant literature and numerical methods, we conduct direct numerical simulations of transitional RBP flows using Nektar++, a spectral/ hp element package. The simulations span over a range of Rayleigh numbers, $Ra \in [0, 10000]$ and Reynolds number $Re \in [0, 2000]$, with unit Prandtl number in a large computational domain. Within this parametric space, we identify five distinct regimes: (1) bistable SDC & ISRs, (2) ISRs, (3) wavy rolls, (4) intermittent rolls, and (5) shear-driven turbulence. The (4) intermittent rolls regime represent a newly identified state characterised by the spatio-temporal intermittent breakdown and regeneration of longitudinal rolls. In the (5) shear-driven turbulent regime, we also observe that intermittent rolls may coexist with turbulent-laminar bands. The spatio-temporal intermittent dynamics of longitudinal rolls highlight its dominant role in transitional RBP flows. To suppress spatial intermittency, we examine the unstable manifolds of the longitudinal rolls in a confined domain, integrating along which leads to turbulence. Depending on Re , this turbulence may occur transiently, decaying towards the unstable laminar base state where the longitudinal rolls can be excited again, forming a quasi-cyclic process referred to as the *thermally-assisted sustaining process (TASP)*. We furnish a state space sketch of the dynamical process, and discuss the relevance of the *TASP* to larger domains, concluding the first part of the thesis.

In the second part, we explore the state space structure of the bistable system between spiral defect chaos (SDC) and ideal straight rolls (ISRs) of Rayleigh-Bénard convection within large domains. By systematically reducing the domain size, we observe that SDC occurs transiently, eventually stabilising into multiple stable invariant solutions, referred to as *elementary states*. These *elementary states* are visually and statistically similar to the localised features of SDC, underpinning the pattern formation of SDC. We also examined the edge between the basin of attractions of ISRs and the elementary states, revealing multiple edge states. Investigating the unstable manifolds of ISRs exhibit two distinct behaviours: (1) unstable ISRs near the Busse balloon connect to stable ISRs and base state via heteroclinic connections, and (2) unstable ISRs further from the Busse balloon lead to SDC, indicating such ISRs lie on boundary between ISRs and SDC. Finally, we present a state space sketch of the *elementary states* organised around SDC, highlighting its ‘building-block’ description of SDC.

Acknowledgements

There are many people who have shaped my experience as a PhD student whom I would like to express my gratitude for. First and foremost, I want to express my deepest gratitude to my supervisors, Spencer and Yongyun. I have learned and grown a lot under their tremendously kind and patient supervision. It is a truly a pleasure to learn from world leading experts in fluid mechanics and computational fluid dynamics, and I will miss the knowledge osmosis process during our weekly catch-ups. Apart from the PhD, they also openly supported personal development opportunities, allowing me to pursue interests such as the Nektar++ redesign project, engaging in graduate teaching assistant roles, pursuing a summer research exchange at LadHyX and an internship at IBM Research, which I am grateful for.

I would like to specially thank Yongyun, who also happens to be my MSc thesis supervisor. Together, we worked the topic of reduced-order modelling of turbulent Couette flows as part of my MSc thesis. Perhaps more importantly, for giving me the confidence I needed to pursue a PhD program at Imperial.

I would also like to thank Lutz, for his kind hospitality, ensuring that I was comfortable at LadHyX in the summer of 2024. Despite being a short three months stint, I learned about advanced modal decomposition techniques and was exposed to the broad fluid mechanics research activities at LadHyX.

I would also like to thank Basman, my Bachelor's thesis supervisor at Nanyang Technological University (NTU), during which we worked on humpback whale leading-edge tubercles for my FYP. I believe it is fair to say that he was primarily responsible for planting the "seed" for my fascination for computational fluid dynamics.

I would also like to thank the Nektar++ community, particularly Henrik, Alex, Chris, Jacques and Dave for their timely responses on compilation errors, segmentation faults and guidance on software principles for contributing to Nektar++.

I would also like to thank my collaborators, Mohammad and Raj, for providing invaluable guidance and advice during the PhD, and also the opportunity to collaborate on physics-informed neural networks.

I would like to also thank Eloisa and Geeth, my project supervisor and manager at IBM Research, for giving an eye-opening opportunity to learn and contribute to AI research activities in a corporate company.

I would thank my fellow PhD students and postdocs from the office, for their endearing support over the 'instabilities' of PhD and London life. I will fondly remember our shared experiences such as unwinding over a cheeky pint on Friday evenings, mario karting in the common room, going to Sagar and exploiting its 50% discount, honest burgers student discounts, going to Wasabi at South

Kensington at closing to get half-priced bentos, countless muffin (Toffee banana is the best) and coffee breaks, peaceful walks around campus, Hyde park runs, booking the swimming pool sessions just to use the sauna, many gym/swim/badminton/climbing sessions, appearing decently surprise to bump into each other in the office on the weekends, and bantering over the weather, reviewers and PhD life. Special thanks to Henrik, Parv, Alex, Kaloyan, Ganlin, Steffi, Lidia, Christian, Kazuki, Priyam, Sid, Elise, Yu Hang, Cheng Wei, Zhao, Zilin, Victor, Mohsen, Guglielmo, João, Yacine and many others, all of whom made London feel like home.

The person who probably deserves the most credit would be my fiancée, Angelica, who have been there at the beginning, ready to lend a listening ear to my monologue on how cool CFD is. The distance between Singapore and London has been tough over the years, and I look forward to building our shared future after the PhD. Last but not least, I am grateful to my loving parents and family, for supporting my academic interests and developments aboard despite the distance.

I would like to acknowledge the generous financial support from the Imperial College President's PhD scholarships, Global Fellows Fund and computing resources from ARCHER2, without which this PhD would not have been possible.

Chi Hin Chan
London
November 2025

Contents

1	Introduction	1
1.1	Overview	1
1.2	Transitional wall-bounded shear flows	4
1.2.1	Linear Stability Analysis	4
1.2.2	Nonlinear dynamical systems	8
1.2.3	Self-sustaining process	11
1.2.4	Spatiotemporal transitional flows	12
1.3	Rayleigh-Bénard convection	15
1.4	Rayleigh-Bénard Poiseuille (RBP) flows	20
1.5	Thesis Outline	22
2	Numerical Methods	25
2.1	Method of weighted residuals	25
2.2	Galerkin Projection	27
2.3	Spectral/ hp element method	29
2.3.1	Domain partition	29
2.3.2	Standard Elements	29
2.3.3	Global assembly	31
2.3.4	Local basis expansions	33
2.3.5	Gaussian quadrature	36
2.3.6	Numerical differentiation	37
2.3.7	Example in 1D	38
2.3.8	Error properties	40
2.4	Numerical methods for solving the N.S equations	41
2.4.1	Velocity Correction Scheme	41
2.4.2	Fourier spectral/ hp modes	44
2.4.3	Maintaining fluid flow through a channel	45
2.5	Stability analysis of the N.S equations	48
2.5.1	Algorithms for linear stability analysis	48
2.5.2	Edge tracking	53

3 Transitional RBP flows	55
3.1 Objectives	55
3.2 Problem formulation	56
3.2.1 Governing equations	56
3.2.2 Numerical Methods	57
3.2.3 Parametric sweep of $Ra-Re$ space	57
3.2.4 Linear Stability Analysis	58
3.3 $Ra-Re$ phase space	59
3.3.1 Classification	59
3.3.2 Spatiotemporal intermittent rolls	62
3.3.3 Co-existence of convection rolls with turbulent bands	65
3.4 The role of longitudinal rolls	65
3.4.1 The thermally-assisted sustaining process (TASP) in a confined domain	65
3.4.2 Variation of Ra and Re on the thermally-assisted sustaining process in $\Gamma = \pi/2$	76
3.4.3 Extending to large domains, $\Gamma = 4\pi$	80
3.5 Summary	83
4 The state space structure of SDC	85
4.1 Objectives	85
4.2 Problem formulation	86
4.2.1 Rayleigh-Benard convection (RBC)	86
4.2.2 Numerical method	87
4.2.3 Linear stability analysis of ISRs	87
4.3 Transient SDC & elementary states	88
4.4 Multiplicity of edge states	95
4.5 Unstable ideal straight rolls	102
4.5.1 Pathways leading to ISRs - heteroclinic orbits	104
4.5.2 Pathways leading to elementary states	106
4.5.3 A pathway to SDC in an extended domain $\Gamma = 4\pi$	108
4.6 Summary	110
5 Conclusions	113
A Appendices	115
A.1 Simulation parameters for $Ra-Re$ sweep	115
A.2 1st and 2nd order statistics	115
A.2.1 Buoyancy-driven regime	115
A.2.2 Shear-driven regime	118
A.3 Growth rates of primary instabilities	118
A.4 Verification of linear stability analysis	122
A.5 Other elementary states and ISRs	122

List of Figures

1.1	Thermoconvective shear flows driven by shear and buoyancy forces across length scales, $L \in [10^{-2}m, 10^3m]$. Examples include (a) chip cooling, (b) chemical vapour deposition and (c) the formation of cloud streets.	1
1.2	The Rayleigh-Bénard Poiseuille (RBP) flow configuration.	3
1.3	(a) Osbourne Reynolds pipe experiment with the dye injection apparatus, illustrating the (b) laminar flow, (c) transitional regime and (d) turbulent flow as the flow speed is increased, taken from Reynolds (1883).	5
1.4	(a) The phase portrait of the toy model with $Re = 15$, where red lines are phase lines of the toy model. The blue trajectory lead to transient growth and the green trajectory do not (b) Time history of blue and green trajectory.	7
1.5	(a) Chaotic trajectories of turbulence of plane Couette flow at $Re = 400$, approaching the an unstable periodic orbit (red) highlighted as yellow, adopted from Kawahara and Kida (2001). (b) State space organisation of turbulence trajectories (black dots) confined around equilibria (circles, dots and squares) and their unstable manifolds (solid lines), heteroclinic connections between them are shown in red. The coordinate system, $(e_{1,2,3})$, is centered on the laminar state, using a linear combination of the upper branch invariant state. (c) State space projection of five periodic orbits (coloured solid lines), embedded within the same space where turbulence evolves in (b), adopted from Cvitanović and Gibson (2010).	9
1.6	A graphical representation of the edge (grey surface) separating the basin of boundary of the laminar and turbulent attractor, consisting of attractors, known as edge states, adapted from Graham and Floryan (2021).	11
1.7	The self-sustaining process, consisting of three phases: (1) Streak formation from linear advection by streamwise vortices, (2) streak breakdown due to streak instability and (3) regeneration of streamwise vortices via nonlinear mechanisms.	12
1.8	A snapshot of turbulent-laminar bands at $Re = 1400$ in a large domain $L/h = 16\pi$, depicting its spatiotemporal intermittent nature. Isovolumetric rendering is based on the spanwise, u' , and wall-normal, v' , perturbation kinetic energy, $E(u', v') = 1/2(u'^2 + v'^2)$, where the perturbation velocities are defined about the laminar state $\mathbf{u}'(\mathbf{x}, t) = \mathbf{u}(\mathbf{x}, t) - U_{lam}(y)$	13

1.9	Turbulent-laminar bands for $t \in [0, 3000]$ in large domains $(L_x, L_z) = (16\pi, 16\pi)$ at (a) $Re = 1800$, (b) $Re = 1600$, (c) $Re = 1400$, (d) $Re = 1200$, (e) $Re = 1100$, (f) $Re = 1050$, (g) $Re = 1000$	14
1.10	The mean decay times (red), τ^d , and mean splitting times (black), τ^s , as a function of Reynolds number, leading to a crossover point at $Re_{cross} \approx 965$, adapted from Gomé, Tuckerman, and Barkley (2020).	15
1.11	(a) Surface tension driven convection leading to the onset of hexagonal Bénard cells in a thin layer of silicone oil, heated from below and cooled by ambient air. A diamond defect appears, likely caused by plate imperfections. (b) Buoyancy driven convection in rigid plates, resulting to concentric convection rolls at 2.9 times the critical Rayleigh number. Both experiments were performed by Koschmieder and Pallas (1974), and the convection patterns were illuminated by aluminum powder, where the dark and bright regions refer to vertical and horizontal motions respectively. These higher resolution images were taken from Van Dyke and Van Dyke (1982).	16
1.12	The Busse balloon describes the stability boundaries of ISRs in a $\varepsilon - q$ space. For larger wavenumbers, the instability mechanisms is described by the skewed-varicose (SV) instability. For smaller wavenumbers, the instability mechanism is described by the Eckhaus instability. For large ε , the instability is described by the onset of oscillatory instability. Busse balloon digitised from Plapp (1997) for $Pr \approx 1$	17
1.13	ISRs experiencing (a) cross-roll instability at $Ra = 3000$, $Pr = 100$ and (b) zig-zag instability at $Ra = 3600$, $Pr = 100$ (Busse & Whitehead, 1971). (c) Skew-varicosed instability at $Ra = 5568$, $Pr = 1$ (Plapp, 1997), and (d) oscillatory instability at $Ra = 10384$, $Pr = 1$ (Cakmur, Egolf, Plapp, & Bodenschatz, 1997a).	18
1.14	The coexistence of spiral defect chaos (SDC, top row) and ideal straight rolls (ISRs, bottom row) at (a,b) $Ra = 3279$, (c,d) $Ra = 6832$ and (e,f) $Ra = 10384$. The domain size is $\Gamma = 50$ and $Pr = 1$, adapted from Cakmur et al. (1997a).	20
1.15	(a) Neutral stability curves of longitudinal rolls (LR), oblique rolls (OR), transverse rolls (LR) and Tollmien-Schlichting (TS) waves, adapted from John Soundar Jerome, Chomaz, and Huerre (2012). The shaded area refers to damped perturbations. Sketch of (b) longitudinal and (c) transverse rolls, adapted from Kelly (1994).	21
2.1	A spectral/ hp element representation of $u(x)$, consisting of three non-overlapping finite elements, each containing a linear combination of local expansion bases of up to $P = 2$	30
2.2	A graphical representation of C^0 across elemental boundaries and the relationship between local basis coefficients, u_0^e, u_P^e , and global basis expansions, u_i	32
2.3	The modified basis for up to $P = 5$ normalised to $-1 \leq \psi_p \leq 1$	34
2.4	Lagrange polynomials for $P = 5$ with nodal values along GLL points.	35
2.5	Two dimensional modified basis with $p = q = 4$ in a standard quadrilateral, $-1 \leq \xi_1, \xi_2 \leq 1$. The modified bases are normalised to $-1 \leq \phi_{pq} \leq 1$	36

2.6	Convergence properties of an exact solution $u = \sin(\pi x)$ to a 1D Helmholtz equation with $\lambda = 1$ and Dirichlet boundary conditions at $x \in [-1, 1]$. h -type refinement is performed on a mesh with fixed $P = 1$ and decreasing h (increasing elements), demonstrating algebraic convergence in a <i>log-log</i> plot of (a). p -type refinement is performed on a mesh with equipspaced two elements and increasing P , demonstrating exponential convergence on a <i>semi-log</i> plot of (b).	41
2.7	(a) Flow rate driven by a pressure gradient from an reservoir elevated by h . (b) Flow driven by a piston at a constant flow rate.	45
2.8	τ_w against Re_c using skin friction coefficients from Dean (1978) with $\rho = U_c = 1$. Experimental scatter points from (Iida & Nagano, 1998; J. Kim, Moin, & Moser, 1987; Patel & Head, 1969; Tsukahara, Iwamoto, Kawamura, & Takeda, 2014).	47
3.1	A conceptual diagram of the $Ra - Re$ phase space illustrates the midplane temperature snapshots, $\theta(x, z) _{y=0}$ for $Re \in [0, 2000]$ and $Ra \in [0, 10000]$, classified into five distinct regimes: (1) SDC & ISRs, (2) ISRs, (3) wavy rolls, (4) intermittent rolls and (5) shear-driven turbulence. The blue solid curves refer to primary neutral curves of the longitudinal and transverse rolls $Ra_{\parallel}, Ra_{\perp}$. The red curve indicates the secondary oscillatory instability of ISRs at $Re = 0$ (Bodenschatz, Pesch, & Ahlers, 2000). Shades of red, green and blue indicate their dominant mechanism, whether driven by buoyancy or shear (or mixed). For $Re > 0$, the mean flow is along the z direction.	60
3.2	Midplane temperature snapshots at $Ra = 3000$, (a) $Re = 0.1$, (b) $Re = 1$, (c) $Re = 10$, (d) $Re = 100$, (e) $Re = 500$, (f) $Re = 1000$	61
3.3	The space-time plots of midplane temperature field, temperature snapshot and phase space trajectories of the Nusselt number against wall shear rate at (a,b,c) $Ra = 10000$ for $Re = 1, 10, 100$; (d,e,f) $Ra = 8000$ for $Re = 1, 10, 100$; and (g,h,i) $Ra = 5000$ for $Re = 1, 10, 100$. The flow patterns are primarily organised into spiral defect chaos, longitudinal rolls, and wavy rolls occurring at $Re = 1, 10, 100$, respectively.	63
3.4	The intermittent rolls regime at $Ra = 8000, Re = 500, t \in [0, 10000]$. (a) The time history of shear on the lower wall and Nusselt number. Space-time ($x-t$) plots of (b) near-wall wall-normal and spanwise perturbation kinetic energy and (c) midplane temperature space-time plot, with the corresponding near-wall and midplane temporal planar snapshots at (d,e) $t = 3736$, (f,g) $t = 6189$, and (h,i) $t = 8680$	64
3.5	Shear-driven turbulence regime at $Ra = 0, Re = 1050, t \in [0, 8000]$. Space-time plots of (a) near-wall wall-normal and spanwise perturbation kinetic energy, (b) midplane temperature space-time plot, and near-wall and midplane temporal planar snapshots at (c,d) $t = 1100$, (e,f) $t = 4491$, and (g,h) $t = 6171$, highlighting a prolonged laminar patch.	66

3.6 Shear-driven turbulence regime at $Ra = 10000, Re = 1050, t \in [0, 8000]$. Spacetime plots of (a) near-wall wall-normal and spanwise perturbation kinetic energy, (b) midplane temperature spacetime plot, and their corresponding near-wall and midplane temporal $x - z$ planar snapshots at (c,d) $t = 1282$, (e,f) $t = 5077$, and (g,h) $t = 6358$, highlighting the coexistence of longitudinal rolls and turbulent bands.	67
3.7 Intermittent dynamics in a confined domain at $Ra = 10000, Re = 1050, t \in [0, 3000]$, $\Gamma = \pi/2$. The time history of the (a) Nusselt number and shear. Temporal snapshots of volumetric temperature, planar near-wall streamwise and spanwise perturbations at (b) $t = 1291.5$, (c) $t = 1480.5$, (d) $t = 1564.5$, (e) $t = 1711.5$. Longitudinal rolls and transient turbulence are observed at (b,d) and (c,e), respectively.	68
3.8 Relaminarisation in a confined domain at $Ra = 0, Re = 1050, t \in [0, 3000], \Gamma = \pi/2$. The time history of the (a) Nusselt number and shear. Temporal snapshots of volumetric temperature at (b) $t = 31.5$, (c) $t = 63$, (d) $t = 157.5$, (e) $t = 672$	70
3.9 Ra -quenching experiments for $Ra = 8000, 5000, 3000, 2000$, at $Re = 1050, \Gamma = \pi/2, t \in [850.5, 5000]$. The time history of (a) shear and (b) volumetric temperature snapshots of the flow condition at $t = 850.5$. Volumetric temperature snapshots for $Ra = 8000$ at (c,d) $t = 1312.5, 1743$, and $Ra = 5000$ at (e,f) $t = 1312.5, 3570$, revealing a longitudinal roll and a turbulent state, respectively. Stable longitudinal rolls emerge for $Ra = 3000$ at (g,h) $t = 1312.5, 4200$, and $Ra = 2000$ at (j,k) $t = 1312.5, 4200$	71
3.10 The growth rates of infinitesimal perturbations linearised about longitudinal rolls, q_{LR} , of spanwise wavenumber of $\alpha d = 4$, against (a) streamwise wavenumber βd , and (b) Ra for $\beta d = 2$. The hatches in (a) refer to wavenumbers smaller than those admissible in $\Gamma = \pi/2$. The dash-dotted line in (b) is a standard quadratic regression yielding $Ra_s \approx 4720$	72
3.11 Time integration along the dominant unstable manifold, $\beta d = 2$, of the longitudinal rolls at $Ra = 5000, Re = 1050, \Gamma = \pi/2$ for $t \in [0, 8000]$. Time history of the (a) Nusselt number and wall shear rate, and (b) midplane temperature space-time plot. This system oscillates between the longitudinal rolls ($LR1 - 4$) and turbulence ($T1 - 4$) over four intervals. Snapshots of temperature at (c) $t = 105$, (d) $t = 1512$, (e) $t = 2446.5$, (f) $t = 2992.5$, (g) $t = 3727.5$, (h) $t = 5103$, (i) $t = 6300$, (j) $t = 6993$	73
3.12 State space projection based on the planar averaged centerline velocity and shear, coloured by the volume normalised perturbation kinetic energy at $Ra = 5000, Re = 1050, \Gamma = \pi/2$, (a) $t \in [0, 800]$, (b) $t \in [0, 68750]$. The open black circles represent the unstable equilibria of longitudinal rolls and the laminar state. Note that the black-crosses, labelled by (T1-4) and (LR1-4), refer to temporal snapshots in figure 3.11, not equilibria solutions.	74
3.13 The thermally-assisted sustaining process (TASP).	75

<p>3.14 The behaviour of the unstable and stable longitudinal rolls at $Ra = 8000, 4000$ for (a,e) $Re = 600$, (b,f) $Re = 700$, (c,g) $Re = 1000$ and (d,h) $Re = 1400$ within $\Gamma = \pi/2$. Each parameter combination consist of three panels, depicting the (top) midplane temperature space-time plot, (mid) time history of the Nusselt number and shear, and (bottom) state space projection based on the planar averaged centerline velocity and shear, coloured by the volume normalised perturbation kinetic energy. 77</p> <p>3.15 A state space sketch of figure 3.14 at $Ra = 8000$, (a) $Re = 600$, (b) $Re = 700$, (c) $Re = 1000$, (d) $Re = 1400$ and $Ra = 4000$ at (e) $Re = 600, 700$, (f) $Re = 1000$, (g) $Re = 1400$. The longitudinal roll is linearly unstable (saddle) at $Ra = 8000$, and is stable at $Ra = 4000$, whereas the laminar state is always linearly unstable (saddle). The blue and orange solid arrows refer to the unstable manifold of longitudinal rolls and the laminar state. The red solid lines denote the chaotic trajectories of turbulence, likely forming a chaotic saddle at $Re = 1000$ and a chaotic attractor at $Re = 1400$. The black-dashed trajectories refer to possible solution trajectories, forming a periodic orbit (P.O) at $Ra = 8000$, $Re = 600, 700$, and a basin of attraction (B.o.A) at $Ra = 8000, Re = 1000$. We note that invariant states could exist at $Ra = 4000, Re = 600, 700$, labelled as a saddle here (Paranjape, Yalniz, Duguet, Budanur, & Hof, 2023). 79</p> <p>3.16 The temperature space-time plots and time history of (τ_w, Nu), for $Ra \in [5000, 10000]$, $Re \in [600, 1400]$ within $\Gamma = \pi/2$. Unstable longitudinal rolls lead to the onset of (1) periodic orbits (yellow), (2) the <i>thermally-assisted sustaining process</i> (green), and (3) sustained turbulence (blue), occurring beyond an $Ra - Re$ boundary, below which longitudinal rolls remain stable (red). 81</p> <p>3.17 The midplane temperature space-time plot, and near-wall wall-normal and spanwise perturbation kinetic energy by normalised by thermal velocity scale, u_κ, and the probability density functions based on planar-averaged centerline velocity and the midplane temperature for $Ra = 10000$ at (a) $Re = 500$, (b) $Re = 750$, (c) $Re = 1000$ and (d) $Re = 1050$. 82</p> <p>4.1 Midplane temperature snapshots, $\theta(x, z) _{y=d/2}$, of spiral defect chaos (SDC) for a domain aspect ratio of (a) $\Gamma = 16\pi$ and (b) 8π. Elementary states of SDC captured when $\Gamma = 4\pi$: (c) steady <i>pacman</i> (PM), (d) relative periodic orbit <i>spiral-defect</i> (SD), (e) relative periodic orbit <i>hooked</i> (HK), and (f) periodic <i>peanut</i> (PN) elementary state. Note that the localised structures indicated by bounding boxes in (a,b) resemble structures in (c-f). Snapshots are captured at 300 diffusive time units, t. 90</p> <p>4.2 (a,b) Time history of the volume ($\bar{V} = L_x L_y L_z$) normalised L2-norm of velocity perturbations from a random initial condition with $\delta = 0.001$ and (c-g) Mid-plane temperature snapshots at $t = 6, 15, 30, 79, 250$. Here, transient chaotic SDC lasts up to $t \approx 70$, before stabilising into an SD state, emerging as a relative periodic orbit with the time period $T \approx 75$ propagating diagonally in the negative x- and z-directions. 91</p>	<hr/>
---	-------

4.3	(a) State-space portrait in the plane of $\ \frac{1}{V}\tilde{\mathbf{u}}\ _2$ and $\ \frac{1}{V}RaPr\tilde{\theta}\ _2$ for SDC from $\Gamma = 16\pi, 8\pi$ (figures 4.1(a,b)), four transient SDC state proceeding to stable elementary states (figures 4.1(c-f), A.6), and fourteen stable stationary ISRs of wavenumbers $2.0 \leq qd \leq 3.35$. Here, the magnitude of q is denoted by the opacity of the filled symbol (●), increasing from the bottom left and turning toward the top left shown as arrows; (b) Zoomed-in view of (a). The legend refers to the figures for respective trajectories preceding snapshots in figure 4.1.	91
4.4	State-space portrait (from figure 3) highlighting the transient SDC states for $\Gamma = 4\pi$ proceeding toward stable elementary states (see figures 4.1(c-f), A.6): steady states (■), travelling waves (×), periodic orbit (dash-dotted line) and relative periodic orbits (solid lines).	93
4.5	Profiles of (a) averaged temperature, (b) root-mean-squared temperature fluctuation, (c) sum of root-mean-squared x - z velocity fluctuations and (d) root-mean-squared wall-normal velocity fluctuations for the SDC and elementary states shown in figures 4.1(a-f) and in Appendix A.5. Note that $\langle \cdot \rangle = \frac{1}{TL_x L_z} \int_{t,x,z} dt dx dz$ refers to the time and plane averaged operator, where T was chosen to be sufficiently long to ensure temporal convergence.	94
4.6	Mid-plane termperature fields of ISRs and elementary states used in Eq. (4.8), and the resulting edge states. Here, ISRs (green borders): (a) $s_{ISR,q=2.06/d}$, (b) $s_{ISR,q=2.24/d}$, (c) $s_{ISR,q=3.16/d}$; elementary states: (d) s_{pacman} , (e) $s_{spiral-defect}$; edge states (black borders): (f) <i>jagged</i> , (g) <i>point-defect</i> , (h) <i>forked</i> and (i) <i>skewed-varicose</i> edge state.	96
4.7	(a) Time history of Nu and (b-e) the corresponding mid-plane temperature field snapshots at $t = 2.0, 6.5, 31.0, 65.5$ along the edge trajectory obtained by bisecting $s_{ISR,q=2.06/d}$ and $s_{spiral-defect}$	97
4.8	Time history of Nu along two opposite directions along the unstable manifold of the <i>jagged</i> edge state: (a) ‘upper’ trajectory leading to a transient SDC for $t \approx 85 - 120$ and subsequently to PM state for $t > 120$ and (f) ‘lower’ trajectory stabilising into $s_{ISR,q=2.06/d}$. Mid-plane temperature fields are visualised in (b-e) along the upper trajectory at $t = 80.5, 90.5, 125.5, 170.5$, and in (g-j) along the lower trajectory at $t = 70.5, 75.5, 80.5, 85.5$	98
4.9	a) Time history of Nu and (b-e) the corresponding mid-plane temperature field snapshots at $t = 4, 13, 22.5, 40.5$ along the edge trajectory obtained by bisecting $s_{ISR,q=2.24}$ and $s_{spiral-defect}$	99
4.10	Time history of Nu along two opposite directions of the unstable manifold of the <i>point-defect</i> edge state: (a) ‘upper’ trajectory leading a stationary elementary state with bubble defect from $t \approx 43 - 163$ and (f) ‘lower’ trajectory decaying to the stable $s_{ISR,q=2.24}$ state. Mid-plane temperature fields are visualised in (b-e) along the upper trajectory at $t = 43.0, 58.0, 83.0, 163.0$, and in (g-j) along the lower trajectory at $t = 38.0, 43.5, 44.5, 53.0$	100

4.11	Phase portrait of the <i>jagged</i> , <i>point-defect</i> , <i>defect</i> and <i>skewed-varicose</i> edge states, along with stable ISRs, elementary states and transient SDC. Green and grey horseshoe lines are the regions, where stable ISRs and edge attractors are expected to be distributed when different sizes of the computational domain are considered.	101
4.12	(a) Primary and secondary (Busse balloon from figure 1 (Decker, Pesch, & Weber, 1994)) stability curves and unstable ISRs with $q = 3.5/d, 4.0/d, 4.5/d$; (b) Variation of the growth rate of instabilities of unstable ISRs as a function of spanwise wavenumber β . (Note that there are a total 13 unstable eigenmodes.)	103
4.13	The phase-space solution trajectories connecting: (a) unstable base (conductive) state between 10 unstable rolls ($q = 5/d$), 7 unstable rolls ($q = 3.5/d$) and 5 stable rolls ($q = 2.5/d$); (b) unstable base (conductive) state between 8 unstable rolls ($q = 5/d$) and 6 stable rolls ($q = 3.16/d$); (c) unstable base (conductive) state between 9 unstable rolls ($q = 4.5/d$) and 6 stable rolls ($q = 3/d$). Here, the size of the arrows indicates the speed of the solution trajectory (or flow).	104
4.14	Asymptotic behaviour of the linear instability ($\hat{q}_{\beta=0.50}$) about unstable ISR $q = 3.5/d$. (a) Modal energy $E_k(t)$, and temperature snapshots, $\theta(x, z) _{y=d/2}$ at (b) $t = 33$, (c) $t = 48.5$, (d) $t = 60$	105
4.15	Asymptotic behaviour along the linear instability of $\hat{s}_{\beta=1.75}$ about unstable ISR $q = 4.5/d$. (a) Modal energy $E_k(t)$, and temperature snapshots $\theta(x, z) _{y=d/2}$ at the onset of secondary instability at (b) $t = 1.25$, (c) $t = 7$, following a transient SDC behaviour at (d) $t = 40$, and settling into a elementary state at (e) $t = 100$, (f) $t = 150$ and (g) $t = 201.75$	107
4.16	State space visualisations using $\ \frac{1}{V}\tilde{\mathbf{u}}\ _2$ and $\ \frac{1}{V}RaPr\tilde{\theta}\ _2$, of SDC, and 14 elementary states with colour schemes based upon figure 4.4. The trajectories of two linear instabilities (purple) $\hat{s}_{\beta=1.25}$, (brown) $\hat{s}_{\beta=1.75}$ about an unstable ISR $q = 4.5/d$ leading to elementary states (see figures 4.15) are shown.	108
4.17	Asymptotic behaviour along the linear instability $\hat{s}_{\beta=1.75}$ about unstable ISR $q = 4.50/d$, in an extended domain $\Gamma = 4\pi$. (a) Modal energy $E_k(t)$, and temperature snapshots $\theta(x, z) _{y=d/2}$, at (b) $t = 1.25$, (c) $t = 7$, (d) $t = 40$, (e) $t = 100$, (f) $t = 125$, (g) $t = 150$	109
4.18	State space sketch containing the base, stable and unstable ISRs, edge, elementary states and SDC in a confined domain. Open circles, (\circ) and filled circles/squares (\bullet, \blacksquare) refer to unstable and stable states. Solid $(-)$ and dashed lines $(--)$ are the solution trajectories along the primary and secondary instabilities respectively, $\lambda_{max}^{Pri,Sec}$ refers to the most unstable primary and secondary linear instability manifolds. Blue, orange and green trajectories denote heteroclinic connections leading toward stable ISRs (trajectories labelled (A-G) and colors adapted from figure 4.13). Dashed-dotted trajectories $(-\cdot-)$ refer to solution trajectories emerging from the edge states (color-coded from figure 4.11). The dotted line (\cdots) represents the boundary between ISRs and SDC, consisting of many stable elementary states.	110

A.1 The wall-normal distribution of temporal and plane- averaged (a) streamwise velocity, (b) temperature, (c) fluctuating wall-normal velocity squared normalised by thermal velocity scale, (d) fluctuating temperature squared and (e) fluctuating span- and streamwise velocities squared normalised by thermal velocity scale of buoyancy- driven regime shaded in red in figure 3.1.	117
A.2 The wall-normal distribution of temporal and plane- averaged (a) streamwise velocity, (b) temperature, (c) fluctuating streamwise velocity squared, (d) fluctuating wall- normal velocity squared, (e) fluctuating spanwise velocities squared, (f) fluctuating Reynolds stresses and (g) fluctuating temperature squared in the shear-driven regime shaded in blue in figure 3.1.	119
A.3 Spacetime plots of near-wall, wall-normal and spanwise perturbation kinetic energy for $Re = 2000$, $t \in [0, 2800]$, $\Gamma = 4\pi$ at (a) $Ra = 10000$, (b) $Ra = 8000$, (c) $Ra = 5000$, (d) $Ra = 3000$, (e) $Ra = 2000$, (f) $Ra = 0$	120
A.4 Growth rates of primary instabilities at $Ra = 10000, 8000, 5000, 3000, 2000$ leading to the onset of longitudinal rolls against spanwise wavenumber of αd at $Re = 1050$. .	121
A.5 Eigenvalues of primary instabilities of RBC at $\varepsilon = 0.7$ computed in Nektar++ compared against a Chebyshev-collocation method with 101 Chebyshev expansions.	121
A.6 Temperature snapshots, $\theta(x, z) _{y=d/2}$, of 10 elementary states confined within a minimal domain $\Gamma = 2\pi$: (a) steady ‘forked-A’ state, (b) steady ‘forked-B’ state, (c) steady ‘forked-c’ state, (d) steady ‘twin-armed’ state, (e) steady ‘tri-rolls’ state, (f) travelling-wave ‘O-a’ state, (g) travelling-wave ‘O-b’ state, (h) steady ‘keyhole’ state, (i) relative periodic orbit ‘eye’ state, (j) relative periodic orbit ‘S’ state	122
A.7 Temperature snapshots, $\theta(x, z) _{y=d/2}$, of 14 stable ideal straight rolls (ISRs) confined within a minimal domain, $\Gamma = 6.28$. Plots (a-n) are ordered in increasing wavenumbers, $q \in (2/d, 3.35/d)$	123

List of Tables

2.1	Examples of weight functions and projection methods	26
2.2	Integration coefficient of stiffly stable schemes from G. E. Karniadakis, Israeli, and Orszag (1991).	44
4.1	A summary of the edge states computed. The first two columns denote the pair of initial conditions considered for edge tracking in Eq. (4.8). The names and classification of the edge states are described in the third column. The last column describes the state transitioned from $\mathbf{s}_{ISR,q}$ for sufficiently large χ in Eq. (4.8).	96
4.2	Asymptotic state of secondary linear instabilities of $q = 3.5/d, 4.0/d, 4.5/d$. Subscripts in ISR refer to asymptotic wavenumber q , e.g., ISR _{2.5} refers to ideal straight rolls with wavenumber of $q = 2.5/d$. The asymptotic behaviours of (a-c) and (d,e) are discussed further in §4.5.1 and §4.5.2 respectively.	103
A.1	The summary of the spatial and temporal resolution for a given Re, Ra . N_z denotes the number of Fourier expansions in the z -direction. $dt, T, d/\kappa$ denotes the timestep, final time and the final time scaled by the thermal timescale.	116

Chapter 1

Introduction

1.1 Overview

Fluid motions driven by buoyancy and frictional forces belongs to class of flows known as thermoconvective shear flows. These flows exhibit rich behaviour, and are of interest in both engineering and meteorology applications spanning across a broad range of length scales.

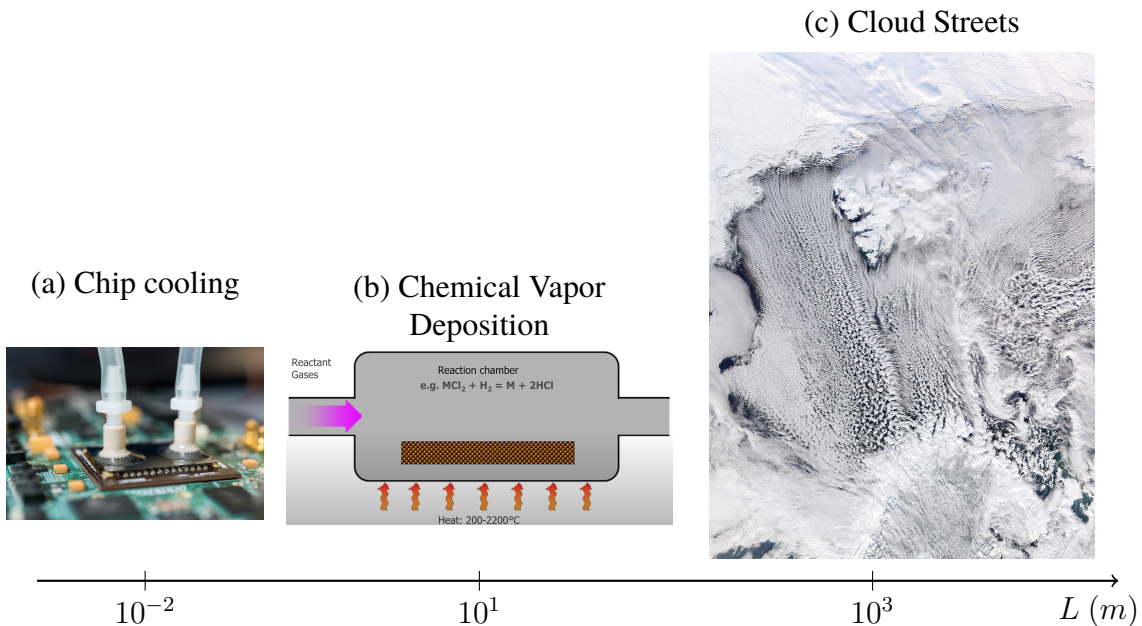


Figure 1.1: Thermoconvective shear flows driven by shear and buoyancy forces across length scales, $L \in [10^{-2} m, 10^3 m]$. Examples include (a) chip cooling, (b) chemical vapour deposition and (c) the formation of cloud streets.

At small scales, around $L \sim 10^{-2} m$, thermoconvective flows are relevant to the cooling of microprocessing chips. The fluid, acting as a medium for dissipating heat, experiences shear and buoyancy forces from the confining walls, and heating. One of the major challenge in this industry is on increasing the density of transistors on a single chip, alluding to Moore's Law, predicting the doubling of transistors on a single chip approximately every two years. One of the major limitations is the challenge of dissipating the excessive heat generated from the densely packed transistors. Fluids,

such as air, water or refrigerants, are often used to transport heat away from the components, and their transport behaviour under the influence of buoyancy and shear remains an open topic ([Kennedy & Zebib, 1983](#); [Ray & Srinivasan, 1992](#)).

At intermediate length scales, $L \sim 1m$, the interaction between buoyancy and frictional forces is important in the fabrication of uniform thin films in chemical vapour deposition (CVD) ([Evans & Greif, 1991](#); [Jensen, Einset, & Fotiadis, 1991](#)). The CVD process typically involves a reactive gases carried by inert gases which flows through a channel with a heated substrate. Upon heating, the reactant gases react chemically on the substrate, depositing material and forming thin films, such as silicon layers. A key challenge in the CVD process is achieving a uniform deposition and maintaining sharp interfaces between layers. The interactions between shear and buoyancy forces often gives rise to boundary layers and thermoconvective rolls, which can disrupt uniform deposition, affecting film quality.

At larger length scales, $L \sim 10^3 m$, the thermoconvective shear flows can be observed in atmospheric flows such as the cloud streets over the Norwegian Sea. These parallel bands of cumulus clouds can stretch over hundreds of kilometres. They form when the relatively warmer sea surface heat up the colder air arriving from the North pole. As the colder air is heated, it rises upwards whilst carrying water vapour, condensing into visible clouds. This circulation is organised into parallel rotating parallel columns of air, forming distinct cloud streets.

The central focus of this thesis is on the investigation of fluid behaviour arising from the interaction between shear and buoyancy forces, a common thread among the physical examples discussed above. We note that by isolating our analysis to the interaction between shear and buoyancy forces, we might neglect other physical mechanisms such as phase change, chemical reactions and evaporation, which may be significant in the context of cooling microprocessors, chemical vapour deposition, and atmospheric boundary layers respectively ([Vallis, Parker, & Tobias, 2019](#)). Nonetheless, the interaction between shear and buoyancy forces remains an open topic and will be the primary focus of this thesis, providing a foundation for future investigations that may include addition mechanisms.

To consider this interaction, we consider an idealised setup, known as the Rayleigh-Bénard-Poiseuille (RBP) flow. This RBP system describes the fluid motion confined between two infinitely extended parallel plates, heated from below and cooled from the top, with an additional pressure gradient driving the flow. The RBP configuration combines the two paradigmatic flow configurations; the classical Rayleigh-Bénard convection (RBC) and plane Poiseuille flow (PPF), driven by buoyancy and shear, respectively. While the onset of convection in RBC, and the transition to subcritical shear-driven turbulence in PPF have been both extensively studied, the transitional regime in which both forces interact remains less understood. Understanding their transitional behaviour and transport properties could have direct implications for the physical examples mentioned above.

The RBP configuration is illustrated in figure 1.1, where z, y, x refer to spatial coordinates denoting the streamwise, spanwise and wall normal directions. L_z, L_x, d and h corresponds to the length, span, depth and half-height of the domain respectively. The RBP system is biperiodic along z and x . The flow is driven by a pressure gradient along the streamwise z direction, $\Delta P = P|_{z=0} - P|_{z=L_z} < 0$, leading to a laminar Poiseuille flow, $w(y) = W_c(1 - y^2)$, where W_c is the laminar centerline velocity.

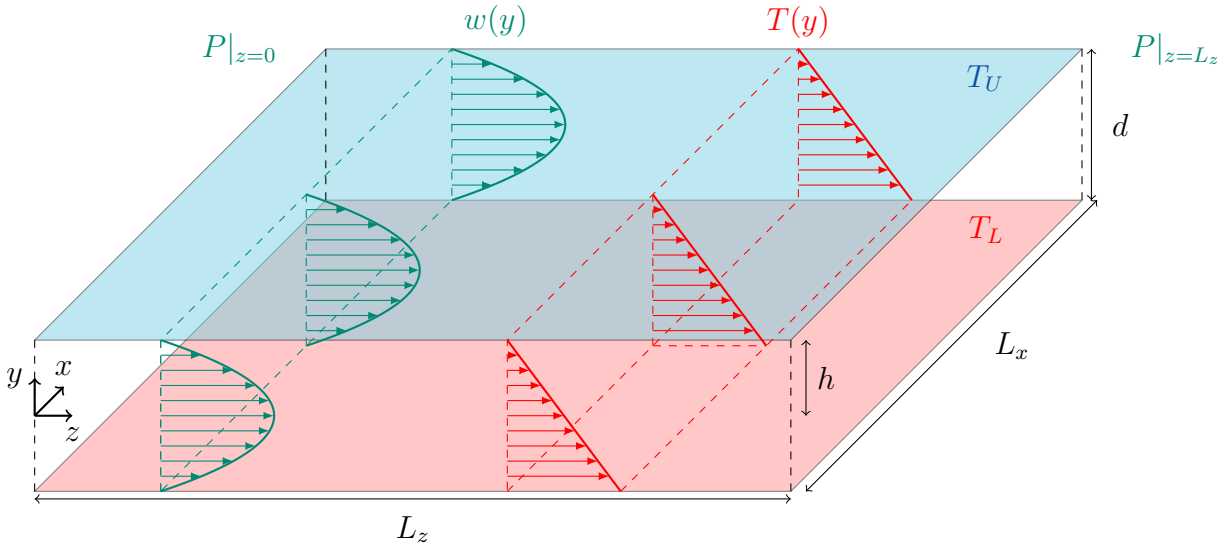


Figure 1.2: The Rayleigh-Bénard Poiseuille (RBP) flow configuration.

We consider a fully developed flow, where the boundary layer developing from the top and the bottom wall meets at the midplane $y = 0$ and entrance effects are therefore neglected. Like the RBC system, the RBP system is unstably stratified. The temperature difference between the lower, T_L , and upper wall, T_U , is always positive, $\Delta T = T_L - T_U > 0$, leading to a stable linear conduction layer along the wall-normal direction, $T(y)$, if ΔT is kept sufficiently small. The behaviour of RBP flows is governed by four dimensionless parameters,

$$Re = W_c h / \nu, \quad Ra = \frac{\eta g d^3 \Delta T}{\nu \kappa}, \quad Pr = \frac{\kappa}{\nu}, \quad \Gamma = L / 2d, \quad (1.1)$$

where Re , Ra , Pr , Γ refers to Reynolds, Rayleigh, Prandtl numbers and aspect ratio and η , g , ν , κ , are the thermal expansion coefficient, acceleration due to gravity, kinematic viscosity, thermal diffusivity, respectively. The Reynolds number, Re , and the Rayleigh number, Ra , are dimensionless parameters that characterise the relative influence of shear and buoyancy respectively. For sufficiently large values of Re and Ra , RBP flows may undergo a transition to shear-driven turbulence or convection-driven convection. In the absence of shear, $Re = 0$, the RBP configuration reduces to the classical buoyancy driven Rayleigh-Bénard convection, which forms a bistable system between stationary and chaotic convection rolls slightly above the critical Ra . The influence of Re on bistability remains unexplored.

In the first part of this thesis, we focus on the transitional regime by investigating whether buoyancy forces promote the transition to shear-driven turbulence and examining the effect of shear on convection in large domains. The second part of this thesis explores the state space structure of a bistable system between a chaotic convection roll state and a stationary convection roll state (see spiral defect chaos and ideal straight rolls in §1.3) of Rayleigh-Bénard convection.

The structure of this introductory chapter is as follows: we begin our discussion on the development of hydrodynamic stability theory of wall-bounded shear flows in §1.2. Theoretical frameworks used in the study of the stability of fluid flow, including linear modal/non-modal stability, nonlinear dynamical systems and the spatio-temporal dynamics of transitional shear flows will be discussed. Throughout

§1.2, we apply these concepts in the context of plane Poiseuille flows (PPF). This followed by the developments of Rayleigh-Bénard convection (RBC) in §1.3. Finally, we review the developments in RBP flows §1.4, before concluding this chapter with an outline of the thesis in §1.5.

1.2 Transitional wall-bounded shear flows

Wall-bounded shear flows concerns the motion of the fluid flowing in parallel to walls, typically bounded by one or more walls. Near the wall, the fluid comes to rest due to the no-slip boundary condition, resulting in a velocity gradient perpendicular to the wall, giving rise to shear within the fluid, commonly known as *wall-bounded shear flows*. Examples include the pressure-driven plane Poiseuille flow (channel flow), Hagen-Poiseuille flow (pipe flow), plane Couette flow and flat plate boundary layers. These geometrically simple configurations provides a convenient framework amenable to the mathematical analysis of fluid motion subjected to shear. Depending on the degree of shear, the fluid motion can be either laminar, where the fluid layers move in smooth parallel 'laminates', or turbulent, characterised by chaotic eddying motions. We also note that there is a transitional regime where both states can coexist discuss later. A central question is predicting the transition from the laminar regime to the turbulence.

The first investigation into this transition was conducted by [Reynolds \(1883\)](#). In his experimental setup, the flow speed through the pipe could be controlled by regulating the inlet pressure, while injecting dye to visualise the flow, as illustrated in figure 1.3(a). At low speeds, the fluid remained laminar, resulting to a single streak of steady dye in figure 1.3(b). As the speed increased, the dye begin to exhibit irregular 'sinuous' motions interspersed with laminar regions shown in figure 1.3(c). This is now referred to as the transitional regime, alternating between the laminar and turbulent states. Beyond a critical speed, the dye breaks down entirely into chaotic 'eddies', mixing with the surrounding fluid and discolouring the flow with dye downstream in figure 1.3(d). This regime is now identified as turbulence.

Reynolds proposed that the threshold between the laminar, transitional and turbulent regimes could be characterised by a non-dimensional parameter, now referred to as the Reynolds number,

$$Re = UD/\nu, \quad (1.2)$$

where U is the centerline velocity in the pipe, D , the pipe diameter and ν , the kinematic viscosity. He observed that flow through the pipe remained *stable* and laminar for $Re < 1900$, while it became *unstable* and turbulent for $Re > 2000$ ([Reynolds, 1895](#)), introducing the notion of flow *stability*.

1.2.1 Linear Stability Analysis

Following Reynolds' experiment, interest towards the mathematical analysis of the stability of laminar flows grew in early 20th century. The mathematical approach typically begins by decomposing the velocity field, $\mathbf{u}(\mathbf{x}, t)$, into a laminar (base) state, $\mathbf{U}(y)$, and the velocity perturbations, $\mathbf{u}'(\mathbf{x}, t)$, with

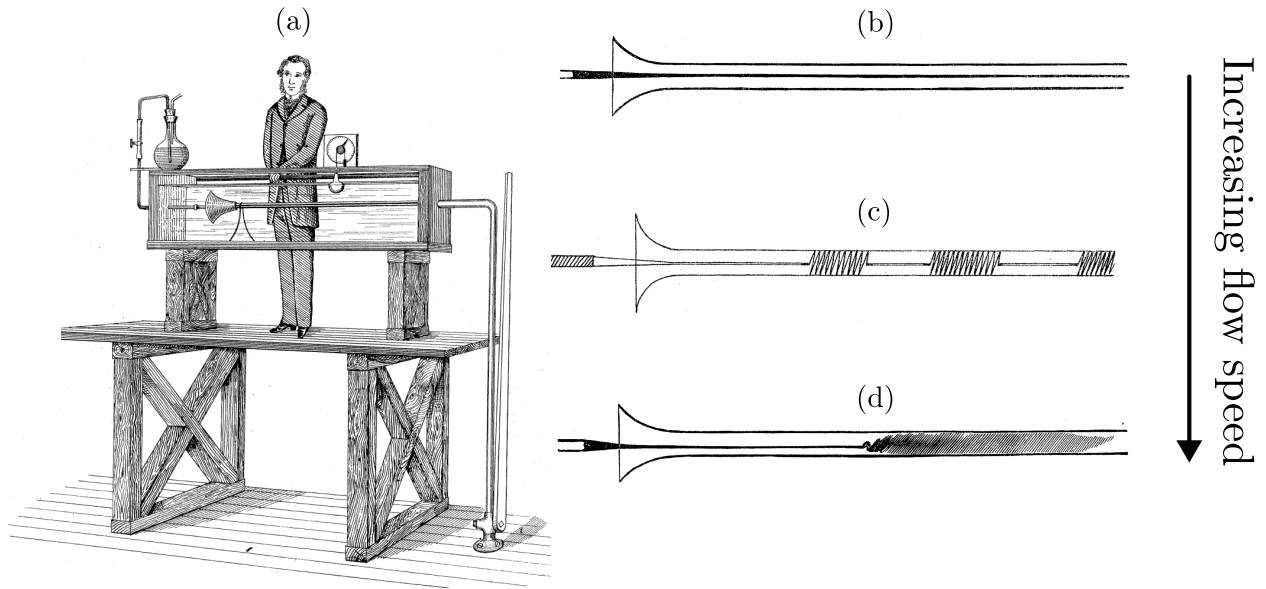


Figure 1.3: (a) Osbourne Reynolds pipe experiment with the dye injection apparatus, illustrating the (b) laminar flow, (c) transitional regime and (d) turbulent flow as the flow speed is increased, taken from [Reynolds \(1883\)](#).

pressure similarly decomposed as,

$$\mathbf{u}(\mathbf{x}) = U(y) + \mathbf{u}'(\mathbf{x}, t), \quad \text{and} \quad p(\mathbf{x}, t) = P(x) + p'(\mathbf{x}, t). \quad (1.3)$$

Substituting into the Navier-Stokes equations and linearising (neglecting nonlinear terms), we get,

$$\frac{\partial \mathbf{u}'}{\partial t} + (U \cdot \nabla) \mathbf{u}' + (\mathbf{u}' \cdot \nabla) U = -\nabla p' + \frac{1}{Re} \nabla^2 \mathbf{u}', \quad (1.4a)$$

$$\nabla \cdot \mathbf{u}' = 0, \quad (1.4b)$$

known as the linearised Navier-Stokes equations. This commonly followed by introducing a wavelike ansatz (mode) for the perturbations, and analysed by considering their behaviour independently, referred to as modal analysis in §1.2.1, or their coupled dynamics, referred to as non-modal analysis in §1.2.1.

Modal analysis

It is convenient to eliminate the pressure terms by reformulating equation (1.4) using the wall-normal perturbation velocity, v' , and wall-normal vorticity, $\eta' = \partial u'/\partial z - \partial w'/\partial x$, variables. Using (v, η) , we introduce a modal ansatz for them,

$$v'(\mathbf{x}, t) = \tilde{v}(y) e^{i(\alpha x + \beta z - \omega t)}, \quad \text{and} \quad \eta'(\mathbf{x}, t) = \tilde{\eta}(y) e^{i(\alpha x + \beta z - \omega t)}. \quad (1.5)$$

where α, β, ω denotes the streamwise and spanwise wavenumbers, and complex frequency (i.e. $\omega = \omega_r + i\omega_i$), respectively. Substituting this ansatz into linearised equations lead to the classical Orr-

Sommerfeld and Squire equations ([Orr, 1907](#); [Schmid & Henningson, 2001](#); [Sommerfeld, 1909](#); [Squire, 1933](#)),

$$\begin{pmatrix} \mathcal{L}_{OS} & 0 \\ i\beta U' & \mathcal{L}_{SQ} \end{pmatrix} \begin{pmatrix} \tilde{v} \\ \tilde{\eta} \end{pmatrix} = i\omega \begin{pmatrix} k^2 - \mathcal{D}^2 & 0 \\ 0 & 1 \end{pmatrix} \begin{pmatrix} \tilde{v} \\ \tilde{\eta} \end{pmatrix}. \quad (1.6a)$$

with

$$\mathcal{L}_{OS} = i\alpha U(k^2 - \mathcal{D}^2) + i\alpha U'' + \frac{1}{Re}(k^2 - \mathcal{D}^2)^2, \quad \mathcal{L}_{SQ} = i\alpha U + \frac{1}{Re}(k^2 - \mathcal{D}^2). \quad (1.6b)$$

where $\mathcal{D} = d/dy$, $k^2 = \alpha^2 + \beta^2$ and U'' is the second derivative of $U(y)$. Equation (1.6a) is a generalised eigenvalue problem with eigenvalue $i\omega$, which determines the growth of perturbations.

The goal of modal stability analysis is to determine the critical Reynolds number Re_c , defined as the lowest value of Re , for all α and β in which $\Im[\omega] = 0$. For $Re > Re_c$, perturbations can grow exponentially, indicating instability. Squire's theorem states that for every unstable three-dimensional perturbation, there exist an unstable two-dimensional perturbation, with a lower Re_c ([Squire, 1933](#)). This implies that the most linearly unstable perturbation of wall-bounded flows is two dimensional. Calculations by [Tollmien \(1928\)](#) and [Schlichting \(1933\)](#) for a flat-plate boundary layer flow yielded a critical Reynolds number based on displacement thickness, δ^* , of $Re_{ind} = U_\infty \delta^* / \nu = 520$ ¹ ([Schlichting & Gersten, 2017](#)). These two dimensional unstable eigenmodes are known as Tollmien-Schlichting (T.S) waves. In plane Poiseuille flow, the critical Reynolds number is $Re_c = 5772.2$ with a critical wavenumber of $\alpha_c = 1.02$ ([Orszag, 1971](#)). However, experiments reveal that transition to turbulence can occur at a lower Reynolds number, around, $Re \sim 1000 - 2000$ ([Davies & White, 1928](#); [Dean, 1978](#); [Iida & Nagano, 1998](#); [Patel & Head, 1969](#); [Tsukahara, Iwamoto, et al., 2014](#)), highlighting a key limitation of modal analysis. Similar discrepancies are observed in plane Couette and pipe flows ([Meseguer & Trefethen, 2003](#)), where the laminar state is linearly stable for all Re , yet transition to turbulence occurs. Despite these limitations, modal analysis predicts instabilities in other systems such as Rayleigh-Bénard convection and Taylor-Couette flow ([Chandrasekhar, 1968](#)). Further extensions of modal stability, including spatial instability analysis ([Huerre & Monkewitz, 1990](#)), and secondary instability ([Orszag & Patera, 1983](#)) are well established and are beyond the scope of this thesis.

Non-modal stability

One of a major limitations of modal analysis is that it treats each eigenmode independently. However, the interaction between decaying eigenmodes can lead to a transient growth, where perturbations amplify temporarily before decaying asymptotically. To demonstrate an example of transient growth, we consider a two-dimensional toy model governing the time-evolution of $\mathbf{q} = (v, \eta)^T$,

$$\frac{d}{dt} \begin{pmatrix} v \\ \eta \end{pmatrix} = \begin{pmatrix} -\frac{1}{Re} & -1 \\ 0 & -\frac{2}{Re} \end{pmatrix} \begin{pmatrix} v \\ \eta \end{pmatrix}, \quad (1.7)$$

¹In the literature of stability theory, Re_{ind} refers to the indifference Reynolds number which is similar to the critical Reynolds number, Re_c . However, boundary layer transition often takes place over a finite distance, and the indifference point is used to disambiguate between the onset of transition and the critical point of completed transition.

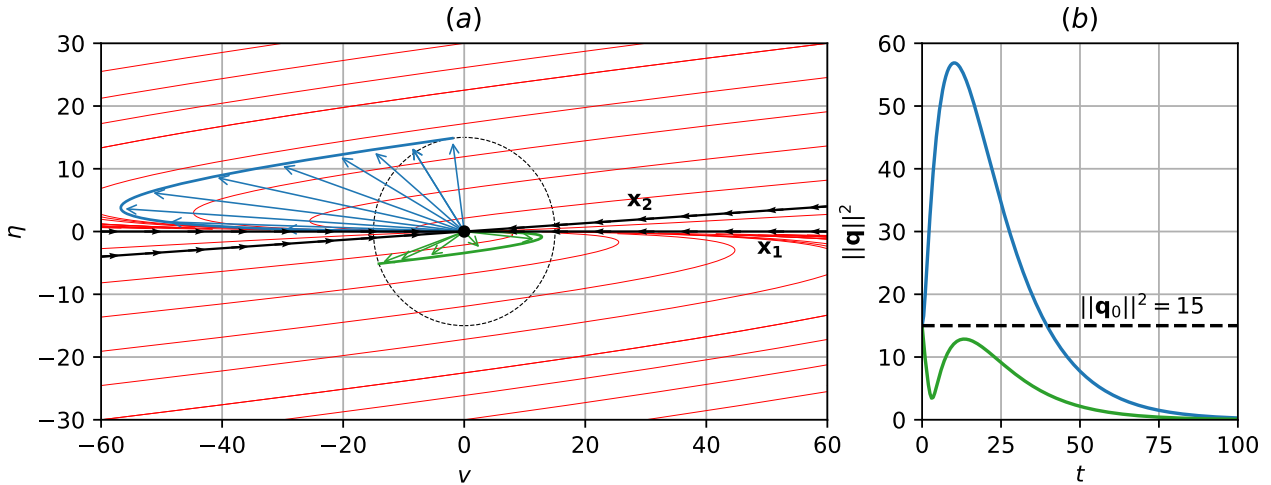


Figure 1.4: (a) The phase portrait of the toy model with $Re = 15$, where red lines are phase lines of the toy model. The blue trajectory lead to transient growth and the green trajectory do not (b) Time history of blue and green trajectory.

where Re refers to the Reynolds number. The toy model has negative eigenvalues, $(\lambda_1, \lambda_2) = (-1/Re, -2/Re)$, indicating asymptotic decay. At $Re = 15$, the eigenvectors, $\mathbf{x}_1 = (1, 0)$, $\mathbf{x}_2 = (1, \frac{1}{\sqrt{Re^2+1}})$, are highly non-orthogonal, becoming almost parallel shown in figure 1.4(a). Notably, they become increasingly linearly dependent as $Re \rightarrow \infty$. For a particular initial condition, the energy $\|q\|^2 = \sqrt{v^2 + \eta^2}$, is amplified four times before decaying in blue trajectory, shown in Figure 1.4(b). Yet for another choice of initial condition, the trajectory decays asymptotically as the green trajectory indicates. Despite decaying eigenmodes, the toy model highlights the significance of transient growth, which depends on the choice of initial condition.

The aim of non-modal stability analysis is to search for optimal initial conditions, $\tilde{\mathbf{q}}_0$, that leads to the maximum amplification, $G(\tau)$, over a time horizon τ . This is posed as an optimistaion problem,

$$G(\tau) = \max_{\tilde{\mathbf{q}}_0 \neq 0} \frac{\langle \tilde{\mathbf{q}}(\tau), \tilde{\mathbf{q}}(\tau) \rangle}{\langle \tilde{\mathbf{q}}_0, \tilde{\mathbf{q}}_0 \rangle}, \quad \text{s.t. } \langle \tilde{\mathbf{q}}_0, \tilde{\mathbf{q}}_0 \rangle = 1, \quad (1.8)$$

where, $\langle \cdot, \cdot \rangle$ denotes the inner-product,

$$\langle \tilde{\mathbf{q}}, \tilde{\mathbf{q}} \rangle = \int_{\Omega} \tilde{\mathbf{q}}^H \tilde{\mathbf{q}} d\Omega, \quad (1.9)$$

and $\tilde{\mathbf{q}}^H$ refers to the complex conjugate transpose of $\tilde{\mathbf{q}}$. By considering the linearised operator of (1.6a), we define a linear operator as,

$$\tilde{\mathbf{q}}(\tau) = \mathcal{A}(\tau) \tilde{\mathbf{q}}_0, \quad (1.10)$$

which takes the solution from initial conditions, $\tilde{\mathbf{q}}_0$, to $\tilde{\mathbf{q}}(\tau)$ at time τ . Subtituting the expression above into equation (1.8),

$$G(\tau) = \max_{\tilde{\mathbf{q}}_0 \neq 0} \frac{\langle \mathcal{A}(\tau) \tilde{\mathbf{q}}_0, \mathcal{A}(\tau) \tilde{\mathbf{q}}_0 \rangle}{\langle \tilde{\mathbf{q}}_0, \tilde{\mathbf{q}}_0 \rangle} = \langle \tilde{\mathbf{q}}_0, \mathcal{A}^\dagger(\tau) \mathcal{A}(\tau) \tilde{\mathbf{q}}_0 \rangle = \lambda_{max}(\mathcal{A}(\tau)^\dagger \mathcal{A}(\tau)), \quad (1.11)$$

where \mathcal{A}^\dagger refers to the adjoint of $\mathcal{A}(t)$. The maximum amplification factor $\max G(t)$ is the largest eigenvalue of $\mathcal{A}^\dagger(\tau)\mathcal{A}(\tau)$. The eigenvalue problem is given as,

$$\mathcal{A}^\dagger(t)\mathcal{A}(t)\tilde{\mathbf{q}}_0 = \lambda\tilde{\mathbf{q}}_0, \quad (1.12)$$

where $\tilde{\mathbf{q}}_0$ refers to the eigenvector denoting the optimal initial condition. For a detailed derivation of the optimal initial conditions or forcing, the reader is referred to [Butler and Farrell \(1992\)](#) and [Schmid \(2007\)](#). An alternative method of computing the optimal transient growth is by analysing the pseudospectral of linear operators discussed by [Trefethen \(1997\)](#).

Both two-, and three-dimensional non-modal analyses reveal mechanisms for transient growth. In two-dimensions, the optimal initial conditions are in the form of near wall vortices tilted upstream, which amplifies transiently via the Orr-mechanism ([Farrell, 1988](#); [Orr, 1907](#); [Reddy, Schmid, & Henningson, 1993](#)). In three-dimensions, streamwise vortices are optimal, leading to the the amplification of streamwise streaks via the well known lift-up effect ([Ellingsen & Palm, 1975](#); [Reddy & Henningson, 1993](#)). Notably, the spacing of these streaks analysed using non-modal analysis at higher Reynolds number has been consistently reported to occur around 100 wall units ([Del Álamo & Jiménez, 2006](#); [Hwang & Cossu, 2010](#); [Pujals, García-Villalba, Cossu, & Depardon, 2009](#)), which supports experimental observations of streak spacing in turbulent boundary layers ([Kline, Reynolds, Schraub, & Runstadler, 1967](#); [Smith & Metzler, 1983](#)).

The main results from non-modal analysis is that three dimensional perturbations can lead to strong transient growth at subcritical Reynolds numbers, contradicting the two dimensional TS waves from modal analysis. Both modal and non-modal mechanisms highlight important insights into the linear mechanisms which might be responsible for the transition from laminar to turbulent flows.

1.2.2 Nonlinear dynamical systems

In the previous section, we have examined the laminar to turbulent transition using linear frameworks. However, the the transition process is ultimately described by the nonlinear Navier-Stokes equations, which motivates the development and adoption of mathematical frameworks beyond linear methbods.

In the context of shear flow turbulence, there has been a growing interests in adopting techniques from nonlinear dynamical systems, interpreting turbulence as a chaotic trajectories which evolves within a finite-dimensional phase space. This phase space refers to a set of solutions satisfying the Navier-Stokes equations, first conjectured to be infinite dimensional by [Hopf \(1948\)](#). He postulated that within the infinite dimension phase space lie a finite dimensional manifold, whose properties depended on viscosity. For large viscosities (i.e. low Re), this finite dimensional space corresponds to a single point, the laminar state. This point may become linearly unstable at a certain critical Reynolds number, bifurcating to form new manifolds, as viscosity is decreased (i.e. Re is increased) further, potentially leading to chaos. The set of such manifolds is referred to *inertial manifolds*, and its existence under certain properties has been established ([Foias, Sell, & Temam, 1988](#)). An implication of this is that the transition to turbulence could be viewed as successive bifurcations from the laminar state, govern by a single control parameter (i.e. the Reynolds numnber), generalised by the so called

routes to chaos scenarios.

Landau (1944) proposed that the transition to turbulence may occur through a sequence of Hopf bifurcations, each introducing a new incommensurate frequency, resulting in quasi-periodic motions on a high-dimensional torus. However, this model did not capture the essential ingredients of turbulence, such as sensitivity of initial conditions and mixing (John, Gunter, & Maria, 1993). Ruelle and Takens (1971) later show that a *strange attractor*, exhibit the key features of chaos, can emerge after three successive Hopf bifurcations from a stationary state, referred to as the *Ruelle-Takens* route to chaos. This scenario has been observed in Taylor-Couette flow (Gollub & Swinney, 1975), and Rayleigh-Bénard convection (Swinney & Gollub, 1978). Other routes to chaos scenarios, such as periodic-doubling (Feigenbaum, 1979), and intermittency (Manneville & Pomeau, 1979) scenarios have been proposed. For a review of these routes to chaos scenarios, the reader is referred to John et al. (1993). Nonetheless, the transition to turbulence is subcritical in shear flow configurations, meaning that the route of chaos scenarios do not necessarily apply through bifurcations from the laminar state.

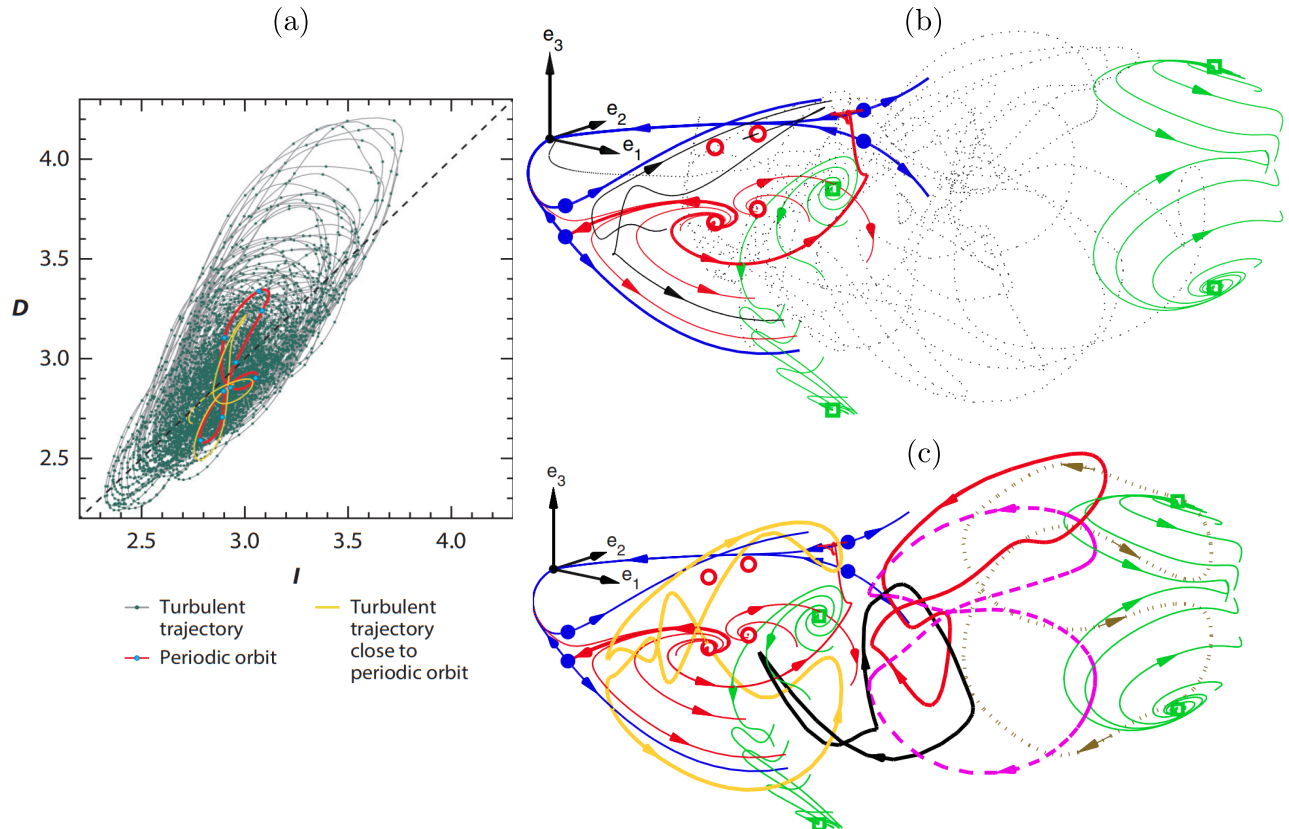


Figure 1.5: (a) Chaotic trajectories of plane Couette flow at $Re = 400$, approaching an unstable periodic orbit (red) highlighted as yellow, adopted from Kawahara and Kida (2001). (b) State space organisation of turbulence trajectories (black dots) confined around equilibria (circles, dots and squares) and their unstable manifolds (solid lines), heteroclinic connections between them are shown in red. The coordinate system, $(e_{1,2,3})$, is centered on the laminar state, using a linear combination of the upper branch invariant state. (c) State space projection of five periodic orbits (coloured solid lines), embedded within the same space where turbulence evolves in (b), adopted from Cvitanović and Gibson (2010).

A major development came with the identification of a pair of non-trivial, unstable equilibrium states in plane Couette flow (Nagata, 1990). This pair referred to as the *lower* and *upper* branches,

emerging from a saddle node bifurcation disconnected from the stable laminar state. The *lower* branch lies closer to the laminar state, while the *upper* branch resides further away in state space. Later, a travelling-wave solution in plane Couette flow also later found by the same author (Nagata, 1997). A family of equilibrium and travelling-wave solutions was found later for plane Couette and plane Poiseuille flows under different boundary conditions (i.e. stress-free, slip and no-slip) were identified by (Waleffe, 2001, 2003). Additional equilibria and travelling-wave solutions were identified by Gibson, Halcrow, and Cvitanović (2008, 2009), along with their heteroclinic connections between them (Halcrow, Gibson, Cvitanović, & Viswanath, 2009). In the context of pipe flow, multiple travelling-wave solutions have also been reported (Duguet, Willis, & Kerswell, 2008; Faisst & Eckhardt, 2003; Kerswell & Tutty, 2007; Pringle, Duguet, & Kerswell, 2009; Wang, Gibson, & Waleffe, 2007; Wedin & Kerswell, 2004). The set of equilibria, and travelling waves, shows good agreement with the statistical quantities (e.g. mean and fluctuations) with direct numerical simulations. However, since they time independent (within a moving reference frame for travelling waves), they do no capture the temporal dynamics of turbulence such as the *self-sustaining process* (SSP) (Hamilton, Kim, & Waleffe, 1995) (see §1.2.3). While these unstable solutions demonstrate good agreements with results from DNS such as the spanwise length scales, and mean and fluctuations, they do not capture the dynamical processes.

The next breakthrough was on the identification of time-dependent unstable solutions in the form of periodic orbits. Kawahara and Kida (2001) computed a pair of periodic orbits in plane Couette, with one exhibiting a single regeneration cycle similar to the SSP (see figure 1.5(a)) while the other exhibits mild modulation of streaks. These periodic orbits are linked by heteroclinic connections. In plane Poiseuille flow, Toh and Itano (2003) also identified periodic orbits displaying bursting behaviour. Using a Newton–Krylov iteration with a hook-step modification, Viswanath (2007) computed multiply relative periodic orbits. These studies conceptualise that the chaotic trajectories of turbulence as being embedded within a set of unstable periodic orbits, evolving along their unstable manifolds (Gibson et al., 2008, 2009; Graham & Floryan, 2021; Halcrow et al., 2009; Viswanath, 2007). An example is shown in figure 1.5, where the chaotic trajectories in figure 1.5(b), reside within the same state space as the periodic orbits, enclosed by equilibria and their heteroclinic connections shown in figure 1.5(c). The set of equilibria, travelling waves and their relative counterparts, are referred to as *invariant solutions* offering a building block description of turbulence. However, they do not provide insight into the transition process, since these solutions already reside in the turbulent attractor.

The transition to turbulence in canonical shear flow configurations are typically subcritical, emerging from the invariant solutions described above, accompanied by an underlying stable laminar state. A consequence of this is that the laminar and turbulent states form a bistable attractors in phase space with a boundary, separating their respective basins of attraction known as the *edge*. Attractors that sit along this edge have been identified and found to possess a saddle-like structure, attracting trajectories within the edge and repelling them toward either the laminar or turbulent state, known as *edge* states. The bisection algorithm used for edge tracking, was first employed in pipe flow experiments by Schneider, Eckhardt, and Yorke (2007), was identified to be chaotic. Time-averaging of this chaotic attractor revealed a close resemblance to the unstable lower branch travelling-wave

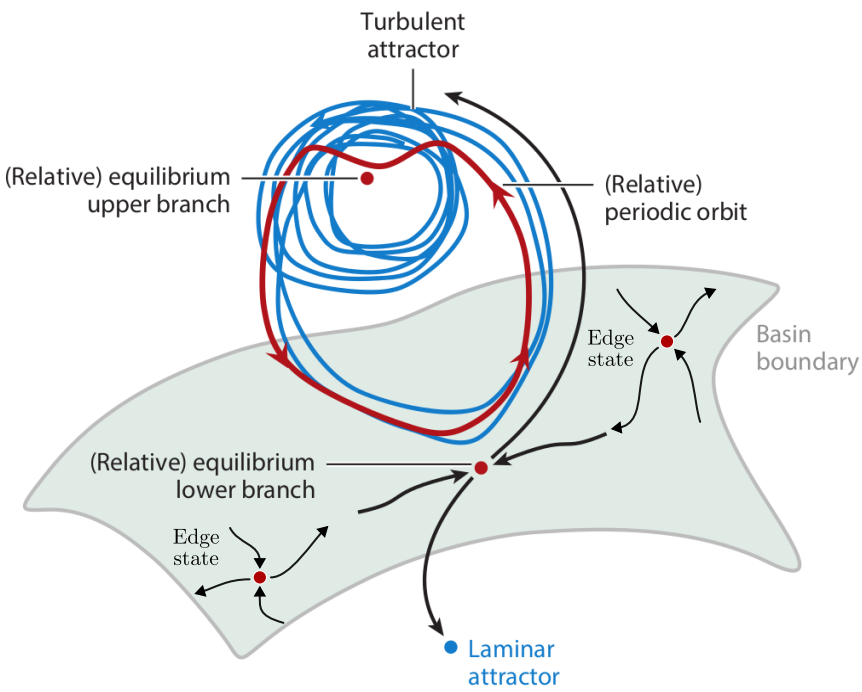


Figure 1.6: A graphical representation of the edge (grey surface) separating the basin of boundary of the laminar and turbulent attractor, consisting of attractors, known as edge states, adapted from [Graham and Floryan \(2021\)](#).

solutions, suggesting that the edge separating basin of attraction between the laminar and turbulent states consist of the lower branch solutions and their symmetries ([Duguet et al., 2008; Pringle et al., 2009](#)). As Reynolds number increases, the edge and the turbulent attractor moves apart ([Schneider & Eckhardt, 2009](#)). In the context of pipe flows, it was recognised that the edge consists of a set of unstable lower branch travelling-wave solutions. A graphical representation of the edge, and edge states, separating the laminar the turbulent states is shown in figure 1.6. Near the onset of subcritical turbulence, turbulence appear to be transient, decaying towards the laminar solution after a finite lifetime ([Bottin, Daviaud, Manneville, & Dauchot, 1998; Faisst & Eckhardt, 2004; Hof, Westerweel, Schneider, & Eckhardt, 2006](#)) This can be interpreted as the turbulent chaotic attractor colliding with the lower branch solution through a *boundary crisis* ([Lai & Tél, 2011](#)), forming a chaotic saddle where solution trajectories may ‘leak’ (relaminarise) towards the laminar state ([Kreilos & Eckhardt, 2012; Mellibovsky & Eckhardt, 2012; Zammert & Eckhardt, 2015](#)). The onset a boundary crisis (transient turbulence) have been also attributed to the emergence of homoclinic tangency in plane Couette flow ([Lustro, Kawahara, Van Veen, Shimizu, & Kokubu, 2019; Van Veen & Kawahara, 2011](#)).

1.2.3 Self-sustaining process

The self-sustaining process (SSP) describe the dynamical interaction between a pair of streaks and quasi-streamwise vortices, considered to be the fundamental process of wall bounded turbulent flows in the near wall region. It is defined by a quasi-cyclic process, consisting of three distinct phases: (1) the formation of streamwise streaks due to a linear advection by streamwise vortices, (2) the wavy

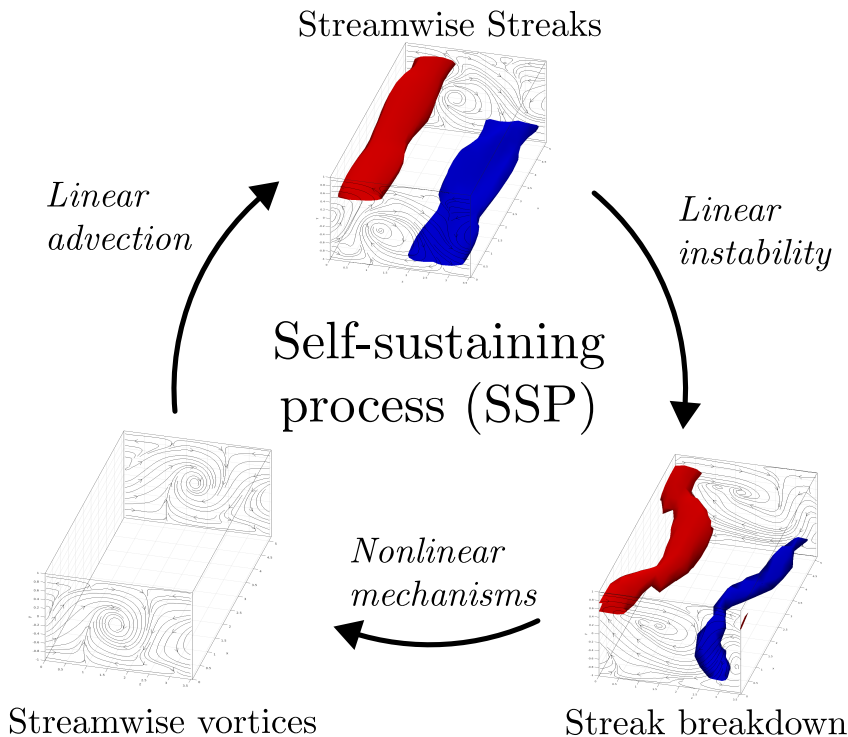


Figure 1.7: The self-sustaining process, consisting of three phases: (1) Streak formation from linear advection by streamwise vortices, (2) streak breakdown due to streak instability and (3) regeneration of streamwise vortices via nonlinear mechanisms.

breakdown of streaks due to linear instability and (3) the regeneration of streamwise vortices via nonlinear mechanisms (Hamilton et al., 1995; Waleffe, 1997; Waleffe, Kim, & Hamilton, 1993). A schematic of the SSP is shown in figure 1.7. While early investigations of the SSP was confined the buffer layer (Hamilton et al., 1995), evidence that the SSP extends towards the logarithmic and outer region has been found (Cossu & Hwang, 2017). In parallel to the SSP, the vortex-wave interaction (VWI) theory developed to describe the sustained interactions between a general class of vortices and waves for asymptotically large Reynolds number (Hall & Smith, 1988, 1990, 1991), was found to be linked to the SSP (Hall & Sherwin, 2010). In particular, the solutions obtained using VWI theory by Hall and Sherwin (2010) is analogous to the lower branch solution from Wang et al. (2007).

1.2.4 Spatiotemporal transitional flows

This section describes the inherent spatiotemporal structure of subcritical turbulence near the onset commonly reported in large extended domains. In this regime, turbulence is characterised by the coexistence of turbulent and laminar structures. Examples of such are found in canonical shear flow systems such as plane Couette flows (Barkley & Tuckerman, 2005, 2007; Duguet, Schlatter, & Henningson, 2010; Prigent, Grégoire, Chaté, & Dauchot, 2003; Reetz, Kreilos, & Schneider, 2019; Tuckerman & Barkley, 2011), Taylor-Couette flows (Prigent & Dauchot, 2002; Prigent et al., 2003), pipe flows (K. Avila et al., 2011; M. Avila, Barkley, & Hof, 2023; M. Avila, Willis, & Hof, 2010; Song, Barkley, Hof, & Avila, 2017) and plane Poiseuille flows (Gomé et al., 2020; Paranjape, 2019; Paranjape, Duguet, & Hof, 2020; Paranjape et al., 2023; Tsukahara, Iwamoto, et al., 2014; Tsukahara,

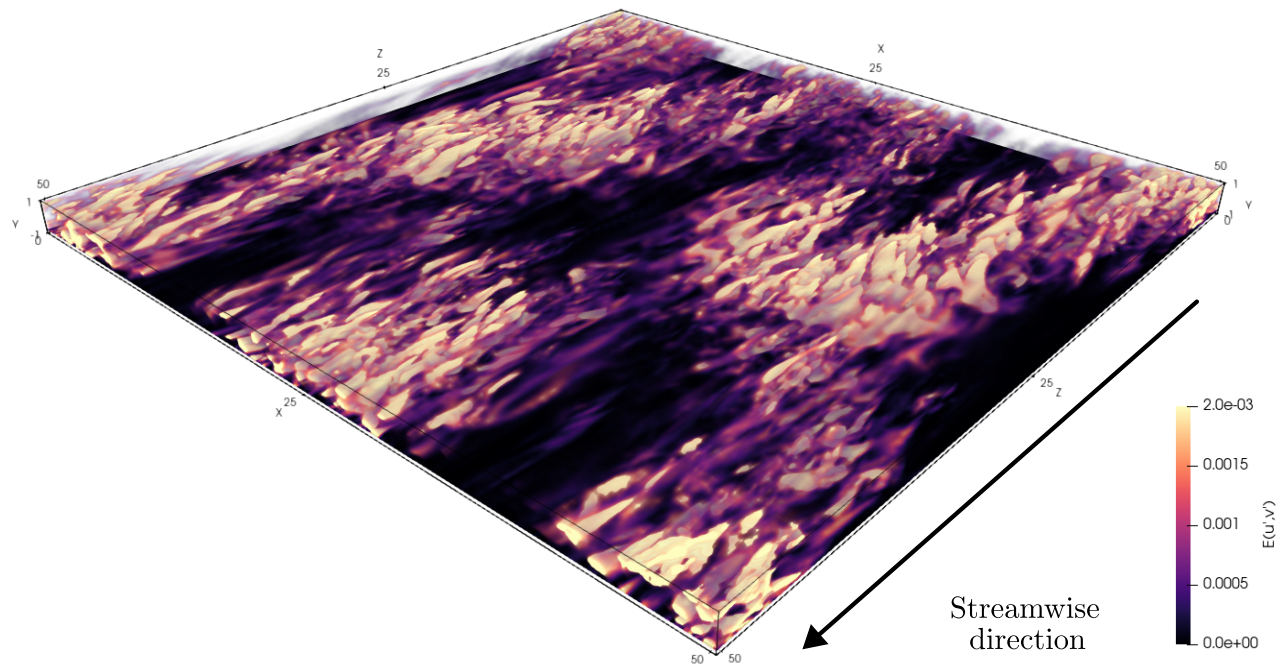


Figure 1.8: A snapshot of turbulent-laminar bands at $Re = 1400$ in a large domain $L/h = 16\pi$, depicting its spatiotemporal intermittent nature. Isovolumetric renderings are based on the spanwise, u' , and wall-normal, v' , perturbation kinetic energy, $E(u', v') = 1/2(u'^2 + v'^2)$, where the perturbation velocities are defined about the laminar state $\mathbf{u}'(\mathbf{x}, t) = \mathbf{u}(\mathbf{x}, t) - U_{lam}(y)$.

[Kawaguchi, & Kawamura, 2014](#); [Tsukahara, Seki, Kawamura, & Tochio, 2014](#); [Tuckerman, Kreilos, Schröbsdorff, Schneider, & Gibson, 2014](#)).

We will focus on the plane Poiseuille flow configuration, where the spatiotemporal intermittent patterns are referred to as oblique turbulent-laminar bands illustrated in figure 1.8 at $Re = 1400$ for $L/h = 16\pi$. The bright and dark regions highlight coexisting spatially localised turbulent and laminar regions. These turbulent-laminar bands occur over a range of Reynolds numbers, and its precise range is dependent on the domain's aspect ratio ([Paranjape et al., 2023](#); [Tsukahara, Kawaguchi, & Kawamura, 2014](#); [Tuckerman et al., 2014](#)). Near the upper Re threshold of this regime, the domain is fully engulfed by uniform, featureless turbulence appearing at $Re = 1800$ in figure 1.8(a). As Re decreases towards $Re = 1050$, spatiotemporal turbulent and laminar structures known as turbulent-laminar bands persist in between $Re \in [1050, 1600]$ shown in figures 1.9(b-f). In particular, these turbulent-laminar appear to have a preferred inclined angle, between $20^\circ \sim 30^\circ$, with streamwise wavelengths of $\lambda_x \sim 60h$, and spanwise wavelengths of $\lambda_z \sim 20h - 30h$ ([Tsukahara, Kawaguchi, & Kawamura, 2014](#)). [Kashyap, Duguet, and Dauchot \(2022\)](#) considered the linear response of the fluctuating turbulent field, and showed that the preferred band angle emerges near 23.2° . In the minimal band unit (MBU) studies of plane Poiseuille flows, the turbulent-bands convect at about $\sim 1\%$ of the bulk velocity, propagating

either upstream or downstream, depending on Re (Gomé et al., 2020; Tuckerman et al., 2014). Notably, the spanwise lengths of the bands are much wider than the half-heights and depends on Re , appearing at $\lambda_z \sim 20h$ for $Re \gtrsim 1400$ and $\lambda_z \sim 40h$ for $Re \lesssim 1100$. Interestingly, the bands alternate between both spanwise lengths between the Re range, merging and splitting continuously (Tuckerman et al., 2014), reminiscent of a puff splitting process in pipe flows (K. Avila et al., 2011). An example of this could have been observed in $Re = 1050$, where the band appears to alternate between different spanwise wavelengths in figure 1.9(f). As Re falls below a certain Re threshold, turbulent bands spontaneously decay and relaminarises (Gomé et al., 2020; Tuckerman et al., 2014). An example is shown in figure 1.9(g).

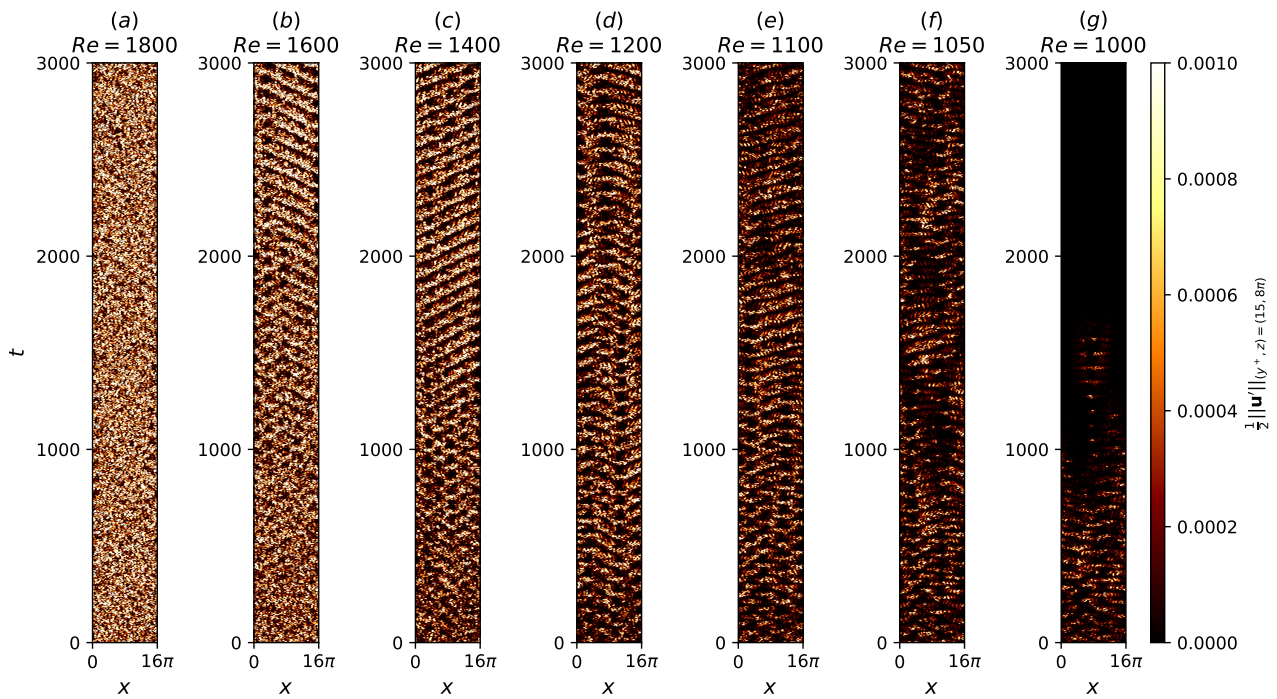


Figure 1.9: Turbulent-laminar bands for $t \in [0, 3000]$ in large domains $(L_x, L_z) = (16\pi, 16\pi)$ at (a) $Re = 1800$, (b) $Re = 1600$, (c) $Re = 1400$, (d) $Re = 1200$, (e) $Re = 1100$, (f) $Re = 1050$, (g) $Re = 1000$.

Gomé et al. (2020) computed the probability distributions for turbulent-laminar band decay, $P(\Delta t^d)$, where Δt^d is the time until decay. A key insight is that the probability distributions of turbulent band decay mimics a memoryless Poisson process,

$$P(\Delta t^d) = \exp(-\Delta t^d/\tau^d(Re)), \quad (1.13)$$

where $\tau^d(Re)$ refers to the mean lifetime for decay as a function of Re . Similarly, the band splitting process also follows a Poisson process,

$$P(\Delta t^s) = \exp(-\Delta t^s/\tau^s(Re)), \quad (1.14)$$

with $\tau^s(Re)$ the mean splitting lifetime. Both τ^d and τ^s exhibit superexponential dependence on Re ,

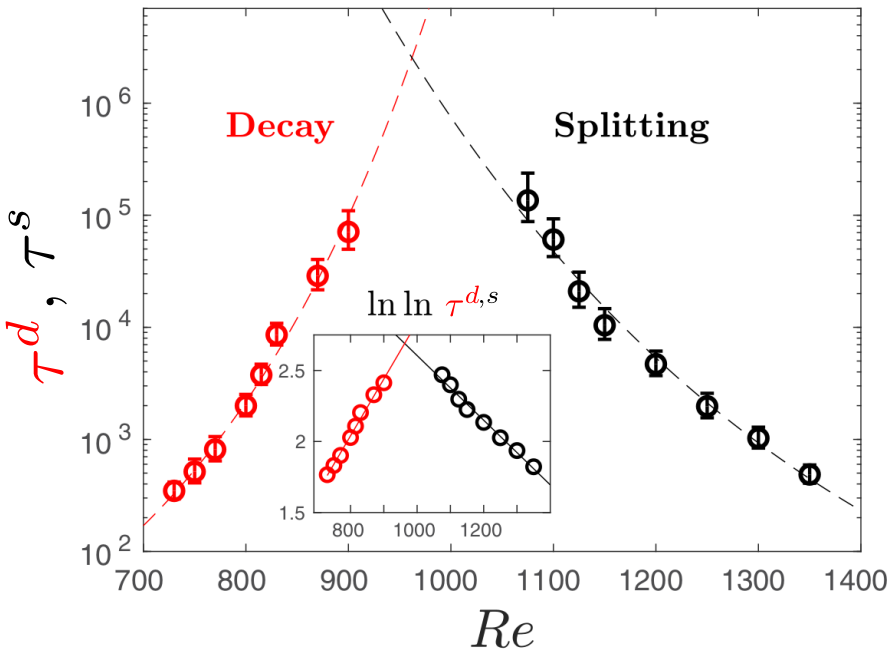


Figure 1.10: The mean decay times (red), τ^d , and mean splitting times (black), τ^s , as a function of Reynolds number, leading to a crossover point at $Re_{cross} \approx 965$, adapted from [Gomé et al. \(2020\)](#).

$$\tau^{d,s} = \exp(\exp(Re)), \quad (1.15)$$

This is shown in figure 1.10, with a crossover point at $Re_{cross} \approx 965$, where both decay and splitting becomes equally probable. This crossover point is considered as the critical Reynolds number for the onset of turbulent bands.

While there has been progress made towards our understanding of infinitely bi-periodic turbulent-laminar bands in MBUs, recent studies of isolated (non-periodic) turbulent bands (ITBs) reveal different behaviour. Notably, ITBs persist at Reynolds number below Re_{cross} at $Re = 700$ for durations exceeding $t = 10000$, exceeding the mean decay lifetime in figure 1.10. The ITBs are characterised by streak generating head and a diffusive upstream tail. ([Shimizu & Manneville, 2019](#); [Tao, Eckhardt, & Xiong, 2018](#); [Xiao & Song, 2020](#); [Xiong, Tao, Chen, & Brandt, 2015](#)). We conclude our discussion on transitional wall-bounded shear flows.

1.3 Rayleigh-Bénard convection

Rayleigh-Bénard convection (RBC) is a paradigmatic fluid configuration describing the motion of the fluid confined between two infinite-parallel plates heated from below and cooled from the top. As the bottom plate is heated, the bottom layer fluid becomes more buoyant and tends to rise, while the colder top fluid layer becomes relatively less buoyant and tends to sink, leading to an overturning of layers. Viscous forces between neighbouring fluid parcels act to resist the motion. As buoyancy overcomes these viscous forces, the fluid layers overturn, resulting in the initiation of buoyancy-driven convection, the physical mechanism underpinning RBC.

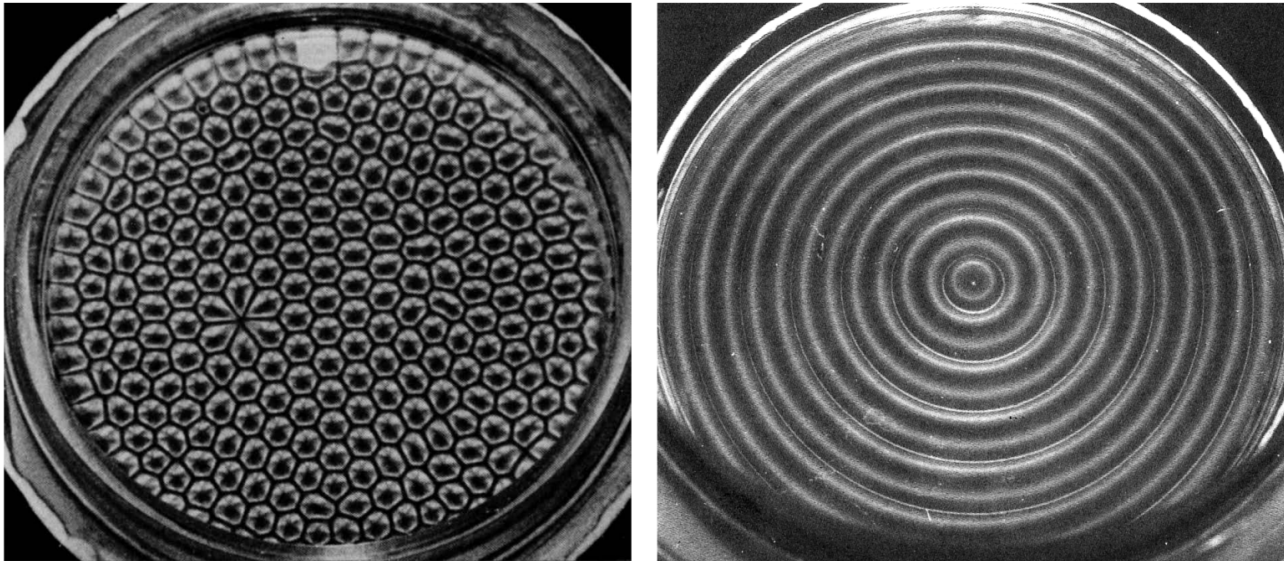


Figure 1.11: (a) Surface tension driven convection leading to the onset of hexagonal Bénard cells in a thin layer of silicone oil, heated from below and cooled by ambient air. A diamond defect appears, likely caused by plate imperfections. (b) Buoyancy driven convection in rigid plates, resulting to concentric convection rolls at 2.9 times the critical Rayleigh number. Both experiments were performed by [Koschmieder and Pallas \(1974\)](#), and the convection patterns were illuminated by aluminum powder, where the dark and bright regions refer to vertical and horizontal motions respectively. These higher resolution images were taken from [Van Dyke and Van Dyke \(1982\)](#).

One of the earliest experimental studies dedicated to buoyancy-driven convection was conducted by Henri Bénard ([Bénard, 1901](#)), who observed the formation of hexagonal convection cells above a certain temperature threshold ΔT . These hexagonal patterns are referred to as Bénard cells are illustrated in figure 1.11(a) (adapted from ([Koschmieder & Pallas, 1974](#))). Subsequently, [Rayleigh \(1916\)](#) carried out one of first linear stability analyses of buoyancy-driven convection, predicting the onset of convection at a critical Rayleigh number of $Ra_c = 657.5$. However, Rayleigh's analysis assumed an idealised free-free boundary conditions, which differed from the rigid-free setup of Bénard's experiment. The linear stability analysis for rigid-free configuration was later performed by [Jeffreys \(1928\)](#) yielding a higher critical Rayleigh number of $Ra_c = 1058$. In the rigid-rigid configuration, the critical Rayleigh number increases further to $Ra_c = 1708$ ([Pellew & Southwell, 1940](#)). The Rayleigh number in Bénard's original experiment contradicted results from linear stability analysis as it was found to be 300 to 1500 smaller than Ra_c for the free-free and rigid-free cases respectively ([Wesfreid, 2017](#)). This contradiction, not recognised by Bénard at the time, lies in the significant role of surface tension in thin fluid layers exposed to air, now known as Bénard-Maragoni (BM) convection ([Block, 1956](#); [Cloot & Lebon, 1984](#); [Manneville, 2006](#); [Wesfreid, 2017](#)). In BM convection, fluid motion is primarily driven by surface tension gradients due to variations of temperature, forming hexagonal cells, as in figure 1.11(a). The preference for hexagonal cells in BM convection was later confirmed based on weakly nonlinear stability analysis ([Cloot & Lebon, 1984](#)). As the fluid layer becomes thicker, surface-tension effects diminish and buoyancy-driven convection becomes dominant. Similarly, placing a rigid lid on top of a thin fluid layer suppresses surface-tension effects, resulting in buoyancy-driven convection (compare between 1.11(a) and (b)) The preferred

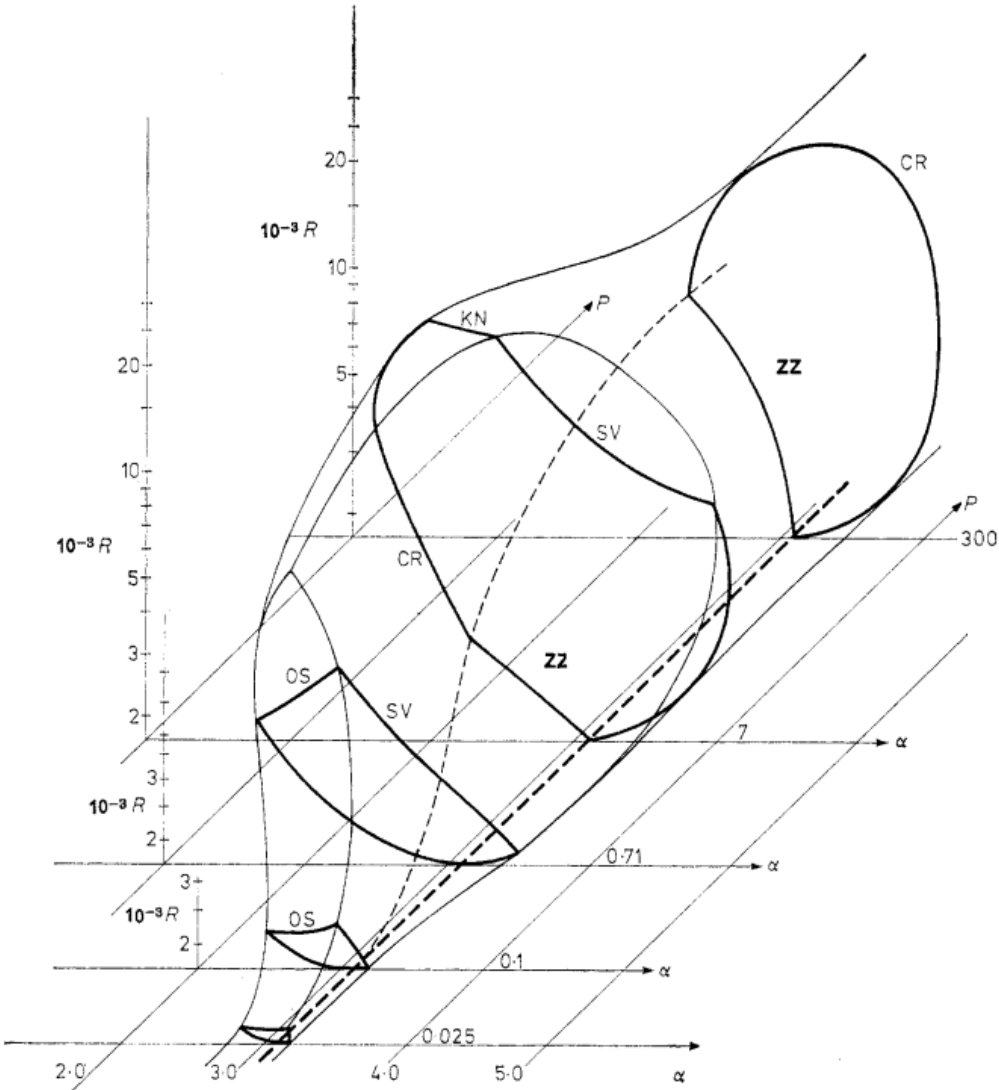


Figure 1.12: The Busse balloon describes the stability boundaries of ISRs in a $\varepsilon - q$ space. For larger wavenumbers, the instability mechanism is described by the skewed-varicose (SV) instability. For smaller wavenumbers, the instability mechanism is described by the Eckhaus instability. For large ε , the instability is described by the onset of oscillatory instability. Busse balloon digitised from [Plapp \(1997\)](#) for $Pr \approx 1$.

convection patterns based on weakly nonlinear stability analysis are the two-dimensional parallel rolls, now referred to as ideal straight rolls (ISRs) ([Bodenschatz et al., 2000](#); [Schlüter, Lortz, & Busse, 1965](#)). In circular containers, the ISRs conform to the geometry of the boundaries, forming concentric convection rolls illustrated in figure 1.11(b). Interestingly, hexagonal cells have been observed in buoyancy-driven flows of non-Boussinesq fluids ([Bodenschatz et al., 2000](#); [Hoard, Robertson, & Acrivos, 1970](#)). In this thesis, we consider the RBP setup (and RBC in chapter 4) with rigid-rigid boundary conditions, bearing critical Rayleigh number of $Ra_c = 1708$. Notably, the corresponding critical wavelength is $q_c = 3.12/d$ (or $\lambda_c \approx 2d$), suggesting that distance separating the plates, d , dictates the length of a single roll, $l_{roll} = \lambda_c/2 \approx d$.

As mentioned earlier, stationary ISRs near q_c emerge just above Ra_c , based on weakly nonlinear stability analysis. ([Eckhaus, 1965](#); [Schlüter et al., 1965](#)). However, this prediction contradicted by

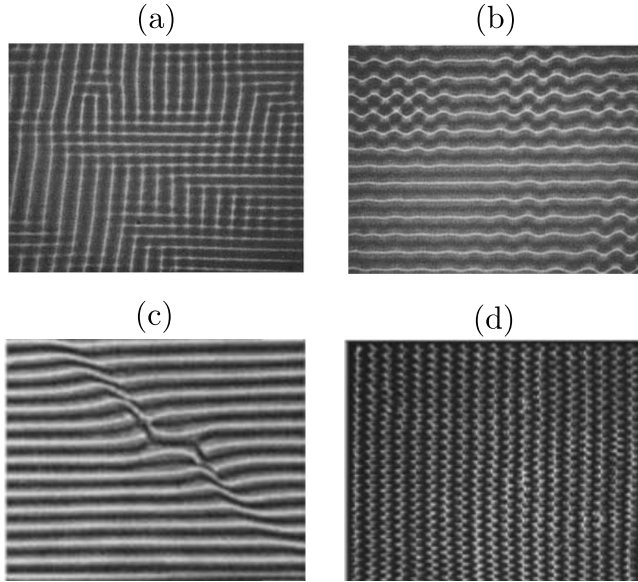


Figure 1.13: ISRs experiencing (a) cross-roll instability at $Ra = 3000, Pr = 100$ and (b) zig-zag instability at $Ra = 3600, Pr = 100$ ([Busse & Whitehead, 1971](#)). (c) Skew-varicosed instability at $Ra = 5568, Pr = 1$ ([Plapp, 1997](#)), and (d) oscillatory instability at $Ra = 10384, Pr = 1$ ([Cakmur et al., 1997a](#)).

the emergence of time-dependent oscillatory ISRs in experiments ([Rossby, 1969](#); [Willis & Deardorff, 1970](#)) at $Ra = 9200$ (or roughly five times Ra_c), where weakly nonlinear stability analysis becomes inapplicable far from threshold. To address this, a secondary stability analysis was employed to study the stability of ISRs further from Ra_c ([Busse, 1972](#)). One of the key results from this analysis is the Busse balloon, which describes the stability boundaries of ISRs as a function of Ra and Pr , and roll wavenumber, α , shown figure 1.12 ([Busse, 1978](#)). The boundaries of the Busse balloon are described by a range of secondary instabilities, each arising from different physical mechanisms ([Busse, 1978](#)). At large Prandtl numbers, $Pr = O(10^2)$, the zig-zag (ZZ) and cross-roll (CR) instabilities delimits the balloon for small and large roll wavenumbers. The zig-zag instabilities cause zig-zag undulations while the CR instabilities generates rolls orthogonal to the underlying ISR structure, effectively increasing or decreasing the roll wavenumber respectively ([Busse & Whitehead, 1971](#)). Examples of these instabilities at $Pr = 100$ are illustrated in figure 1.13(a,b).

At moderate Prandtl numbers, $Pr = O(1)$, the Busse balloon is bounded by the skewed varicosed (SV) for high roll wavenumbers and the oscillatory (OS) instability at large Ra . The skewed-varicosed (SV) instability leads to roll-pinch where pinched rolls merged into a single roll, reducing roll wavenumber while the oscillatory instability leads to the onset of an oscillatory ISRs. Examples of the respective instabilities at $Pr = 1$ are shown in figure 1.13(c,d). At higher wavenumbers, the skewed varicose (SV) instability becomes relevant at intermediate Prandtl numbers, characterised by roll pinching and merging that effectively reduces the roll wavenumber. Finally, the Eckhaus instability (not shown), related to the symmetry of the system, appears close to the Ra_c , leading a disturbance parallel to the underlying rolls which either creates or destroy rolls such that the resultant roll wavenumber adheres to the stability boundaries ([Lowe & Gollub, 1985](#)). Near $Pr = 1$, the Eckhaus instability coincides with the crossroll instability (figure 6 from [Bodenschatz et al. \(2000\)](#),

adapted from [Plapp \(1997\)](#).)

In this thesis, we focus on fluids with $Pr = 1$, where secondary instabilities such as skewed-varicose, Eckhaus and cross-roll instabilities typically arise. While the stability boundaries of the Busse balloon have been experimentally verified ([Busse & Whitehead, 1971](#); [Croquette, 1989a](#); [Plapp, 1997](#)), accurately predicting the wavenumber of ideal straight rolls (ISRs) remain difficult due to hysteresis and the existence of multiple stable ISRs of different roll wavenumbers. As Ra continuously increases, ISRs with wavenumbers outside the Busse Balloon undergo the secondary instabilities (described above) that drive their wavenumbers back to the stable boundaries. The hysteretic behaviour highlights that the roll wavenumber of the ISRs is strongly dependent on the system's history ([Bodenschatz et al., 2000](#)).

It is worth noting that the ISRs are the exception rather than the rule in RBC ([Croquette, 1989b](#)). A range of non-ISR states, such as squares, travelling or stationary target patterns, giant rotating spirals, and oscillatory convection, have been observed over the years ([Borońska & Tuckerman, 2010a, 2010b](#); [Croquette, 1989a](#); [Hof, Lucas, & Mullin, 1999](#); [Le Gal, Pocheau, & Croquette, 1985](#); [Plapp, 1997](#); [Rüdiger & Feudel, 2000](#)). For example, [Hof et al. \(1999\)](#) identified eight stationary and two oscillatory state in cylindrical RBC with small aspect ratios at the same Rayleigh number. These results were later verified in numerical simulations and bifurcation analysis, revealing up to twelve stable branches near the onset ($Ra \leq 2500$) and the potential for hundreds more as Ra increases ([Borońska & Tuckerman, 2010a, 2010b](#); [Ma, Sun, & Yin, 2006](#)).

In larger domains ($\Gamma \geq 28$), giant rotating spirals were found and have been investigated ([Plapp & Bodenschatz, 1996](#); [Plapp, Egolf, Bodenschatz, & Pesch, 1998](#)). Experimental and numerical studies of RBC with varying sidewall boundary conditions (i.e. thermally insulating, conducting an no-slip) ([Bouillé, Dallas, & Farrell, 2022](#); [M. Paul, Chiam, Cross, Fischer, & Greenside, 2003](#); [Siggers, 2003](#); [Tuckerman & Barkley, 1988](#)), non-Boussinesq convection ([Bodenschatz et al., 1992](#)), and rotational effects ([Hu, Ecke, & Ahlers, 1997](#)) were investigated, where multiple states were also reported. In inclined RBC, [Reetz and Schneider \(2020\)](#); [Reetz, Subramanian, and Schneider \(2020\)](#) identified up to sixteen stable and unstable invariant states, along with heteroclinic orbits connecting them. These findings indicate that RBC support a rich variety of coexisting stables states beyond ISRs, resulting to a system with multiple stable states above the critical Rayleigh number. To complicate matters further, RBC also exhibits spatiotemporal chaotic states.

In the late 1990s, convection rolls exhibiting spatio-temporal chaotic behaviour known as spiral defect chaos (SDC) were observed within the same stability boundaries where ISRs were expected ([Ahlers, n.d.](#); [Cakmur et al., 1997a](#); [Chiam, Paul, Cross, & Greenside, 2003](#); [Decker et al., 1994](#); [Egolf, Melnikov, & Bodenschatz, 1998](#); [Egolf, Melnikov, Pesch, & Ecke, 2000](#); [Hu, Ecke, & Ahlers, 1993, 1995](#); [Morris, Bodenschatz, Cannell, & Ahlers, 1993, 1996](#); [Vitral et al., 2020](#)). Notably, ISRs emerge with carefully prepared initial conditions while uncontrolled initial conditions lead to SDC. It is now well established that SDC exists as intrinsic attractor of RBC, independent of sidewall conditions [Morris et al. \(1996\)](#), forming a bistable system with ISRs ([Cakmur et al., 1997a](#)) across a range of Ra at $Pr = 1$ illustrated in figure 1.14. However, this bistability appears to be Prandtl number dependent. At $Pr = 4$, the SDC appears to be transient decaying towards ISRs over long

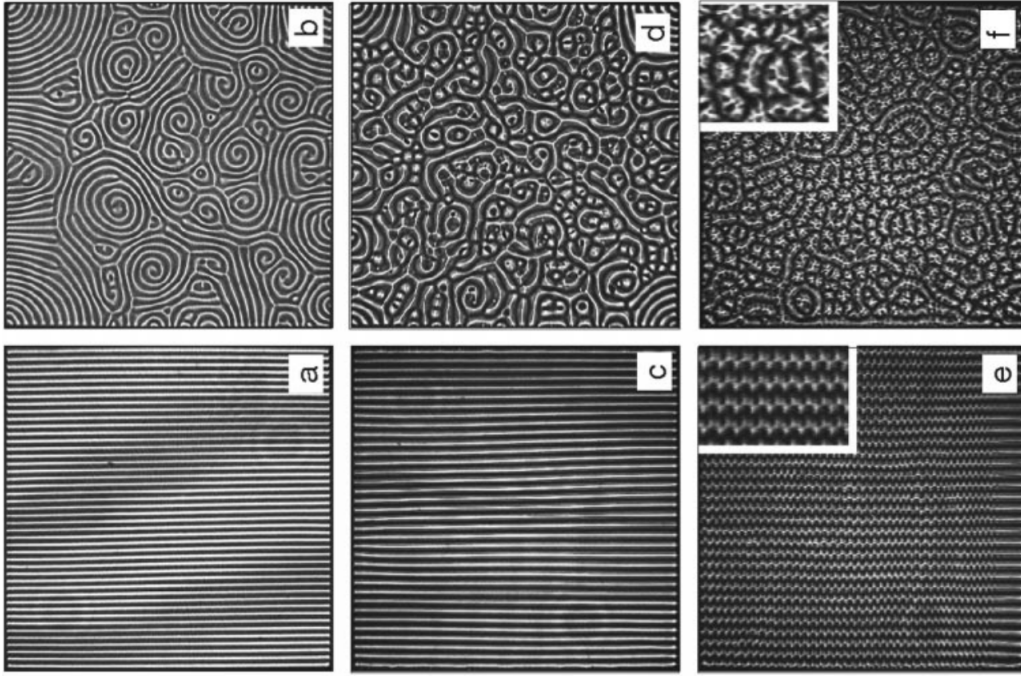


Figure 1.14: The coexistence of spiral defect chaos (SDC, top row) and ideal straight rolls (ISRs, bottom row) at (a,b) $Ra = 3279$, (c,d) $Ra = 6832$ and (e,f) $Ra = 10384$. The domain size is $\Gamma = 50$ and $Pr = 1$, adapted from [Cakmur et al. \(1997a\)](#).

periods ([Bajaj, Cannell, & Ahlers, 1997](#)). SDC has also been replicated in numerical simulations using two-dimensional Swift-Hohenberg equations ([Karimi, Huang, & Paul, 2011; Schmitz, Pesch, & Zimmermann, 2002; Swift & Hohenberg, 1977; H. Xi & Gunton, 1995; H.-w. Xi, Gunton, & Viñals, 1993](#)). The critical Rayleigh number for the onset of SDC, Ra_s , depends on the domain's aspect ratio, and Prandtl number ([Bajaj et al., 1997; Bodenschatz et al., 2000; Cakmur, Egolf, Plapp, & Bodenschatz, 1997b; Hu et al., 1995](#)). SDC has been primarily reported in large aspect ratio domains ($\Gamma \gtrsim 20$), suggesting a minimal domain size for SDC to occur ([Bodenschatz et al., 2000](#)). This is consistent with the leading Lyapunov exponents of SDC which becomes smaller with decreasing Γ ([Egolf et al., 2000; M. R. Paul, Einarsson, Fischer, & Cross, 2007](#)). To better characterise SDC, several studies have investigated its spatial-temporal properties, such as the averaged roll-curvature [Hu et al. \(1995\)](#), probability distribution of spirals [Ecke, Hu, Mainieri, and Ahlers \(1995\); Liu and Ahlers \(1996\)](#) and correlation length-/time-scales ([Cakmur et al., 1997b; Morris et al., 1993, 1996](#)). Specifically, the correlation length-scales were found to grow exponentially with ([Cakmur et al., 1997b; Morris et al., 1993, 1996](#)), suggesting that transition from ISRs to SDC is related to phase transitions. Similar ‘SDC-like’ has been observed in other pattern-formation systems, including rotating RBC [Hu et al. \(1997\)](#), dielectric barrier discharge [Dong, Liu, Liu, He, and Fan \(2005\)](#) and advection diffusion reaction systems [Affan and Friedrich \(2014\)](#).

1.4 Rayleigh-Bénard Poiseuille (RBP) flows

This section describes the developments of Rayleigh-Bénard Poiseuille (RBP) flows, integrating key findings from both plane Poiseuille flow (PPF) and Rayleigh-Bénard convection (RBC) systems

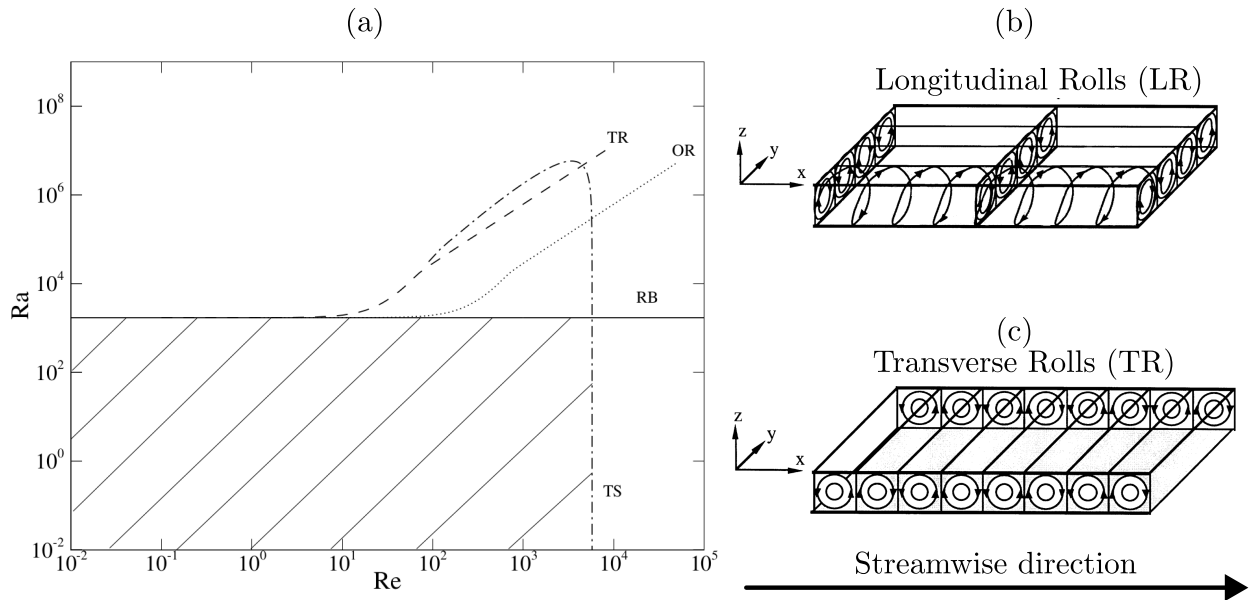


Figure 1.15: (a) Neutral stability curves of longitudinal rolls (LR), oblique rolls (OR), transverse rolls (TR) and Tollmien-Schlichting (TS) waves, adapted from [John Soundar Jerome et al. \(2012\)](#). The shaded area refers to damped perturbations. Sketch of (b) longitudinal and (c) transverse rolls, adapted from [Kelly \(1994\)](#).

discussed in §1.2 and §1.3 respectively. The neutral stability curves in the Rayleigh-Bénard Poiseuille (RBP) comprising of both plane Poisueuille flow (PPF) and Rayleigh-Bénard convection (RBC) systems, are bounded by the onset of Tollmien-Schlichting waves at $Re_c = 5772.22$ ([Orszag, 1971](#)), and by the onset of convection rolls at $Ra_c = 1708$ ([Pellew & Southwell, 1940](#)), respectively. In RBP systems, the imposed mean Poiseuille flow in the RBP system breaks the rotational symmetry of the convection rolls, categorising them based on their orientation to the mean flow direction, namely: longitudinal, transverse and oblique rolls. These primary instabilities were first investigated by [Gage and Reid \(1968\)](#) in an infinitely extended layer. For longitudinal rolls, the linearised system reduces to the classical RBC problem. Thus, the critical Rayleigh number remains unchanged at $Ra_{\parallel} = Ra_c = 1708.8$ with a critical wavenumber, $\alpha_{\parallel} = \alpha_c = 3.13$, independent of Reynolds number and Prandtl number ([Kelly, 1994](#); [Pellew & Southwell, 1940](#)). In contrast, the critical Rayleigh number for the onset of transverse rolls increases with Re , and is also dependent on Pr ([Gage & Reid, 1968](#); [Müller, Lücke, & Kamps, 1992](#); [Nicolas, Mojtabi, & Platten, 1997](#)). The critical Rayleigh number for the onset of obliqued rolls can derived using by applying a Squire transformation ([Squire, 1933](#)) to transverse roll system. For a given Ra , the corresponding critical Re for the onset of oblique rolls is higher than that for transverse rolls ([Gage & Reid, 1968](#)). The neutral stability curves for the three different rolls are illustrated in figure 1.15.

Experimental studies in channels with large transverse aspect ratios (i.e. span-to-depth) showed the onset of longitudinal rolls ([Akiyama, Hwang, & Cheng, 1971](#); [Fukui, Nakajima, & Ueda, 1983](#); [Ostrach & Kamotani, 1975](#)), while transverse rolls are more prevalent in narrower channels ([Luijkh, Platten, & Legros, 1981](#); [Ouazzani, Caltagirone, Meyer, & Mojtabi, 1989](#); [Ouazzani, Platten, & Mojtabi, 1990](#)). Linear stability analysis of longitudinal rolls for finite channels confirms that Ra_{\parallel} remains fairly independent for transverse aspect ratios greater than five, and increases quickly below that. Hence,

for small Re , critical Rayleigh number of transverse rolls is smaller than that of longitudinal rolls, $Ra_{\perp} < Ra_{\parallel}$, giving rise to transverse rolls (Nicolas, Luijckx, & Platten, 2000). However, laminar Poiseuille flow where observed in the same parameter space where transverse rolls were expected from linear stability analysis Ouazzani et al. (1989). This discrepancy was resolved by Müller et al. (1992), who showed that transverse rolls may be convectively or absolutely unstable, with the transition boundary corroborating with experimental data. Later, Carrière and Monkewitz (1999) showed that demonstrated that longitudinal rolls are always convectively unstable. Nonmodal stability analysis of subcritical RBP by John Soundar Jerome et al. (2012) revealed that the optimal transient growth is primarily dominated by streamwise rollers similar to those of PPF (Reddy & Henningson, 1993), with a spanwise wavenumber of $\beta_{opt} \approx 2.05$. The maximum amplification factor, G_{max} increases modestly with Ra , and the critical wavenumber approaches α_{\parallel} , indicative of longitudinal rolls.

For $Re > 0$ in infinite domains, the longitudinal rolls emerge as the dominant primary instability (Gage & Reid, 1968), and their secondary stability was analysed by Clever and Busse (1991). They identified a time-dependent, wavy instability near $Re \sim 100$, giving rise to tertiary solutions in the form of wavy rolls. These wavy rolls have been observed experimentally and were found to be convectively unstable (Nicolas, Xin, & Zoueidi, 2010; Pabiou, Mergui, & Bénard, 2005; Pabiou, Nicolas, Xin, & Mergui, 2003). Clever and Busse (1991) also hypothesised that the wavy rolls are less efficient at transporting heating than longitudinal rolls for the same Ra , which was later confirmed numerically by Nicolas, Zoueidi, and Xin (2012). The influence of finite transverse aspect ratios on the onset of wavy rolls have also been studied (Nicolas et al., 2010; Xin, Nicolas, & Quéré, 2006), where the critical Ra was found to be approximately 1.5 times higher than in infinite domains Clever and Busse (1991). Furthermore, the effect of external excitation has been explored, showing that increased excitation amplitude can reduce the development length required for the formation of wavy roll (Nicolas et al., 2010, 2012). In the turbulent regime, shear driven turbulence has been shown to enhance heat transport in RBP flows (Pirozzoli, Bernardini, Verzicco, & Orlandi, 2017; Scagliarini, Einarsson, Gylfason, & Toschi, 2015; Scagliarini, Gylfason, & Toschi, 2014). Extensions of the RBP configuration, such as flows over wavy walls or with sinusoidal thermal forcing have been investigated, potentially offering a reduction in drag and enhancing heat transport (Hossain, Floryan, & Floryan, 2012; Hossain & Floryan, 2016, 2020). For a comprehensive overview of RBP flows, the reader is referred to the reviews by Kelly (1994) and Nicolas (2002).

1.5 Thesis Outline

In this thesis, I focus on the transitional behaviour of fluid flow in Rayleigh-Bénard Poiseuille systems by conducting direct numerical simulations and linear stability analysis. Notably, the onset of instabilities does not necessarily lead to turbulence and may give rise to flow regimes that are neither fully laminar nor fully turbulent. For clarity, we refer to these flow regimes collectively as the transitional regime.

While significant progress has been made in understanding the transition process of Rayleigh-Bénard convection and plane Poiseuille flows separately, their combined effects remains largely

unexplored. For instance, do convection rolls promote the transition to shear driven turbulence? And conversely, how does shear affect the bistable dynamics between ideal straight rolls (ISRs) and spiral defect chaos (SDC)? These questions are explore in §3.

Although the co-existence of ISRs and SDC as bistable states in Rayleigh-Bénard convection is well established, the existence of multiple states raises further questions about the notion of bistability. In §4, we investigate the state-space structure underlying ISRs and SDC, identifying several stable invariant solutions referred to as *elementary* states that underpin the pattern formation of SDC.

The thesis is structured into the follows:

1. §1 provides the introduction and a review of relevant literature.
2. §2 presents the numerical methods, including the spectral/*hp* element method, algorithms for solving the Navier-Stokes equations, linear stability analysis and edge tracking.
3. §3 introduces the $Ra - Re$ phase space of RBP flows, with a particular focus on the role of longitudinal rolls in sustaining turbulence. We introduce the *thermally-assisted sustaining process* - an alternative route towards turbulence via linearly unstable longitudinal rolls
4. §4 explores the organisation of the state space of spiral defect chaos and ideal straight rolls $Ra = 2903$, accompanied by *elementary* states, edge states and highlight some pathways towards SDC
5. Finally, §5 concludes this thesis and suggests possible avenues of future research.

Chapter 2

Numerical Methods

In this chapter, we will discuss the fundamentals of numerical methods relevant for solving the Navier-Stokes equations. We begin the discussion of the method weighted of residuals (§2.1) and the spatial discretisation using spectral/ hp element methods in one dimension (§2.3). This is followed by techniques for solving the Navier-Stokes equations (§2.4), such as the velocity-correction scheme, enforcing a constant flow rate and the quasi-3D approach for semi-homogeneous domains. This chapter concludes with numerical techniques for performing stability analysis of the Navier-Stokes equations (§2.5), including eigenvalue computation and edge tracking.

2.1 Method of weighted residuals

Spatial discretisation errors, or residuals, arise as one seeks an approximate solution to some partial differential equation (PDE). The method of weighted residuals provides a generic mathematical framework in which constraints on the residual could be applied flexibly, defining the spatial discretisation scheme and its convergence properties. We approximate the solution of PDE by considering a finite expansion of a suitable basis, to which its coefficients are sought after by minimising the inner product between the PDE and a test (or weight) function. To demonstrate this, we consider a linear partial differential equation as,

$$\mathbf{L}[u(x)] = 0, \quad x \in \Omega, \tag{2.1}$$

where \mathbf{L} refers to a linear spatial differential operator subjected to some boundary conditions within the domain, Ω , while $u(x)$ refers to the exact solution of \mathbf{L} . Examples of PDEs with linear spatial differential operators include the Laplace equation, $\nabla^2 u = 0$, Poisson equation, $\nabla^2 u - f = 0$, and the Helmholtz equation, $\nabla^2 u - \lambda u + f = 0$. We suppose that the exact solution $u(x)$ can be approximated (discretised) by N finite number of global basis (or expansion) functions, $\Phi(x)$.

$$u(x) \approx u^\delta(x) = \sum_{i=0}^{N-1} \hat{u}_i \Phi_i(x), \tag{2.2}$$

where $u^\delta(x)$ refers to the approximate solution of $u(x)$, consisting of a linear combination of the product between the i^{th} basis coefficient, \hat{u}_i , and the i^{th} global basis expansion, $\Phi_i(x)$, defined within

Ω . Since $u^\delta(x)$ is an approximate solution of equation (2.5), we expect a residual (or error) between the exact solution, $u(x)$, and $u^\delta(x)$,

$$\mathbf{L}[u^\delta(x)] = R[u^\delta(x)], \quad (2.3)$$

where $R[u^\delta(x)]$ refers to the residual which depends on the approximate solution $u^\delta(x)$ and varies within Ω . In other words, equation (2.3) might not be satisfied everywhere in Ω . Next, we need to place restrictions on the residual, such that it the residual approaches zero, $R \rightarrow 0$, and the approximate solution approaches the exact solution, $u^\delta(x) \rightarrow u(x)$. The method of weighted residuals places a restriction on the residual by applying an inner product between the governing equation, and N test (or weight) functions, $v_j(x)$, and setting it to zero,

$$(v_j(x), R[u^\delta(x)]) = 0, \quad j = 0, \dots, N - 1. \quad (2.4)$$

Definition 2.1.1 (Inner product). The inner product between two functions $f(x)$ and $g(x)$ is,

$$(f, g) = \int_{\Omega} f(x)g(x)dx.$$

By enforcing equation (2.4), the discrete problem becomes a system of N ordinary differential equations to solve for the N basis coefficients, \hat{u}_i . The choice of test function defines the projection methods, and examples of different projection methods are shown in table 2.1. We emphasise that the method of weighted residuals only describes the projection method, but does not specify the type of basis expansions, as we will discuss later in §2.3. The choice of projection method coupled with suitable basis expansions will have different solution convergence properties. Of particular interest is on how quickly the residual vanishes as the number of basis expansions increases. For instance, by considering the Galerkin method coupled with Fourier expansions, one can expect exponential convergence for a sufficiently smooth problem which is desirable for an efficient representation of turbulent dynamics.

Weight functions	Projection method
$v_j(x) = \delta(x - x_j)$	Collocation
$v_j(x) = \begin{cases} 1 & \text{if } x \in \Omega_j \\ 0 & \text{if } x \notin \Omega_j \end{cases}$	Finite-Volume
$v_j(x) = \phi_j$	Galerkin
$v_j(x) = \frac{\partial R}{\partial \hat{u}_j}$	Least-squares

Table 2.1: Examples of weight functions and projection methods

2.2 Galerkin Projection

Galerkin projection remains as a standard projection method in the context of the finite element methods, where the test functions, $v(x)$, are chosen to be lie in the same functional space as the global basis functions, $\Phi(x)$. To demonstrate the Galerkin projection method, we consider that the differential operator earlier in equation (2.1) as a 1D Helmholtz equation,

$$\mathbf{L}[u(x)] \equiv \frac{\partial^2 u(x)}{\partial x^2} - \lambda u(x) + f(x) = 0, \quad x \in \Omega := [0, l] \quad (2.5a)$$

$$u(0) = g_D, \quad \left. \frac{\partial u}{\partial x} \right|_{x=l} = g_N. \quad (2.5b)$$

where λ is a real positive constant, $f(x)$ is a forcing function, and Ω refers to the spatial domain bounded between 0 and l . To ensure that problem is well posed, Dirichlet and Neumann boundary conditions, g_D and g_N , are imposed at $x = 0$ and $x = l$ respectively. Equation 2.5 is commonly referred to as the strong or classical form.

The subsequent step is to take the inner product of the equation (2.5) with a test function, $v(x)$, that satisfies the homogeneous Dirichlet boundary conditions by definition, i.e. $v(0) = 0$, and setting the inner product to zero,

$$(v(x), \mathbf{L}[u(x)]) = \int_0^l v(x) \left[\frac{\partial^2 u(x)}{\partial x^2} - \lambda u(x) + f(x) \right] dx = 0, \quad (2.6)$$

akin to applying the method of weighted residuals (§2.1). Next, we perform integration by parts,

$$\underbrace{\int_0^l \frac{\partial v}{\partial x} \frac{\partial u}{\partial x} dx}_{a(v,u)} + \underbrace{\int_0^l \lambda v u dx}_{f(v)} = \underbrace{\int_0^l v f dx}_{f(v)} + \left[v \frac{\partial u}{\partial x} \right]_0^l. \quad (2.7a)$$

$$a(v, u) = f(v). \quad (2.7b)$$

Equation (2.7a) is typically referred to as the weak ¹ form of equation (2.5). The weak form can be represented in compact notation in equation (2.7b), where $a(v, u)$ is bilinear and symmetric. In structural mechanics, $a(u, u)$ is commonly referred to as the *strain energy*. To ensure that the *strain* energy is finite, we restrict the choice of solutions $u(x)$ to lie in the solution space,

$$\mathcal{U} := \{u \mid u \in H^1(\Omega), u(0) = g_D\}, \quad (2.8)$$

where $u \in H^1$ refers to functions of u belonging to Sobolev space of order 1, and satistfying the Dirichlet condition, $u(0) = g_D$, at $x = 0$.

¹The notions of the *weak* and *strong* forms refer to the smoothness (regularity) required of admissible solutions. In the weak formulation, the highest derivative involved is up to first-order, so the solution space is H^1 . This space is generally larger than that of the strong formulation, which required $u \in H^2(\Omega)$. Since $H^2(\Omega) \subset H^1(\Omega)$ the weak formulation imposeds a ‘less stringent’ constraint of the solution space of admissible functions.

Definition 2.2.1 (Sobolev space). We define Sobolev space of order $n \geq 1$ on Ω ,

$$H^n(\Omega) = \{u \mid u \in L_2(\Omega), D^\alpha u \in L_2(\Omega), \forall \alpha : \alpha \leq n\},$$

where $D^\alpha u$ refers to derivatives up to order α and $L_2(\Omega)$ refers to functions that are square integrable.

Definition 2.2.2 (L_2 space). The space $L_2(\Omega)$ refers to functions that are square integrable,

$$(u, u)_{L_2} = \int_{\Omega} |u(x)|^2 d\Omega < \infty. \quad (2.9)$$

In other words, H^1 functions satisfy the condition that the integral of the square of the function and its first derivative is finite, consistent with the highest order derivative in the weak formulation of equation (2.6). Similarly, the space of test functions, \mathcal{V} , is defined as,

$$\mathcal{V} := \{v \mid v \in H^1, v(0) = 0\}, \quad (2.10)$$

where $v \in H^1$ refer to test functions belonging to the Sobolev space of order 1, and is defined to be zero, $v(0) = 0$ on Dirichlet boundary condition, $x = 0$. The generalised weak form is finding $u(x) \in \mathcal{U}$, such that

$$a(v, u) = f(v), \quad \forall v \in \mathcal{V}. \quad (2.11)$$

At this point, function spaces \mathcal{U} and \mathcal{V} , contain infinitely many possible functions and equation (2.11) is therefore infinite dimension. To obtain an approximate solution, $u^\delta(x)$, we restrict ourselves to finite dimensional subspaces, $\mathcal{U}^\delta \subset \mathcal{U}$, and $\mathcal{V}^\delta \subset \mathcal{V}$. Then, the problem is to find $u^\delta \in \mathcal{U}^\delta$, such that

$$a(v^\delta, u^\delta) = f(v^\delta), \quad v^\delta \in \mathcal{V}^\delta. \quad (2.12)$$

The subspaces $u^\delta \in \mathcal{U}^\delta$ and $v^\delta \in \mathcal{V}^\delta$ are not the same (compare the Dirichlet boundary conditions of equations (2.8) and (2.10)), necessary for the standard Galerkin projection procedure where they should lie in the same subspace. To ensure that they belong to the same space, we lift the solution u^δ into two parts,

$$u^\delta = u^{\mathcal{H}} + u^{\mathcal{D}}. \quad (2.13)$$

where $u^{\mathcal{H}} \in \mathcal{V}^\delta$ satisfies the homogeneous Dirichlet condition (e.g. is zero on Dirichlet boundaries), belonging to the same subspace as $v^\delta \in \mathcal{V}^\delta$, while $u^{\mathcal{D}} \in \mathcal{U}^\delta$ satisfies the Dirichlet boundary conditions $u^{\mathcal{D}}(0) = g_D$. Finally, the standard Galerkin projection method is to solve for $u^{\mathcal{H}} \in \mathcal{V}^\delta$,

$$a(v^\delta, u^{\mathcal{H}}) = f(v^\delta) - a(v^\delta, u^{\mathcal{D}}). \quad (2.14)$$

This concludes the classical Galerkin formulation, where we have converted a continuous PDE into a discrete problem amenable to standard direct or iterative linear solvers. Under certain assumptions of a , a solution is guaranteed under the Lax-Milgram theorem (Lax & Milgram, 1955). The order in which we perform integration by parts followed by defining the finite solution space is crucial. Reversing this order can introduce jumps in the solution derivatives between the element boundaries.

2.3 Spectral/*hp* element method

While the procedure for approximating a solution of a PDE using the classical Galerkin projection technique has been described, the spatial discretisation scheme, related to the choice of basis (and test) functions, remains undiscussed.

In this section, we introduce the spectral/*hp* element method (Patera, 1984), a spatial discretisation scheme in which the solution domain is partitioned into a set of non-overlapping finite elements of size h , within which the solution represented as a linear combination of continuous orthogonal polynomial functions up to order P . This approach combines the geometric flexibility of classical finite-element methods (Strang & Fix, 2008), which allow complex geometries to be represented, with the exponential convergence properties of spectral methods (Gottlieb & Orszag, 1977). For the reasons above, the spectral/*hp* element method provides an attractive framework for approximating PDE solutions at a given cost, as we shall see later. This section is organised as follows: domain partition, standard elements, assembly process, modal and nodal expansion functions, numerical integration and differentiation, a 1D example before concluding with error properties of the spectral/*hp* element method.

2.3.1 Domain partition

The first step concerns the partitioning the domain into a set of finite elemental regions. We consider an example in one dimension within Ω , and partition it into a set of N_{el} elements, where Ω^e , refers to the elemental partitions with $1 \geq e \geq N_{el}$, such that they meet at their boundaries and do not overlap,

$$\Omega = \bigcup_{e=1}^{N_{el}} \Omega^e, \quad \text{where } \bigcap_{e=1}^{N_{el}} \Omega^e = \emptyset \quad (2.15)$$

where the e^{th} element is defined as,

$$\Omega^e = \{x \mid x_{e-1} \geq x \geq x_e\}. \quad (2.16)$$

Each element can be represented by a linear combination of orthogonal basis expansions. The basis expansions can be either modal or nodal expansions, as we shall see later.

2.3.2 Standard Elements

In general, we expect to work with non-uniform elements that may have arbitrarily shapes, making the definition of basis expansions potentially unwieldy. To simplify the formulation, it is convenient to define a *standard* element,

$$\Omega_{st} = \{\xi \mid -1 \geq \xi \geq 1\}, \quad (2.17)$$

where Ω_{st} refers to the standard element defined in local coordinates, $\xi \in [-1, 1]$. Within this standard element, the formulation of basis expansions, as well as differential and integration operations, can be carried out in the local coordinate system ξ , before mapping the solution back to the global domain,

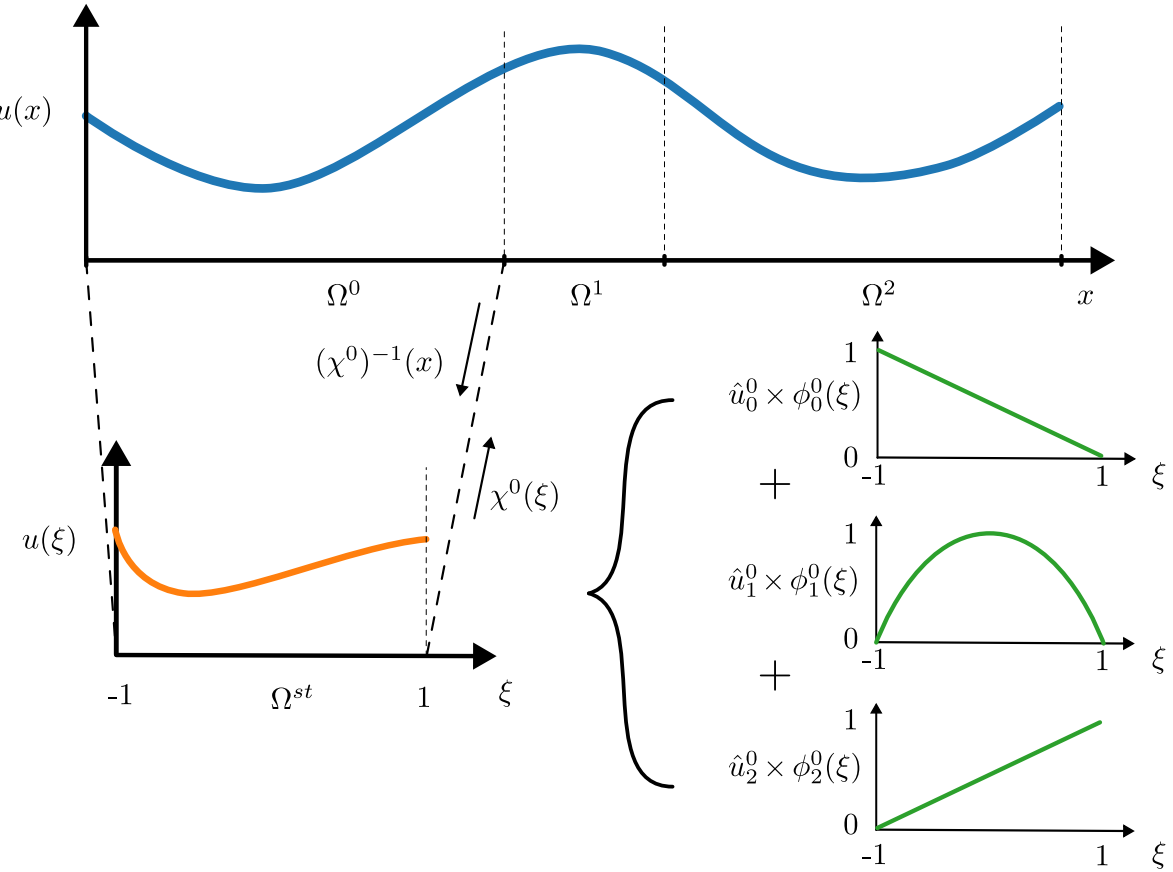


Figure 2.1: A spectral/ hp element representation of $u(x)$, consisting of three non-overlapping finite elements, each containing a linear combination of local expansion bases of up to $P = 2$.

x . We can map the standard element into any arbitrary global coordinates based on a linear mapping $\chi^e : \Omega_{st} \rightarrow \Omega$,

$$x = \chi^e(\xi) = \frac{1 - \xi}{2} x_e + \frac{1 + \xi}{2} x_{e+1}, \quad \xi \in \Omega_{st} \quad (2.18)$$

which for this case has an analytical inverse, $(\chi^e)^{-1}(x)$,

$$\xi = (\chi^e)^{-1}(x) = 2 \frac{x - x_{e-1}}{x_e - x_{e-1}} - 1, \quad x \in \Omega^e. \quad (2.19)$$

For illustration purposes, we consider that the standard element can be represented by three local basis expansions of polynomial order of up to $P = 2$,

$$\phi_0^e(\xi) = \frac{1 - \xi}{2}, \quad \phi_1^e(\xi) = (1 + \xi)(1 - \xi), \quad \phi_2^e(\xi) = \frac{1 + \xi}{2}, \quad (2.20)$$

where ϕ_0^e , ϕ_2^e and ϕ_1^e refers to the linear and quadratic local basis expansions of the e^{th} element. These local basis expansions is illustrated in figure 2.1. The approximate solution is now represented as,

$$u^\delta(x) = \sum_{e=1}^{N_{el}} \sum_{i=0}^P \hat{u}_i^e \phi_i^e(\xi). \quad (2.21)$$

where \hat{u}_i^e refers to the local expansion basis coefficients. The approximate solution, $u^\delta(x)$, now lie within the solution space \mathcal{U}^δ defined as,

$$\mathcal{U}^\delta := \{u^\delta \mid u^\delta \in H^1, u^\delta(\chi^e(\xi)) \in \phi_i^e(\xi), \forall i : 0 \leq i \leq P, \forall e : 1 \leq e \leq N_{el}\} \quad (2.22)$$

We note that the local basis expansion shown here are not strictly orthogonal polynomials. By modifying them with Jacobi polynomials, they may become orthogonal with increasing P as we see later.

2.3.3 Global assembly

In this section, we introduce the concept of global assembly (or direct stiffness summation) which relates the global basis expansions (equation (2.2)), $\Phi_i(x)$, to the local basis expansions (equation (2.21)), $\phi_i^e(x)$, where the solution can be approximated using either formulation,

$$u^\delta(x) = \sum_{i=0}^{N-1} \hat{u}_i \Phi_i(x) = \sum_{e=1}^{N_{el}} \sum_{i=0}^P \hat{u}_i^e \phi_i^e(\chi^e(\xi)). \quad (2.23)$$

In general, we can represent the global and local basis coefficients each as a column vector,

$$\hat{\mathbf{u}}_g = \begin{pmatrix} \hat{u}_0 \\ \vdots \\ \hat{u}_N \end{pmatrix}, \quad \hat{\mathbf{u}}_l = \begin{pmatrix} \hat{\mathbf{u}}^0 \\ \vdots \\ \hat{\mathbf{u}}^{N_{el}-1} \end{pmatrix}, \quad (2.24)$$

where $\hat{\mathbf{u}}^e = (\hat{u}_0^e, \dots, \hat{u}_P^e)^T$, $\hat{\mathbf{u}}_g \in \mathbb{R}^N$, $\hat{\mathbf{u}}_l \in \mathbb{R}^{N_{loc}}$ and $N_{loc} = N_{el}(P + 1)$. As there can be more local degrees of freedom than global degrees of freedom, $N_{loc} > N$, we need to impose some conditions on the local expansion coefficients. One of the common approach is to enforce C^0 continuity across elemental boundaries, referred to as the continuous Galerkin projection. Following the definition of local basis expansions in equation (2.20), we can enforce the solution to be equivalent at the elemental boundary using the condition,

$$\hat{u}_P^{e-1} = \hat{u}_0^e. \quad (2.25)$$

The graphical representation of this condition enforcing C^0 continuity between the element boundaries for three finite elements with $P = 2$ local basis expansions, and the relationship between global and local basis coefficients are shown in figure 2.2. We can relate the global and local basis coefficients with an assembly matrix, $\mathbf{A} \in \mathbb{R}^{N_{loc} \times N}$,

$$\hat{\mathbf{u}}_l = \mathbf{A} \hat{\mathbf{u}}_g. \quad (2.26)$$

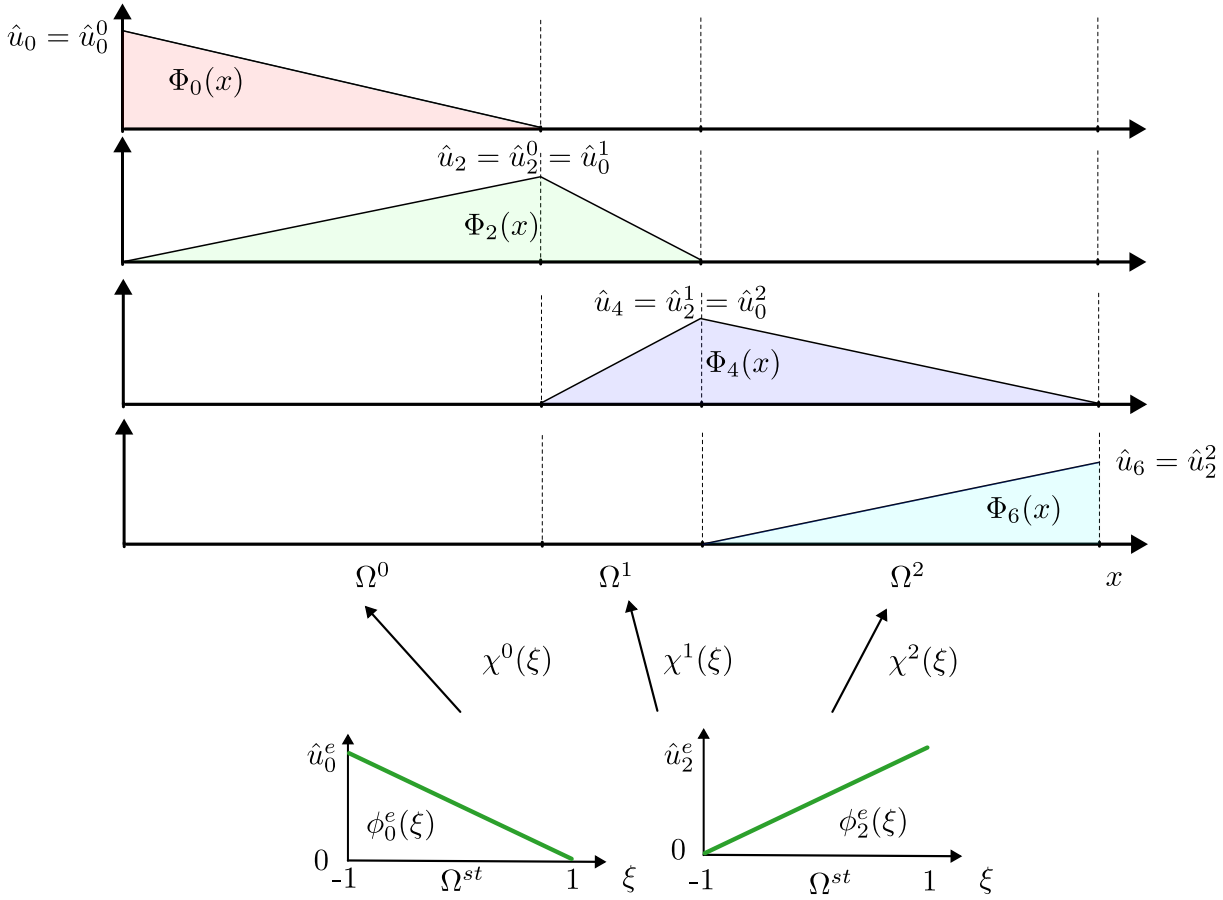


Figure 2.2: A graphical representation of C^0 across elemental boundaries and the relationship between local basis coefficients, u_0^e , u_P^e , and global basis expansions, u_i .

In the case for $P = 2$ and three finite elements as in the case of figures 2.1 and 2.2, the assembly matrix and the vectors of global and local basis coefficients are given as,

$$\hat{\mathbf{u}}_l = \begin{pmatrix} \hat{u}_0^1 \\ \hat{u}_1^1 \\ \hat{u}_2^1 \\ \hat{u}_0^2 \\ \hat{u}_1^2 \\ \hat{u}_2^2 \\ \hat{u}_0^3 \\ \hat{u}_1^3 \\ \hat{u}_2^3 \end{pmatrix}, \quad \mathbf{A} = \begin{pmatrix} 1 & 0 & 0 & 0 & 0 & 0 & 0 \\ 0 & 1 & 0 & 0 & 0 & 0 & 0 \\ 0 & 0 & 1 & 0 & 0 & 0 & 0 \\ 0 & 0 & 1 & 0 & 0 & 0 & 0 \\ 0 & 0 & 0 & 1 & 0 & 0 & 0 \\ 0 & 0 & 0 & 0 & 1 & 0 & 0 \\ 0 & 0 & 0 & 0 & 1 & 0 & 0 \\ 0 & 0 & 0 & 0 & 0 & 1 & 0 \\ 0 & 0 & 0 & 0 & 0 & 0 & 1 \end{pmatrix}, \quad \hat{\mathbf{u}}_g = \begin{pmatrix} \hat{u}_0 \\ \hat{u}_1 \\ \hat{u}_3 \\ \hat{u}_4 \\ \hat{u}_5 \\ \hat{u}_6 \end{pmatrix}, \quad (2.27)$$

The assembly matrix \mathbf{A} ‘scatters’ the global degrees of freedom to local degrees of freedom, while the transpose of it, \mathbf{A}^T , performs the reverse, referred to as global assembly. For example, we wish to perform integration in the domain Ω ,

$$\mathbf{I}_g[j] = (\Phi_j(x), u^\delta(x)), \quad (2.28)$$

where $\mathbf{I}_g \in \mathbb{R}^N$ refers to a vector containing the integral between $\Phi_i(x)$ and $u^\delta(x)$. This is related to first performing integration using local expansion basis within standard elements, and then assembling using \mathbf{A}^T ,

$$\mathbf{I}_g = \mathbf{A}^T \mathbf{I}_l, \quad (2.29a)$$

where,

$$\mathbf{I}_g = \begin{bmatrix} \mathbf{I}_0 \\ \vdots \\ \mathbf{I}_{N_g-1} \end{bmatrix}, \quad \mathbf{I}_l = \begin{bmatrix} \mathbf{I}^0 \\ \vdots \\ \mathbf{I}^{N_{el}-1} \end{bmatrix}, \quad \text{with} \quad \mathbf{I}^e = \begin{bmatrix} \int_{-1}^1 \phi_0^e(\xi) u(\chi^e) \frac{d\chi^e}{d\xi} d\xi \\ \vdots \\ \int_{-1}^1 \phi_{P-1}^e(\xi) u(\chi^e) \frac{d\chi^e}{d\xi} d\xi \end{bmatrix}, \quad (2.29b)$$

and $\mathbf{I}_l \in \mathbb{R}^{N_{loc}}$ refer to the vector of integration operations performed within a standard element. In the spectral/ hp element approach, we perform integration and differentiation using local basis expansions within a standard element. After doing so, we assemble the local operations from the standard element to the global domain by using \mathbf{A}^T , as we shall show later using a 1D example. We note that the structure of assembly matrix is generally sparse, where the entries either contain 0, 1 or -1 in multidimensional formulation. Therefore, the assembly matrix is not constructed in practice, and a mapping array is used instead.

2.3.4 Local basis expansions

The choice of local basis expansions, $\phi_i^e(\xi)$, concerns the representation of the solution, and the convergence properties of the numerical solver, in particular, the condition number of the mass and laplacian matrices. In general, the local basis expansions can be classified into two groups, either *modal* or *nodal* expansions.

Modal expansions

Modal expansions, or hierarchical expansions, describes a set of expansion basis where an expansion set (\mathcal{X}_{P-1}^δ) of order $P - 1$, is contained within a set (\mathcal{X}_P^δ) of order P , e.g. $\mathcal{X}_{P-1}^\delta \subset \mathcal{X}_P^\delta$. An example of modal expansions are the Jacobi polynomials, $P_p^{\alpha,\beta}(x)$, representing a family of solutions to the Sturm-Liouville problem within, $x \in [-1, 1]$. The Jacobi polynomials become symmetric for $\alpha = \beta$, referred to ultraspheric polynomials. Special cases of ultraspheric polynomials are the Legendre polynomials, $\alpha = \beta = 1$, and the Chebyshev polynomials, $\alpha = \beta = 1/2$. Within the Nektar++ framework, we utilise the *modified* basis, based on Jacobi polynomials that are modified (hence the name),

$$\phi_p(\xi) \rightarrow \psi_p(\xi) = \begin{cases} \frac{1-\xi}{2} & \text{for } p = 0 \\ \left(\frac{1-\xi}{2}\right) \left(\frac{1+\xi}{2}\right) P_{p-1}^{1,1}(\xi) & \text{for } 0 < p < P \\ \frac{1+\xi}{2} & \text{for } p = P, \end{cases} \quad (2.30)$$

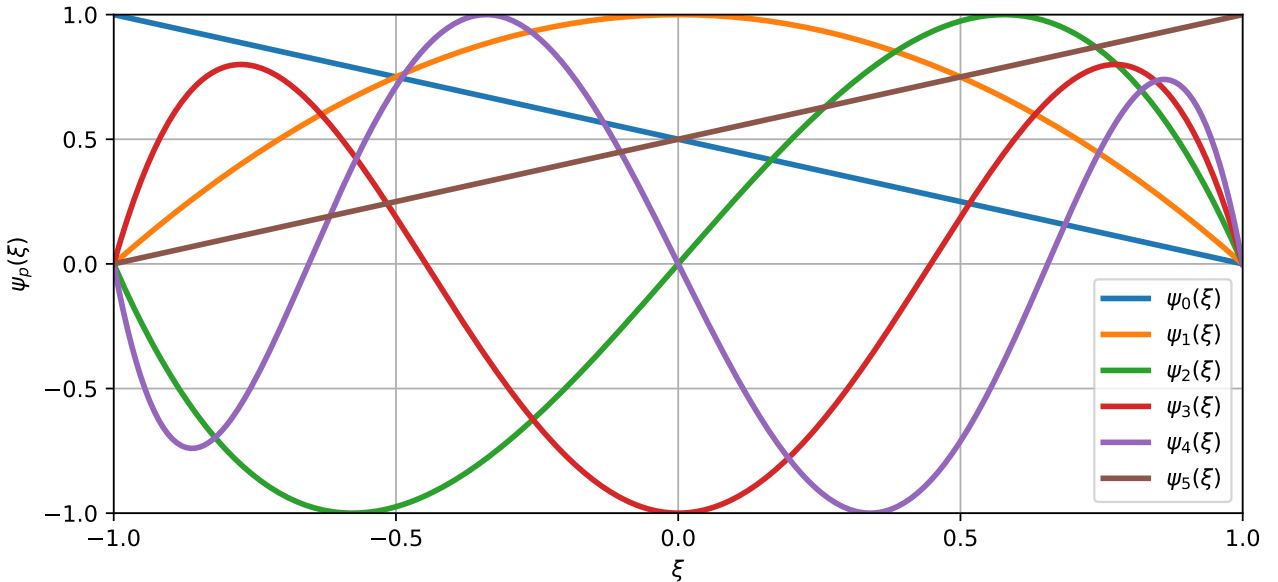


Figure 2.3: The modified basis for up to $P = 5$ normalised to $-1 \leq \psi_p \leq 1$.

We note that $\phi_p(\xi)$ refers to a general local expansion basis while $\psi_p(\xi)$ to definition of the modified basis. The one-dimensional expansion modes of the modified basis of up to $P = 5$ is shown in figure 2.3. The linear modes, corresponding to $p = 0$ and $p = P$, are the only expansions which has a magnitude of at the boundaries, referred to as boundary modes. The modified basis for $0 < p < P$, are hierarchical, and have non-zero values except at the boundaries, referred to as interior/bubble modes. Decomposing the local expansions into interior and boundary mode essentially via a partition of unity, ensures that the linear modes, $P = 1$, supports the C^0 continuity across element boundaries. So strictly speaking, the modified basis is only modal for $P > 1$.

Nodal expansions

Nodal expansions are basis expansions that are non-hierarchical, $\mathcal{X}_{P-1}^\delta \not\subset \mathcal{X}_P^\delta$. An example of nodal expansions are the Lagrange polynomials,

$$\phi_p(\xi) \rightarrow h_p(\xi) = \frac{\prod_{q=0, q \neq p}^P (\xi - \xi_q)}{\prod_{q=0, q \neq p}^P (\xi_p - \xi_q)} \quad (2.31)$$

The Lagrange polynomials, $h_p(\xi)$, are particular attractive as it has a unit value at discrete nodal values, ξ_q , and zero everywhere else, $h_p(\xi_q) = \delta_{pq}$, which implies that

$$u^\delta(\xi_q) = \sum_{p=0}^P \hat{u}_p h_p(\xi_q) = \sum_{p=0}^P \hat{u}_p \delta_{pq} = \hat{u}_q, \quad (2.32)$$

where the Lagrange coefficient \hat{u}_q is the same as the value evaluated at the node ξ_q . The nodal values, ξ_q , are based on the Gauss-Lobatto-Legendre (GLL) points which will be defined later in §2.3.5. The nodal distribution based on GLL points is crucial for obtaining well-behaved Lagrange polynomials, as the use of equispaced nodal points leads to oscillations between nodes. Figure 2.4 presents Lagrange

expansions evaluated along the GLL points.

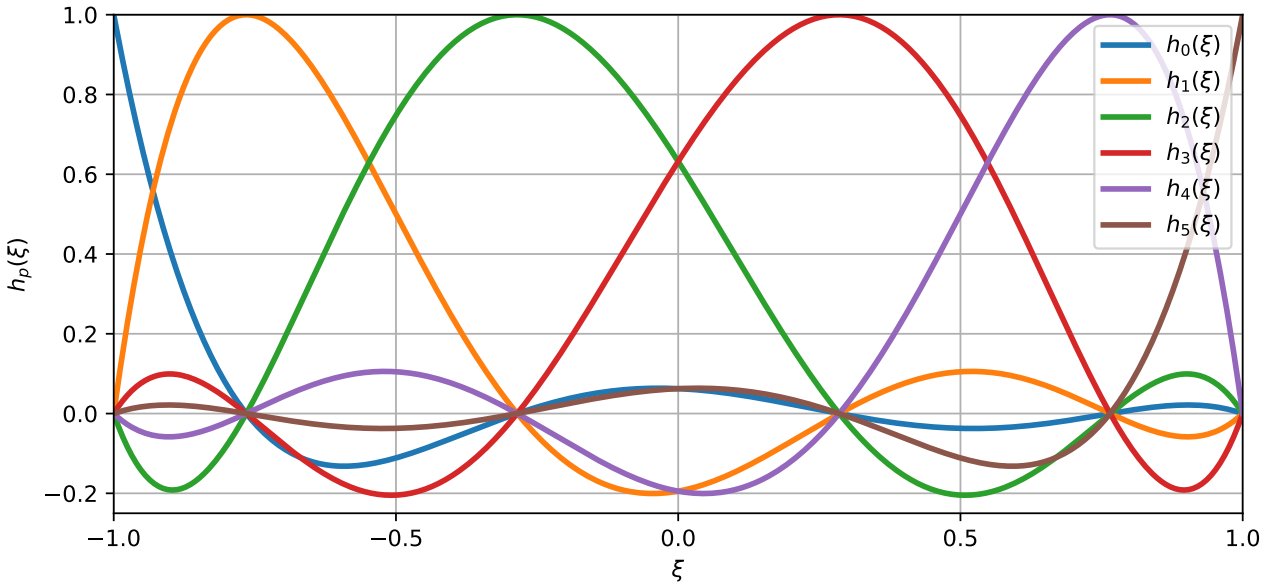


Figure 2.4: Lagrange polynomials for $P = 5$ with nodal values along GLL points.

Multi-dimensional expansions

We have introduced modal and nodal expansions in one dimension, and its extension to multi-dimensions bases can be generalised using a tensorial expansion of the local expansion bases. The standard element in a two dimensional quadrilateral, \mathcal{Q}^2 , and a three dimensional hexahedral \mathcal{H}^3 , are given as,

$$\mathcal{Q}^2 = \{-1 \leq \xi_1, \xi_2 \leq 1\}, \quad \mathcal{H}^3 = \{-1 \leq \xi_1, \xi_2, \xi_3 \leq 1\} \quad (2.33)$$

where ξ_1, ξ_2, ξ_3 refers to the local coordinates in multi-dimensions. Thus, the multi-dimensional expansion bases for quadrilaterals and hexadrales using modified bases are simply a tensor product of the one dimensional modified bases,

$$\phi_{pq}(\xi_1, \xi_2) = \psi_q(\xi_1)\psi_q(\xi_2), \quad \text{and} \quad \phi_{pqr}(\xi_1, \xi_2, \xi_3) = \psi_q(\xi_1)\psi_q(\xi_2)\psi_r(\xi_3). \quad (2.34)$$

An example of the modal tensorial bases, for $p = q = 4$ in a standard quadrilateral element is shown in figure 2.5. While we have discussed the tensorial the expansions for regular domains such as the standard quadrilateral and hexahedral elements, the extensions for simplex domains such as triangles, tetrahedrals, prisms and pyramids commonly used to represent complex geometries, are less straightforward. The challenge for simplexes is that the local coordinates, ξ_1, ξ_2, ξ_3 , become dependent where a direct tensorial expansion becomes unwieldy. Instead, a collapsed coordinate system is introduced, providing a transformation from a standard simplex element to a standard regular element. In this thesis, we utilise quadrilateral elements. The reader is referred to [G. Karniadakis and Sherwin \(2005\)](#) for more details about the multi-dimensional formulation of regular and simplex elements.

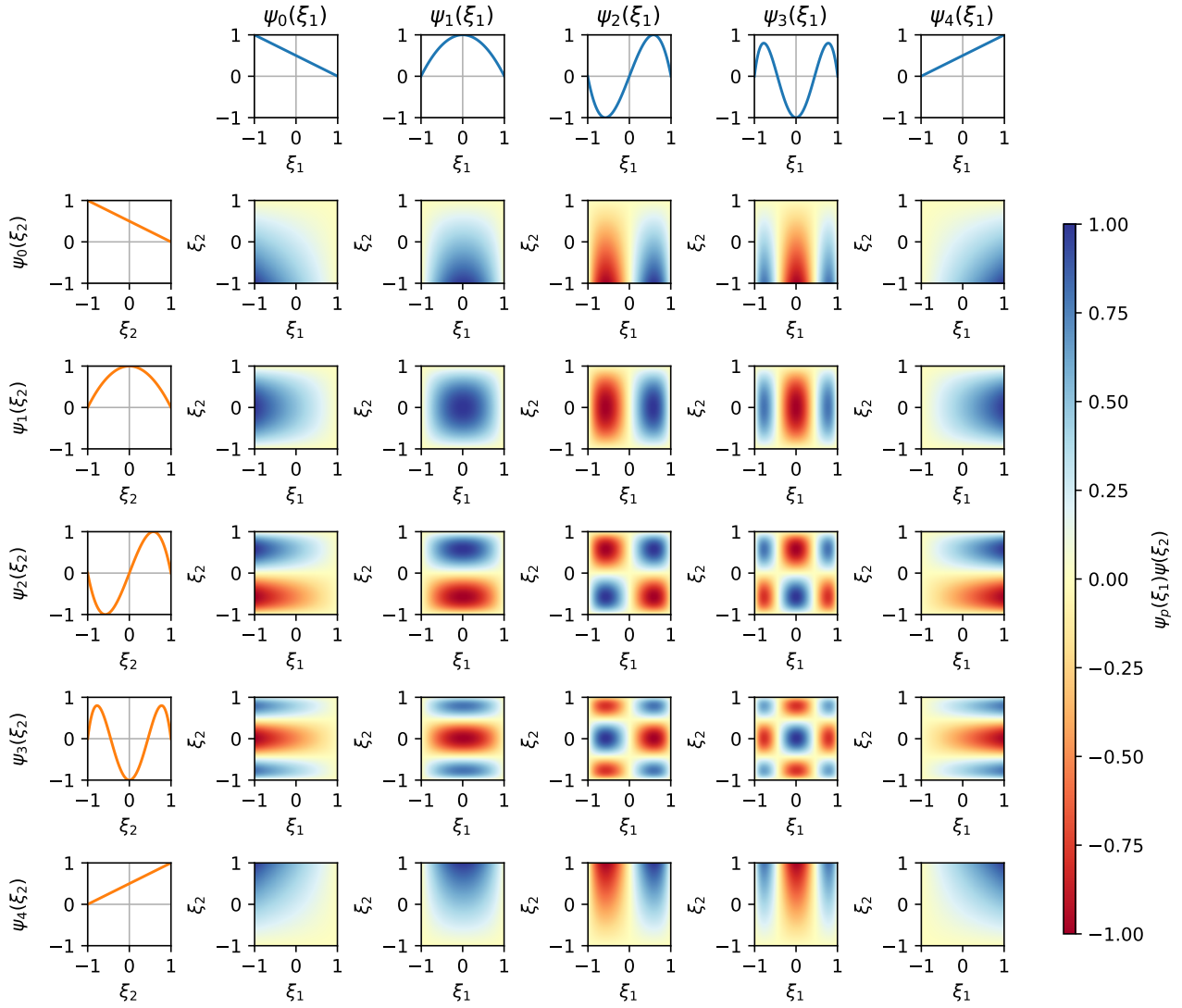


Figure 2.5: Two dimensional modified basis with $p = q = 4$ in a standard quadrilateral, $-1 \leq \xi_1, \xi_2 \leq 1$. The modified bases are normalised to $-1 \leq \phi_{pq} \leq 1$.

2.3.5 Gaussian quadrature

In the Galerkin formulation, we perform integration between basis functions rountinely, and an efficient numerical technique is therefore sought. Suppose we want to approximate the integral of a function, $u(\xi)$, in a standard element numerically given as,

$$\int_{-1}^1 u(\xi) d\xi = \sum_{i=0}^{Q-1} w_i u(\xi_i) + R(u). \quad (2.35)$$

The premise is determine the optimal number of quadrature points, Q , integration weights, w_i , and zeros, ξ_i , in which the integral error, $R(u)$, can be minimised. If $u(\xi)$ is of polynomial order of P , we may expect that we require at least $P + 1$ equispaced points to represent $u(\xi)$ sufficiently. Using Gaussian quadrature rules, we can approximate an integral of a function of order P , with far fewer than $P + 1$ points with specific integration weights and zeros. In general, Gaussian quadrature rules can be grouped into three categories: Gauss, Gauss-Radau and Guderauss-Lobatto quadrature. The

main difference between the three categories are on the inclusion of the end points. Gauss quadrature rule evaluates the integral without the end points $\xi = \pm 1$. Gauss-Radau quadrature rule either select one of the end points, often at $\xi = -1$. Gauss-Lobatto quadrature rule consider both end points. We will only focus on describing the Gauss-Lobatto quadrature rules and the zeros of Jacobi polynomials known as the Gauss-Lobatto-Jacobi quadrature rules given as,

$$\xi_i^{\alpha,\beta} = \begin{cases} -1 & i = 0, \\ \xi_{i-1,Q-2}^{\alpha+1,\beta+1} & i = 1, \dots, Q-2, \\ 1 & i = Q-1, \end{cases} \quad (2.36a)$$

$$w_i^{\alpha,\beta} = \begin{cases} (\beta + 1)C_{0,Q-2}^{\alpha,\beta}, & i = 0, \\ C_{i,Q-2}^{\alpha,\beta}, & i = 1, \dots, Q-2, \\ (\alpha + 1)C_{Q-1,Q-2}^{\alpha,\beta}, & i = Q-1, \end{cases} \quad (2.36b)$$

$$C_{i,Q-2}^{\alpha,\beta} = \frac{2^{\alpha+\beta+1}\Gamma(\alpha+Q)\Gamma(\beta+Q)}{(Q-1)(Q-1)!\Gamma(\alpha+\beta+Q+1)[P_{Q-1}^{\alpha,\beta}(\xi_i)]^2} \quad (2.36c)$$

where $w_i^{\alpha,\beta}, \xi_i^{\alpha,\beta}$ are the zeros (or sometimes referred to as quadrature points) and weights of the Gauss-Lobatto-Jacobi quadrature rules, and Γ refers to the Gamma function. For $\alpha = \beta = 0$, the quadrature points is known as the Gauss-Lobatto-Legendre (GLL) points, typically employed for Lagrange polynomials to ensure stability. By evaluating the discrete integral (equation (2.35)) using the zeros and integrations weights (equation (2.36)), we can obtain an exact integral of the function $u(\xi)$, of polynomial order P , with at least $Q \geq (P+3)/2$ quadrature points.

2.3.6 Numerical differentiation

In the same fashion as Gaussian quadrature rules, we want to evaluate the derivative of a function, $u^\delta(\xi)$ numerically. Suppose that we want to differentiate in x using local coordinates given as,

$$\frac{du^\delta(\xi)}{dx} = \frac{du^\delta(\xi)}{d\xi} \frac{d\xi}{dx} = \sum_{p=0}^P \hat{u}_p \frac{d\phi_p(\xi)}{d\xi} \frac{d\xi}{dx}, \quad (2.37)$$

where $d\xi/dx$ is the jacobian. The primary step involves evaluating the derivative of the local expansion bases, $d\phi_p(\xi)/d\xi$. By exploiting the Kronecker delta property of Lagrange polynomials, any polynomials can be conveniently represented by a sum of Lagrange polynomials. Suppose that the solution has polynomial order P , we can represent exactly it with $P+1$ Lagrange polynomials, $\phi_p(\xi) \rightarrow h_p(\xi)$. Its derivative through $Q \geq P+1$ discrete nodal points, ξ_i for all $i = 0, 1, \dots, Q-1$, is expressed as,

$$\frac{du^\delta(\xi)}{d\xi} \Big|_{\xi=\xi_i} = \sum_{j=0}^P \hat{u}_j \frac{dh_j(\xi)}{d\xi} \Big|_{\xi=\xi_i} = \sum_{j=0}^P d_{ij} \hat{u}_j, \quad (2.38)$$

where $\mathbf{D} = [d_{ij}] \in \mathbb{R}^{Q \times Q}$ refers to the differential matrix containing values of the derivative of the Lagrange polynomials at the quadrature points. Since we are evaluating the derivative along nodal (collocated) points, it is referred to as *collocation* differentiation. The general form for collocation differentiation based on Lagrange polynomials can be expressed as,

$$d_{ij} = \frac{dh_j(\xi)}{d\xi} \Big|_{\xi=\xi_i} = \begin{cases} \frac{g'_Q(\xi_i)}{g'_Q(\xi_j)} \frac{1}{\xi_i - \xi_j}, & i \neq j, \\ \frac{g''_Q(\xi_i)}{2g'_Q(\xi_i)}, & i = j, \end{cases} \quad g_Q(\xi) = \prod_{j=0}^{Q-1} (\xi - \xi_j). \quad (2.39)$$

Since d_{ij} only depends on the choice of zeros, alternative forms of $g'_q(\xi_j)$ and $g''_q(\xi_j)$ for the a choice of zeros can be found in Appendix C of [G. Karniadakis and Sherwin \(2005\)](#). To perform collocation differentiation using modal basis such as the modified basis, $u^\delta(\xi) = \sum_{j=0}^P \hat{u}_j \psi_j(\xi)$, we need to represent the solution in nodal coordinates,

$$\frac{du^\delta(\xi)}{d\xi} \Big|_{\xi=\xi_i} = \frac{d}{d\xi} \sum_{j=0}^P \hat{u}_j \psi_j(\xi) \Big|_{\xi=\xi_i} = \mathbf{D}\mathbf{B}\hat{\mathbf{u}}, \quad (2.40)$$

where $\mathbf{B} \in \mathbb{R}^{Q \times (P+1)}$ refers to the standard matrix which transforms the solution from coefficient space, $\hat{\mathbf{u}} \in \mathbb{R}^{P+1}$, to nodal space, $\mathbf{u} \in \mathbb{R}^Q$, known as the backwards transform operation, $\mathbf{u} = \mathbf{B}\hat{\mathbf{u}}$.

2.3.7 Example in 1D

We have outlined the basic formulation of spectral/*hp* element methods in a single dimension. To conclude the section on spectral/*hp* element methods, we will describe its solution procedure, converting the weak form of the Helmholtz equation into a system of linear equations, and introduce the mass and laplacian matrices. Starting from the weak form,

$$\lambda \int vu \, dx + \int \frac{\partial v}{\partial x} \frac{\partial u}{\partial x} \, dx = \int vf \, dx + \left[v \frac{du}{dx} \right]_0^l, \quad x \in [0, l], \quad (2.41a)$$

with boundary conditions,

$$u(0) = g_D, \quad \frac{du}{dx} \Big|_{x=l} = g_N. \quad (2.41b)$$

We wish to seek the approximate solution $u(x) \approx u^\delta(x)$. Suppose they can be discretised by spectral/*hp* elements with N_{el} elements and $P + 1$ local expansion basis,

$$u^\delta(x) = \sum_{i=0}^N \hat{u}_i \Phi_i(x) = \sum_{e=1}^{N_{el}} \sum_{i=0}^P \hat{u}_i^e \phi_i^e(\xi), \quad (2.42a)$$

with test functions similarly defined as,

$$v^\delta(x) = \sum_{i=0}^N \hat{v}_i \Phi_i(x) = \sum_{e=1}^{N_{el}} \sum_{i=0}^P \hat{v}_i^e \phi_i^e(\xi) \quad (2.42b)$$

Substituting the expansions of u^δ, v^δ into the weak form (equation (2.41a)) and evaluating the first term on the left hand side using numerical quadrature over Q quadrature points within a standard region, the e^{th} elemental contribution becomes,

$$\begin{aligned} \int_{-1}^1 \sum_{i=0}^P \hat{v}_i^e \phi_i^e(\xi) \sum_{j=0}^P \hat{u}_j^e \phi_j^e(\xi) \frac{d\chi^e}{d\xi} d\xi &= \sum_{e=0}^{N_{el}-1} \sum_{q=0}^{Q-1} \left[\sum_{i=0}^P \hat{v}_i^e \phi_i^e(\xi_q) \sum_{j=0}^P \hat{u}_j^e \phi_j^e(\xi_q) \right] J^e w_q^e \\ &= (\hat{\mathbf{v}}^e)^T (\mathbf{B}^e)^T \mathbf{W}^e \mathbf{B}^e \hat{\mathbf{u}}^e \\ &= \hat{\mathbf{v}}^T \mathbf{M}^e \hat{\mathbf{u}}^e \end{aligned} \quad (2.43)$$

where the elemental mass matrix is defined as

$$\mathbf{M}^e = (\mathbf{B}^e)^T \mathbf{W}^e \mathbf{B}^e \in \mathbb{R}^{(P+1) \times (P+1)}. \quad (2.44)$$

Here, $\mathbf{B}^e \in \mathbb{R}^{Q \times (P+1)}$ refers to the elemental basis matrix, and $\mathbf{W}^e \in \mathbb{R}^{Q \times Q}$, the elemental weight matrix, a diagonal matrix consisting of the product between integration weights, w_q^e , and the element's jacobian, $J^e = \frac{d\chi^e}{d\xi}$.

$$\mathbf{B}^e = \begin{bmatrix} \phi_0^e(\xi_0) & \cdots & \phi_P^e(\xi_0) \\ \vdots & \ddots & \vdots \\ \phi_0^e(\xi_Q) & \cdots & \phi_P^e(\xi_Q) \end{bmatrix}, \quad \mathbf{W}^e = \begin{bmatrix} w_0^e J^e & & 0 \\ & \ddots & \\ 0 & & w_{Q-1}^e J^e \end{bmatrix} \quad (2.45)$$

Next, we evaluate the e^{th} elemental contribution of the second term on the left hand side,

$$\begin{aligned} \int_{-1}^1 \sum_{i=0}^P \hat{v}_i^e \frac{d\phi_i^e}{d\xi} \sum_{j=0}^P \hat{u}_j^e \frac{d\phi_j^e}{d\xi} \left(\frac{d\chi^e}{d\xi} \right)^{-1} d\xi &= \sum_{e=0}^{N_{el}-1} \sum_{q=0}^{Q-1} \left[\sum_{i=0}^P \hat{v}_i^e D_{qi}^e \phi_i^e(\xi_q) \sum_{j=0}^P \hat{u}_j^e D_{qj}^e \phi_j^e(\xi_q) \right] \frac{w_q^e}{J^e} \\ &= (J^e)^{-1} \hat{\mathbf{v}}^T (\mathbf{B}^e)^T (\mathbf{D}^e)^T \mathbf{W}^e \mathbf{D}^e \mathbf{B}^e \hat{\mathbf{u}}^e \\ &= (J^e)^{-1} \hat{\mathbf{v}}^T \mathbf{L}^e \hat{\mathbf{u}}^e \end{aligned} \quad (2.46)$$

where the elemental Laplacian matrix is defined as

$$\mathbf{L}^e = (J^e)^{-1} (\mathbf{B}^e)^T (\mathbf{D}^e)^T \mathbf{W}^e \mathbf{D}^e \mathbf{B}^e \in \mathbb{R}^{(P+1) \times (P+1)}, \quad (2.47)$$

and $\mathbf{D}^e \in \mathbb{R}^{Q \times Q}$ refers to the differential matrix defined in equation (2.39). Moving onto the first term on the right hand side,

$$\begin{aligned} \int_{-1}^1 \sum_{i=0}^P \hat{v}_i^e \phi_i^e(\xi) f^e(\xi) \frac{d\chi^e}{d\xi} d\xi &= \sum_{q=0}^P \sum_{i=0}^P \hat{v}_i^e \phi_i^e(\xi_q) f^e(\xi_q) J^e w_q^e, \\ &= \hat{\mathbf{v}}^T (\mathbf{B}^e)^T \mathbf{W}^e \mathbf{f}^e \\ &= \hat{\mathbf{v}}^T \hat{\mathbf{f}}^e, \end{aligned} \quad (2.48)$$

where $\hat{\mathbf{f}}^e$ is the elemental forcing vector. By assembling all elemental contributions, $1 \leq e \leq N_{el}$, we obtain the local system of linear equations,

$$\begin{bmatrix} [\lambda \mathbf{M}^1 + \mathbf{L}^1] & \cdots & \mathbf{0} \\ \vdots & \ddots & \vdots \\ \mathbf{0} & \cdots & [\lambda \mathbf{M}^{N_{el}} + \mathbf{L}^{N_{el}}] \end{bmatrix} \begin{bmatrix} \hat{\mathbf{u}}^1 \\ \vdots \\ \hat{\mathbf{u}}^{N_{el}} \end{bmatrix} = \begin{bmatrix} \hat{\mathbf{f}}^1 \\ \vdots \\ \hat{\mathbf{f}}^{N_{el}} \end{bmatrix} \quad (2.49a)$$

or in compact form,

$$[\lambda \mathbf{M}_l + \mathbf{L}_l] \hat{\mathbf{u}}_l = \hat{\mathbf{f}}_l. \quad (2.49b)$$

where $\mathbf{M}_l \in \mathbb{R}^{N_{el}(P+1) \times N_{el}(P+1)}$, $\mathbf{L}_l \in \mathbb{R}^{N_{el}(P+1) \times N_{el}(P+1)}$, $\hat{\mathbf{u}}_l \in \mathbb{R}^{N_{el}(P+1)}$ and $\hat{\mathbf{f}}_l \in \mathbb{R}^{N_{el}(P+1)}$ refers to the local mass matrix, local laplacian matrix, vector of local expansion coefficients and local forcing vector. To enforce C^0 continuity across elemental boundaries, we pre-multiply equation (2.49) with the assembly map, \mathbf{A}^T , and express local coefficients as global coefficients,

$$\mathbf{A}^T [\lambda \mathbf{M}_l + \mathbf{L}_l] \mathbf{A} \hat{\mathbf{u}}_g = \mathbf{A}^T \hat{\mathbf{f}}_l. \quad (2.50)$$

Finally, we consider the boundary conditions by lifting $u^\delta(x) = u^\mathcal{H}(x) + u^\mathcal{D}(x)$

$$\mathbf{A}^T [\lambda \mathbf{M}_l + \mathbf{L}_l] \mathbf{A} \hat{\mathbf{u}}_g^\mathcal{H} = \mathbf{A}^T \hat{\mathbf{f}}_l + \mathbf{A}^T [\lambda \mathbf{M}_l - \mathbf{L}_l] \mathbf{A} \hat{\mathbf{u}}_g^\mathcal{D}. \quad (2.51)$$

We then solve this system for the homogeneous coefficients $\hat{\mathbf{u}}_g^\mathcal{H}$.

2.3.8 Error properties

Suppose we consider $P + 1$ orthogonal polynomials spanning the polynomial space of \mathcal{P}_P , the energy norm of the error, $\|\varepsilon\|_E = \|u(x) - u^\delta(x)\|_E$ ² for element size of h and polynomial order P , satisfies the convergence property (Babuška & Suri, 1994),

$$\|\varepsilon\|_E \leq Ch^{\mu-1} P^{-(k-1)} \|u\|_k, \quad (2.52)$$

²The energy norm is defined as $\|u\|_E = \sqrt{a(u, u)}$, where $a(u, u)$ is the bilinear operator introduced in equation (2.7b). It is a measure of functions belonging to the *energy* space which are H^1 functions.

where $\mu = \min(k, P + 1)$, and C is independent of h , P and u . To illustrate this convergence property, we consider the exact solution, $u = \sin(\pi x)$, to the 1D Helmholtz problem (equation (2.5)) on the domain $x \in [-1, 1]$ with Dirichlet boundary conditions on both ends and $\lambda = 1$. This convergence

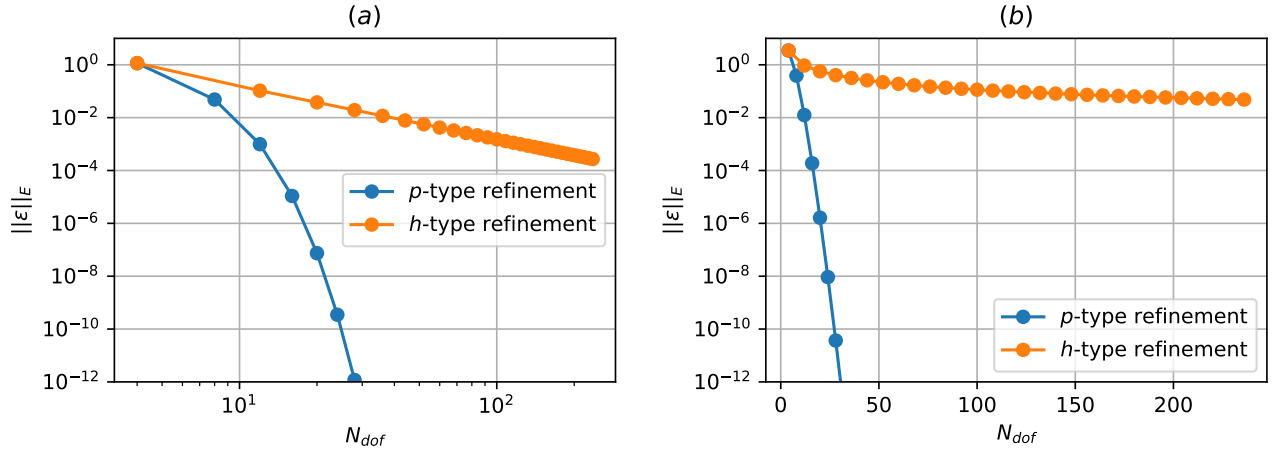


Figure 2.6: Convergence properties of an exact solution $u = \sin(\pi x)$ to a 1D Helmholtz equation with $\lambda = 1$ and Dirichlet boundary conditions at $x \in [-1, 1]$. h -type refinement is performed on a mesh with fixed $P = 1$ and decreasing h (increasing elements), demonstrating algebraic convergence in a *log-log* plot of (a). p -type refinement is performed on a mesh with equispaced two elements and increasing P , demonstrating exponential convergence on a *semi-log* plot of (b).

property arising from the h - and p -type refinements is shown in figure 2.6. To ensure consistency between two types of refinement, the number of degrees of freedom, N_{dof} , is shown on the abscissa, which scales as $\mathcal{O}(h) \sim \mathcal{O}(N_{dof}^{-1})$ and $\mathcal{O}(p) \sim \mathcal{O}(N_{dof})$. For h -refinement, the number of elements is doubled on a mesh with fixed polynomial order $P = 1$, demonstrating algebraic convergence, $\|\varepsilon\|_E \sim \mathcal{O}(h)$ in figure 2.6(a). For p -refinement, the polynomial order P is increased on a mesh with two equispaced elements, showing exponential convergence, $\|\varepsilon\|_E \sim \mathcal{O}(c^p)$ where c is a constant, in figure 2.6(b).

2.4 Numerical methods for solving the Navier-Stokes equations

2.4.1 Velocity Correction Scheme

The spatial discretisation of the Helmholtz operator and its numerical solution procedure has been discussed using the spectral/ hp element methods. Here, we describe the numerical methods that is used to solve the Navier-Stokes equations given as,

$$\frac{\partial \mathbf{u}}{\partial t} + (\mathbf{u} \cdot \nabla) \mathbf{u} = -\nabla p + \nu \nabla^2 \mathbf{u} + \mathbf{f} \quad (2.53a)$$

$$\nabla \cdot \mathbf{u} = 0, \quad (2.53b)$$

with boundary conditions,

$$\mathbf{u} = 0, \quad \text{on } \partial\Omega. \quad (2.53c)$$

In the above, the primitive variables are velocity and pressure (\mathbf{u}, p) and we assumed unit density, $\rho = 1$, with the kinematic viscosity appearing as the control parameter. The time evolution of velocity is explicitly expressed in equation (2.53a), but does not appear for the pressure, which is coupled to the velocity field, enforcing the incompressibility condition. Several strategies exist for addressing the coupled velocity-pressure fields by

1. Solving the coupled system such as the Uzawa algorithm,
2. Splitting methods,

We adopt splitting methods, which solves the of the Navier-Stokes equation by splitting them into ‘subequations’, and solving them sequentially. These methods, belonging to the broader family of projection methods introduced by [Chorin \(1967\)](#) and [Témam \(1969\)](#), and can be further classified into pressure-correction or velocity-correction schemes. This thesis employs the use of the high-order velocity-correction scheme introduced by [G. E. Karniadakis et al. \(1991\)](#) and further explained by [Guérmond and Shen \(2003\)](#). We rewrite the incompressible Navier-Stokes equations in semi-discrete form with using linear and nonlinear operators as,

$$\frac{\partial \mathbf{u}}{\partial t} = \mathbf{N}(\mathbf{u}) - \nabla p + \nu \mathbf{L}(\mathbf{u}), \quad (2.54a)$$

$$\nabla \cdot \mathbf{u} = 0, \quad (2.54b)$$

with boundary conditions,

$$\mathbf{u}|_{\Omega} = 0, \quad \mathbf{u}(t = 0) = \mathbf{u}_0. \quad (2.54c)$$

The nonlinear, \mathbf{N} , linear, \mathbf{L} , operators are obtained from a suitable spatial-discretisation method such as the spectral/ hp element method. The nonlinear and linear operators are defined as,

$$\mathbf{N}(\mathbf{u}) \equiv -(\mathbf{u} \cdot \nabla) \mathbf{u}, \quad \mathbf{L}(\mathbf{u}) \equiv \nabla^2 \mathbf{u}, \quad (2.55)$$

To minimise aliasing errors in the quadratic nonlinear terms, we performing numerical integration by increasing the number of quadrature points to $Q \geq (P + 3)/2$. To advance the velocity at time step, \mathbf{u}^n , to the next time step, \mathbf{u}^{n+1} , we integrate equation (2.54) over a time step Δt ,

$$\mathbf{u}^{n+1} - \mathbf{u}^n = \underbrace{\int_{t_n}^{t_{n+1}} \mathbf{N}(\mathbf{u}) dt}_{\Delta t \sum_{q=0}^{J_e-1} \beta_q \mathbf{N}(\mathbf{u}^{n-q})} - \underbrace{\int_{t_n}^{t_{n+1}} \nabla p dt}_{\Delta t \nabla \bar{p}^{n+1}} + \nu \underbrace{\int_{t_n}^{t_{n+1}} \mathbf{L}(\mathbf{u}) dt}_{\Delta t \sum_{q=0}^{J_i-1} \gamma_q \mathbf{L}(\mathbf{u}^{n+1-q})}. \quad (2.56)$$

The velocity correction scheme ‘splits’ equation (2.54) into three steps shown as underbraces, which are evaluated successively from left to right. The first step we perform is to extrapolate the advection velocities, by approximating the nonlinear terms using an explicit scheme such as the Adams-Bashforth family of J_e order,

$$\frac{\hat{\mathbf{u}} - \sum_{q=0}^{J_e-1} \alpha_q \mathbf{u}^{n-q}}{\Delta t} = \sum_{q=0}^{J_e-1} \beta_q \mathbf{N}(\mathbf{u}^{n-q}), \quad (2.57)$$

where $\hat{\mathbf{u}}$ is denotes the primary intermediate velocity field desired and α_e, β_e refers to the time integration coefficients for a prescribe J_e -th order, described later. After evaluting $\hat{\mathbf{u}}$, we move onto the second term in equation (2.56), which defines the pressure at time step $n + 1$ as,

$$\frac{\hat{\mathbf{u}} - \hat{\mathbf{u}}}{\Delta t} = -\nabla p^{n+1}. \quad (2.58)$$

$\hat{\mathbf{u}}$ denotes as the secondary intermediate velocity. In this single equation, we seek to obtain two unknown solutions, $\hat{\mathbf{u}}$ and p^{n+1} , which is ill-posed, and seek to impose certain restrictions. The splitting method assumes that the secondary intermediate velocity is divergence free, $\nabla \cdot \hat{\mathbf{u}} = 0$, and satisfies the Dirichlet boundary conditions normal to the boundary, $\hat{\mathbf{u}} \cdot \mathbf{n} = \mathbf{u}|_{\Omega} \cdot \mathbf{n}$. By considering the assumptions above and the divergence of equation (2.58), we obtain the pressure Poisson equation with the primary intermediate velocity acting as the forcing term,

$$\nabla^2 p^{n+1} = \nabla \cdot \left(\frac{\hat{\mathbf{u}}}{\Delta t} \right) \quad (2.59a)$$

and boundary conditions,

$$\frac{\partial p^{n+1}}{\partial n} = \mathbf{n} \cdot \left(\frac{\hat{\mathbf{u}} - \hat{\mathbf{u}}}{\Delta t} \right). \quad (2.59b)$$

While the pressure boundary condition (2.59b) is straightforward to evaluate, it is sensitive to large splitting errors (G. E. Karniadakis et al., 1991). To overcome this, we consider a high-order boundary condition of pressure, obtained by taking the dot product with respect to the normal of equation (2.54),

$$\frac{\partial p^{n+1}}{\partial t} = - \sum_{q=0}^{J_e-1} \beta_q \left[\frac{1}{\Delta t} \mathbf{u}^{n-q} + \nu [\nabla \times (\nabla \times \mathbf{u}^{n-q})] + (\mathbf{u}^{n-q} \cdot \nabla) \mathbf{u}^{n-q} \right] \cdot \mathbf{n}. \quad (2.60)$$

Notably, the linear operator is expressed as $\mathbf{L}(\mathbf{u}) = \nabla(\nabla \cdot \mathbf{u}) - \nabla \times (\nabla \times \mathbf{u})$, where the divergence is set to zero, favouring numerical stability (G. E. Karniadakis et al., 1991; Orszag, Israeli, & Deville, 1986). J_e is the order the explicit scheme as in equation (2.57). After solving for the pressure Poisson equation, the secondary intermediate velocity could be subsequently obtained using equation (2.58). After which, we can move onto the final substep in equation (2.56), by solving a Helmholtz equation for \mathbf{u}^{n+1} ,

$$\frac{\gamma_0 \mathbf{u}^{n+1} - \hat{\mathbf{u}}}{\Delta t} = \nu \sum_{q=0}^{J_i-1} \gamma_q \mathbf{L}(\mathbf{u}^{n+1-q}), \quad (2.61)$$

where the linear terms are treated based similar to the family of Adams-Moulton implicit scheme and J_i, γ_q denotes the order of the scheme and time integration coefficients, completing the velocity correction scheme. The time integration coefficients are determined from stiffly stable schemes shown in table 2.2, an improvement from the Adams-family schemes (G. E. Karniadakis et al., 1991). The high order velocity correction scheme and be summarised in a three step process of the following,

$$\mathbf{u}^n \xrightarrow{\mathbf{N}(\mathbf{u}^n)} \hat{\mathbf{u}} \xrightarrow{\nabla^2 p} \hat{\mathbf{u}} \xrightarrow{\mathbf{L}(\hat{\mathbf{u}})} \mathbf{u}^{n+1},$$

Coefficients	1 st order	2 nd order	3 rd order
γ_0	1	3/2	11/6
α_0	1	2	3
α_1	0	-1/2	-3/2
α_2	0	0	1/3
β_0	1	2	3
β_1	0	-1	-3
β_2	0	0	1

Table 2.2: Integration coefficient of stiffly stable schemes from [G. E. Karniadakis et al. \(1991\)](#).

evolving the velocity fields at time step n to $n + 1$.

2.4.2 Fourier spectral/ hp modes

Fourier-Chebyshev-Fourier type discretisation have been recognised as preferred method for performing direct numerical simulations (DNS) of transitional or turbulent incompressible channel flows ([J. Kim et al., 1987](#)) owing to its efficient representation of the inhomogeneous wall-normal directions and the homogeneous streamwise and spanwise directions, using Chebyshev and Fourier expansions respectively.

The Fourier spectral/ hp element method draws on this approach, where the homogeneous and the inhomogeneous directions are represented by the Fourier expansions and spectral/ hp elements respectively. This approach has been commonly referred to as the Quasi-3D or (2.5D) approach, allowing for the representation of two inhomogeneous directions. For example, in the turbulent channel flows with riblets, the Fourier expansions are used to represent the periodic streamwise, while the spectral/ hp elements are used to discretise the wall-normal direction. In the analysis of three-dimensional wakes of cylinders where the Fourier expansions are treated in the spanwise directions. In this thesis, we routinely use the the Quasi-3D approach, consisting of the 2D spectral/ hp elements with 1D Fourier expansions are used to discretise the cross stream plane and streamwise flow respectively. The velocity and pressure in the spectral/ hp plane is described by two dimensional modified bases with Fourier expansions,

$$\begin{bmatrix} \mathbf{u}^\delta(x, y, z, t) \\ p^\delta(x, y, z, t) \end{bmatrix} = \sum_{k=0}^{N_z-1} \sum_{p=0}^P \sum_{q=0}^P \psi_p(x) \psi_q(y) e^{ik\beta z} \begin{bmatrix} \hat{\mathbf{u}}_{p,q,k}(t) \\ \hat{p}_{p,q,k}(t) \end{bmatrix} = \sum_{k=0}^{N_z-1} e^{ik\beta z} \begin{bmatrix} \tilde{\mathbf{u}}_k(x, y, t) \\ \tilde{p}_k(x, y, t) \end{bmatrix} \quad (2.62)$$

where $\beta = \frac{2\pi}{L_z}$ is the spanwise wavenumber, L_z the spanwise length, N_z the number of Fourier expansions. Substituting equation 2.62 into the Navier-Stokes equations and taking the Fourier transform (equivalently to the Galerkin projection with respect to Fourier expansion as a test function) yields a system of N_z decoupled equations, amenable for parallel processing,

$$\frac{\partial \tilde{\mathbf{u}}_k}{\partial t} = -\tilde{\nabla}_k \tilde{p}_k + \nu(\nabla_{x,y}^2 - k^2 \beta^2) \tilde{\mathbf{u}}_k - [\widehat{(\mathbf{u} \cdot \nabla) \mathbf{u}}]_k \quad (2.63a)$$

$$-k\beta \tilde{\nabla} \cdot \tilde{\mathbf{u}}_k = 0, \quad k = 0, \dots, N_z - 1 \quad (2.63b)$$

where, $\tilde{\nabla}_k = (\frac{\partial}{\partial x}, \frac{\partial}{\partial y}, ik\beta)$, $\nabla_{x,y}^2 = (\frac{\partial^2}{\partial x^2}, \frac{\partial^2}{\partial y^2})$ and $[(\widehat{\mathbf{u} \cdot \nabla} \mathbf{u})_k]$ refers to the Fourier-transformed of the k^{th} nonlinear term.

2.4.3 Maintaining fluid flow through a channel

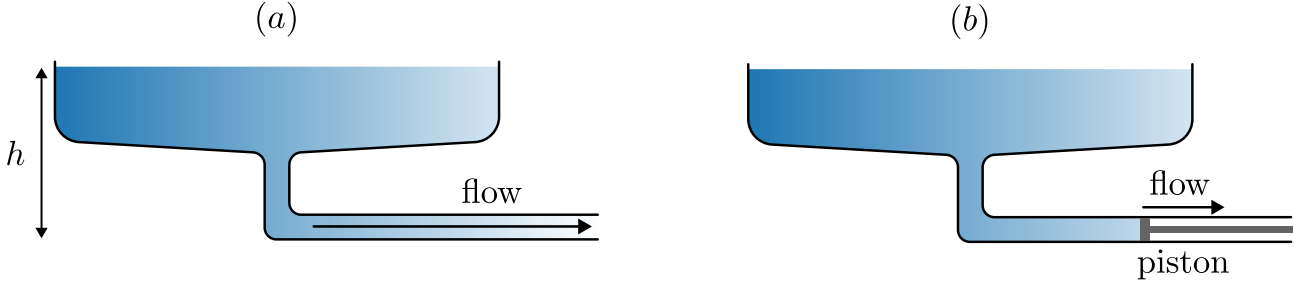


Figure 2.7: (a) Flow rate driven by a pressure gradient from a reservoir elevated by h . (b) Flow driven by a piston at a constant flow rate.

In general, there are two approaches to drive a fluid flow through a channel, either by maintaining a constant pressure drop, or a constant volumetric flux (flow rate). This difference is illustrated in figure 2.7, whereby the flow through the channel is driven by a constant pressure drop from an elevated reservoir of constant height h in figure 2.7(a), while a piston moves at a constant speed rightwards, drawing fluid through the channel at a constant volumetric flux in figure 2.7(b).

Constant pressure via body-forcing

If we were to assign the homogeneous direction (i.e. discretised based on Fourier expansions) as the streamwise direction, a pressure difference cannot be prescribe directly due to the enforced periodicity. Instead, we replace the constant pressure drop with a constant body force $\mathbf{f} = f_x \hat{\mathbf{e}}_x$ in the streamwise direction,

$$\frac{\partial u}{\partial t} + (u \cdot \nabla) u = -\nabla p + \nu \nabla^2 u + f_x, \quad (2.64)$$

The central question now becomes what is the magnitude of body force required to maintain a laminar or turbulent flow. To begin this discussion, we assume that we can decompose our flow variables into a mean and a fluctuating component,

$$u(x, y, t) = U(y) + u'(x, y, t), \quad (2.65)$$

where $U(y) = \langle u \rangle$ refers to the averaged velocity and $\langle \cdot \rangle = \frac{1}{T L_x L_z} \int \cdot dz dx dt$ refers to the temporal and span-averaged operator. The fluctuating component is defined with an average of 0, i.e. $\langle u' \rangle = 0$. Next, we substitute this decomposition into equation (2.64), and perform the averaging operation,

$$\begin{aligned} & \left\langle \frac{\partial(U + u')}{\partial t} + (U + u') \frac{\partial(U + u')}{\partial x} + (V + v') \frac{\partial(V + v')}{\partial y} \right. \\ & \left. = -\frac{\partial(P + p')}{\partial x} + \nu \nabla^2(U + u') + F_x + f'_x \right\rangle. \end{aligned} \quad (2.66)$$

For a statistically stationary turbulent (or laminar) channel flow with periodic streamwise boundary conditions, we can make the following assumptions:

1. stationary flow $\frac{\partial U}{\partial t} = 0$,
2. fully-developed in x , $\frac{\partial}{\partial x} \rightarrow 0$,
3. $\frac{\partial V}{\partial y} = 0$, as a consequence of continuity and the no-slip boundary condition.
4. $\langle u', v', w', p' \rangle = 0$, based on the definition of fluctuations,
5. $\frac{\partial p}{\partial x} = 0$ due to the enforced periodicity in x .

Applying the assumptions above, the mean momentum equations simplify into,

$$\langle F_x \rangle = \left\langle \frac{\partial(u'v')}{\partial y} \right\rangle - \nu \frac{\partial U^2}{\partial y^2}, \quad (2.67)$$

where the body force on the left-hand side balances the sum of Reynolds stresses and viscous diffusion on the right-hand side. Next, we integrate the expression from $y \in [-1, 1]$,

$$2F_x = [\langle u'v' \rangle]_{y=-1}^{y=1} + \nu \left[\frac{\partial U}{\partial y} \Big|_{y=1} - \frac{\partial U}{\partial y} \Big|_{y=-1} \right]. \quad (2.68)$$

The wall shear stress is defined by $\tau_w = \nu \frac{\partial U}{\partial y} \Big|_{y=1}$ (ρ is assumed to be 1), and it is antisymmetric about the channel centreline, $\nu \frac{\partial U}{\partial y} \Big|_{y=1} = -\nu \frac{\partial U}{\partial y} \Big|_{y=-1}$. Due to the no-slip condition, the Reynolds shear stresses is zero, i.e. $[u'v'] \Big|_{y=-1,1} = 0$. Hence, the expression above simplifies to,

$$\tau_w = F_x. \quad (2.69)$$

In other words, the body force F_x is balanced by the wall shear stress (drag), τ_w , along the channel walls. In the case of laminar flow, τ_w can be determined analytically, and the body force required for sustaining a laminar flow for a velocity profile of $u(y) = 1 - y^2$, is $F_x = -2\nu$. However, to determine the wall shear stress (and hence the magnitude of body force) is not as straightforward task for transitional or turbulent channel flow as there isn't an analytical expression for τ_w and its dependence on Reynolds number. Instead, we can only rely on empirical relations of turbulent channel flow between the skin friction coefficient, $c_f = \tau_w / \frac{1}{2}\rho U_c^2$ and Reynolds number Re_c from [Dean \(1978\)](#).

$$c_f = 0.00302 Re_c^{-1/4}, \quad (2.70)$$

where Re_c is the Reynolds number based on the laminar centerline velocity. Similarly, the skin friction coefficient for the case of laminar flow is $c_f = 4/Re_c$ ([Dean, 1978](#)). Figure 2.8 illustrates the relationship between τ_w and Re_c of channel flow using empirical relationship from [Dean \(1978\)](#) (here $\rho = U_c = 1$) and experimental data from [Iida and Nagano \(1998\)](#); [J. Kim et al. \(1987\)](#); [Patel and Head \(1969\)](#); [Tsukahara, Iwamoto, et al. \(2014\)](#). While the empirical relation for laminar flow,

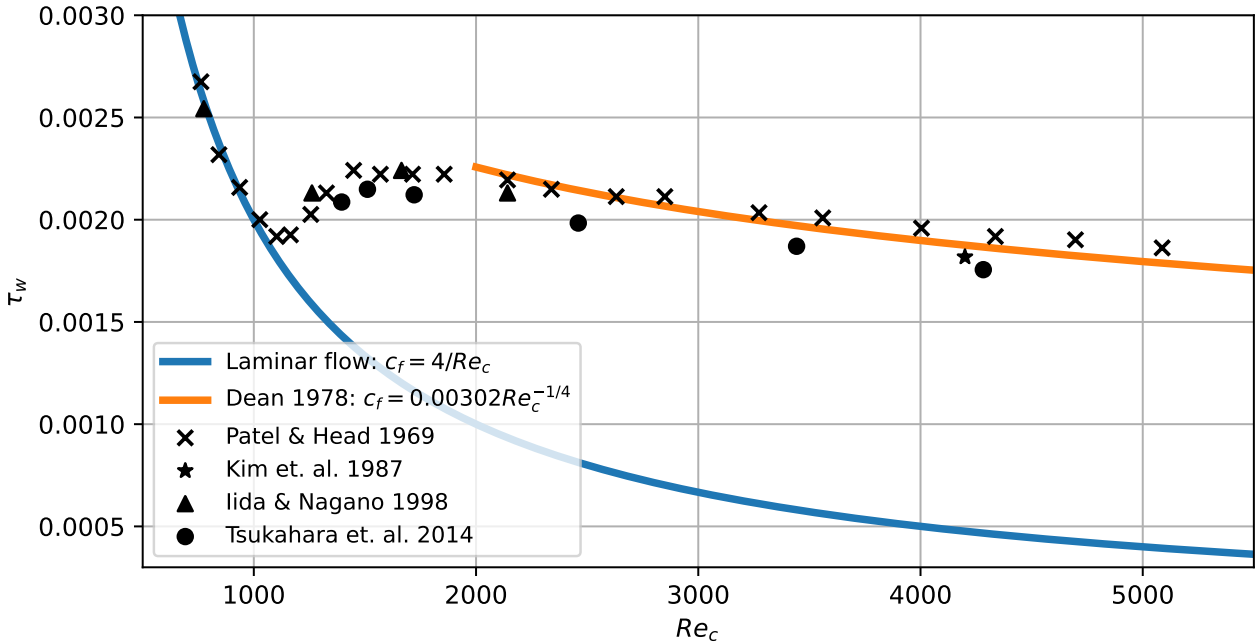


Figure 2.8: τ_w against Re_c using skin friction coefficients from [Dean \(1978\)](#) with $\rho = U_c = 1$. Experimental scatter points from ([Iida & Nagano, 1998](#); [J. Kim et al., 1987](#); [Patel & Head, 1969](#); [Tsukahara, Iwamoto, et al., 2014](#)).

$Re_c \lesssim 1000$ and turbulent flow $Re_c \gtrsim 2000$ appears reasonably robust, the wall shear stress in the transitional region is lacking therefore, the body forcing approach is not preferred.

Constant volumetric flux

An alternative approach is to enforce a constant volumetric flux, illustrated using the piston method in figure 2.7(b). We employ the efficient Green's function approach introduced by [Chu and Karniadakis \(1993\)](#), and outline its solution procedure. The volumetric flux is defined as,

$$Q(\mathbf{u}) = \frac{1}{A_s} \int_R \mathbf{u} \cdot d\mathbf{R}, \quad (2.71)$$

where $Q(\cdot)$ refer to the flow rate operator through the surface R with surface area of A_s . The idea is to append a correction velocity, \mathbf{u}_{corr} , to the velocity field at time step n , \mathbf{u}^n , such that the corrected solution, $\bar{\mathbf{u}}^n = \mathbf{u}^n + \mathbf{u}_{corr}$, has the desired volumetric flux $\bar{Q} = Q(\bar{\mathbf{u}}^n)$. While adding two solutions together is straightforward, the resultant velocity field may not directly satisfy the Navier-Stokes equations. Fortunately, we can leverage the velocity correction scheme which (in general) evaluates the nonlinear advection terms followed by a linear terms (pressure and dissipation). This process is summarised as,

$$\begin{cases} \frac{\partial \mathbf{u}}{\partial t} = \mathbf{N}(\mathbf{u}) \\ \mathbf{u}(\mathbf{x}, 0) = \mathbf{u}^n \end{cases} \xrightarrow{\hat{\mathbf{u}}(\mathbf{x}, \Delta t)} \begin{cases} \frac{\partial \mathbf{u}}{\partial t} = -\nabla p + \nu \mathbf{L}(\mathbf{u}) \\ \mathbf{u}(\mathbf{x}, 0) = \hat{\mathbf{u}}(\mathbf{x}, \Delta t), \end{cases} \quad (2.72)$$

where $\mathbf{u}(\mathbf{x}, 0) = \mathbf{u}^n$ and $\hat{\mathbf{u}}(\mathbf{x}, \Delta t)$ refer to the initial condition for the nonlinear advection terms, and the intermediate velocity, the initial condition for the linear terms, respectively. Since the second step correspond to solving the linear Stokes equation, any solution of the linear Stokes (such as \mathbf{u}_{corr}) added to the final solution will still satisfy the linear Stokes equations - a property of linear differential equations. We consider the linear Stokes equation governing the evolution of the correction velocity,

$$\frac{\partial \mathbf{u}_{corr}}{\partial t} = -\nabla p_{corr} + \nu \mathbf{L}(\mathbf{u}_{corr}) + \alpha^n \hat{\mathbf{e}}_x, \quad (2.73)$$

where α^n is the undetermined magnitude of body force at time step n in the streamwise direction, $\hat{\mathbf{e}}_x$, required to maintain the desired flow rate $\bar{Q} = Q(\mathbf{u}^n) + Q(\mathbf{u}_{corr})$. Since \mathbf{u}_{corr} is appended to \mathbf{u}^n , the initial condition for \mathbf{u}_{corr} must be $\mathbf{u}_{corr}(\mathbf{x}, 0) = 0$, so that \mathbf{u}^n remains compatible with the initial conditions in equation (2.72). Since α^n is undetermined, we normalise the equation with respect to α^n , yielding the linear Stokes equations with unit forcing,

$$\frac{\partial \mathbf{v}}{\partial t} = -\nabla \hat{p} + \nu \mathbf{L}(\mathbf{v}) + \hat{\mathbf{e}}_x, \quad \mathbf{v}(\mathbf{x}, 0) = \mathbf{0}, \quad (2.74)$$

where $\mathbf{v} = \mathbf{u}_{corr}/\alpha^n$ and $\hat{p} = p_{corr}/\alpha^n$. The corrected velocity field becomes

$$\bar{\mathbf{u}} = \mathbf{u} + \alpha^n \mathbf{v}^1, \quad (2.75)$$

where \mathbf{v}^1 is solution field obtained by solving equation (2.74) in the first time step. To match the target volumetric flux, \bar{Q} , we need to scale α^n such that,

$$\bar{Q} = Q(\bar{\mathbf{u}}^n) = Q(\mathbf{u}^n) + Q(\alpha^n \mathbf{v}^1). \quad (2.76)$$

which gives,

$$\alpha^n = \frac{\bar{Q} - Q(\mathbf{u}^n)}{Q(\mathbf{v}^1)}, \quad (2.77)$$

evaluated at every time step n . The Green's function approach is computationally efficient as we only need to compute \mathbf{v}^1 and $Q(\mathbf{v}^1)$ once during the first time step and reuse it for subsequent time steps. The process of adding the correction velocity at the end of velocity correction scheme can be summarised in the procedure as follows,

$$\mathbf{u}^n \xrightarrow{\mathbf{N}(\mathbf{u}^n)} \hat{\mathbf{u}} \xrightarrow{\nabla^2 p} \hat{\mathbf{u}} \xrightarrow{\mathbf{L}(\hat{\mathbf{u}})} \mathbf{u}^{n+1} \xrightarrow{\alpha^{n+1} \mathbf{v}^1} \bar{\mathbf{u}}^{n+1}.$$

2.5 Stability analysis of the Navier-Stokes equations

2.5.1 Algorithms for linear stability analysis

In this section, we present a general overview of the numerical procedure for linear stability analysis. Linear stability analysis examines the stability of a base flow by considering the evolution of infinitesimal perturbations. These perturbations in general, may either grow or decay exponentially, indicating

whether the base flow is linearly unstable or stable respectively. In §1.2, we introduced linear stability analysis in the context of wall-bounded shear flows leading to the Orr-Sommerfeld equations, where the base flows depend on a single inhomogeneous and two homogeneous directions, commonly referred to as local³ stability analysis. For example, the laminar Poiseuille flow, $U(y) = 1 - y^2$ and the laminar Couette flow $U(y) = y$, $y \in [-1, 1]$. For some flows such as boundary layers, wakes and jets, their base flows are not strictly parallel. By considering a weak dependence on the stream and spanwise directions, their stability are described by the parabolised stability equations (Herbert, 1997). When the base flow depends on two spatially inhomogeneous directions, $U(x, y)$, or three spatially inhomogeneous directions, $U(x, y, z)$, the analysis of such states are commonly referred to as biglobal or triglobal stability analysis, respectively (Theofilis, 2003). If the base flow is time-dependent, such as in the secondary instability of cylinder flows, we use Floquet stability analysis (Henderson & Barkley, 1996).

In this section, we consider a time-independent base flow and consider a generic decomposition of the velocity field in three spatial dimensions,

$$\mathbf{u}(\mathbf{x}, t) = \mathbf{U}(\mathbf{x}) + \mathbf{u}'(\mathbf{x}, t), \quad (2.78)$$

where $\mathbf{U}(\mathbf{x})$, $\mathbf{u}'(\mathbf{x}, t)$ refers to the base flow and perturbations. Substituting this into the Navier-Stokes equations and linearising,

$$\frac{\partial \mathbf{u}'}{\partial t} = -(\mathbf{U} \cdot \nabla) \mathbf{u}' - (\mathbf{u}' \cdot \nabla) \mathbf{U} - \nabla p' + \frac{1}{Re} \nabla^2 \mathbf{u}', \quad (2.79a)$$

$$\nabla \cdot \mathbf{u}' = 0. \quad (2.79b)$$

This can be rewritten as,

$$\frac{\partial}{\partial t} \mathbf{q}' = \mathcal{L} \mathbf{q}', \quad \mathcal{L} = \begin{bmatrix} -(\mathbf{U} \cdot \nabla) - (\nabla \mathbf{U}) + \frac{1}{Re} \nabla^2 & -\nabla \\ \nabla \cdot & 0 \end{bmatrix}, \quad (2.80)$$

where \mathcal{L} refer to the linearised operator and, $\mathbf{q}' = (\mathbf{u}', p')^T$. Assuming an initial perturbation, $\mathbf{q}'(\mathbf{x}, t=0) = \mathbf{q}_0$, its evolution to time T is given by,

$$\mathbf{q}(\mathbf{x}', T) = \mathcal{A}(T, Re) \mathbf{q}_0, \quad \text{where } \mathcal{A}(T, Re) = \exp(\mathcal{L}T). \quad (2.81)$$

We assume that the perturbations can be represented as a normal mode,

$$\mathbf{q}'(\mathbf{x}, t) = \tilde{\mathbf{q}}(\mathbf{x}) \exp(\lambda t) + \text{c.c} \quad (2.82)$$

where $\lambda_j, \tilde{\mathbf{q}}_j(\mathbf{x})$ refer to the j^{th} eigenvalue and eigenmode, and c.c refers to the complex conjugate.

³Referring to being spatially local in the context of ‘real’ flows which are typically inhomogeneous in all directions

Substituting the normal mode into equation (2.81), we obtain an eigenvalue problem,

$$\mathcal{A}(T, Re)\tilde{\mathbf{q}}_j = \mu_j \tilde{\mathbf{q}}_j, \quad \mu_j = \exp(\lambda_j T). \quad (2.83)$$

where μ_j refers to the eigenvalue of $\mathcal{A} = \exp(\mathcal{L}T)$, and we typically set $T = 1$ (Barkley, Blackburn, & Sherwin, 2008). The real component of the eigenvalues determine the stability of the base flow, which can be either,

1. Unstable: $\Re(\lambda) > 0$,
2. Stable: $\Re(\lambda) < 0$,
3. Neutral: $\Re(\lambda) = 0$.

This concludes the mathematical overview of linear stability analysis, and the challenge lies in the computing the eigenpairs of \mathcal{A} efficiently. For large matrices, $\mathcal{A} \in \mathbb{R}^{M \times M}$ (assuming it is real here for simplicity), direct eigenvalue solvers such as the QR algorithm costing $O(M^3)$ might be computationally infeasible. Another concern is that we are typically only interested in the most dangerous (leading) eigenvalues of largest real parts, and not the full spectrum. Lastly, we do not have access to \mathcal{A} in a time stepping based code.

Power Iteration Method

A simple method in computing the dominant eigenpair is the power iteration method,

Definition 2.5.1 (Power iteration). Given a diagonalisable matrix $\mathbf{A} \in \mathbb{R}^{n \times n}$ and a non-zero vector \mathbf{x}_0 , the sequence of matrix vector products between them (we neglect normalisation here),

$$\mathbf{A}\mathbf{x}_0, \mathbf{A}^2\mathbf{x}_0, \mathbf{A}^3\mathbf{x}_0, \dots, \mathbf{A}^k\mathbf{x}_0. \quad (2.84)$$

approaches the eigenvector of \mathbf{A} with the largest magnitude. i.e. $\tilde{\mathbf{x}}_1 = \lim_{k \rightarrow \infty} \mathbf{A}^k \mathbf{x}_0$. The dominant eigenvalue, λ_1 , can be computed using the Rayleigh quotient, $\lambda_1 = \frac{\tilde{\mathbf{x}}_1^T \mathbf{A} \tilde{\mathbf{x}}_1}{\tilde{\mathbf{x}}_1^T \tilde{\mathbf{x}}_1}$.

Arnoldi Method

A generalisation of the power method is the Arnoldi method (Arnoldi, 1951), belonging to a class of Krylov subspace iterative methods, for performing a Hessenberg reduction.

Definition 2.5.2 (Krylov Subspaces). Given a matrix $\mathbf{A} \in \mathbb{R}^{n \times n}$ and a non-zero vector $\mathbf{x}_0 \in \mathbb{R}^n$, the k^{th} -Krylov subspace, $\mathcal{K}_n(\mathbf{A}, \mathbf{x}_0, k)$ is defined by,

$$\mathcal{K}_n(\mathbf{A}, \mathbf{x}_0, k) = \text{span}\{\mathbf{x}_0, \mathbf{A}\mathbf{x}_0, \mathbf{A}^2\mathbf{x}_0, \mathbf{A}^3\mathbf{x}_0, \dots, \mathbf{A}^{k-1}\mathbf{x}_0\}. \quad (2.85)$$

Definition 2.5.3 (Hessenberg reduction). The Hessenberg reduction is a matrix decomposition technique commonly used for the computing eigenpairs of matrices. Given a unsymmetric matrix

$A \in \mathbb{R}^{N \times N}$ (we assume that A is real for simplicity), we seek a decomposition of the form,

$$A = QHQ^T, \quad (2.86)$$

where,

- $H \in \mathbb{R}^{N \times N}$ is an upper Hessenberg matrix (i.e. $a_{i,j} = 0$ for $i > j + 1$)
- $Q \in \mathbb{R}^{N \times N}$ is an orthonormal matrix (i.e. $Q^{-1} = Q^T$), whose columns q_1, \dots, q_N , form an orthonormal basis.

The Hessenberg reduction shows that A and H are similar matrices, which have the same eigenvalues. If $Ax = \lambda x$, using $Q^T = Q^{-1}$ and multiplying (2.86) by x ,

$$Ax = QHQ^{-1}x \Rightarrow \lambda x = QHQ^{-1}x \Rightarrow \lambda Q^{-1}x = HQ^{-1}x \Rightarrow \lambda y = Hy. \quad (2.87)$$

Hence, $\lambda(A) = \lambda(H)$, and their eigenvectors are related by $x = Qy$.

The Arnoldi method generates a sequences of vectors $[u_0, \mathcal{A}u_0, \dots, \mathcal{A}^{k-1}u_0]$ that spans the k -dimensional Krylov subspace. These vectors, are known as Arnoldi vectors (Golub & Van Loan, 2013), are used to construct an orthogonal matrix via the Gram-Schmidt process, $Q = [q_1, q_2, \dots, q_k] \in \mathbb{R}^{M \times K}$. This is equivalent to performing a partial Hessenberg reduction of $\mathcal{A} = QHQ^T$, where the eigenvalues of $\mathcal{A} \in \mathbb{R}^{N \times N}$ can be approximated by a smaller Hessenberg matrix $H \in \mathbb{R}^{k \times k}$, suitable for a direct eigenvalue computation using the QR algorithm, The k -step Arnoldi factorisation of \mathcal{A} gives,

$$\mathcal{A}Q_k = Q_k H_k + r_k e_k^T, \quad (2.88)$$

where $H \in \mathbb{R}^{k \times k}$ refers to the upper Hessenberg matrix, $e_k = [0, \dots, 0, 1] \in \mathbb{R}^k$, and $r_k \in \mathbb{R}^N$ is a residual vector. If $x = Q_k y$, and $Hy = \lambda y$ then,

$$(\mathcal{A} - I\lambda)x = (e_k^T y)r_k. \quad (2.89)$$

In other words, the residual vector difference between the approximation of $\lambda(\mathcal{A})$, using $\lambda(H)$. If $\|r_k\| = 0$, then $\lambda(H) \subseteq \lambda(\mathcal{A})$.

We now present the Arnoldi method by generating k Arnoldi vectors,

$$T_k = [u_0, u_1, \dots, u_{k-1}] = \left[u_0, \frac{\mathcal{A}(T, Re)u_0}{\alpha_1}, \frac{\mathcal{A}(T, Re)u_1}{\alpha_2}, \dots, \frac{\mathcal{A}(T, Re)u_{k-1}}{\alpha_k} \right], \quad (2.90)$$

where α_j is scaled such that $\|u_j\| = 1$. Following (Barkley et al., 2008), the projection of \mathcal{A} onto the Krylov subspace is given as,

$$\mathcal{A}T_k = T_{k+1}D_k^{(k+1)}, \quad (2.91)$$

where $D_k^{(k+1)} \in \mathbb{R}^{(k+1) \times k}$ is a shifted diagonal matrix with entries $D_{ij} = \alpha_i \delta_{i,j+1}$. We assume that T_k and T_{k+1} admit QR decompositions,

$$\mathcal{A}Q_k R_k = Q_{k+1} R_{k+1} D_k^{(k+1)}, \quad (2.92)$$

where $\mathbf{Q}_k \in \mathbb{R}^{N \times k}$, $\mathbf{R}_k \in \mathbb{R}^{k \times k}$ and $\mathbf{Q}_{k+1}, \mathbf{R}_{k+1}$ are similarly defined. The upper Hessenberg matrix $\mathbf{H}_k^{(k+1)} \in \mathbb{R}^{(k+1) \times k}$ is defined as,

$$\mathbf{H}_k^{(k+1)} = \mathbf{R}_{k+1} \mathbf{D}_k^{(k+1)} \mathbf{R}_k^{-1}, \quad (2.93)$$

in which the last row of $\mathbf{H}_k^{(k+1)}$ only contains a single non-zero entry, $h^* = h_{k,k-1}$. By substituting the definition of the upper Hessenberg matrix and separating the last row of $\mathbf{H}_k^{(k+1)}$ we obtain,

$$\mathcal{A}\mathbf{Q}_k = \mathbf{Q}_k \mathbf{H}_k + h^* \mathbf{q}_k \mathbf{e}_k^T. \quad (2.94)$$

Equation (2.94) describes the projection of \mathcal{A} onto the Krylov subspace spanned by orthonormal bases \mathbf{Q}_k , yielding a smaller \mathbf{H}_k matrix. The accuracy of this approximation is dictated by the magnitude of the residual term, $h^* \mathbf{q}_k \mathbf{e}_k^T$. Assuming that \mathbf{H}_k is diagonalisable as $\mathbf{H}_k = \Psi_k \Lambda_k \Psi_k^{-1}$, we multiply equation (2.94) by Ψ_k ,

$$\mathcal{A}\mathbf{Q}_k \Psi_k = \mathbf{Q}_k \Psi_k \Psi_k^{-1} \mathbf{H}_k \Psi_k + h^* \mathbf{q}_k \mathbf{e}_k^T \Psi_k. \quad (2.95)$$

Simplifying the expression above we get,

$$\mathcal{A}\mathbf{V}_k = \mathbf{V}_k \Lambda_k + h^* \mathbf{q}_k \mathbf{e}_k^T \Psi_k, \quad (2.96)$$

where Λ_k contains the k eigenvalues and $\mathbf{V}_k = \mathbf{Q}_k \Psi_k$ the eigenvectors of \mathcal{A} . The error in approximating the j^{th} eigenpair is given by,

$$\varepsilon_j = \|\mathcal{A}\mathbf{v}_j - \lambda_j \mathbf{v}_j\| = \|h^* \mathbf{q}_k \mathbf{e}_k^T \psi_j\| = |h^*| |\mathbf{v}_j[k-1]|, \quad (2.97)$$

where $\mathbf{v}_j[k-1]$ is the last component of the eigenvector \mathbf{v}_j .

Lastly, we are generally interested in obtaining the eigenpairs with the largest real part. We introduce exponential power method ([Tuckerman & Barkley, 2000](#)), which is naturally considered by time stepping an initial perturbation \mathbf{q}'_0 from $t = 0$ to T ,

$$\mathbf{q}'(T) = \exp(\mathcal{L}T) \mathbf{q}'_0 = \mathcal{A}(T) \mathbf{q}'_0. \quad (2.98)$$

The dominant eigenvalues, μ , of \mathcal{A} obtained from the Arnoldi method described above, which correspond to the eigenvalue of the largest real part λ , of \mathcal{L} by $\mu = \exp(\lambda T)$, where T is typically set to 1. For further details on this algorithm, the reader is referred to [Tuckerman and Barkley \(2000\)](#) and [Barkley et al. \(2008\)](#) for more details.

In summary, the algorithm described above have been implemented in Nektar++, referred to as the ‘modified’ Arnoldi algorithm, which modifies the existing time-stepper code with a wrapper function that generates Arnoldi vectors and solves the Hessenberg matrix using the subroutine dgeev from LAPACK (Linear Algebra PACKage, [Anderson et al., 1999](#)). The modified Arnoldi algorithm has been verified against using a separate implementation based on the third-party package ARPACK (ARnoldi PACKage ([Lehoucq, Sorensen, & Yang, 1998](#))) ([Rocco, 2014](#)).

2.5.2 Edge tracking

In this section, we consider the dynamical system perspective on the subcritical transitional shear flows where the linearly stable laminar co-exist with the chaotic attractor of the turbulent dynamics. The edge is defined as the region that separates the basin of attraction between the laminar and turbulent state. Along this edge, sit local attractors, referred to as edge states which could manifest as travelling-waves, tori, and high-order invariant sets. A common technique employed for edge tracking is often based on the bisection method ([Khapko et al., 2016](#); [Schneider et al., 2007](#); [Skufca, Yorke, & Eckhardt, 2006](#)), which is performed by repeatedly bisecting the initial conditions given as,

$$\mathbf{q}_0(\mathbf{x}, 0; \chi) = \chi \mathbf{q}_L(\mathbf{x}) + (1 - \chi) \mathbf{q}_T(\mathbf{x}) \quad (2.99)$$

where \mathbf{q}_0 refers to an initial condition consisting of a weighted sum of the bisection parameter, $\chi \in [0, 1]$, between a laminar state, \mathbf{q}_L , and a turbulent state, \mathbf{q}_T . For an initial condition given by $\mathbf{q}_0(\mathbf{x}, 0; \chi = 0) = \mathbf{q}_T$, or $\mathbf{q}_0(\mathbf{x}, 0; \chi = 1) = \mathbf{q}_L$ the solution trajectory will continue along the turbulent attractor or relaminarise respectively. Hence, there could be (at least) one intermediate value of the bisection parameter, $\chi^* \in [0, 1]$, where the solution trajectory evolves along the edge, neither falling towards the turbulent nor laminar attractor. The method of finding χ^* is based on the bisection, where we perform n successive bisections between χ_L^n, χ_T^n , where χ_L^n and χ_T^n leads to relaminarisation and turbulence respectively. This necessitates n direct numerical simulations using initial conditions updated by $\mathbf{q}_0(\mathbf{x}, 0; \chi^n = \frac{1}{2}(\chi_L^n + \chi_T^n))$ and having a stopping criteria to determine if the solution is about to relaminarise or become turbulent. A stopping criteria based on turbulent kinetic energy and wall shear stress is often used. This edge is often unstable and we often require χ^* to be considerably accurate to remain such that the initial condition could evolve along the edge for sufficient time, T . After we have determined χ^* and T , the bisection method can be restarted between by replacing the $\mathbf{q}_L(\mathbf{x}) = \mathbf{q}_0(\mathbf{x}, T, \chi_L)$ and $\mathbf{q}_T(\mathbf{x}) = \mathbf{q}_0(\mathbf{x}, T; \chi_T)$, which are close to each other in state space but diverge to the laminar and turbulent states after a long time $t > T$. After a certain number of r restarted bisections, the solution trajectory may converge towards an attractor along the edge - an edge state, acting as a separatrix between the turbulent and laminar attractor. We describe the algorithm of edge tracking in [algorithm 2.5.2](#). To disambiguate between the iterative processes, we perform r number of restarted bisections in an ‘outer-loop’ which contains n number of bisections within an ‘inner-loop’.

Algorithm 1 Algorithm for edge tracking between a turbulent and laminar state

```

1: Initialise maxBisects, maxRepeat           ▷ Maximum n and repeated bisections
2: Initialise stopCriteria                   ▷ Tolerance for stopping criteria (e.g., wall-shear stress)
3: r ← 0                                     ▷ Iterating over r repeated bisections
4: while r < maxRepeat do
5:   if r == 0 then
6:     qL, qT ← input()                  ▷ Initial laminar and turbulent states
7:   end if
8:   χL ← 0, χT ← 1, χ ←  $\frac{1}{2}(\chi_L + \chi_T)$  ▷ Initialise bisection coefficients
9:   q0 ← χqT + (1 - χ)qL            ▷ Initialise initial condition
10:  n ← 0                                    ▷ Iterating over n bisections
11:  while n < maxBisects do
12:    t ← 0, Δ ← 106
13:    while Δ > stopCriteria do          ▷ Assuming that the edge is unstable
14:      qt+1 ← TimeIntegrate(qt, Δt)  ▷ Perform DNS for a single time-step
15:      Δ ← |qt+1 - q0|              ▷ Measuring the deviation from initial condition
16:      t++
17:    end while
18:    if isTurbulent(qt) then        ▷ Check if terminal state is turbulent
19:      χL ← χ                         ▷ qL gets a larger weight
20:      if n == maxBisects - 1 then
21:        qT ← qt                  ▷ Save turbulent-leaning initial condition
22:        break
23:      end if
24:    else
25:      χT ← χ
26:      if n == maxBisects - 1 then    ▷ Save laminar-leaning initial condition
27:        qL ← qt                  ▷ Save laminar-leaning initial condition
28:        break
29:      end if
30:    end if
31:    χ ←  $\frac{1}{2}(\chi_L + \chi_T)$        ▷ Update initial conditions
32:    q0 ← χqL + (1 - χ)qT
33:    n++
34:  end while
35:  r++
```

Chapter 3

Transitional Rayleigh-Bénard Poiseuille flows

In this chapter, we will investigate the transitional flow regimes arising from the interaction between buoyancy and shear in Rayleigh-Bénard Poiseuille (RBP) flows within large and small domains. In particular, the transition boundaries between the bistable system consisting of spiral defect chaos (SDC) and ideal straight rolls (ISRs) in Rayleigh-Bénard convection (see §1.3), and subcritical turbulence in plane Poiseuille flows (see §1.2) under the influence of Re and Ra are not known.

Using Nektar++, a spectral/ hp element package, we conduct direct numerical simulations over a range of Rayleigh numbers, $Ra \in [0, 10000]$, Reynolds numbers, $Re \in [0, 2000]$ and unit Prandtl number, we identify five distinct regimes: (1) bistable SDC & ISRs, (2) ISRs, (3) wavy rolls, (4) intermittent rolls, and (5) shear-driven turbulence. The newly identified intermittent rolls state, features longitudinal rolls that spontaneously decay towards the laminar state. In the transitional shear-driven turbulent regime, longitudinal rolls may coexist with turbulent-laminar bands. The role of longitudinal rolls in transitional RBP flows is apparent, and we examine the unstable manifold of longitudinal rolls in a confined domain, integrating along which led to transient turbulence, decaying towards the laminar state before regenerating into longitudinal rolls again, forming a quasi-cyclic process introduced as the *thermally-assisted sustaining process (TASP)*. Near the intermittent roll regime, a periodic orbit emerges between the longitudinal rolls and the laminar state within a confined domain. Above a certain Re threshold, the unstable longitudinal rolls provide an intermediate pathway for the transition from the laminar state to turbulence. Finally, we provide a state space sketch of the dynamical processes, emphasising the role of longitudinal rolls in transitional RBP in confined domains, and discuss connections to the large domains.

3.1 Objectives

While the linear stability characteristics of laminar RBP flows have been well studied (see §1.4), the transition to shear-driven turbulence remains and the related nonlinear dynamics remain largely unexplored.

As the first step towards understanding the transition in RBP flows, the main objective of this chapter is to perform exploratory direct numerical simulations (DNS) of transitional RBP flows while investigating the impact of Re on the bistability between SDC and ISRs in RBC as well as the influence

of Ra on turbulent-laminar bands in PPF. For this purpose, we consider a relatively wide range of parameter space given by $Ra \in [0, 10000]$ and $Re \in [0, 2000]$ at $Pr = 1$ in both large and confined domains ($\Gamma = 4\pi, \pi/2$, in particular). Given that this study is largely exploratory, we will focus on identifying different flow regimes and providing key insights into their dynamical processes. Due to the large parameter space, we do not intend to perform an extensive bifurcation analysis that involves the computation and analysis of the invariant solutions, which could be computationally very costly, especially in a large domains.

The chapter is organised as follows: in §3.2, we describe the problem formulation, governing equations, the numerical methods and setup. In §3.3, we present the Ra - Re phase space, identifying five distinct regimes and their coarse-grained transition boundaries. We also show a new ‘intermittent roll’ regime and discuss the coexistence of longitudinal rolls with turbulent-laminar bands, highlighting the role of longitudinal rolls in transitional RBP flows. In §3.4, we perform a numerical experiment, in which simulations are performed along the unstable manifolds of longitudinal rolls in a confined domain, $\Gamma = \pi/2$. We will see that this reveals a quasi-cyclic process between shear-driven turbulence, longitudinal rolls, and the laminar state referred as the *thermally-assisted sustaining process (TASP)* in §3.4.1, and subsequently discuss the relevance of the *TASP* to larger domains in §3.4.2. Finally, we provide a summary in §3.5 containing some perspectives for future work.

3.2 Problem formulation

3.2.1 Governing equations

The motion of fluid flow in an RBP system (see §1.1), is governed by the non-dimensionalised Navier-Stokes equations with Boussinesq approximation,

$$\frac{\partial \mathbf{u}}{\partial t} + (\mathbf{u} \cdot \nabla) \mathbf{u} = -\nabla p + \frac{1}{Re} \nabla^2 \mathbf{u} + \frac{Ra}{8PrRe^2} \theta \mathbf{j}, \quad (3.1a)$$

$$\frac{\partial \theta}{\partial t} + (\mathbf{u} \cdot \nabla) \theta = \frac{1}{RePr} \nabla^2 \theta, \quad (3.1b)$$

$$\nabla \cdot \mathbf{u} = 0, \quad (3.1c)$$

with the following boundary conditions at the wall,

$$\mathbf{u}|_{y=\pm h} = 0, \quad \theta|_{y=-h} = 1, \quad \theta|_{y=h} = 0, \quad (3.2)$$

and periodic boundary conditions in the planar x and z directions. $\mathbf{u}(\mathbf{x}, t)$ denotes the non-dimensionalised velocity scaled by the laminar centreline velocity, W_c , i.e. $W_{lam}(y) = W_c(1 - y^2)$. $\mathbf{x} = (x, y, z)$ and t denote the non-dimensionalised spatial and temporal coordinates scaled by the half-height, h and the advective time scale, W_c/h , where x, y, z refers to the spanwise, wall-normal and streamwise directions, respectively. p refers to the non-dimensionalised pressure scaled by ρW_c^2 ,

and $\theta (\equiv (T - T_U)/\Delta T)$ refers to the non-dimensionalised temperature with T being the absolute temperature. \mathbf{j} denotes the unit vector in the y -direction.

We note that the rescaled $Ra/8$ term in the momentum forcing terms is equivalent to the Rayleigh number scaled based on the half-depth, h , since Ra is scaled based on depth, d , in classical RBC. The Rayleigh number, Ra , Reynolds number Re and Prandtl number, Pr are defined in §1.1. We set $Pr = 1$ in this study. For the Rayleigh-Bénard convection problem, we note that the equation (3.1) becomes singular at $Re = 0$. In such cases, we solve the non-dimensionalised incompressible Navier-Stokes equations based on thermal length, velocity and temporal scales given in §4.2.

3.2.2 Numerical Methods

The governing equations are solved numerically using Nektar++, an open-source spectral/ hp -element package (Cantwell et al., 2015; Moxey et al., 2020). The computational mesh consists of 2D quadrilateral elements in the $x - y$ plane generated using Gmsh (Geuzaine & Remacle, 2009) and then imported into Nektar++ using Nekmesh (Green et al., 2024). We discretise the spatial domain based on the quasi-3D approach, employing spectral/ hp elements in the $x - y$ plane and Fourier expansions in the z (see §2.4.2). We emphasise that the streamwise direction is in z . The discretised equations are solved using a velocity correction scheme, based on a second-order stiffly splitting scheme, where the nonlinear advection and forcing terms are treated explicitly, while the pressure and diffusion terms are treated implicitly (see §2.4.1). The 3/2 and polynomial dealiasing rule for the Fourier expansions and spectral/ hp elements are applied during the evaluation of the nonlinear advection terms. To sustain the flow for $Re > 0$, we use a Green's function approach to impose a constant volumetric flux (see §2.4.3).

3.2.3 Parametric sweep of Ra - Re space

We consider fifty-two numerical simulations at $Re = 0, 0.1, 1, 10, 100, 500, 750, 1000, 1050, 2000$, and $Ra = 0, 2000, 3000, 5000, 8000, 10000$ at $Pr = 1$ with a large aspect ratio of $\Gamma = 4\pi$. Their spatial and temporal numerical resolutions and time-integration horizon, T , are described in the Appendix A.1. The initial conditions of all cases are sampled from a statistically stationary solution. Laminar solutions are obtained for $Ra = 0$, $Re \leq 1000$, with the given set of parameters and are omitted from the analysis. For all the cases considered here, we maintain the same spatial resolution except $Re = 2000$, where the number of Fourier expansions was doubled. The temporal resolution between the numerical simulations differs due to time scales arising from the different flow physics, as we shall see later. We have also considered a mesh independence study for the end case of $Ra = 10000$, $Re = 2000$, where doubling the number of Fourier modes or increasing the polynomial order by 1 led to a $< 1\%$ change in near-wall transport properties defined by the Nusselt number, $Nu = -\langle d\theta/dy_{y=-1} \rangle_{x,z} d/\Delta T$, and shear, $\langle dw/dy|_{y=-1} \rangle_{x,z}$, on the lower wall, where $\langle \cdot \rangle_{x,z} = 1/(L_x L_z) \int_{z,x} \cdot dx dz$ refer to the plane-averaged operator.

3.2.4 Linear Stability Analysis

In §3.4, we will perform numerical experiments where small disturbances are added along the unstable manifolds of longitudinal rolls. This is rooted in linear stability methods discussed earlier in §1.2, and its numerical technique is presented in §2.5.1. To determine the unstable manifolds, we consider a small disturbance about the longitudinal roll state,

$$\mathbf{u}(\mathbf{x}, t) = \mathbf{u}_{LR}(\mathbf{x}) + \hat{\mathbf{u}}(\mathbf{x}, t), \quad (3.3a)$$

$$\theta(\mathbf{x}, t) = \theta_{LR}(\mathbf{x}) + \hat{\theta}(\mathbf{x}, t), \quad (3.3b)$$

$$p(\mathbf{x}, t) = p_{LR}(\mathbf{x}) + \hat{p}(\mathbf{x}, t), \quad (3.3c)$$

where $\mathbf{q} = [\mathbf{u}, \theta, p]^T$, $\mathbf{q}_{LR} = [\mathbf{u}_{LR}, \theta_{LR}, p_{LR}]^T$ and $\hat{\mathbf{q}} = [\hat{\mathbf{u}}, \hat{\theta}, \hat{p}]^T$ refers to the solution vector, the longitudinal state and the disturbances respectively. We substitute equation (3.3) into (3.1) and neglect the nonlinear terms, leading to the linearised equations,

$$\frac{\partial \hat{\mathbf{q}}}{\partial t} = \mathcal{A}(\mathbf{q}_{LR}; Re, Ra, Pr)\hat{\mathbf{q}}, \quad (3.4a)$$

where

$$\mathcal{A}(\mathbf{q}_{LR}; Re, Ra, Pr) = \begin{pmatrix} -(\mathbf{u}_{LR} \cdot \nabla) - (\nabla \mathbf{u}_{LR} \cdot) + 1/Re \nabla^2 & \frac{Ra}{8Re^2Pr} \hat{\mathbf{j}} & -\nabla \\ -(\nabla \theta_{LR} \cdot) & -(\mathbf{u}_{LR} \cdot \nabla) + \nabla^2 & 0 \\ \nabla \cdot & 0 & 0 \end{pmatrix}. \quad (3.4b)$$

Consider that the longitudinal rolls are invariant along the z -direction, which are also assumed to be periodic in x -direction, and the following form of normal-mode solution can be considered,

$$\hat{\mathbf{q}}(\mathbf{x}, t) = \check{\mathbf{q}}(x, y)e^{i(\alpha x + \beta z) + \lambda t} + \text{c.c}, \quad (3.5)$$

where λ , α and β are the complex frequency, the spanwise wavenumber (or the Floquet exponent), and the stream wavenumber, respectively. Using the periodic nature of $\check{\mathbf{q}}(x, y)$ in the x -direction, (3.5) can also be written as

$$\hat{\mathbf{q}}(\mathbf{x}, t) = \left[\sum_{n=-\infty}^{\infty} \check{\mathbf{q}}_n(y) e^{i \frac{2\pi}{L_x} (n+\sigma)x} \right] e^{i\beta z + \lambda t} + \text{c.c}, \quad (3.6)$$

where $\sigma (= \alpha L_x / (2\pi))$ is the Floquet detuning parameter with $0 \leq \sigma \leq 1/2$. In this study, we will only consider the identification of the unstable manifolds of longitudinal rolls in a fixed computational domain; therefore, the fundamental mode, $\sigma = 0$, is of sole interest. Substituting equation (3.6) into (3.4) result to a discretised eigenvalue problem with the eigenvalue λ . The wavenumber β , is restricted to discrete values of $\beta = 2\pi m / L_z$, and m is a positive integer for the given computational

domain. The resulting eigenvalue problems are solved using an iterative Arnoldi algorithm based on time-stepping schemes implemented in Nektar++ (see §2.5.1).

3.3 *Ra-Re* phase space

3.3.1 Classification

We present the results obtained from the DNS of transitional RBP flows, focusing on the parameter space defined by Rayleigh numbers in the range $Ra \in [0, 10000]$, and Reynolds numbers in the range of $Re \in [0, 2000]$ (see Appendix A.1 for the full details).

For all numerical simulations, an initial condition, consists of a Gaussian white noise with zero mean and unit variance, superimposed onto the laminar base state (i.e. conduction state at $Re = 0$). The RBP system is then time-integrated until a statistically stationary state is reached, which typically requires a time of $t = O(10)$ to $O(10^2)$. At the two end points of the Re -spectrum considered (i.e. $Re = 0, 2000$), SDC and subcritical shear-driven turbulence appear. Figure 3.1 shows the snapshots of the midplane temperature, $\theta(x, z)|_{y=0}$, of different flow regimes on the Ra - Re phase space. The solid blue curves represent the neutral stability boundaries for the longitudinal and transverse rolls as $Ra_{\parallel} = 1708$ and $Ra_{\perp} = f(Re)$, respectively (Gage & Reid, 1968). In the absence of shear at $Re = 0$, these curves merge into the classical critical RBC instability at $Ra_c = 1708$, as ISRs become rotationally invariant about the wall-normal axis. ISRs may undergo secondary instability for $Ra > Ra_{\parallel}$, and an approximate boundary of this is indicated by a red arrow roughly indicates the secondary neutral stability boundary, marking the onset of oscillatory instabilities of ISRs within $Ra \gtrsim 5000$ (Clever & Busse, 1974). We note that the phase diagram in figure 3.1 is not-to-scale plotted serving as a conceptual reference to distinguish between different flow states and their coarse-grained transition boundaries.

In this Ra - Re phase space, we categorise the flow behaviour into five distinct regimes: (1) bistability between SDC and ISRs (SDC & ISRs), (2) ideal straight rolls (ISRs), (3) wavy rolls, (4) intermittent rolls, and (5) shear-driven turbulence. The categories are defined based on common flow structures (patterns), and/or dynamical characteristics, ranging from equilibrium solutions to intermittent and chaotic dynamics. Furthermore, we sort out these states based on their first and second-order statistical properties, where they appear independent of Re in the buoyancy-dominated regime (shaded in red), and Ra in the shear-dominated regime (shaded in blue), discussed in detail in Appendix A.2. In the mixed regime shaded in green, both Ra and Re are important.

Given that the buoyancy-dominated regime is relatively well studied (RBC flow, in particular), here we only provide a brief description of the simulation results in this regime, with further magnified flow fields shown in figure 3.2. In the buoyancy-dominated regime, the flow structures are predominantly organised with convection rolls, such as SDC, transverse, oblique, longitudinal rolls (and ISRs with no mean flow), or oscillatory rolls. The bistability between SDC and ISRs is preserved for $Ra \geq 3000$ at $Re = 0.1$ (refer to figure 3.2(a)) and $Re = 1$ for $Ra \geq 5000$ (see also figure 3.3(a,d,g)). There exists a maximum Re , beyond which SDC disappears, we denote this as Re_s , and its dependence on Ra is demarcated by the black dashed lines on the left side of figure 3.1. Notably, an oblique roll

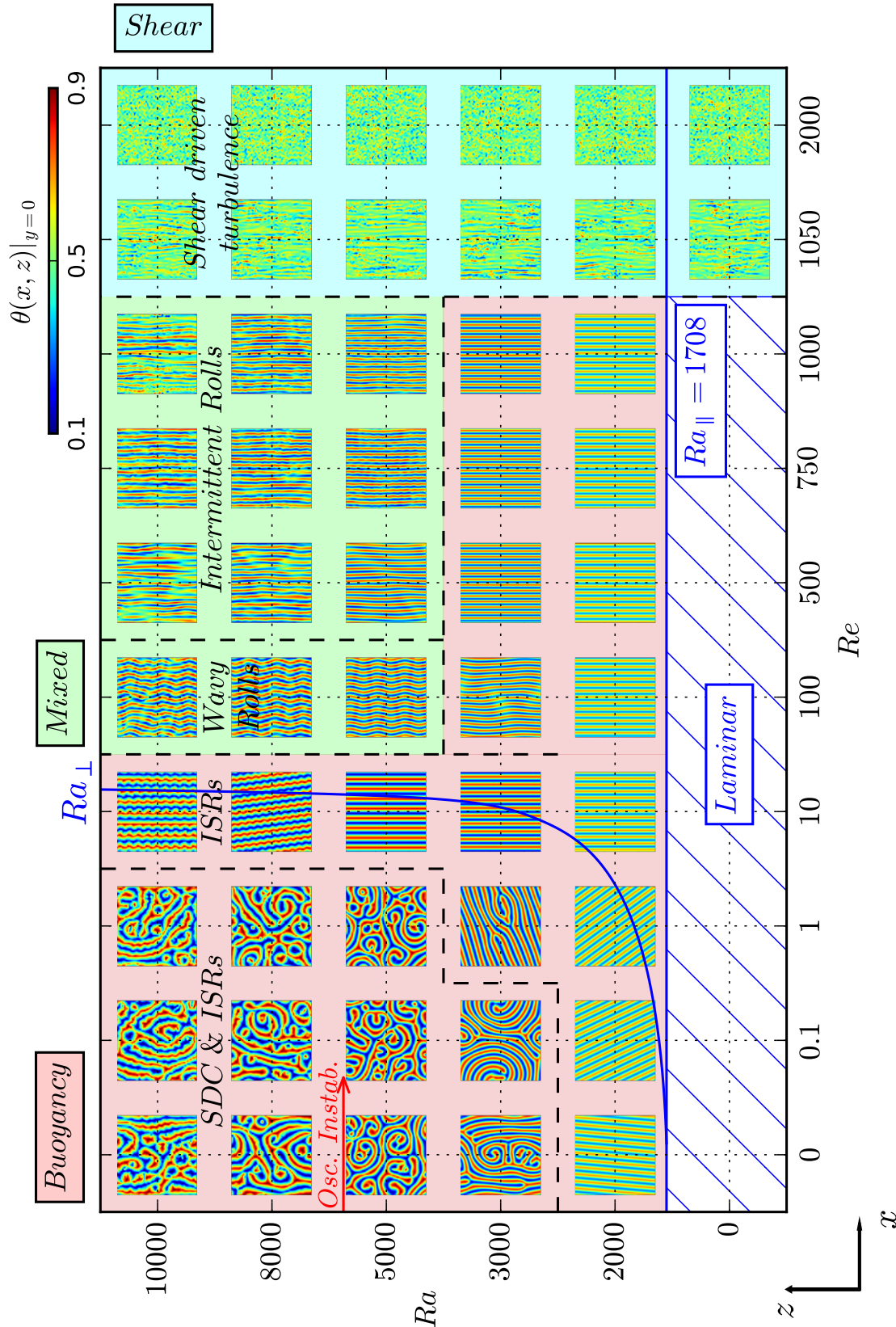


Figure 3.1: A conceptual diagram of the Ra - Re phase space illustrates the midplane temperature snapshots, $\theta(x, z)|_{y=0}$ for $Re \in [0, 2000]$ and $Ra \in [0, 10000]$, classified into five distinct regimes: (1) SDC & ISRs, (2) ISRs, (3) wavy rolls, (4) intermittent rolls and (5) shear-driven turbulence. The blue solid curves refer to primary neutral curves of the longitudinal and transverse rolls $Ra_{||}$, Ra_{\perp} . The red curve indicates the secondary oscillatory instability of ISRs at $Re = 0$ (Bodenschatz et al., 2000). Shadings of red, green and blue indicate their dominant mechanism, whether driven by buoyancy or shear (or mixed). For $Re > 0$, the mean flow is along the z direction.

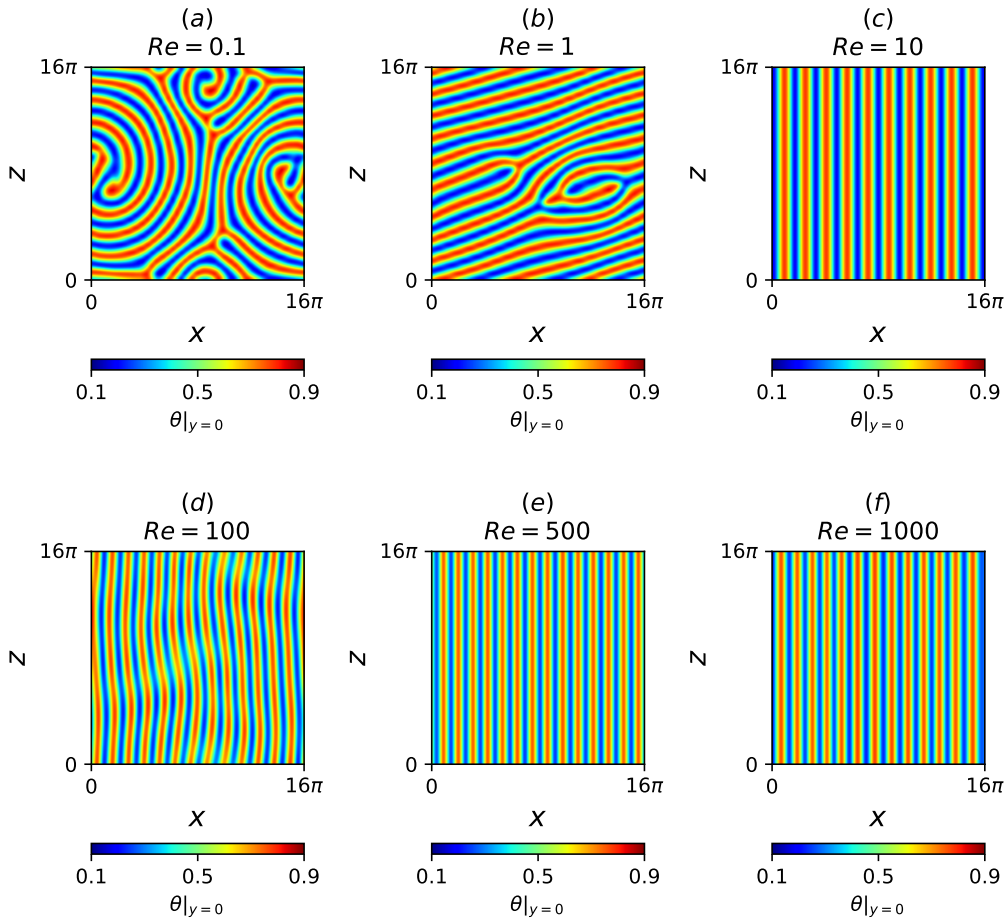


Figure 3.2: Midplane temperature snapshots at $Ra = 3000$, (a) $Re = 0.1$, (b) $Re = 1$, (c) $Re = 10$, (d) $Re = 100$, (e) $Re = 500$, (f) $Re = 1000$.

with a ‘hooked-like’ defect is observed at $Re = 1$, $Ra = 3000$ shown in figure 3.2(b), reminiscent of the multiple ‘non-ISR’ states in RBC (see references in §1.3). At $Re = 10$, the SDC disappears and longitudinal rolls with a spanwise wavenumber of $\alpha d = 2.5$ emerge, illustrated in figure 3.2(c), suggesting that the roll wavenumber adheres to the stability boundaries of the Busse balloon (see also figure 6 in Bodenschatz et al., 2000). As Re is increased further to 1000, the longitudinal rolls emerge as the preferred solution at $Ra = 2000, 3000$. The non-dimensionalised spanwise wavenumber of longitudinal rolls observed at $Ra = 3000$ and $Re = 100, 500, 10000$, shown in figure 3.2(d-f) respectively, is approximately $\alpha d \approx 3.3$, which lies outside of the stability boundaries of the Busse balloon in RBC (figure 6 in Bodenschatz et al., 2000). This suggests that the stability boundaries of the longitudinal rolls may change as Re increases. Interestingly, a stable ‘pinched’ longitudinal roll pattern emerges at $Re = 100$ $Ra = 3000$, reminiscent of a skew-varicose instability shown in figure 3.2(d). Unlike the secondary skewed-varicose instability observed in RBC (which reduces the wavenumber of an unstable ISR by pinching adjacent rolls together (Bodenschatz et al., 2000, see figure 7)), a stable ‘pinched’ tertiary state emerges here.

Figure 3.3 presents a detailed analysis of the coarse-grained transition boundaries between SDC and ISRs in the range $Re \in [1, 10]$, and from ISRs to wavy rolls for $Re \in [10, 100]$ across high Rayleigh numbers considered, $Ra \in [5000, 10000]$. As Re increases from 1 to 10, SDC regime

(see figure 3.3(a,d,g)) vanishes and longitudinal rolls emerge, as shown in figure 3.3(b,e,h) for $Ra = 10000, 8000, 5000$, respectively. These longitudinal rolls may undergo short-wavelength modulations, indicative of the secondary oscillatory instability of RBC occurring above $Ra \gtrsim 5000$ (Clever & Busse, 1974). This results in the development of oscillatory longitudinal rolls described by a relative periodic orbit at $Ra = 8000$, and a chaotic state at $Ra = 10000$, shown in figure 3.3(e,b) respectively.

The footprint of oscillatory convection rolls is also evident in the SDC regime at $Ra = 10000$, $Re = 1$, shown in figure 3.3(a). As Re increases from 10 to 100, the longitudinal rolls exhibit longer wavelength modulations, indicative of the wavy instability (Clever & Busse, 1991; Pabiou et al., 2005). This gives rise to wavy longitudinal rolls, appearing as a travelling wave, quasi-periodic tori, and a chaotic state at $Ra = 5000, 8000, 10000$, shown in figure 3.3(i,f,c) respectively. The wavelengths of the streamwise waviness and the spanwise periodic longitudinal roll appear to be approximately three intervals of streamwise length, $\Lambda_z \sim L_z/3$, and twelve intervals of spanwise length, $\Lambda_x \sim L_x/12$, respectively. Hence, the ratio between the streamwise waviness wavelength and the spanwise roll is about 4, consistent with the ratio observed by Clever and Busse (1991).

3.3.2 Spatiotemporal intermittent rolls

As Re approaches $Re = 500$, the wavy rolls disappear. Instead, a new regime, referred to as intermittent rolls, is observed. In this regime, the longitudinal rolls remain as the dominant convection structure, interspersed with a spatio-temporal intermittent breakdown towards the laminar state. This behaviour is illustrated for $(Ra, Re) = (8000, 500)$ in figure 3.4(a) using the temporal oscillations of the plane-averaged shear rate on the lower wall, $\langle \tau_w \rangle_{x,z}$, and the Nusselt number, Nu . We note $\tau_w = 2$ and $Nu = 1$ for the laminar solution.

The spatio-temporal intermittent breakdown of the longitudinal rolls towards the laminar state is observed in figure 3.4(b), where the bright and dark regions in the space-time plot of near-wall spanwise and wall-normal perturbation kinetic energy ($\mathcal{E}_{u'+v'} = 1/2(u'^2 + v'^2)$) at $(y^+, z) = (15, 8\pi)$, highlight the co-existence of longitudinal rolls and spatially localised laminar states; here, $\mathbf{u}' = \mathbf{u} - W_{lam}(y)$ and $y^+ = (y + 1)/Re_\tau$ with $Re_\tau = u_\tau h/\nu$, where u_τ is the friction velocity. A similar observation is made with the space-time plot of midplane temperature, $\theta|_{(y,z)=(0,8\pi)}$, in figure 3.4(c), where the elongated red/blue contours correspond to up-/down-welling regions of longitudinal rolls, and the green regions indicate spatially-localised laminar states. The two near-wall transport properties, the wall shear rate and the Nusselt number, exhibit strong correlations. For example, at $t = 3736$, both peaks reveal a spatially coherent longitudinal roll structure in figure 3.4(d,e). There are also dips observed at $t = 6189$ and $t = 8680$, indicative of the spatially local breakdown towards the laminar state, as shown in figures 3.4(f,g) and 3.4(h,i), respectively. In summary, the longitudinal rolls enhance heat and momentum transfer towards the walls, but they appear to be intermittently disrupted by the breakdown towards the laminar state. To better understand this behaviour, we later consider the temporal dynamics in a confined domain, $\Gamma = \pi/2$, where the spatial intermittency is artificially suppressed (see §3.4.1).

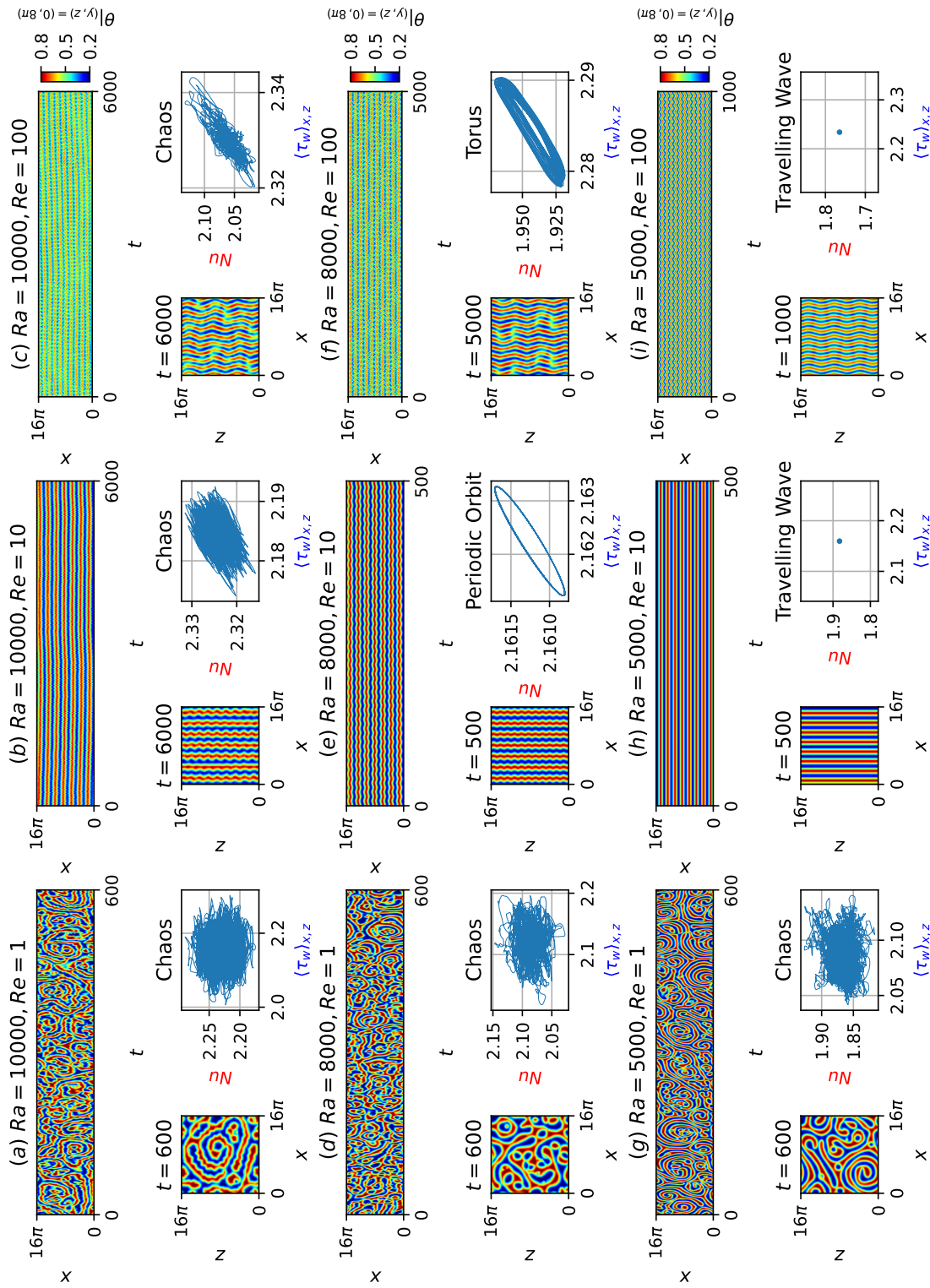


Figure 3.3: The space-time plots of midplane temperature field, temperature snapshot and phase space trajectories of the Nusselt number against wall shear rate at (a,b,c) $Ra = 10000$ for $Re = 1, 10, 100$; (d,e,f) $Ra = 8000$ for $Re = 1, 10, 100$; and (g,h,i) $Ra = 5000$ for $Re = 1, 10, 100$. The flow patterns are primarily organised into spiral defect chaos, longitudinal rolls, and wavy rolls occurring at $Re = 1, 10, 100$, respectively.

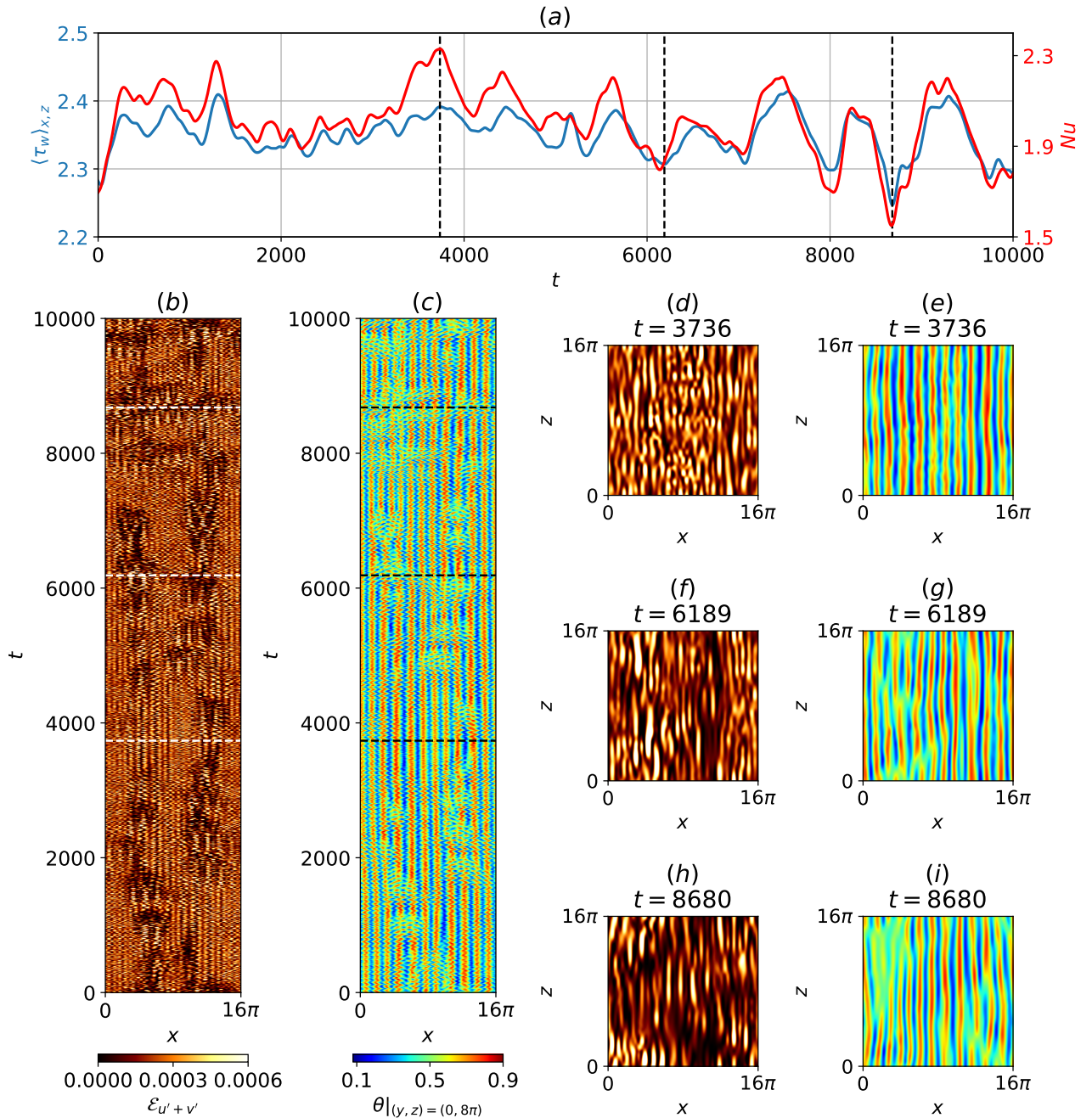


Figure 3.4: The intermittent rolls regime at $Ra = 8000$, $Re = 500$, $t \in [0, 10000]$. (a) The time history of shear on the lower wall and Nusselt number. Space-time (x - t) plots of (b) near-wall wall-normal and spanwise perturbation kinetic energy and (c) midplane temperature space-time plot, with the corresponding near-wall and midplane temporal planar snapshots at (d,e) $t = 3736$, (f,g) $t = 6189$, and (h,i) $t = 8680$.

3.3.3 Co-existence of convection rolls with turbulent bands

As Re approaches $Re = 1050$, shear-driven turbulence emerges as spatio-temporal intermittent turbulent-laminar bands, where turbulent and laminar regions can co-exist (Tuckerman, Chantry, & Barkley, 2020). In the absence of buoyancy (i.e. $Ra = 0$), these bands emerge clearly shown in figure 3.5. The space-time plot of the near-wall wall-normal and spanwise perturbation kinetic energy, $\mathcal{E}_{u'+v'}$, at $y^+ = 15$ in figure 3.5(a) highlights this co-existence, where the turbulent and laminar regions are indicated by dark and bright areas, respectively. In particular, a period of prolonged laminar state is observed at $t = 1100, 4491, 6171$, represented by localised green regions in the space-time plot of midplane temperature, $\theta|_{(y,z)=(0,8\pi)}$, in figure 3.5(b). The prolonged laminar states are also evident in the near-wall and midplane temporal snapshots of figures 3.5(c-h), shown as large pockets of dark and green regions that fill approximately half of the spatial domain.

Next, we consider the influence of buoyancy on the turbulent-laminar bands and compare two distinctly different cases of buoyancy using $Ra = 0$ and $Ra = 10000$ at $Re = 1050$. In the latter case, the typical features of the turbulent-laminar bands depicted as alternate dark and bright bands are also seen in the space-time plot of near-wall wall-normal and spanwise perturbation kinetic energy, $\mathcal{E}_{u'+v'}$, in figure 3.6(a). However, some important differences emerge compared to the former case (in $Ra = 0$). In particular, the midplane temperature snapshots, $\theta|_{(y,z)=(0,8\pi)}$, at $t = 1282, 5077, 6358$ in figures 3.6(d,f,h) reveal some localised regions of streamwise-aligned red and blue contour stripes, likely indicating the presence of longitudinal rolls. These longitudinal roll regions are typically located next to neighbouring turbulent (bright) regions in the near-wall perturbation kinetic energy snapshots in figures 3.6(c,e,g), suggesting that longitudinal rolls co-exist with turbulent patches at $Ra = 10000$. However, we caution that although they are relatively weak, similar red and blue contour stripes are also observed at $Ra = 0$, where longitudinal rolls are not expected, as shown in figure 3.5(f). In this case, these weak elongated red and blue contour stripes are likely to be from the near-wall streaks.

Nonetheless, turbulence occurs more spatially intermittently at $Ra = 0$, containing prolonged pockets of laminar regions, while turbulent regions at $Ra = 10000$ appear more visibly consistently (compare figures 3.5a with 3.6a). In other words, the presence of longitudinal rolls may promote turbulence locally, and we will investigate this issue further in §3.4.

3.4 The role of longitudinal rolls

3.4.1 The thermally-assisted sustaining process (TASP) in a confined domain

Given the complexities in the spatio-temporal dynamics observed in §3.3, we consider simulations confined to a domain defined by $\Gamma = \pi/2$, where longitudinal rolls and localised turbulence could be viewed as spatially isolated. We start from a numerical simulation at $Ra = 10000$ and $Re = 1050$ in $\Gamma = \pi/2$, integrated in time for $t \in [0, 3000]$. The initial condition has been sampled from a statistically stationary turbulent field at $Re = 2000$ for $Ra = 10000$, and the Re is then slowly lowered to $Re = 1050$. The time history for $t \in [0, 3000]$ of the two near-wall transport properties, the Nusselt number and the shear rate on the lower wall, is presented in figure 3.7, together with

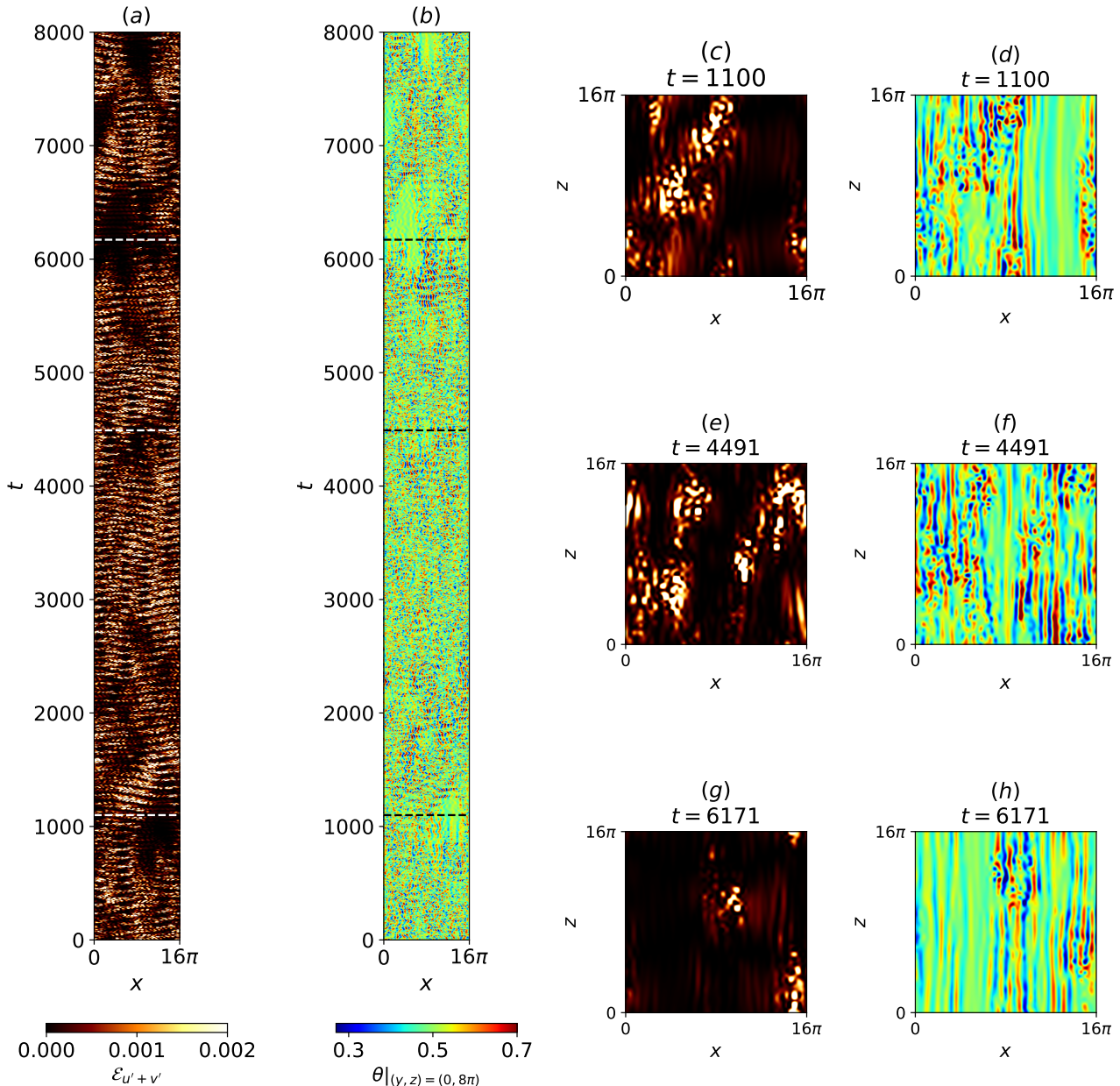


Figure 3.5: Shear-driven turbulence regime at $Ra = 0$, $Re = 1050$, $t \in [0, 8000]$. Space-time plots of (a) near-wall wall-normal and spanwise perturbation kinetic energy, (b) midplane temperature space-time plot, and near-wall and midplane temporal planar snapshots at (c,d) $t = 1100$, (e,f) $t = 4491$, and (g,h) $t = 6171$, highlighting a prolonged laminar patch.

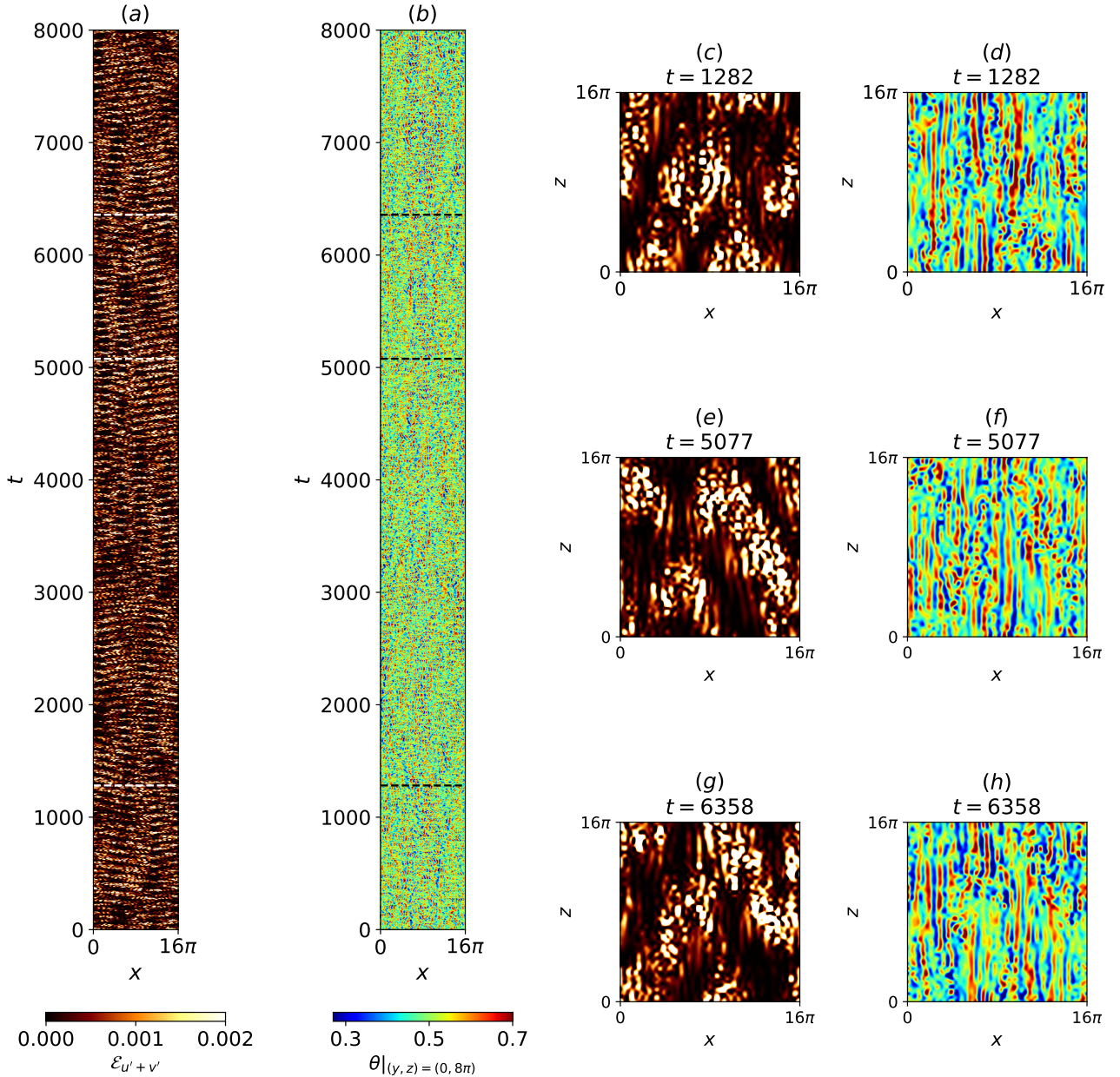


Figure 3.6: Shear-driven turbulence regime at $Ra = 10000$, $Re = 1050$, $t \in [0, 8000]$. Space-time plots of (a) near-wall wall-normal and spanwise perturbation kinetic energy, (b) midplane temperature spacetime plot, and their corresponding near-wall and midplane temporal $x - z$ planar snapshots at (c,d) $t = 1282$, (e,f) $t = 5077$, and (g,h) $t = 6358$, highlighting the coexistence of longitudinal rolls and turbulent bands.

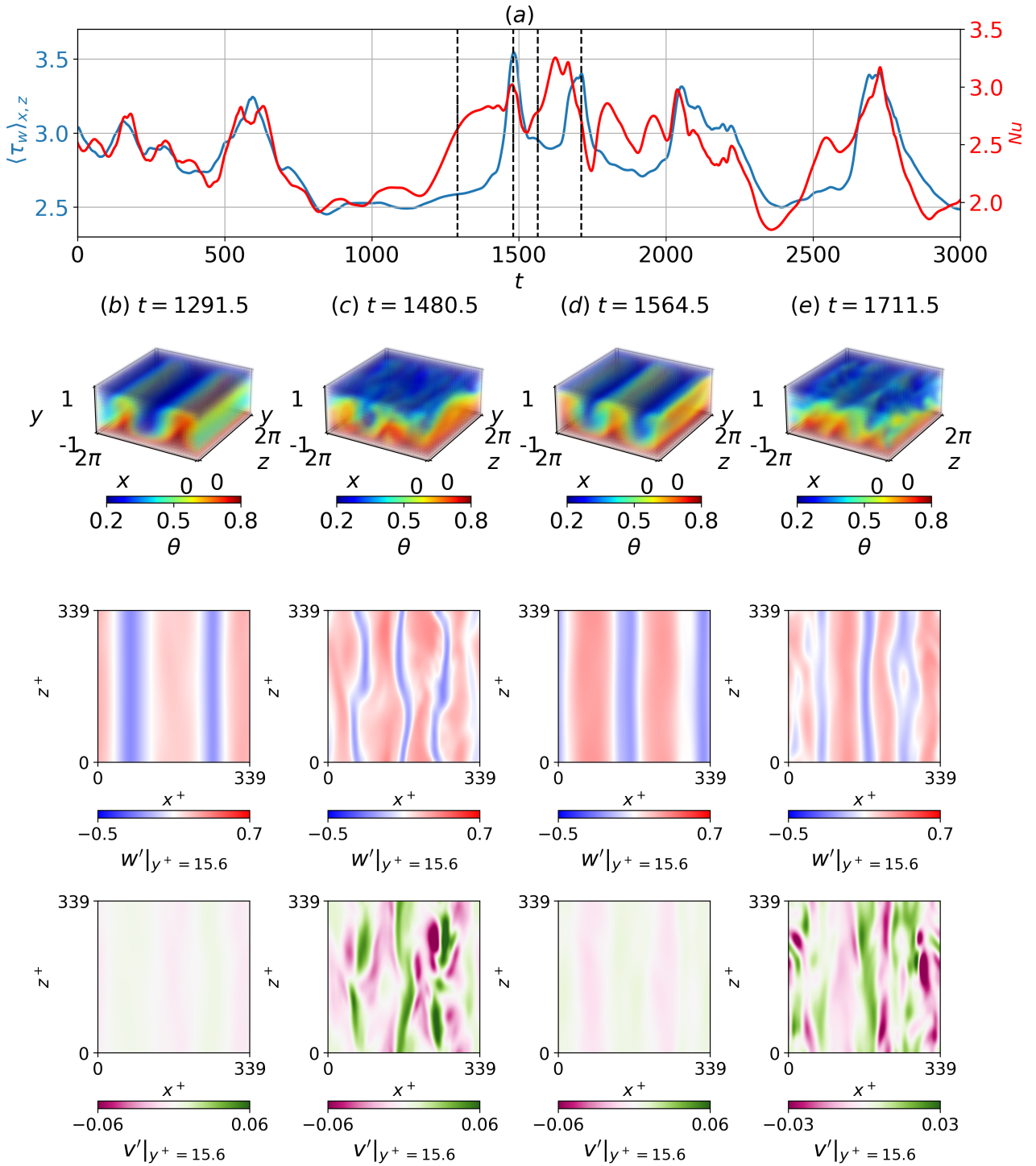


Figure 3.7: Intermittent dynamics in a confined domain at $Ra = 10000$, $Re = 1050$, $t \in [0, 3000]$, $\Gamma = \pi/2$. The time history of the (a) Nusselt number and shear. Temporal snapshots of volumetric temperature, planar near-wall streamwise and spanwise perturbations at (b) $t = 1291.5$, (c) $t = 1480.5$, (d) $t = 1564.5$, (e) $t = 1711.5$. Longitudinal rolls and transient turbulence are observed at (b,d) and (c,e), respectively.

snapshots of the temperature, $\theta(\mathbf{x})$, and the near-wall streamwise and spanwise perturbation velocities, $w'|_{y^+=15}, v'|_{y^+=15}$ at selected times. In this confined domain, the dynamics of the system exhibits temporal intermittency, where the solution trajectory appears to wander between longitudinal rolls and highly disorganised chaotic flow fields, characterised by low- and high-near-wall transport properties, respectively.

Starting from a longitudinal roll state of spanwise wavenumber of $\alpha d = 4$ at $t = 1291.5$ in figure 3.7(b), the solution erupts into a highly disorganized turbulent state at $t = 1480.5$, marked by a disordered temperature field in figure 3.7(c). During this breakdown, the near-wall snapshots of streamwise perturbation velocity, $w'|_{y^+=15}$, and wall-normal perturbation velocity, $v'|_{y^+=15}$, illustrated in the bottom panels of figures 3.7(c), reveal three pairs of high- and low-speed streaks, each with an average spanwise wavelength of $\Lambda_x^+ \approx 339/3 = 113$ (where $\Lambda_x^+ = u_\tau \Lambda_x / \nu$ refers to non-dimensionalised wavelength), close to the mean streak spacing ($\Lambda_x^+ \sim 100$) commonly reported in shear flow turbulence (Hamilton et al., 1995; J. Kim et al., 1987; Kline et al., 1967). These streaks appear to be meandering, negatively correlated with wall-normal perturbation velocities, reminiscent of a streak breakdown process (Hamilton et al., 1995), or a bursting event (H. T. Kim, Kline, & Reynolds, 1971), where high (low)-speed streaks are brought close to (away from) the wall, enhancing near-wall transport quantities. The enhancement is reflected in large increments in the Nusselt number and wall shear rate of roughly 40% at $t = 1480.5$ in figure 3.7(a). Subsequently, the solution trajectory returns to a longitudinal roll state at $t = 1564.5$, before erupting into turbulence at $t = 1711.5$ (see figures 3.7(d,e) respectively). This suggests that the turbulence has a finite lifetime, occurring transiently before decaying towards the laminar state at $Re = 1050$ (Hof et al., 2006; Schneider et al., 2007), which is linearly unstable, leading to the onset of longitudinal rolls where transient turbulence could be re-excited again.

To test this hypothesis, we consider a numerical simulation at $Ra = 0$, $Re = 1050$, in $\Gamma = \pi/2$, where longitudinal rolls cannot appear. The initial condition is taken from a stationary turbulent solution at a higher Re of $Re = 2000$, which is then slowly lowered to $Re = 1050$, and then integrated in time for $t \in [0, 700]$. The time history of the Nusselt number, Nu , and the wall shear rate, $\langle \tau_w \rangle_{x,z}$, is reported in figure 3.8, with the temperature snapshots, $\theta(\mathbf{x})$, at selected time units. An initial turbulent flow field decays towards the laminar solution in $t \in [0, 700]$. Comparing the results between $Ra = 0$ and $Ra = 10000$, we propose that the longitudinal rolls at $Ra = 10000$ could mediate a transition mechanism between unstable laminar state and transient turbulence, so that the entire nontrivial flow dynamics could be sustained indefinitely.

Next, we investigate the impact of longitudinal rolls on this proposed mechanism at different Ra . We capture the flow quantities for $Ra = 10000$ and $Re = 1050$ at $t = 850.5$ (just before the onset of longitudinal rolls, see figure 3.7), and use as an initial condition to perform four numerical simulations by lowering Ra instantly to $Ra = 8000, 5000, 3000, 2000$, respectively and time-integrated further to $t \in [850.5, 5000]$. The time history of the wall shear rate, $\langle \tau_w \rangle_{x,z}$, and the temperature snapshots, $\theta(\mathbf{x})$, of these experiments of ‘ Ra -quenching’ are presented in figure 3.9. The time history of shear is visibly intermittent for $Ra = 8000, 5000$, depicted as the orange and green trajectories in figure 3.9(a), similar to $Ra = 10000$. At $Ra = 8000, 5000$, the longitudinal rolls emerge approximately

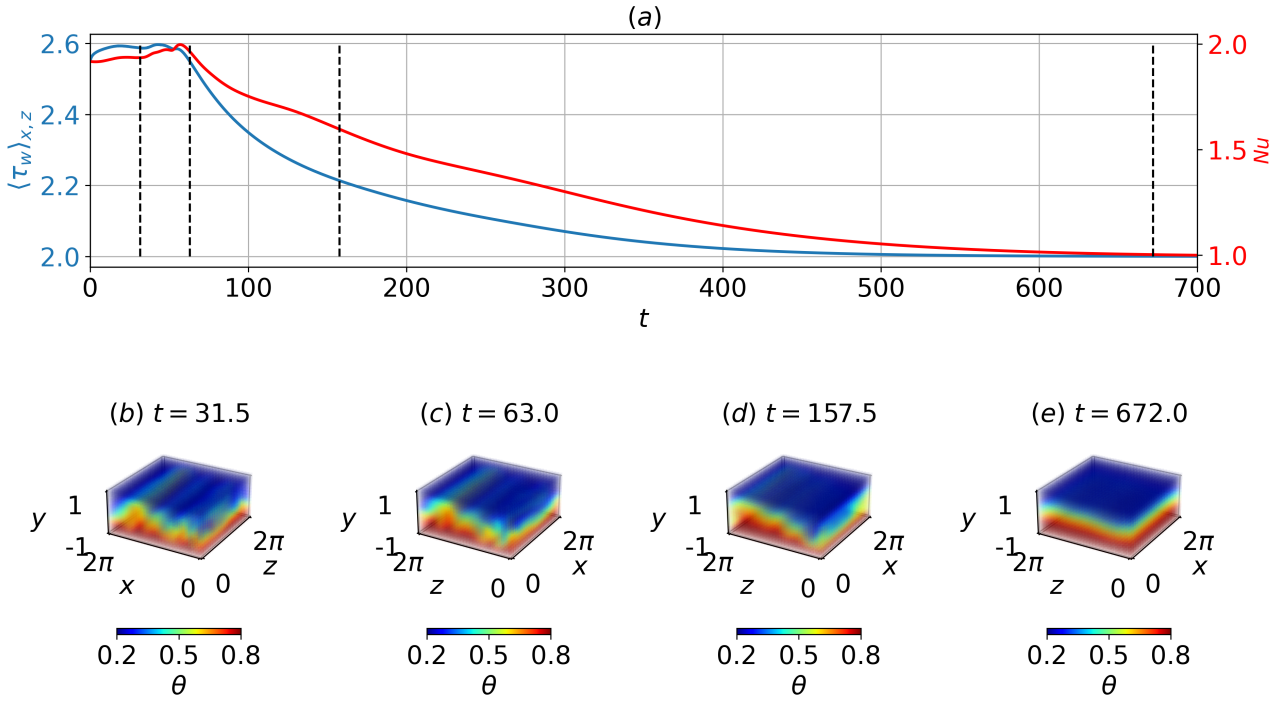


Figure 3.8: Relaminarisation in a confined domain at $Ra = 0$, $Re = 1050$, $t \in [0, 3000]$, $\Gamma = \pi/2$. The time history of the (a) Nusselt number and shear. Temporal snapshots of volumetric temperature at (b) $t = 31.5$, (c) $t = 63.0$, (d) $t = 157.5$, (e) $t = 672.0$.

at $t = 1312.5$ (see figures 3.9(c,e)), before erupting into turbulence at $t = 1743$ and $t = 3570$ in figures 3.9(d,f), respectively. This is then accompanied by a large spike in the wall shear rate before dipping briefly, shown as the orange and green trajectories of figure 3.9(a). As Ra is lowered further to $Ra = 3000, 2000$, the transients begin to decay into a longitudinal state from $t = 850.5$ to $t = 1312.5$, which remains stable until $t = 4200$ illustrated by figure 3.9(h,j), accompanied by the red and purple asymptotic trajectories in figure 3.9(a). This suggests that the longitudinal rolls are likely to be linearly unstable for $Ra = 8000, 5000$, leading to turbulence, while remaining stable for $Ra = 3000, 2000$. In particular, the longitudinal roll state at $Ra = 5000$ remained saturated for a longer period $t \in [1500, 3400]$ (green curve in figure 3.9(a)), indicating that the growth rate of the linear instability is smaller than for $Ra = 8000$. We note that the longitudinal rolls in figure 3.9 have a spanwise wavenumber of $\alpha d = 4$, which corresponds to the wavenumber of the dominant primary instability (see Appendix A.3), indicating that it is the most preferred wavenumber within the confined domain.

To understand the stability characteristics of the longitudinal rolls, we perform a linear stability analysis about the longitudinal roll state ($\alpha d = 4$), at $Ra = 10000, 8000, 5000, 3000, 2000$. The details of linear stability analysis are described in §3.2.4, where λ and $\tilde{\mathbf{q}}(x, y)e^{i\beta z}$ refer to the eigenvalue and eigenmode. The longitudinal roll (base) states, \mathbf{q}_{LR} , are obtained by time integrating an initial condition consisting of the laminar (conduction) state, superimposed by the primary eigenmode, $\alpha d = 4$, at $Ra = 10000, 8000, 5000, 3000, 2000$, in a two-dimensional $x - y$ plane, suppressing any three-dimensional perturbations numerically. The growth rates as a function of discrete streamwise wavenumbers, $2 \leq \beta d \leq 5$, are presented in figure 3.10. We note that the admissible streamwise

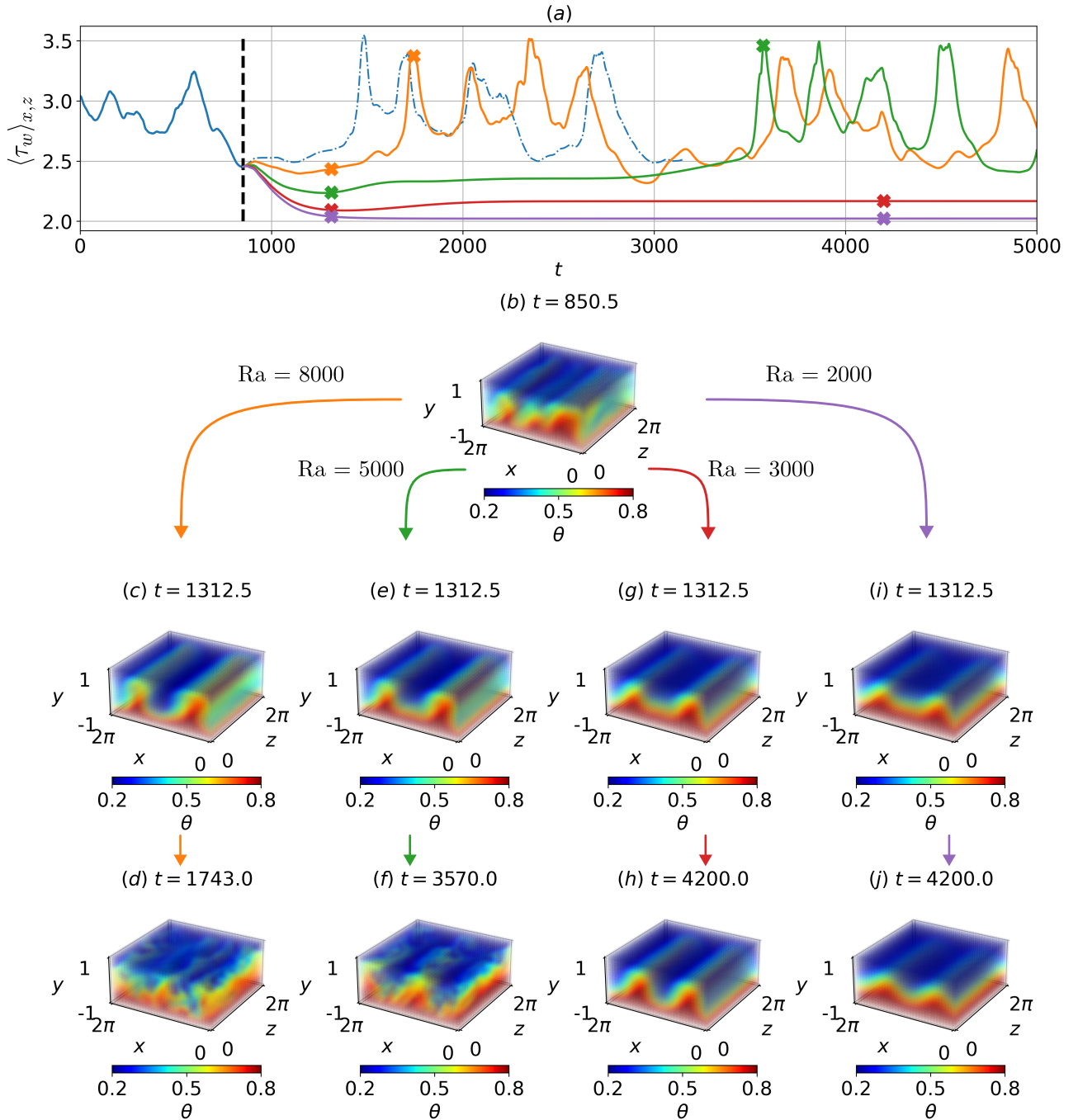


Figure 3.9: Ra -quenching experiments for $Ra = 8000, 5000, 3000, 2000$, at $Re = 1050$, $\Gamma = \pi/2$, $t \in [850.5, 5000]$. The time history of (a) shear and (b) volumetric temperature snapshots of the flow condition at $t = 850.5$. Volumetric temperature snapshots for $Ra = 8000$ at (c,d) $t = 1312.5, 1743$, and $Ra = 5000$ at (e,f) $t = 1312.5, 3570$, revealing a longitudinal roll and a turbulent state, respectively. Stable longitudinal rolls emerge for $Ra = 3000$ at (g,h) $t = 1312.5, 4200$, and $Ra = 2000$ at (j,k) $t = 1312.5, 4200$.

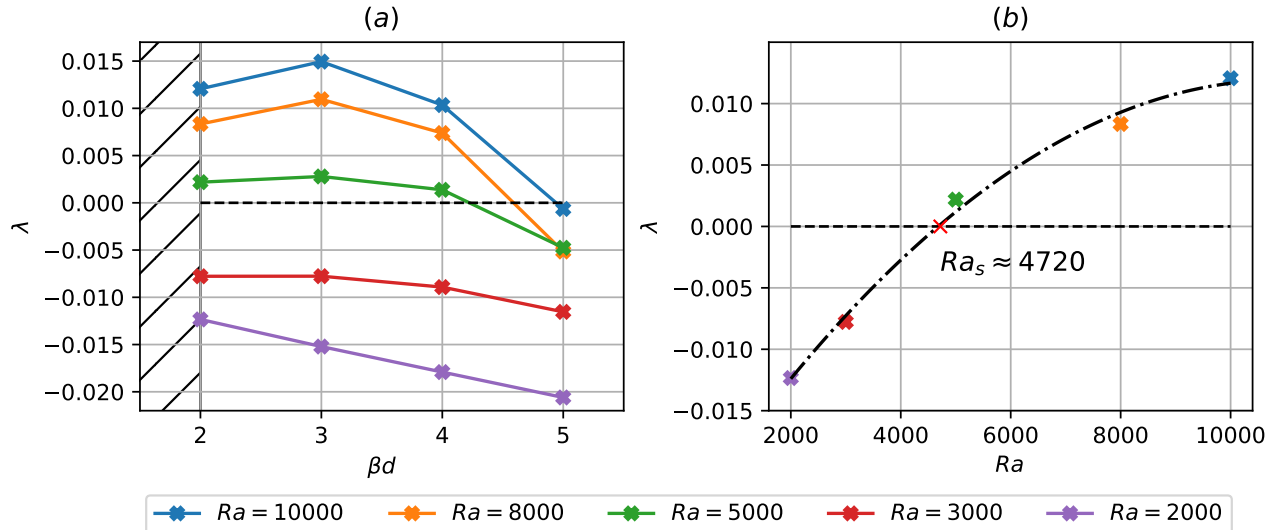


Figure 3.10: The growth rates of infinitesimal perturbations linearised about longitudinal rolls, \mathbf{q}_{LR} , of spanwise wavenumber of $\alpha d = 4$, against (a) streamwise wavenumber βd , and (b) Ra for $\beta d = 2$. The hatches in (a) refer to wavenumbers smaller than those admissible in $\Gamma = \pi/2$. The dash-dotted line in (b) is a standard quadratic regression yielding $Ra_s \approx 4720$.

wavenumbers within $\Gamma = \pi/2$ are $\beta d = m$, where m is a positive even integer, $m = 2, 4, \dots$, and $\beta d = 3, 5$ are included for completeness. The longitudinal rolls are linearly unstable for $Ra \geq 5000$, while they remain stable for $Ra \leq 3000$, which confirms our hypothesis earlier. In particular, the growth rates between $Ra = 5000$ and $Ra = 10000$ differ by an order of magnitude, which could explain the prolonged period of saturation in the green curve of figure 3.9(a). The dominant secondary instability of longitudinal rolls in $\Gamma = \pi/2$ has a streamwise wavenumber of $\beta d = 2$. Using a standard quadratic regression, the critical Rayleigh number for disturbances with $\beta d = 2$ is approximately $Ra_s \approx 4720$, presented in figure 3.10(b).

Following this, we examine the dominant unstable manifold ($\beta d = 2$) of the longitudinal rolls ($\alpha d = 4$) at $Ra = 5000$, by considering an initial condition,

$$\mathbf{q}_0(\mathbf{x}, t = 0) = \mathbf{q}_{LR}(x, y) + (\check{\mathbf{q}}(x, y)e^{i\beta z} + c.c.). \quad (3.7)$$

Here, $\check{\mathbf{q}}e^{i\beta z}$ is an eigenmode for the streamwise wavenumber β , and its amplitude was scaled such that its total energy is defined by

$$\delta = \frac{1}{V} \int_{\Omega} (\hat{\mathbf{u}}(\mathbf{x})^T \hat{\mathbf{u}}(\mathbf{x}) + \frac{Ra}{8Re^2Pr} \hat{\theta}(\mathbf{x})^2) d\Omega = 10^{-3}. \quad (3.8)$$

We have also considered that $\delta = 10^{-2}, 10^{-4}$, but $\delta = 10^{-3}$ was found to be small enough to ensure linear growth while large enough without requiring a large number of time steps.

The initial condition is time-integrated for $t \in [0, 8000]$, and its time history of the near-wall transport properties, the space-time plot of the mid-plane temperature, $\theta|_{(y,z)=(0,\pi)}$, are presented in figure 3.11, with snapshots of temperature, $\theta(\mathbf{x})$, and near-wall streamwise and spanwise perturbation velocities, $w'|_{y^+=15}, v'|_{y^+=15}$ at some selected times. The intermittent trajectory is visually apparent,

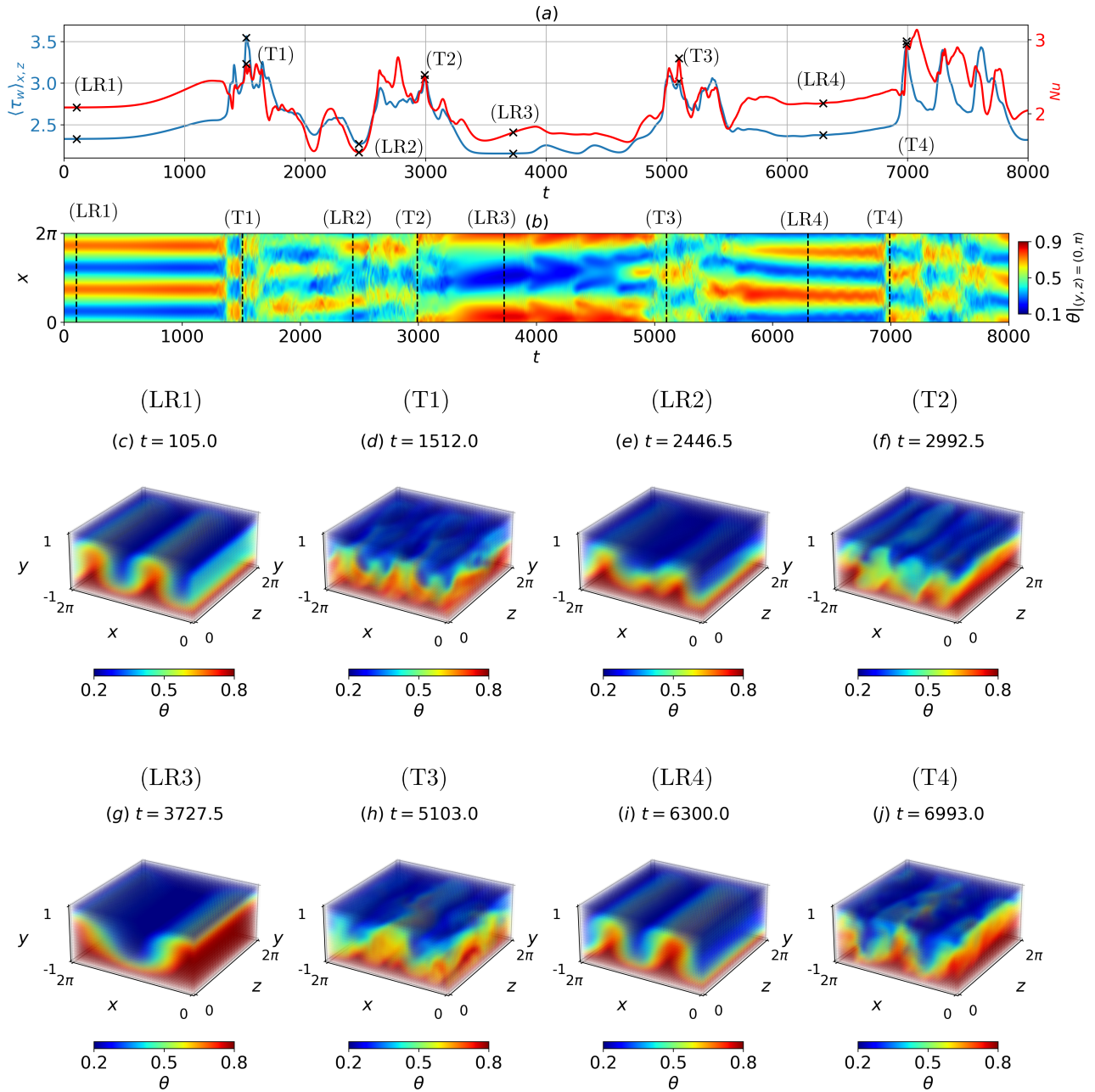


Figure 3.11: Time integration along the dominant unstable manifold, $\beta d = 2$, of the longitudinal rolls at $Ra = 5000$, $Re = 1050$, $\Gamma = \pi/2$ for $t \in [0, 8000]$. Time history of the (a) Nusselt number and wall shear rate, and (b) midplane temperature space-time plot. This system oscillates between the longitudinal rolls (LR1 – 4) and turbulence (T1 – 4) over four intervals. Snapshots of temperature at (c) $t = 105$, (d) $t = 1512$, (e) $t = 2446.5$, (f) $t = 2992.5$, (g) $t = 3727.5$, (h) $t = 5103$, (i) $t = 6300$, (j) $t = 6993$.

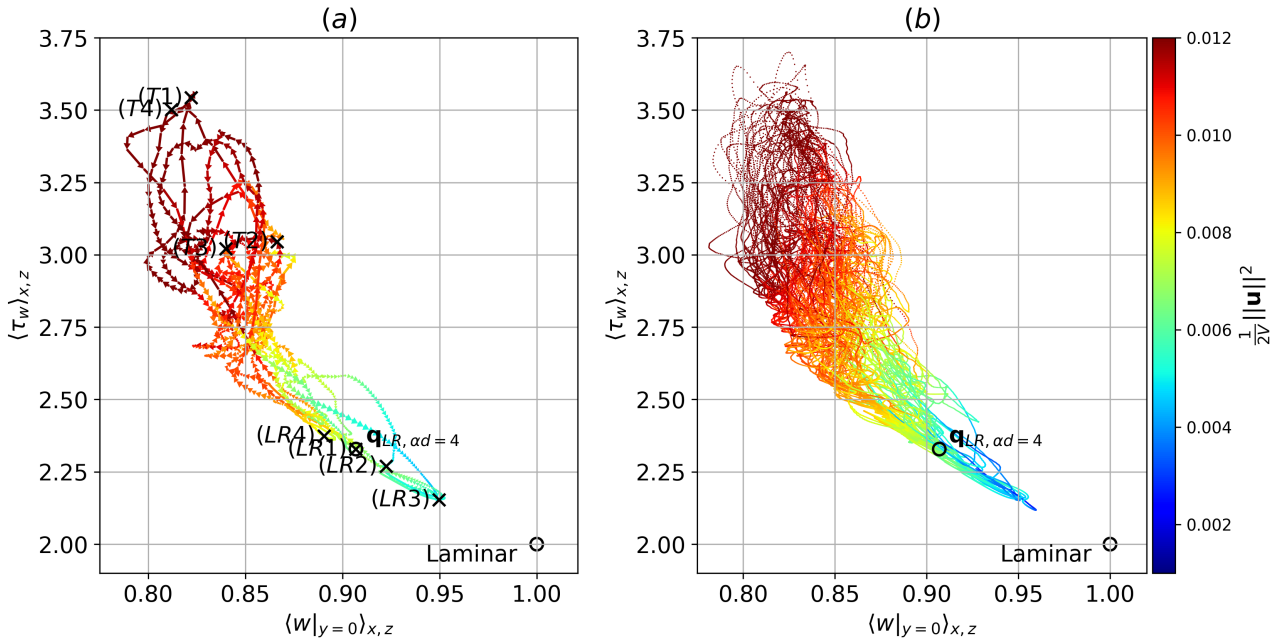


Figure 3.12: State space projection based on the planar averaged centerline velocity and shear, coloured by the volume normalised perturbation kinetic energy at $Ra = 5000$, $Re = 1050$, $\Gamma = \pi/2$, (a) $t \in [0, 800]$, (b) $t \in [0, 68750]$. The open black circles represent the unstable equilibria of longitudinal rolls and the laminar state. Note that the black-crosses, labelled by (T1-4) and (LR1-4), refer to temporal snapshots in figure 3.11, not equilibria solutions.

oscillating between longitudinal rolls and transient turbulence over four cycles for $t \in [0, 8000]$: for example, the regions of low and high near-wall transport quantities in figure 3.11(a) correspond well to the organised and disordered longitudinal rolls in figure 3.11(b), respectively. As the solution emerges from the unstable manifold of the longitudinal roll state, ($LR1$) in figure 3.11(c), the trajectory erupts into turbulence at $t = 1512$, marked by a disordered volumetric temperature field in snapshot ($T1$) in figure 3.11(d). Turbulence occurs transiently, and the solution decays towards a longitudinal roll-like state at $t = 2446.5$, shown by snapshot ($LR2$) in figure 3.11(e), forming a single cycle. The intermittent cycle repeats over three subsequent intervals, where the transient turbulent state and longitudinal rolls emerge at $t = 2992.5, 5103, 6993$, and $t = 3727.5, 6300$, as shown in the snapshots ($T2, 3, 4$) and ($LR3, 4$) in figures 3.11(f,h,j) and 3.11(g,i), respectively. Lastly, we show that the dominant unstable manifold of the longitudinal rolls is connected to a transient turbulent state. Interestingly, a longitudinal roll with $\alpha d = 2$ sometimes emerges after turbulence decays, shown as the snapshot ($LR3$). This suggests that other unstable manifolds may well be linked to the transition to transient turbulence.

To better visualise the temporal dynamics in figure 3.11, we project the solution trajectory onto the space composed of two state observables: planar averaged centerline velocity, $\langle w|_{y=0} \rangle_{x,z}$, the wall shear rate, $\langle \tau_w \rangle_{x,z}$ coloured by the volume-averaged perturbation kinetic energy, $1/(2V) \|\mathbf{u}'\|^2$, in figure 3.12, where $\|\mathbf{u}'\|^2 = \int_{\Omega} \mathbf{u}'^H \mathbf{u}' dV$ with Ω being the flow domain. These observables are chosen because they are found to distinguish well the regions of turbulent states, longitudinal roll states, and the laminar state that reside around $(0.82, 3.2)$, $(0.90, 2.32)$, and at $(1, 2)$, respectively. Indeed, the temporal snapshots of ($T1 - 4$) appear around the representative location of turbulent

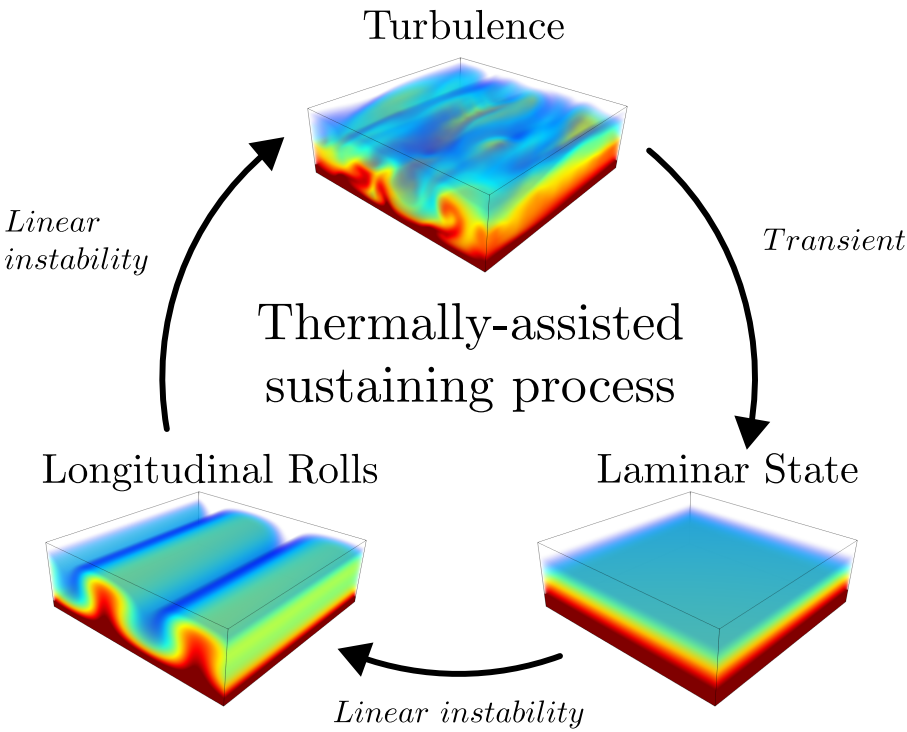


Figure 3.13: The thermally-assisted sustaining process (TASP).

states, $(0.82, 3.2)$, and the snapshots of $(LR1 - 4)$ and an equilibrium related to the longitudinal roll state with the spanwise wavenumber $\alpha d = 4$ (denoted by $\mathbf{q}_{LR,\alpha d=4}$) are seen around $(0.90, 2.32)$.

The solution trajectory emerges from the unstable manifold of the longitudinal roll state, $\mathbf{q}_{LR_{\alpha d=4}}$, evolving towards turbulent states around $(0.85, 3.2)$, characterised by a high wall shear rate. At this Re , the turbulence is transient in the confined domain, occurring with a finite lifetime, eventually decaying towards the laminar state (Paranjape et al., 2023; Tuckerman et al., 2020; Zammert & Eckhardt, 2014). As the solution trajectory approaches the laminar solution at $(1, 2)$, it abruptly reverses towards the longitudinal roll state near $(0.95, 2.15)$, $(LR3)$ due to the buoyancy-driven linear instability of the laminar base state in the RBP flow. Subsequently, the solution trajectory could depart along an unstable manifold of the longitudinal rolls again, forming a cyclic process.

To see if this cycle could be sustained indefinitely, we consider a longer time horizon, $t \in [0, 68750]$, illustrated in figure 3.12(b). The solution trajectory wanders between the ‘cloud’ of transient turbulence at the top left corner (in red), and longitudinal roll and laminar states (in blue) in the bottom right, forming a basin of attraction between the unstable longitudinal rolls, transient turbulence, and the unstable laminar base state. This basin of attraction is likely established above a critical Ra as the longitudinal rolls become linearly unstable (i.e. $Ra \gtrsim Ra_s \approx 4720$, see figure 3.10(b)), and the instability of the longitudinal rolls provides an intermediate pathway towards transient turbulence, which could be regenerated again - a ‘self-sustaining’ dynamical process. We refer to this process as the *thermally-assisted sustaining process (TASP)*, inspired by the self-sustaining process (SSP) from turbulent shear flows (see §1.2.3). A schematic of the TASP is illustrated in figure 3.13.

3.4.2 Variation of Ra and Re on the thermally-assisted sustaining process in $\Gamma = \pi/2$

In this section, we further explore the behaviour of the *TASP* as Re and Ra are varied. We consider eight different cases at $Ra = 8000, 4000$ and $Re = 600, 700, 1000, 1400$. The results of these eight cases, where longitudinal rolls are unstable at $Ra = 8000$ or stable at $Ra = 4000$, are shown in figure 3.14, depicting the space-time plots of the midplane temperature, $\theta|_{y=0}(x, t)$, the time history of the Nusselt number, Nu , and the wall shear rate, $\langle \tau_w \rangle_{x,z}$ and the state space portrait using the plane-averaged centerline velocity, $\langle w|_{y=0} \rangle_{x,z}$, the wall shear rate. For all cases, except $Ra = 4000$, $Re = 1000$ and $Re = 1400$, their initial conditions are prepared from the laminar state, superimposed by a random noise based on a Gaussian distribution with zero mean and unit variance, scaled to a total energy of $\delta = 10^{-3}$ (see (3.8) for the definition). For the exceptional cases at $Ra = 4000$, $Re = 1000$ and $Re = 1400$, where subcritical turbulence and stable longitudinal rolls are expected, their initial conditions are obtained by gradually lowering Re from a statistically stationary turbulent solution at $Ra = 4000$, $Re = 2000$.

We first consider $Re = 1000$ (figures 3.14(c,g)). At $Ra = 8000$ (figure 3.14(c)), the trajectory visits transient turbulence near $t = 7200$, decaying towards the longitudinal roll state, \mathbf{q}_{LR} with roll wavenumber $\alpha d = 4$, at $t = 7400$, before regenerating again, consistent with the *TASP* in §3.4.1. As Ra is lowered to 4000 (figure 3.14(g)), the solution trajectory decays towards the longitudinal roll state, \mathbf{q}_{LR} . In this case, the longitudinal rolls are linearly stable, confirming our hypothesis earlier that the *TASP* is only established when longitudinal rolls become linearly unstable above a certain Ra -threshold (i.e. $Ra \gtrsim Ra_s \approx 4720$).

At $Re = 1400$, $Ra = 4000$, the solution trajectory remains within the turbulent ‘cloud’ near $(0.8, 3.8)$ for $t \in [0, 10000]$, as illustrated in figure 3.14(h). This suggests that turbulence in this case might be an attractor sustaining indefinitely, although we have not investigated whether the turbulent chaotic saddle at $Re = 1000$ truly transitioned into an attractor at $Re = 1400$. As Ra is increased to 8000, the solution trajectory originating from the laminar state, evolves towards the unstable longitudinal roll state, \mathbf{q}_{LR} at $t = 1550$, transitioning into turbulence at $t = 1800$. Therefore, in this case, the linearly unstable longitudinal rolls serve as an intermediate transitional pathway between the laminar base state and subcritical turbulence, whereas at $Ra = 4000$, a bistability between stable longitudinal rolls (not shown) and turbulence is expected.

Next, we examine the behaviour of *TASP* as Re decreases towards the intermittent regime at $Re = 600, 700$, where a periodic orbit emerges between the longitudinal roll and the laminar state (figure 3.14(a,b,e,f)). At $Re = 600$, $Ra = 8000$ in figure 3.14(a), the solution trajectory initially evolves towards the longitudinal roll state, \mathbf{q}_{LR} , which is linearly unstable and breaks down towards the laminar state at $t = 2200$. This breakdown is evidenced by the trajectory’s proximity to the laminar state in state space and the presence of a narrow green patch in the midplane temperature spacetime plot. The longitudinal roll state is regenerated again, forming a periodic orbit with a period of $T_{period} = 8098 - 6108 = 1990$, oscillating between the longitudinal roll and laminar state over five intervals within $t \in [0, 10000]$. As Re increases slightly to 700, the periodic orbit persists over a shorter period of $T_{period} = 3889 - 3386 = 503$. A notable difference is observed in the regenerated

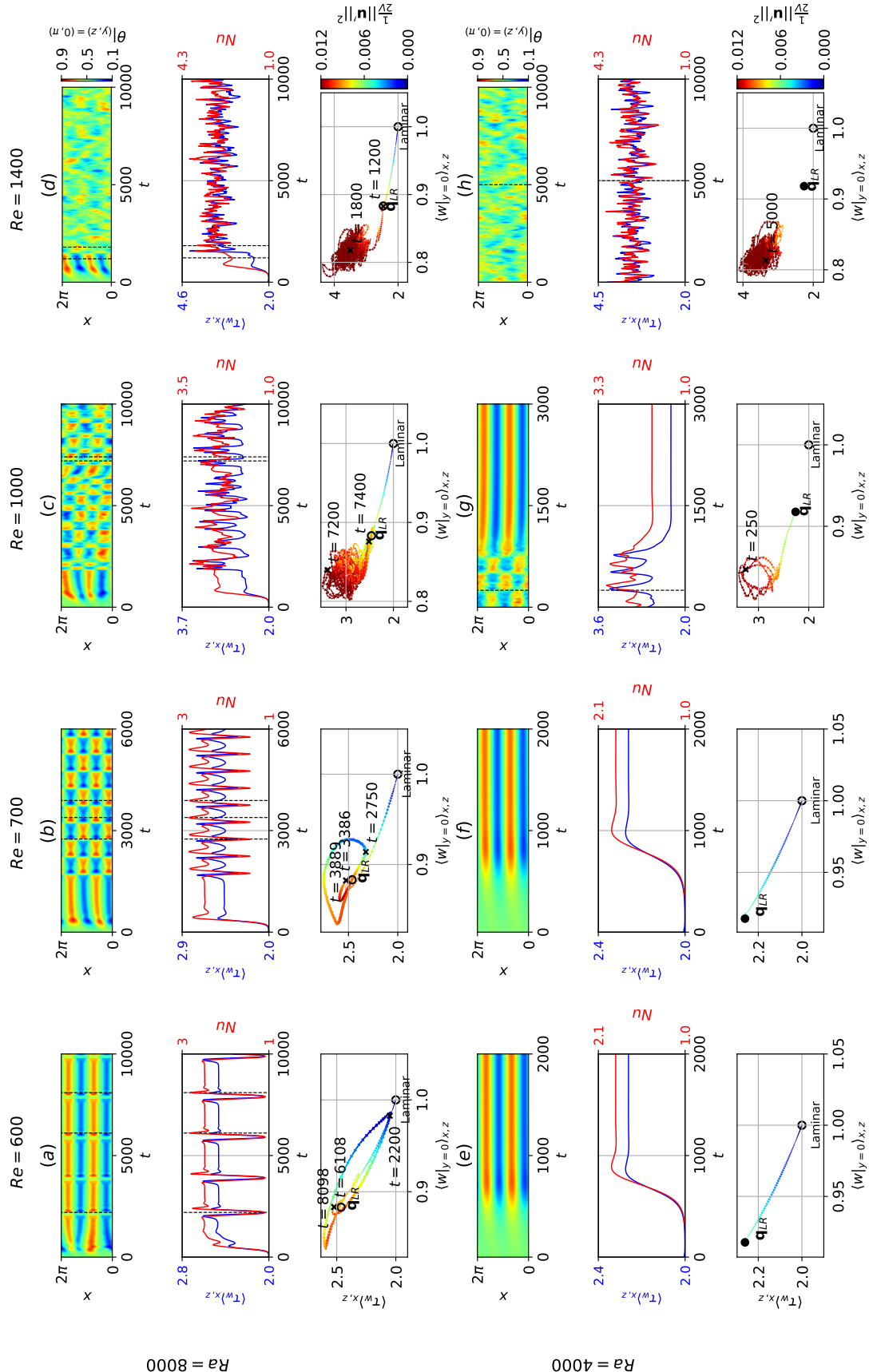


Figure 3.14: The behaviour of the unstable and stable longitudinal rolls at $Ra = 8000, 4000$ for (a,e) $Re = 600$, (b,f) $Re = 700$, (c,g) $Re = 1000$ and (d,h) $Re = 1400$ within $\Gamma = \pi/2$. Each parameter combination consist of three panels, depicting the (top) midplane temperature space-time plot, (mid) time history of the Nusselt number and shear, and (bottom) state space projection based on the planar averaged centerline velocity and shear, coloured by the volume normalised perturbation kinetic energy.

longitudinal rolls, which is continuously translated by $L_x/2$ in the x -direction. Additionally, as Re increases from 600 to 700, the trajectory moves further away from the laminar state during breakdown, suggesting an increasing attraction towards the longitudinal roll state, \mathbf{q}_{LR} (compare $t = 2200$ in figure 3.14(a) and $t = 2750$ in figure 3.14(b)). When Ra is lowered to $Ra = 4000$, the periodic orbit disappears and the trajectory stabilises into the longitudinal roll state, \mathbf{q}_{LR} , at $Re = 600, 700$ (figure 3.14(e,f)).

To summarise the dynamical processes identified in figure 3.14, we present their state space sketch in figure 3.15. At $Ra = 8000$, $Re = 600$ and $Re = 700$, the longitudinal rolls become linearly unstable, breaking down to the laminar state before being regenerated, forming a periodic orbit enclosed by black dotted paths in figures 3.15(a,b). For $Re = 700$, the regenerated longitudinal roll is continuously translated by $L_x/2$, suggesting a possible merger of two periodic orbits into one as sketched in figure 3.14(b). Future bifurcation studies are required to establish this, providing an avenue for future work. As Ra is lowered to $Ra = 4000$, the laminar state stabilises into the longitudinal rolls in figure 3.15(e). However, the flow in this regime may contain some invariant solutions (e.g [Paranjape et al., 2023](#)), denoted as saddle points here. Integrating along the unstable manifold of longitudinal roll states at $Ra = 8000$, $Re = 1000$ leads to transient turbulence, which eventually decays to the laminar state before regenerating the longitudinal rolls again, forming the TASP in figure 3.15(c). In contrast, at $Ra = 4000$, $Re = 1000$, the longitudinal rolls become linearly stable, eliminating the intermediate (orange) pathway towards turbulence. Therefore, the transient turbulence stabilises into longitudinal rolls, as shown with the black-dashed trajectory in figure 3.15(f). For $Ra = 8000$, $Re = 1400$, the linearly unstable longitudinal rolls provide an intermediate pathway towards turbulence from the laminar state, as sketched in figure 3.15(d), breaking the bistability between the laminar state and subcritical turbulence seen at $Ra = 4000$ in figure 3.15(g). This difference highlights the contribution of unstable longitudinal rolls towards the transition to turbulence within $\Gamma = \pi/2$.

We have examined the dynamics of unstable longitudinal rolls, as the Reynolds number, Re , and the Rayleigh number, Ra , are varied, identifying three key dynamical processes: (1) periodic orbits between longitudinal rolls and the laminar state (figure 3.15(a,b)), (2) the TASP, where transient turbulence can be sustained (figure 3.15(c)) and (3) an intermediate transitional pathway towards sustained turbulence (figure 3.15(d)). To establish a connection between these processes and refine their transitional boundaries, we conduct a further parametric study over fifteen numerical simulations at $Ra = 4000, 6000, 10000$ and $Re = 600, 800, 900, 1200, 1400$ for $\Gamma = \pi/2$. Figure 3.16 presents the midplane temperature space-time plot along with the time history of the wall shear rate, $\langle \tau_w \rangle_{x,z}$ and the Nusselt number, Nu . For all simulations, the initial conditions are prepared from the laminar state, superimposed with a random noise based on a Gaussian distribution with zero mean and unit variance, scaled to a total energy of $\delta = 10^{-3}$ (see definition in (3.8)). Due to the subcritical nature of turbulence and expected stable longitudinal rolls, exceptions are made for $Ra = 4000$, $Re = 900, 1200, 1400$, where initial conditions are taken from gradually lowering Re from a statistically stationary turbulent state at $Ra = 4000$, $Re = 2000$. The *thermally-assisted sustaining process* is highlighted in green for $Ra \in [6000, 10000]$ and $Re \in [900, 1200]$, where temporally intermittent shear and Nusselt number fluctuations are observed, accompanied by a mixture of organised and disorganised flow structures in

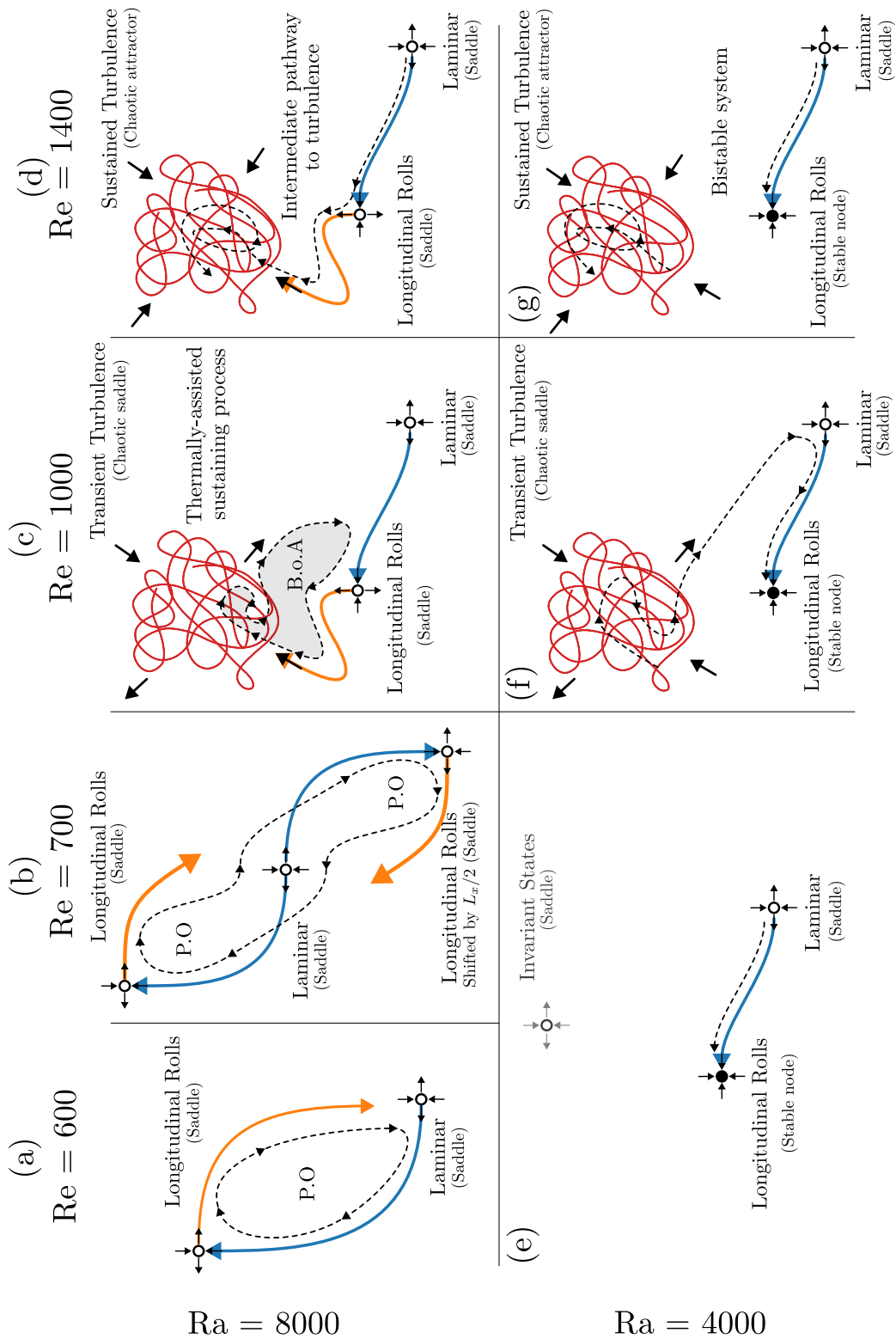


Figure 3.15: A state space sketch of figure 3.14 at $\text{Ra} = 8000$, (a) $\text{Re} = 600$, (b) $\text{Re} = 700$, (c) $\text{Re} = 1000$, (d) $\text{Re} = 1400$ and $\text{Ra} = 4000$ at (e) $\text{Re} = 600, 700$, (f) $\text{Re} = 1000$, (g) $\text{Re} = 1400$. The longitudinal roll is linearly unstable (saddle) at $\text{Ra} = 8000$, and is stable at $\text{Ra} = 4000$, whereas the laminar state is always linearly unstable (saddle). The blue and orange solid arrows refer to the unstable manifold of longitudinal rolls and the laminar state. The red solid lines denote the chaotic trajectories of turbulence, likely forming a chaotic saddle at $\text{Re} = 1000$ and a chaotic attractor at $\text{Re} = 1400$. The black-dashed trajectories refer to possible solution trajectories, forming a periodic orbit (P.O) at $\text{Ra} = 8000$, $\text{Re} = 600, 700$, and a basin of attraction (B.o.A) at $\text{Ra} = 8000$, $\text{Re} = 1000$. We note that invariant states could exist at $\text{Ra} = 4000$, $\text{Re} = 600, 700$, labelled as a saddle here (Paranjape et al., 2023).

the temperature space-time plots. Here, longitudinal rolls provide an intermediate pathway towards transient turbulence. For the same Re and as Ra lowers to 4000, transient turbulence eventually decays into stable longitudinal rolls labelled as ‘transient turbulence’ in figure 3.16. Periodic and quasi-periodic orbits between longitudinal rolls and the laminar state appear for $Ra = 10000$, $Re = 600, 800$ and $Ra = 6000$, $Re = 800$, establishing threshold values of Ra and Re shaded in yellow. Below this threshold, solutions stabilise into longitudinal rolls shaded in red. Although longitudinal rolls are linearly stable at $Ra = 4000$, $Re = 1400$, turbulence is sustained at least for a sufficiently long time, shaded blue at $Re = 1400$ and labelled as ‘sustained turbulence’ in figure 3.16. In this case, a bistable system forms between longitudinal rolls and turbulence at $Ra = 4000$, while longitudinal rolls provide an intermediate pathway to turbulence for $Ra \geq 6000$.

3.4.3 Extending to large domains, $\Gamma = 4\pi$.

In this section, we return to the simulation results in the large domain $\Gamma = 4\pi$ and try to establish the relevance of the local dynamical processes identified in the confined domain $\Gamma = \pi/2$. It should be mentioned that, by doing so, the discussion in this section does not fully account for the spatial interactions between the flow structures. However, we will see that many important flow features can be well explained based on the simulation results from the confined domain. The understanding of the full spatio-temporal dynamics deems to a formidable task at this point and is beyond the scope of this study.

Here, we will focus on $Re = 500, 750, 1000, 1050$ for $Ra = 10000$ presented in figure 3.17, illustrating their space-time plots of the midplane temperature, $\theta|_{(y,z)=(0,8\pi)}$, and the near-wall wall-normal and spanwise perturbation kinetic energy, $\mathcal{E}_{w'+v'}$, at $y^+ = 15$. Furthermore, to statistically characterise the flow structures, we calculate the joint probability distribution function (PDF) using the velocity and temperature in the midplane, $f(w|_{y=0}, \theta|_{y=0})$.

At $Ra = 10000$, $Re = 500$, the breakdown of longitudinal rolls towards the laminar state is observed, highlighted by spatially-localised green spots in the midplane temperature plots, and dark regions in the near-wall perturbation kinetic energy spacetime plot near $t = 500, 3800$ in figure 3.17(a). As Re increases from 500 to 750, the breakdown towards the laminar state remains visually apparent. The spatio-temporal dynamics between longitudinal rolls and the laminar state observed in the large domain in this regime are reminiscent of the stable periodic orbits identified between them in a confined domain, although the dynamics in the large domain is much more complex due to the spatial interactions between different flow structures. There is a noticeable decrease in the number of green and dark regions between the space-time figures 3.17(a) and (b), suggesting fewer laminar events at $Re = 750$. Indeed, this difference is further reflected in their PDFs, where the probability of laminar events, at $(w|_{y=0}, \theta|_{y=0}) = (1, 0)$, depicted as the ‘head’ of the ‘arc-shaped’ PDF, decreasing in intensity from $Re = 500$ (figure 3.17(a)) to $Re = 750$ (figure 3.17(b)). This suggests fewer laminar state events and more occurrences of the longitudinal roll state. It is also consistent with the result from the confined domain case, where the solution trajectory becomes increasingly attracted towards the longitudinal roll state from $Re = 600$ and $Re = 700$ at $Ra = 8000$ (figures 3.14(a,b)).

At $Re = 1000$, we observe the coexistence of the laminar state, the longitudinal rolls, and

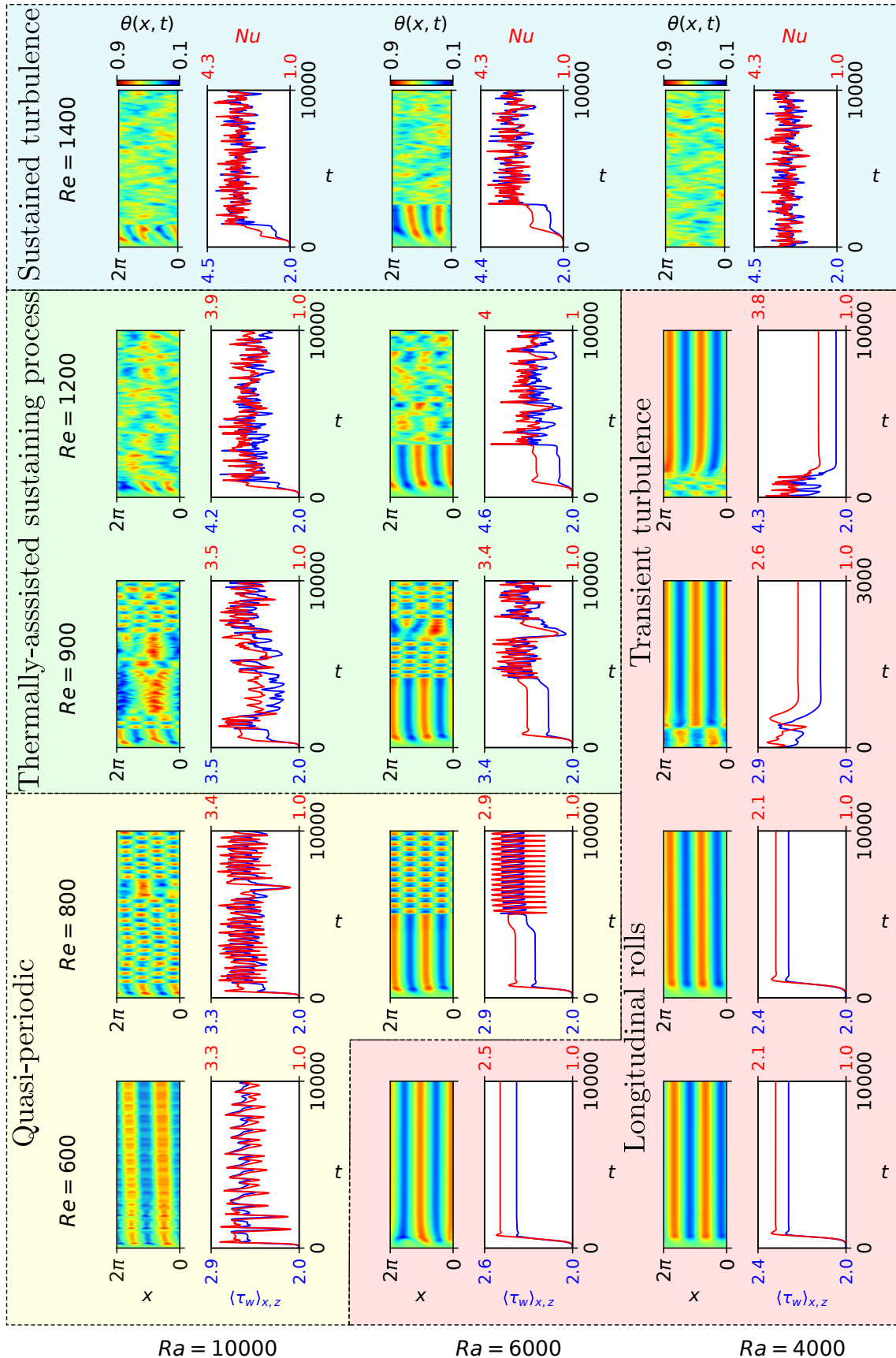


Figure 3.16: The temperature space-time plots and time history of (τ_w, Nu) , for $Ra \in [5000, 10000]$, $Re \in [600, 1400]$ within $\Gamma = \pi/2$. Unstable longitudinal rolls lead to the onset of (1) periodic orbits (yellow), (2) the *thermally-assisted sustaining process* (green), and (3) sustained turbulence (blue), occurring beyond an $Ra - Re$ boundary, below which longitudinal rolls remain stable (red).

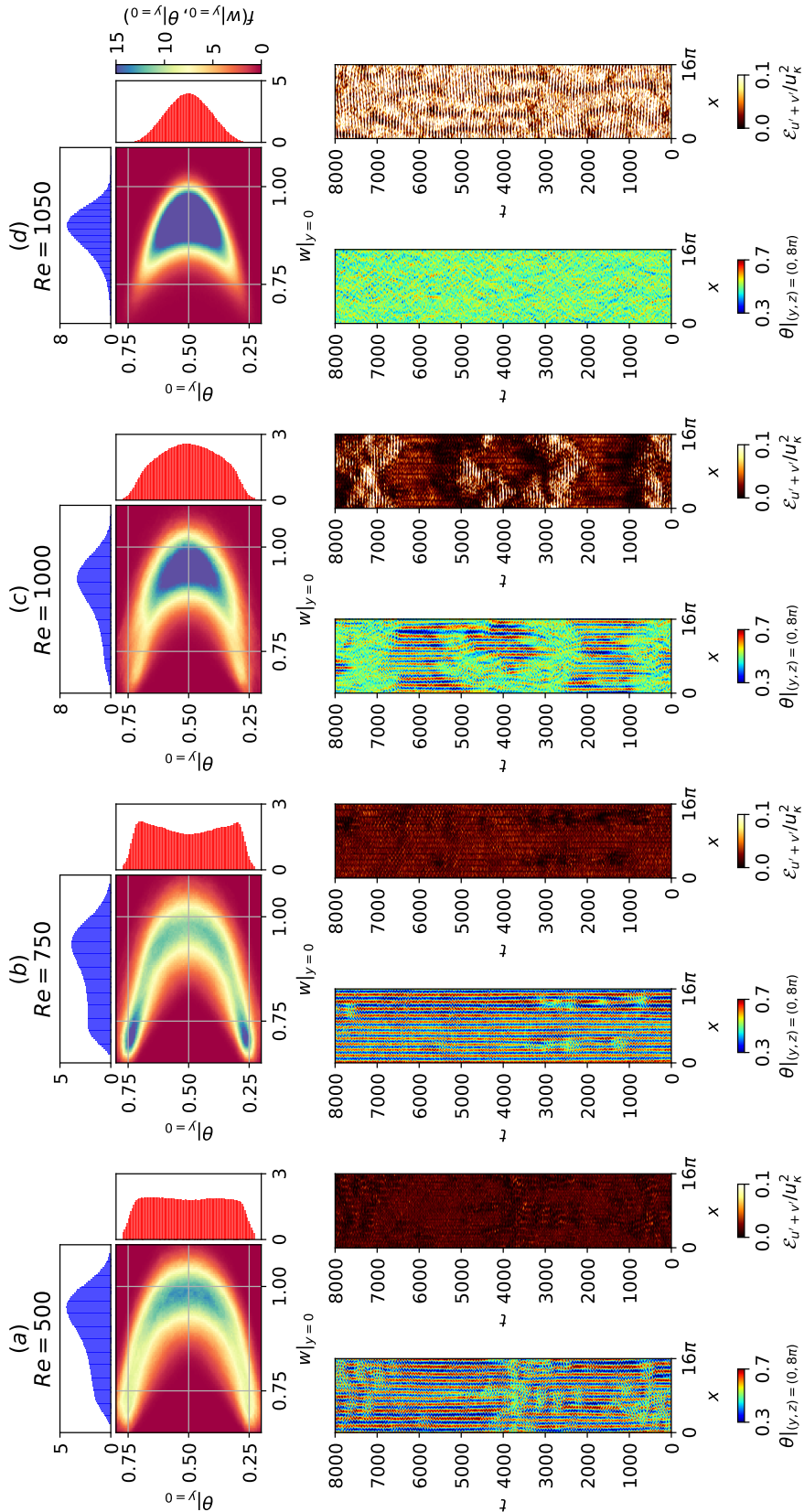


Figure 3.17: The midplane temperature space-time plot, and near-wall wall-normal and spanwise perturbation kinetic energy by normalised by thermal velocity scale, u_κ , and the probability density functions based on planar-averaged centerline velocity and the midplane temperature for $Ra = 10000$ at (a) $Re = 500$, (b) $Re = 750$, (c) $Re = 1000$ and (d) $Re = 1050$.

turbulence, as can be seen from the dark, bright and very bright regions in the near-wall wall-normal and spanwise perturbation velocities in figure 3.17(c). Starting at $t = 2000$, the longitudinal rolls that appear as elongated red/blue contour strips in figure 3.17(c) erupt into turbulence at $t = 2500$, appearing as very bright spots in the space-time plot of near-wall perturbation kinetic energy $\mathcal{E}_{u'+v'}$ of figure 3.17(c). Turbulence is transient, decaying towards the laminar state at $t = 3000$, as indicated by the dark patches. By $t = 4000$, longitudinal rolls are regenerated, appearing as red/blue elongated contour strips in the space-time midplane temperature plot, $\theta|_{(y,z)=(0,8\pi)}$ of figure 3.17(c). This process resembles *TASP* in a confined domain (figure 3.15(c)), suggesting that a similar process may be present in the large domain.

As Re approaches $Re = 1050$, turbulence appears more uniformly in space and time, as seen in figure 3.17(d). The increase in turbulent events is reflected by the PDFs, where a ‘D’-shaped PDF absent in $Re = 750$, gradually increases in intensity from $Re = 1000$ to $Re = 1050$. The lack of prolonged laminar regions, previously identified for $Ra = 0$ (figure 3.5, highlights the role of longitudinal rolls in providing an intermediate pathway from laminar to turbulent state, identified in a small domain (figure 3.14(d)).

3.5 Summary

We conclude by summarising the key findings of the transitional RBP flow in figure 3.1, where we have identified five distinct regimes and their rough transition boundaries. At low Re , the flow structures are primarily organised by buoyancy-driven convection rolls, consistent with RBC studies, including features such as the bistability between ISRs and SDC and the secondary oscillatory instability. We have shown that SDC disappears between $0.1 < Re < 1$, and the critical Re at which this occurs warrants further investigation. At intermediate Re , we identify a new regime known as intermittent rolls, marked by the breakdown and regeneration of longitudinal rolls. As Re approaches the onset of shear-driven turbulence, we observe the co-existence of longitudinal rolls with turbulent-laminar bands. This highlights the importance of longitudinal rolls in spatially extended RBP flows. Due to the enforced periodic boundary condition in our simulations, the longitudinal rolls are continuously excited, rather than convected out as in the case of impulse disturbances (Carrière & Monkewitz, 1999; Pabiou et al., 2005). In finite length experiments, careful control of system noise will likely facilitate the occurrence of this intermittent regime.

By considering a confined domain, we showed that the linearly unstable longitudinal rolls could provide a transition mechanism towards turbulence, referred to as the *thermally-assisted sustaining process* (*TASP*). Finally, we examined how *TASP* mechanism evolves as Ra and Re are varied, and discuss its implications for spatially extended domains. Further work may include a bifurcation analysis study of the *TASP* within confined domains and minimal band unit, establishing dynamical connections between invariant solutions where large spatial intermittency structures are expected to be important in the transitional regime (Tuckerman et al., 2020).

Chapter 4

The state space structure of Spiral Defect Chaos

The co-existence of ideal straight rolls (ISRs) and spiral-defect chaos (SDC) as bistable states in Rayleigh-Bénard convection above the onset of the linear instability is well established in extended spatial domains ($\Gamma \geq 40$ where Γ is the aspect ratio of the domain). However, multiple stable states have also been found independently, raising questions about the precise understanding of this observed bistability in extended domains. In this study, we isolate the localised structures of SDC by gradually reducing the spatial domain. By minimising the domain systematically to $\Gamma = 2\pi$, SDC appears transiently and eventually stabilises into new stable states referred to as elementary states. These elementary states are visibly and statistically similar to the spatially local patterns of SDC, indicative of invariant solutions underpinning the pattern formation in SDC.

To understand the state space structure further, we have examined the edge between ISRs and the elementary states, revealing multiple edge states, and conducted a series of numerical simulations along the unstable manifolds of unstable ISRs. The unstable ISRs near the Busse balloon are connected to stable ISRs and the base state through networks of heteroclinic orbits, forming a basin of attraction for each stable ISR. In contrast, the unstable ISRs further from the Busse balloon contain some unstable manifolds, along which the solution trajectory leads to SDC, suggesting that these unstable ISRs sit on the boundary between stable ISRs and SDC. Finally, we propose a state-space structure around the basic heat conduction state, stable/unstable ISRs, elementary states and transient SDC.

4.1 Objectives

The bistability between SDC and ISR is well established, but this also opens a question of how it is connected with the previous findings of multiple stable states (see §1.3). It is worth noting that a possible parameter in exploring this connection appears to be the domain size. Bistability has been reported in domains much larger ($\Gamma = 50$) than the multiple states found in small-to-moderate domains ($\Gamma \leq 10$) (Cakmur et al., 1997a). Furthermore, giant rotating spirals have been found in domains comparable to the horizontal length scale of SDC (Plapp & Bodenschatz, 1996; Plapp et al., 1998). Under this premise, the scope of this study is to explore how SDC, ISRs and multiple states are

organised within a state space, where stable/unstable equilibria and their manifolds (or linear stability) could provide useful physical insights into the state transition dynamics.

Motivated by the observation that SDC consists of several localised structures that resemble multiple states (i.e. travelling waves, spirals, asymmetric states), we first seek to isolate these states by minimising the domain systematically. Confined within the minimal domain, SDC is found to appear only transiently and does not sustain for a long time. The transient SDC state eventually stabilises into a large number of stable multiple states, which will be referred to as the ‘elementary’ states of SDC, and they are subsequently found within the minimal domain. As we shall see later, these elementary states remarkably resemble local structures of SDC observed in wide computational domains, indicating that they possibly underpin the formation of SDC. Next, the state-space boundaries between SDC and ISRs are explored by employing the edge-tracking technique (Schneider et al., 2007; Skufca et al., 2006), unveiling the existence of multiple edge states sitting on the boundaries. Finally, to understand the role of the unstable ISRs outside the Busse balloon, we perform a series of numerical experiments, in which a small perturbation is added along the unstable manifolds of several (unstable) ISRs outside of the Busse balloon. We shall see that some of their unstable manifolds are connected to stable ISRs within the Busse balloon, while the others are linked to transient SDC, which is subsequently stabilised into an elementary state. This suggests that some of the unstable ISRs act as signposts for the state-space boundary between stable ISRs and SDC (and/or elementary states).

The main contributions of the present chapter can be briefly summarised as follows,

1. Discovery of a number of stable invariant solutions which underpin the localised structures of SDC by minimising the computational domain for SDC (section 4.3);
2. Computation of some of multiple ‘edge states’ sitting on the separatrix between SDC and ISRs (section 4.4);
3. Several heteroclinic orbits connecting unstable ISRs and stable ISRs near the boundaries of the Busse balloon (section 4.5.1);
4. The role of unstable ISRs far from the Busse balloon acting as a signpost between ISRs and SDC (section 4.5.2).

4.2 Problem formulation

4.2.1 Rayleigh-Benard convection (RBC)

The motion of fluid flow in an RBC system (see §1.1), is governed by the non-dimensionalised Navier-Stokes equations with Boussinesq approximation,

$$\frac{\partial \mathbf{u}}{\partial t} + (\mathbf{u} \cdot \nabla) \mathbf{u} = -\nabla p + Pr \nabla^2 \mathbf{u} + Ra Pr \theta \mathbf{j}, \quad (4.1a)$$

$$\frac{\partial \theta}{\partial t} + (\mathbf{u} \cdot \nabla) \theta = \nabla^2 \theta, \quad (4.1b)$$

$$\nabla \cdot \mathbf{u} = 0, \quad (4.1c)$$

with the following boundary conditions at the wall,

$$\mathbf{u}|_{y=0,1} = 0, \quad \theta|_{y=0} = 1, \quad \theta|_{y=1} = 0, \quad (4.2a)$$

and the periodic boundary condition in the horizontal direction. Here, t denotes the time scaled by the vertical thermal diffusion time, d^2/κ , and $\mathbf{x}(= (x, y, z))$ is the spatial coordinates non-dimensionalised by d , where x and z are two orthogonal horizontal directions and y is the vertical direction. $\mathbf{u}(= (u, v, w))$ is the velocity vector scaled with κ/d , p the pressure scaled with $\rho\kappa^2/d^2$, $\theta(\equiv (T - T_U)/\Delta T)$ the non-dimensional temperature with T being the absolute temperature, and \mathbf{j} denotes the unit vector in y -direction. The Rayleigh number and the Prandtl numbers are defined as in §1.1: $Ra = \alpha gd^3\Delta T/\nu\kappa$, Prandtl number $Pr = \nu/\kappa$. $Pr = 1$ is set. We note that the aspect ratio is redefined as $\Gamma = L/d$ in this section.

4.2.2 Numerical method

The governing equations are solved numerically using Nektar++, an open-source spectral/ hp -element method framework (Cantwell et al., 2015; Moxey et al., 2020). An initial computational mesh, composed of quadrilateral elements, in the x - y plane is generated using Gmsh (Geuzaine & Remacle, 2009) and then refined by Nekmesh, the mesh generator available in Nektar++. Several computational domains of different sizes are prepared: $(L_x, L_y, L_z) = (16\pi, 1, 16\pi), (8\pi, 1, 8\pi), (4\pi, 1, 4\pi), (2\pi, 1, 2\pi)$. The spatial domain is discretised using a quasi-3D approach with spectral/ hp elements in x - y domain and Fourier expansions in z -direction. The discretised equations are subsequently solved using a velocity-correction method based on a second-order implicit-explicit temporal scheme (see §2.4.1). Since different computational domain sizes were considered, the spatial distribution of spectral/ hp elements in the x - y plane and Fourier expansions along z was kept constant. A spatial resolution of $(\Delta x, \Delta y|_{y=0,d}, \Delta y|_{y=d/2}, \Delta z) = (0.1\pi, 0.0549, 0.367, 0.25\pi)$ with polynomial order $P = 4$, and temporal resolution of $\Delta t = 0.0125$ was sufficient to establish numerical independence – for example, the Nusselt number, $Nu(= - \int_{x,z} \frac{\partial \theta}{\partial y}|_{y=0} dx dz)$, varies less than 10^{-5} when P was increased to $P = 5$.

4.2.3 Linear stability analysis of ISRs

As discussed in §4.1, we will perform a set of numerical experiments, in which a small perturbation about several unstable ISRs is added along their unstable manifolds. To obtain the direction of the unstable manifolds (i.e. linear instability eigenfunctions), we consider a small perturbation about the ISR (base) state:

$$\mathbf{u}(\mathbf{x}, t) = \mathbf{u}_{ISR,q}(\mathbf{x}) + \mathbf{u}'(\mathbf{x}, t), \quad (4.3a)$$

$$\theta(\mathbf{x}, t) = \theta_{ISR,q}(\mathbf{x}) + \theta'(\mathbf{x}, t), \quad (4.3b)$$

$$p(\mathbf{x}, t) = p_{ISR,q}(\mathbf{x}) + p'(\mathbf{x}, t), \quad (4.3c)$$

where $\mathbf{s} = [\mathbf{u}, \theta, p]^T$, $\mathbf{s}_{ISR,q} = [\mathbf{u}_{ISR,q}, \theta_{ISR,q}, p_{ISR,q}]^T$ and $\mathbf{s}' = [\mathbf{u}', \theta', p']^T$ refers to solution vector, the ISR (base) state of a given wavenumber, q , and the perturbation respectively. The theoretical background of this section is discussed earlier in §1.2, and its numerical technique is presented in §2.5.1. Substitution of (4.3) into (4.1) leads to the following linearised equations:

$$\frac{\partial \mathbf{s}'}{\partial t} = \mathcal{A}(\mathbf{s}_{ISR,q}; Ra, Pr)\mathbf{s}', \quad (4.4a)$$

where

$$\mathcal{A}(\mathbf{s}_{ISR,q}; Ra, Pr) = \begin{pmatrix} -(\mathbf{U} \cdot \nabla) - (\nabla \mathbf{U} \cdot) + Pr\nabla^2 & RaPr\hat{\mathbf{j}} & -\nabla \\ -(\nabla \Theta \cdot) & -(\mathbf{U} \cdot \nabla) + \nabla^2 & 0 \\ \nabla \cdot & 0 & 0 \end{pmatrix}. \quad (4.4b)$$

For the sake of simplicity here, we will only consider the ISRs invariant along z -direction. Since the ISRs are also assumed periodic in x -direction, the following form of normal-mode solution can be considered:

$$\mathbf{s}'(\mathbf{x}, t) = \check{\mathbf{s}}(x, y)e^{i(\alpha x + \beta z) + \lambda t} + \text{c.c}, \quad (4.5)$$

where λ , α and β are the complex frequency, the streamwise wavenumber (or the Floquet exponent), and the spanwise wavenumber, respectively. Using the periodic nature of $\check{\mathbf{s}}(x, y)$ in x -direction, (4.5) can also be written as

$$\mathbf{s}'(\mathbf{x}, t) = \left[\sum_{n=-\infty}^{\infty} \check{\mathbf{s}}_n(y) e^{i \frac{2\pi}{L_x} (n+\epsilon)x} \right] e^{i\beta z + \lambda t} + \text{c.c}, \quad (4.6)$$

where $\epsilon (= \alpha L_x / (2\pi))$ is the Floquet detuning parameter with $0 \leq \epsilon \leq 1/2$. Since the stability analysis here will be limited to the identification of unstable manifolds of ISRs in a fixed computational domain, $\epsilon = 0$ (fundamental mode) is considered only - note that the modes associated with $\epsilon \neq 0$ are only observed in the x domains greater than L_x .

Substituting (4.6) into (4.4) leads to a discretised eigenvalue problem in terms of the eigenvalue λ , where the wavenumber in the z -direction must be restricted to be $\beta = 2\pi m / L_z$, and m is a positive integer, for the given computational domain. The resulting eigenvalue problems are solved using a time-stepper-based iterative Arnoldi algorithm (see 2.5.1). The eigenvalues of primary instabilities of RBC computed in Nektar++ are also verified against those obtained with a Chebyshev-collocation method in Appendix A.4.

4.3 Transient SDC and elementary states in minimal domain

In this section, we seek to capture localised structures of SDC using a minimal domain by systematically reducing the domain by half in the homogeneous (x - z) directions. A random noise, characterised by

Gaussian white noise (0 mean and 1 variance), generated with a total energy of

$$\delta = \frac{1}{\bar{V}} \int_{\Omega} \tilde{\mathbf{u}}(\mathbf{x})^T \tilde{\mathbf{u}}(\mathbf{x}) + RaPr\tilde{\theta}(\mathbf{x})^2 d\Omega \approx O(10^{-3}), \quad (4.7)$$

where $\tilde{\mathbf{u}}(\mathbf{x})$ and $\tilde{\theta}(\mathbf{x})$ refer to the perturbation velocity and temperature about the base state $\mathbf{U}(\mathbf{x}) = \mathbf{0}$ and $\Theta(y) = 1 - y$, is introduced as an initial condition to the system. Here, we note that the first term of the integrand in (4.7) is the kinetic energy of the perturbation velocity and the second one measures the potential energy from the perturbation temperature.

The system is time integrated for 300 units of vertical thermal diffusion time $t (= d^2/\kappa)$. The resulting mid-plane temperature snapshots $\theta(x, z)|_{y=d/2}$ at $t = 300$ exhibit features of spiral defect chaos, as shown in figure 4.1. When the domain size is large, for instance, $\Gamma = 16\pi$ shown in figure 4.1(a), features of SDC consist of many repeating localised spirals, defects and dislocations. Reducing the domain in half to $\Gamma = 8\pi$, shown in figure 4.1(b), led to a spatially less extensive chaotic state, revealing a single spiral, with some defects and dislocations. Surprisingly, a further reduction of the domain in half, $\Gamma = 4\pi$, does not lead to sustained SDC, but rather, a transient SDC state before settling into stable ‘elementary’ states. These elementary states are identified as *pacman* (PM), *spiral-defect* (SD), *hooked* (HK), and *peanut* (PN) states in figure 4.1 (c-f), which resemble the localised features of SDC (see the coloured bounding boxes in figures 4.1(a,b)). These states represent stable invariant solutions of (4.1). Specifically, PM state represents a steady equilibrium, SD and HK states are characterised by relative periodic orbits ¹, and the PN state is a periodic orbit (Gibson et al., 2008).

An example of a transient SDC state is shown in figure 4.2(a), where spirals, a typical feature of SDC (Morris et al., 1993), form spontaneously with a chaotic transient (figures 4.2(c-e)), before stabilising into an SD state with a period of $T \approx 75$ (figures 4.2(f,g)). In addition to the elementary states presented in figures 4.1(c-f), we have identified ten additional elementary states, each independently preceded by a transient SDC state, and fourteen stable ISRs of varying wavenumbers (see Appendix A.5). We intentionally restrict the spatial domain to identify nontrivial invariant solutions apart from ISRs. This method follows the well-established approach of the minimal flow unit of plane Couette flow (Jiménez & Moin, 1991), where nontrivial solutions within small domains exhibit coherent ‘streak-roll’ structures that reproduce the statistics of turbulent (Kawahara & Kida, 2001). In total, we have identified 28 states with $\Gamma = 4\pi$. Minimising the domain further to $\Gamma = 2\pi$ only led to stable ISRs at least for the random initial conditions we have examined in this study. We therefore consider $\Gamma = 4\pi$ as the minimal domain, in which both transient SDC and elementary states exist. It is worth mentioning that solutions to multiple states were obtained in smaller domains with $\Gamma = 4$, but in a cylindrical domain (Borońska & Tuckerman, 2010a; Ma et al., 2006).

To show whether SDC and elementary states are related, we compare their state space trajectories and the averaged wall-normal temperature profiles. Since the full state space is very high-dimensional, with its dimensionality determined by the number of degrees of freedom dictated by the spatial discretisation scheme, it is therefore very challenging, if not impossible, to visualise the full state space in its entirety. Here, we choose the volume ($\bar{V} = L_x L_z L_y$) normalised L2-norms of velocity

¹Relative periodic orbit is a type of periodic orbit whereby the solution trajectory after a period T returns to its initial state that is continuously translated in the horizontal directions.

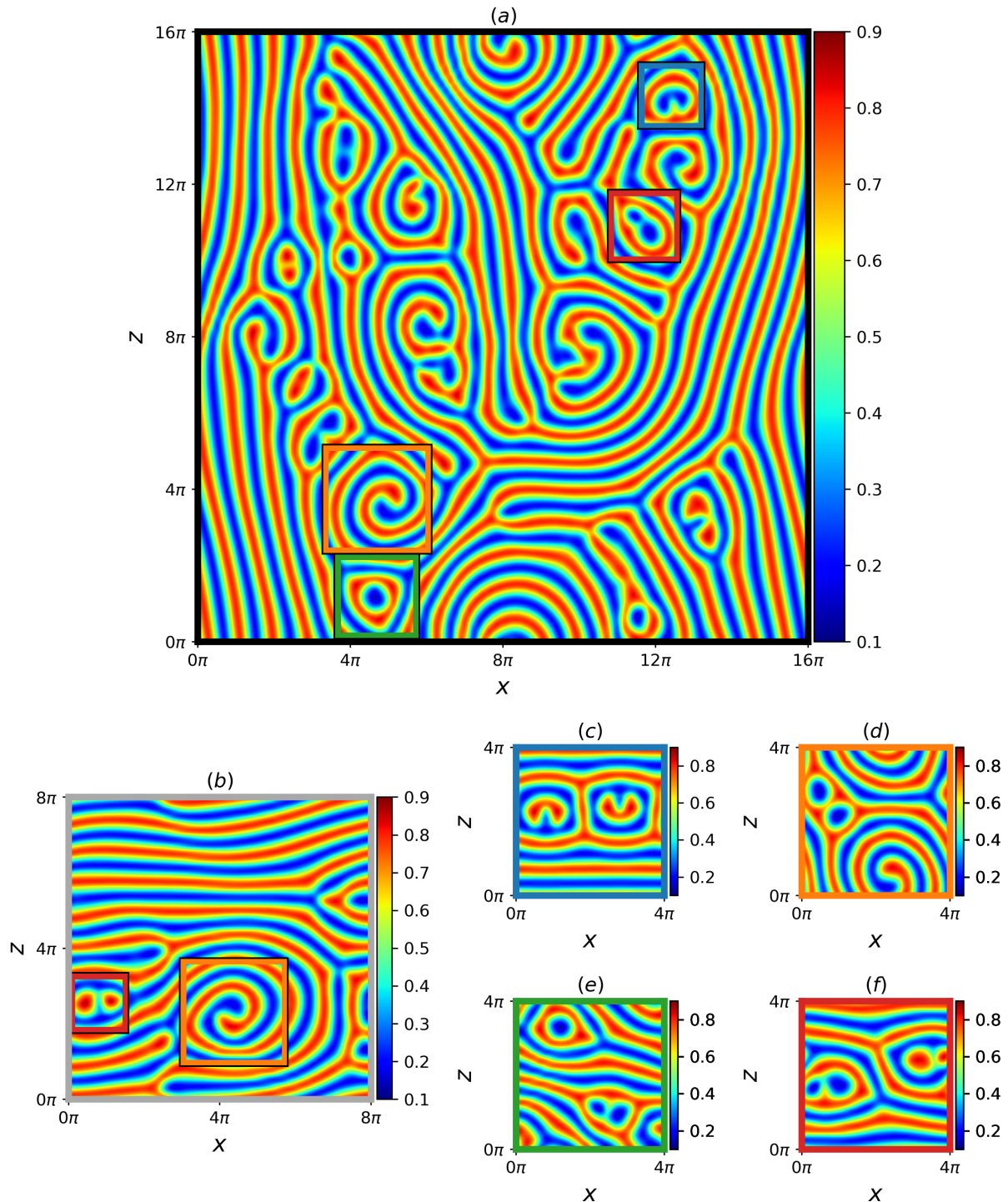


Figure 4.1: Midplane temperature snapshots, $\theta(x, z)|_{y=d/2}$, of spiral defect chaos (SDC) for a domain aspect ratio of (a) $\Gamma = 16\pi$ and (b) 8π . Elementary states of SDC captured when $\Gamma = 4\pi$: (c) steady *pacman* (PM), (d) relative periodic orbit *spiral-defect* (SD), (e) relative periodic orbit *hooked* (HK), and (f) periodic *peanut* (PN) elementary state. Note that the localised structures indicated by bounding boxes in (a,b) resemble structures in (c-f). Snapshots are captured at 300 diffusive time units, t .

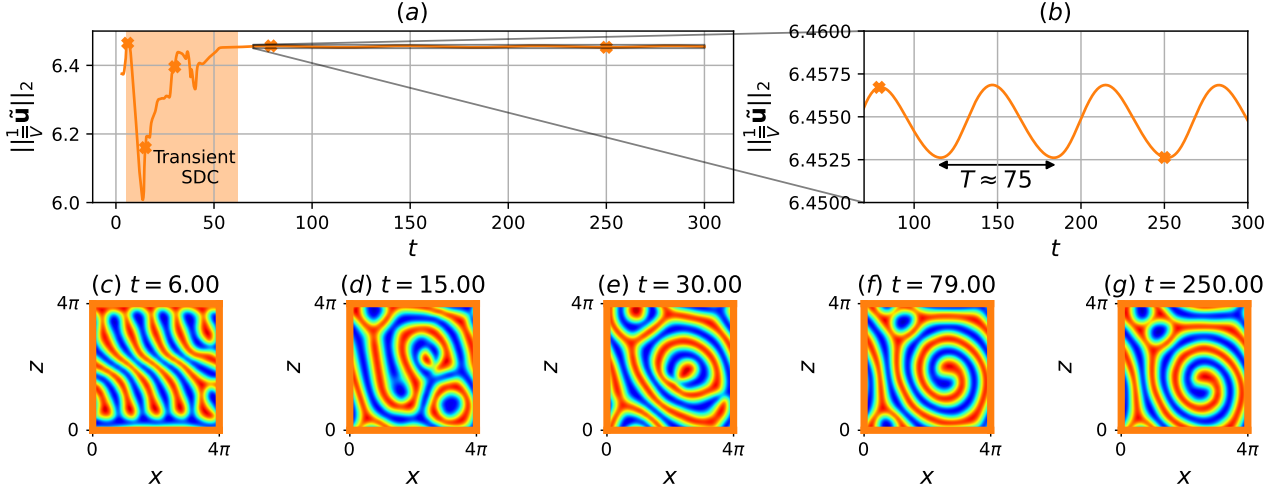


Figure 4.2: (a,b) Time history of the volume ($\bar{V} = L_x L_y L_z$) normalised L2-norm of velocity perturbations from a random initial condition with $\delta = 0.001$ and (c-g) Mid-plane temperature snapshots at $t = 6, 15, 30, 79, 250$. Here, transient chaotic SDC lasts up to $t \approx 70$, before stabilising into an SD state, emerging as a relative periodic orbit with the time period $T \approx 75$ propagating diagonally in the negative x - and z -directions.

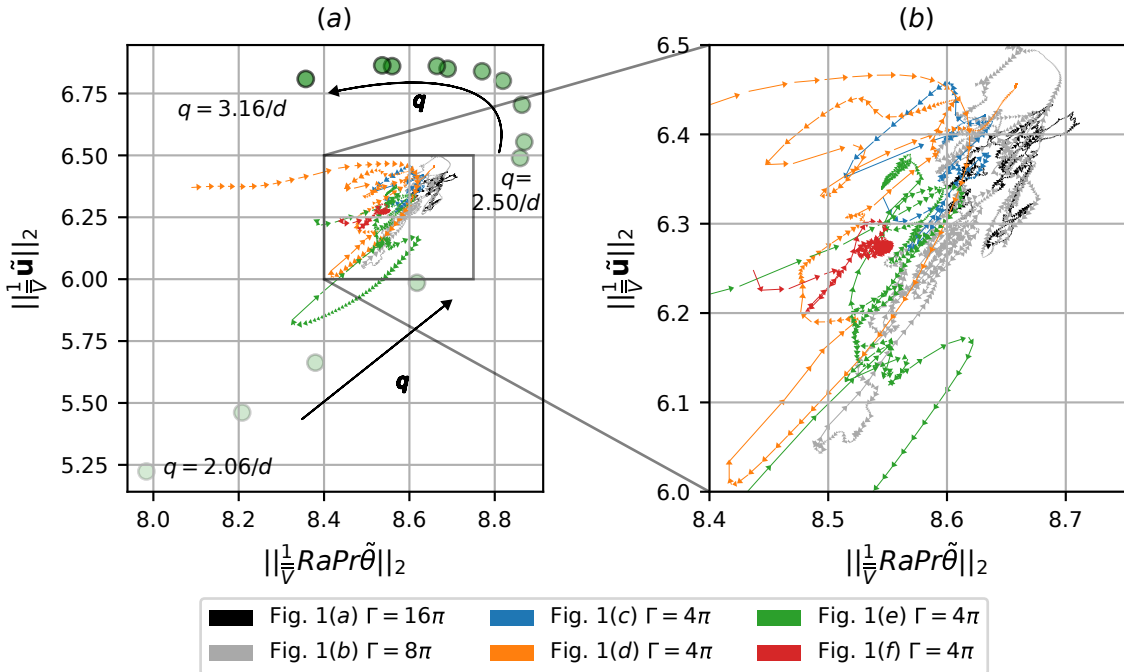


Figure 4.3: (a) State-space portrait in the plane of $\|\frac{1}{\bar{V}}\tilde{\mathbf{u}}\|_2$ and $\|\frac{1}{\bar{V}}RaPr\tilde{\theta}\|_2$ for SDC from $\Gamma = 16\pi, 8\pi$ (figures 4.1(a,b)), four transient SDC state proceeding to stable elementary states (figures 4.1(c-f)), A.6, and fourteen stable stationary ISRs of wavenumbers $2.0 \leq qd \leq 3.35$. Here, the magnitude of q is denoted by the opacity of the filled symbol (●), increasing from the bottom left and turning toward the top left shown as arrows; (b) Zoomed-in view of (a). The legend refers to the figures for respective trajectories preceding snapshots in figure 4.1.

($\|\frac{1}{V}\tilde{\mathbf{u}}\|_2$) and temperature ($\|\frac{1}{V}RaPr\tilde{\theta}\|_2$) perturbations as state space observables, describing the deviation from the conduction state and providing a consistent depiction across different domain sizes, as we shall see later. It is also worth highlighting that the perturbation kinetic/thermal energies are integral quantities and therefore may not distinguish between states that are spatially symmetric or are translations of one another (i.e., ISRs of the same wavenumber that differ in phase). Other integral quantities, such as the Nusselt number, do not provide a clear separation between SDC and ISR. We emphasise that our choice of projection does not capture the full dimensionality of the system, and our intent in using this projection is to provide a qualitative ‘slice’ of its high-dimensional dynamics. As in other studies of turbulent shear flow (see references in §1.2.2), low-dimensional projections are commonly used to visualise an otherwise high-dimensional state space. We also note that different choices of projection will naturally change the figures.

Figure 4.3 presents the two chaotic trajectories of SDC from $\Gamma = 16\pi, 8\pi$, four of fourteen transient SDC trajectories obtained and fourteen stable fixed-points of ISRs from $\Gamma = 4\pi$ on a two-dimensional state portrait based on the volume normalised L2-norms of velocity and temperature perturbations. The trajectories begin from $t = 3$, as those for $t < 3$ contain artificial transients and are omitted for clarity. The state space trajectories of SDC ($\Gamma = 16\pi, 8\pi$) and the transient SDC states for $\Gamma = 4\pi$ appear approximately between $(8.4, 6) \lesssim (\|\frac{1}{V}\tilde{\mathbf{u}}\|_2, \|\frac{1}{V}RaPr\tilde{\theta}\|_2) \lesssim (8.7, 6.5)$ shown in figure 4.3(b). This suggests that they are presumably the same type of SDC emerging in different domains. The closely packed chaotic trajectories are in contrast to the ISRs populating sparsely.

The transient SDC trajectories eventually stabilise into fourteen elementary states in figure 4.4, where the transient SDC trajectories from figure 4.3 are now omitted. Obscured by the transient SDC trajectories initially, the elementary states in figure 4.4 emerge as seven steady states (■), two travelling waves (×), one periodic orbit (dash-dotted line) and four relative periodic orbits (solid line). The SDC trajectories for $\Gamma = 16\pi, 8\pi, 4\pi$ appear near the fourteen elementary states, approximately bounded between $(8.5, 6) \lesssim (\|\frac{1}{V}\tilde{\mathbf{u}}\|_2, \|\frac{1}{V}RaPr\tilde{\theta}\|_2) \lesssim (8.7, 6.5)$ (figure 4.4), in contrast to the larger region occupied by ISRs between $(8, 5.25) \lesssim (\|\frac{1}{V}\tilde{\mathbf{u}}\|_2, \|\frac{1}{V}RaPr\tilde{\theta}\|_2) \lesssim (8.8, 7)$ (figure 4.3(a)). Notably, the state space trajectories of SDC and the elementary states are in close vicinity to the ISR of wavenumbers $q = 2.5/d$ (see figures 4.3), which corroborates with the averaged wavenumber of SDC, $q_{avg} \approx 2.5/d$ (Decker et al., 1994; Morris et al., 1993).

The comparison between the time-averaged mean temperature profile, mean-squared temperature fluctuations, and mean-squared velocity fluctuations of SDC (figures 4.1(a,b)) and elementary states (figures 4.1(c-f) and figure A.6) are presented in figure 4.5. In figure 4.5(c), we present the sum of mean-squared x - and z - velocity fluctuations due to horizontal isotropy. The mean temperature profiles of the elementary states closely match those of SDC (figure 4.5(a)). Notably, the mean-squared temperature and velocity fluctuations between SDC states (grey and black dashed curves) of figures 4.5(b-d) are similar. The mean-squared temperature and velocity fluctuations profiles of elementary states are comparable to those of SDC but are, in general, slightly larger in magnitude.

The spatial-temporal complexity of SDC reduces when the domain size is reduced from $\Gamma = 16\pi$ to $\Gamma = 8\pi$, i.e. less disordered spatial features. Reducing the domain from $\Gamma = 8\pi$ to $\Gamma = 4\pi$ led to transient SDC before stabilising into many elementary states. From the conventional view, especially

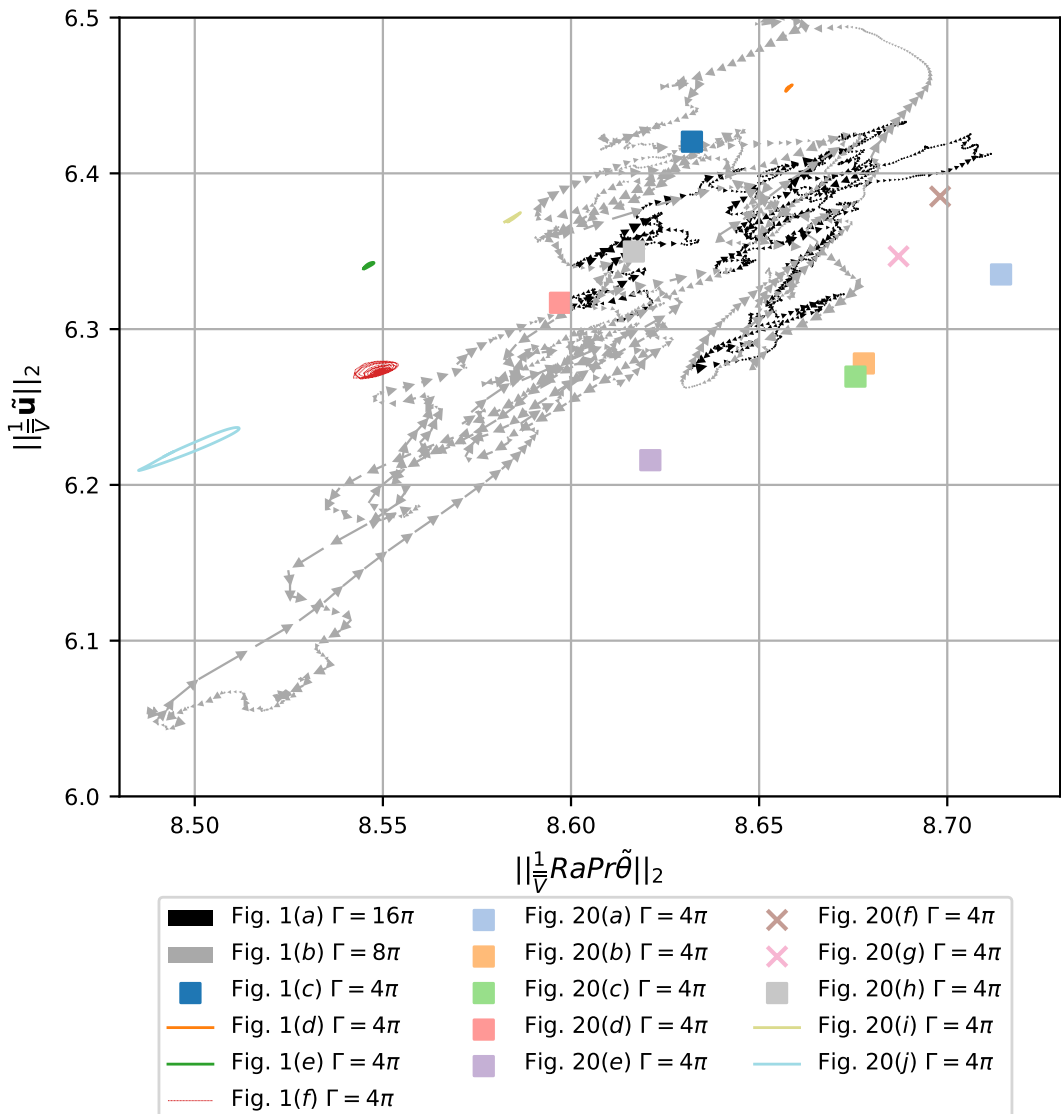


Figure 4.4: State-space portrait (from figure 3) highlighting the transient SDC states for $\Gamma = 4\pi$ proceeding toward stable elementary states (see figures 4.1(c-f), A.6): steady states (■), travelling waves (✗), periodic orbit (dash-dotted line) and relative periodic orbits (solid lines).

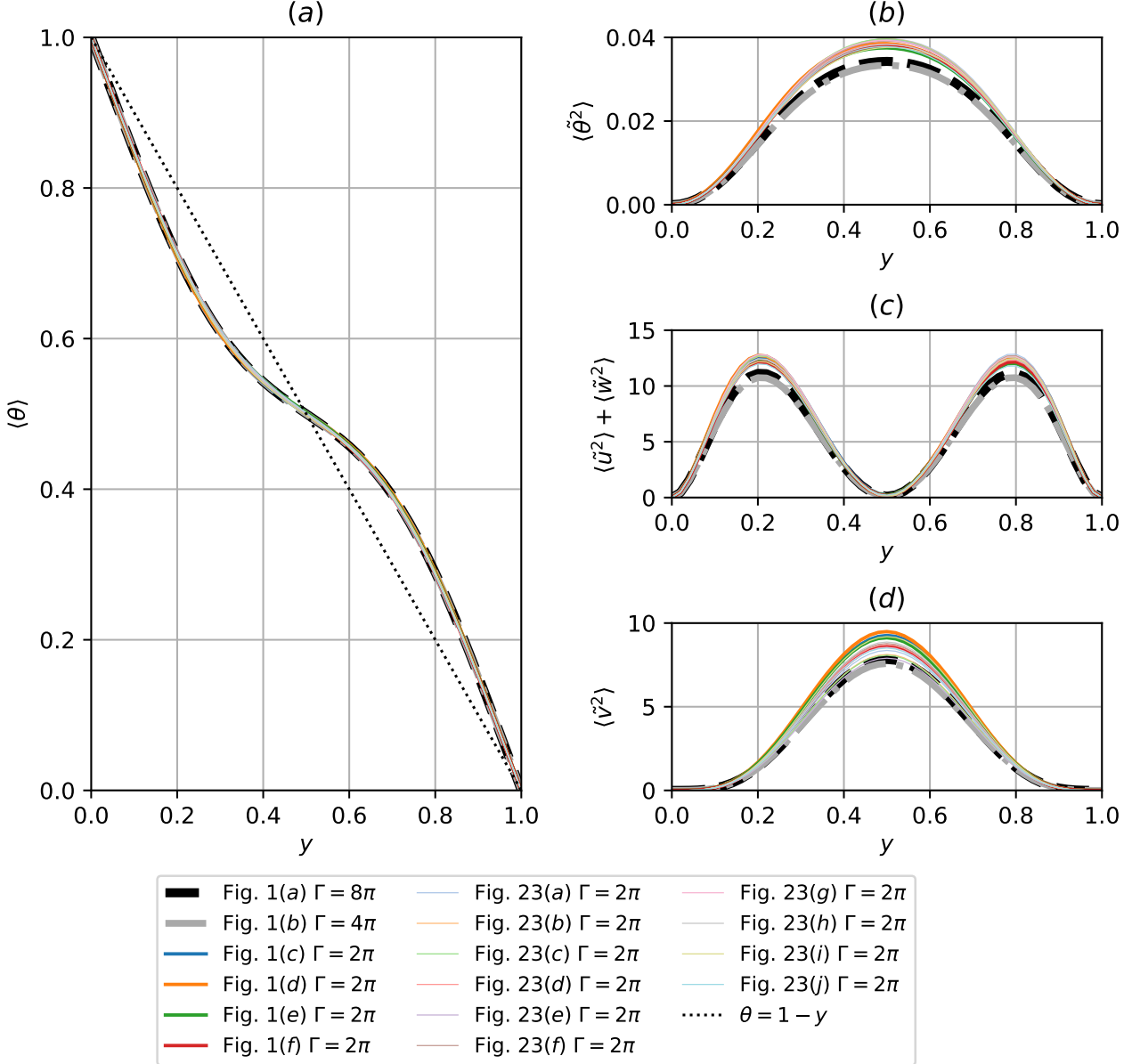


Figure 4.5: Profiles of (a) averaged temperature, (b) root-mean-squared temperature fluctuation, (c) sum of root-mean-squared x - z velocity fluctuations and (d) root-mean-squared wall-normal velocity fluctuations for the SDC and elementary states shown in figures 4.1(a-f) and in Appendix A.5. Note that $\langle \cdot \rangle = \frac{1}{T L_x L_z} \int_{t,x,z} dt dx dz$ refers to the time and plane averaged operator, where T was chosen to be sufficiently long to ensure temporal convergence.

made in the context of shear flow turbulence, this is unexpected as the chaotic state (i.e. turbulence) is commonly described as solution trajectories wandering around unstable invariant solutions (see §1.2.2). However, in this particular case observed in RBC, the chaotic state (i.e. SDC) stabilised into stable invariant solutions (elementary states) instead, in contrast to shear flow turbulence where invariant solutions are expected to be unstable. Despite this distinguished feature of the state space, each of the elementary states is still seen to emerge in a spatially localised manner of SDC in an extended domain (figure 4.1), and their spatially-averaged statistics are remarkably similar to those of SDC in extended domains (figure 4.5). Therefore, we consider the elementary states in the minimal domain to be the ‘building blocks’ structure of SDC.

4.4 Multiplicity of edge states

The stable nature of many ISRs and elementary states underpinning SDC implies the existence of state-space boundaries between them (i.e. edge). In this section, we perform the edge tracking between the stable manifolds of ISRs and elementary states to compute the attractors on the edge (i.e. edge states). For the edge tracking, we use the bisection method (see §2.5.2), with an initial condition given by

$$\mathbf{s}_0(\mathbf{x}, t = 0) = \chi \mathbf{s}_{ISR,q} + (1 - \chi) \mathbf{s}_{elementary}, \quad (4.8)$$

where $\mathbf{s}_0(= [\mathbf{u}_0, \theta_0, p_0]^T)$ refers to an initial condition consisting of a weighted sum, $\chi \in [0, 1]$, between a stable ISR state, $\mathbf{s}_{ISR,q}$ of a wavenumber q , and an elementary state, $\mathbf{s}_{elementary}$ where the subscript refers to its names in figures 4.1(c-f).

Given the large number of stable ISRs and elementary states, we shall focus on the computation of the edge states considering three of the stable ISRs and two of the elementary states. However, in principle, the edge tracking is technically possible with other stable ISRs and elementary states. As such, in general, multiple edge states are expected. The three ISRs are related to three different wavenumbers, denoted by $\mathbf{s}_{ISR,q=2.06/d}$, $\mathbf{s}_{ISR,q=2.24/d}$, $\mathbf{s}_{ISR,q=3.16/d}$ (figures A.7(b,d,j)) respectively, and the two elementary states are SD state, $\mathbf{s}_{spiral-defect}$ (figure 4.1(c)), and PM state, \mathbf{s}_{pacman} (figure 4.1(d)). Using this set of stable ISRs and elementary states, we aim to track the edge near $\mathbf{s}_{ISR,q}$ in the direction of $\mathbf{s}_{elementary}$ by bisecting the initial condition with χ in (4.8), whereby one of the two trajectories across the edge decays toward $\mathbf{s}_{ISR,q}$ and the other is attracted toward transient chaotic state (i.e. SDC), referred to as the ‘lower’ and ‘upper’ trajectories respectively. The bisection of the initial condition is carried out by monitoring the difference in two trajectories with Nu (i.e. ΔNu). When the two trajectories reach a certain time at which $\Delta Nu > 0.0007$, the bisection of the initial condition is repeated using the flow fields from the two different trajectories by replacing $\mathbf{s}_{ISR,q}$ and $\mathbf{s}_{elementary}$ in (4.8) with them. This process is repeated until the edge trajectory reaches an attractor (i.e. an edge state).

$s_{ISR,q}$	$s_{elementary}$	Edge state	State transitioned
$s_{ISR,q}=2.06/d$	$s_{spiral-defect}$	Jagged (Stationary)	Transient Chaos
$s_{ISR,q}=2.06/d$	s_{pacman}	Jagged (Stationary)	Transient Chaos
$s_{ISR,q}=2.24/d$	$s_{spiral-defect}$	Point-defect (Travelling wave)	$s_{bubble-defect}$
$s_{ISR,q}=2.24/d$	s_{pacman}	Forked (Relative Periodic Orbit)	Transient Chaos
$s_{ISR,q}=3.16/d$	$s_{spiral-defect}$	Skewed-varicose (Stationary)	Transient Chaos
$s_{ISR,q}=3.16/d$	s_{pacman}	Skewed-varicose (Stationary)	Transient Chaos

Table 4.1: A summary of the edge states computed. The first two columns denote the pair of initial conditions considered for edge tracking in Eq. (4.8). The names and classification of the edge states are described in the third column. The last column describes the state transitioned from $s_{ISR,q}$ for sufficiently large χ in Eq. (4.8).

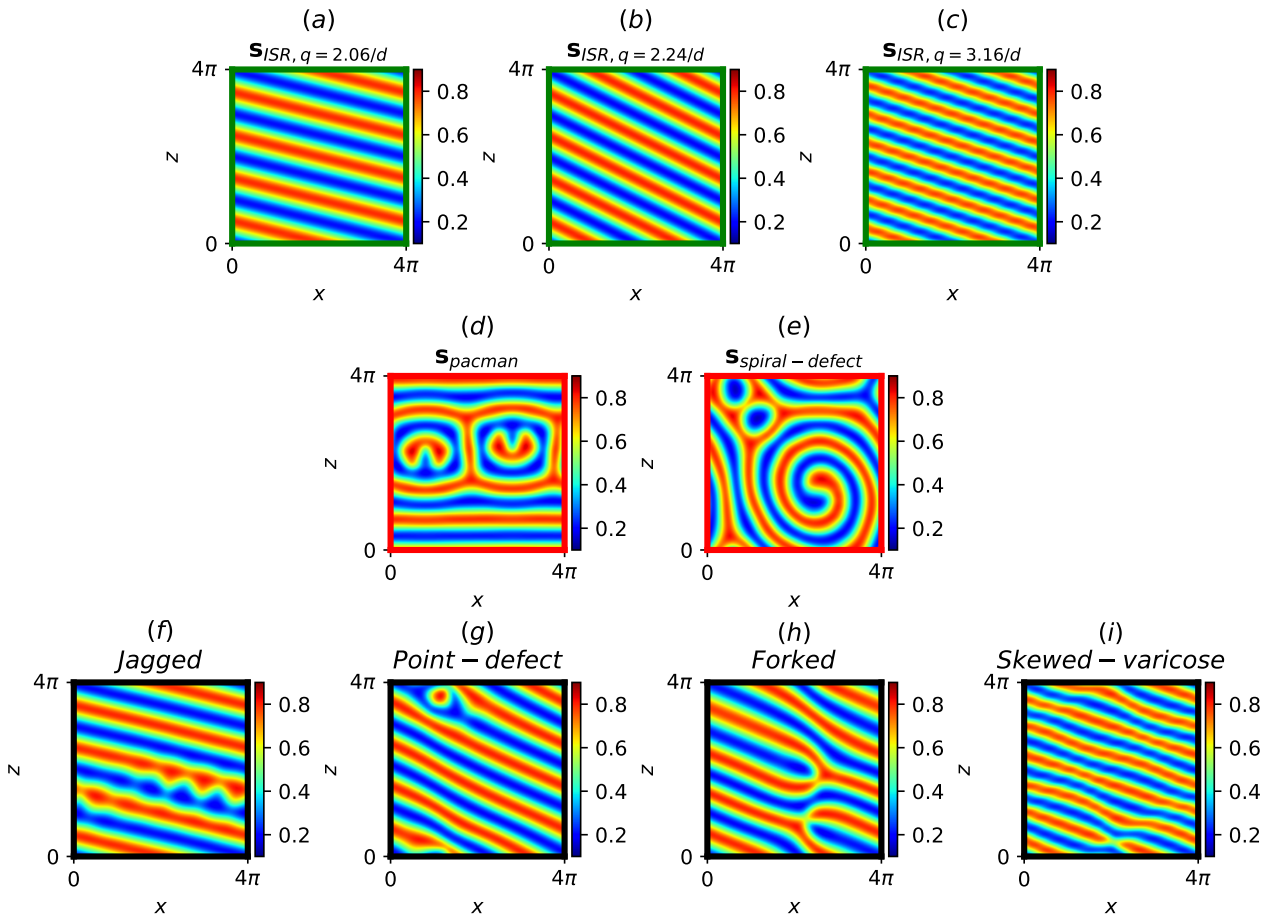


Figure 4.6: Mid-plane temperature fields of ISRs and elementary states used in Eq. (4.8), and the resulting edge states. Here, ISRs (green borders): (a) $s_{ISR,q}=2.06/d$, (b) $s_{ISR,q}=2.24/d$, (c) $s_{ISR,q}=3.16/d$; elementary states: (d) s_{pacman} , (e) $s_{spiral-defect}$; edge states (black borders): (f) *jagged*, (g) *point-defect*, (h) *forked* and (i) *skewed-varicose* edge state.

Table 4.1 summarises the edge states and their dynamical properties computed from six combinations of $s_{ISR,q}$ and $s_{elementary}$ states, and they are visualised with the mid-plane temperature field in figure 4.6. The convection patterns of edge states are often featured with mild spatial complexity compared to SDC and the elementary states. In particular, their patterns contain the underlying convection pattern of $s_{ISR,q}$ with spatially localised defects. We obtained four edge states: specifically, the *jagged* and *skewed-varicose* edge states are stationary, and the *point-defect* and *forked* edge states

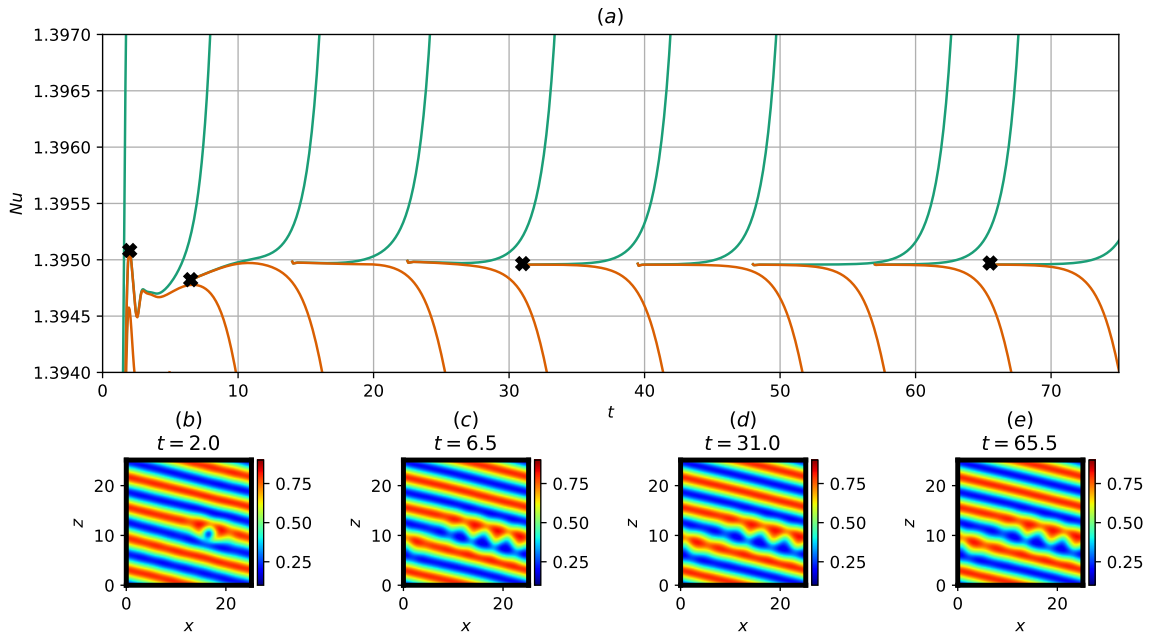


Figure 4.7: (a) Time history of Nu and (b-e) the corresponding mid-plane temperature field snapshots at $t = 2.0, 6.5, 31.0, 65.5$ along the edge trajectory obtained by bisecting $s_{ISR,q=2.06/d}$ and $s_{spiral-defect}$.

are travelling wave and a relative periodic orbit respectively. The *jagged*, *skewed-varicose* and *forked* edge states lie on the boundary, separating the basins of attraction of stable $s_{ISR,q}$ from transient SDC. In the case of the *point-defect* edge state, the solution trajectory is found to bypass the transient SDC state, directly settling into a stable elementary state characterised by bubble-like convection roll defects, $s_{bubble-defect}$. Since the *jagged*, *skewed-varicose*, *forked* edge states are similar in nature, acting as separatrices between $s_{ISR,q}$ states and transient SDC, we will focus our analysis on the *jagged* edge state only, alongside the *point-defect* edge state.

Using Nu as an observable, successive bisections between $s_{ISR,q=2.06/d}$ and $s_{spiral-defect}$ reveal the trajectory along the edge, as illustrated in figure 4.7. The trajectory along the edge spans from $t \approx 0 - 15$, and is initially characterised by a ‘speckled’ defect (figure 4.7(b)). The ‘speckled’ defect grows into a spatially localised jagged-like defect as the trajectory is attracted to the *jagged* stationary edge state from $t \approx 6.5$ onwards (figures 4.7(c-e)). We further examine the two trajectories in the opposite directions along the unstable manifold of the *jagged* edge state in figure 4.8, where the ‘upper’ trajectory evolves into a transient SDC and the ‘lower’ trajectory decays into the original stable $s_{ISR,q=2.06/d}$ state. Starting from the ‘upper’ trajectory (figure 4.8(a)), the spatially localised jagged defect grew in the direction normal to the roll orientation at $t = 80.5$ (figure 4.8(b)), contaminating the adjacent roll structure and propagating through the domain where transient SDC emerges from $t > 80.5$, lasting up to $t \approx 120$ (a snapshot of transient chaotic SDC regime at $t = 90.5$ is shown in figure 4.8(c)). The trajectory subsequently stabilises into a travelling-wave PM elementary state described by ‘pac-man’ like patterns, propagating along the $-x$ direction from $t = 125.5$ to $t = 170.5$ (figures 4.8(d,e)). This is reminiscent of a secondary cross-roll instabilities experienced by low-wavenumber ISRs (such as $s_{ISR,q=2.06/d}$ considered here), where a defect propagates in the direction perpendicular to the rolls (Bodenschatz et al., 2000). Along the ‘lower’ trajectory (figure 4.8(f)),

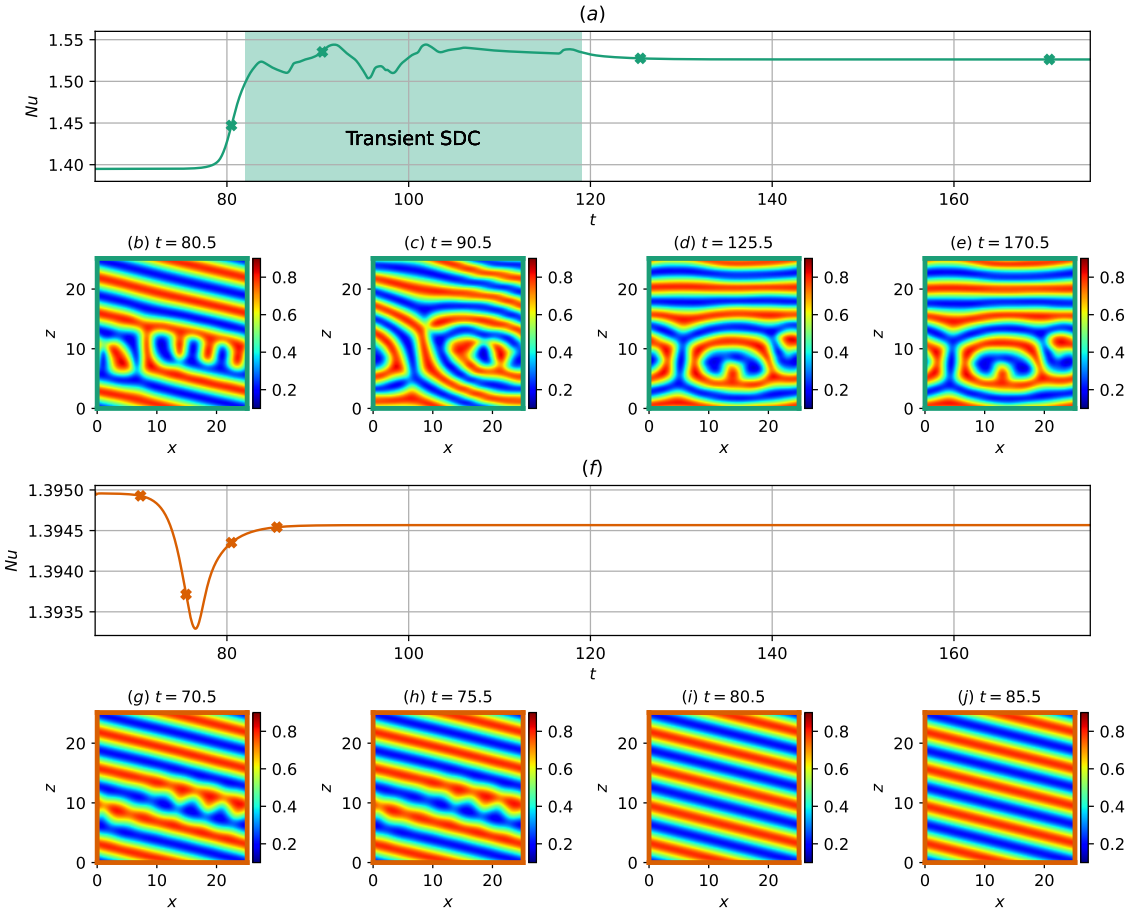


Figure 4.8: Time history of Nu along two opposite directions along the unstable manifold of the jagged edge state: (a) ‘upper’ trajectory leading to a transient SDC for $t \approx 85 – 120$ and subsequently to PM state for $t > 120$ and (f) ‘lower’ trajectory stabilising into $s_{ISR,q=2.06/d}$. Mid-plane temperature fields are visualised in (b–e) along the upper trajectory at $t = 80.5, 90.5, 125.5, 170.5$, and in (g–j) along the lower trajectory at $t = 70.5, 75.5, 80.5, 85.5$.

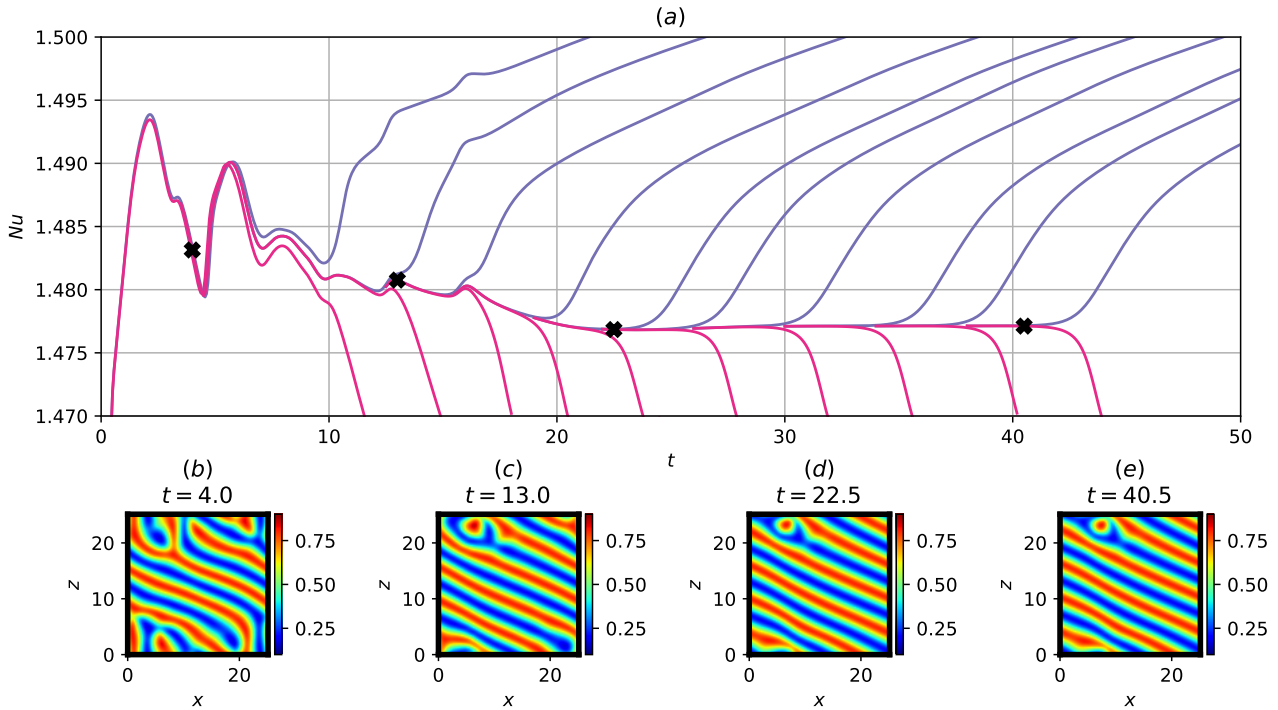


Figure 4.9: a) Time history of Nu and (b-e) the corresponding mid-plane temperature field snapshots at $t = 4, 13, 22.5, 40.5$ along the edge trajectory obtained by bisecting $s_{ISR,q=2.24}$ and $s_{spiral-defect}$.

the jagged defects diffuses from $t = 70.5$ to $t = 75.5$, decaying into the stable $s_{ISR,q=2.06/d}$ state at $t = 80.5$ (figures 4.8(g-j)).

Next, we analyse the edge trajectory obtained bisecting between $s_{spiral-defect}$ and $s_{ISR,q=2.24}$ in figure 4.9. The trajectory along the edge from $t = 4$ (figure 4.9(b)) is described by time-dependent convection structures. The edge trajectory began to be stabilised into the *point-defect* edge state from $t = 13$ onwards (figure 4.9(c)), propagating along x direction from $t = 22.5$ (figures 4.9(d,e)). It is characterised by the convection structure of the $s_{ISR,q=2.24}$ state with a pointed defect structure, hence referred to as the *point-defect* edge state.

The upper and lower trajectories through two opposite directions of the unstable manifold of the travelling wave *point-defect* edge state are subsequently examined in figure 4.10. Integrating along the upper trajectory (figure 4.10(a)), the spatially localised point-defect structure grew from $t = 43$ to $t = 83$ (figures 4.10(b-d)), saturating into a stationary elementary state at $t = 163$ (figure 4.10(e)) characterised by $s_{ISR,q=2.24}$ with a large bubble defect. Along the lower trajectory (figure 4.10(f)), the spatially localised point defect merged onto the adjacent convection roll from $t = 38$ to $t = 44.5$ (figures 4.10(g,h,i)), stabilising into the $s_{ISR,q=2.24/d}$ state at $t = 53$ (figure 4.10(j)). It is worth noting that, in this particular case, no chaotic transient in the form of SDC has been observed.

Finally, figure 4.11 depicts a state space portrait of stable ISRs, SDC and the edge/elementary states found here. As seen previously, SDC and elementary states are seen to be clustered around the region of $\|\frac{1}{V}\tilde{\mathbf{u}}\|_2 \approx 6.3$ and $\|\frac{1}{V}RaPr\tilde{\theta}\|_2 \approx 8.6$, whereas stable ISRs are distributed along a horseshoe-shaped band (green line). The edge states found in this study are located not far from the (green) horseshoe-shaped band of ISRs, as they presumably lie in a smaller (grey) horseshoe-shape band situated between ISRs and SDC or elementary states. While we have identified four edge states,

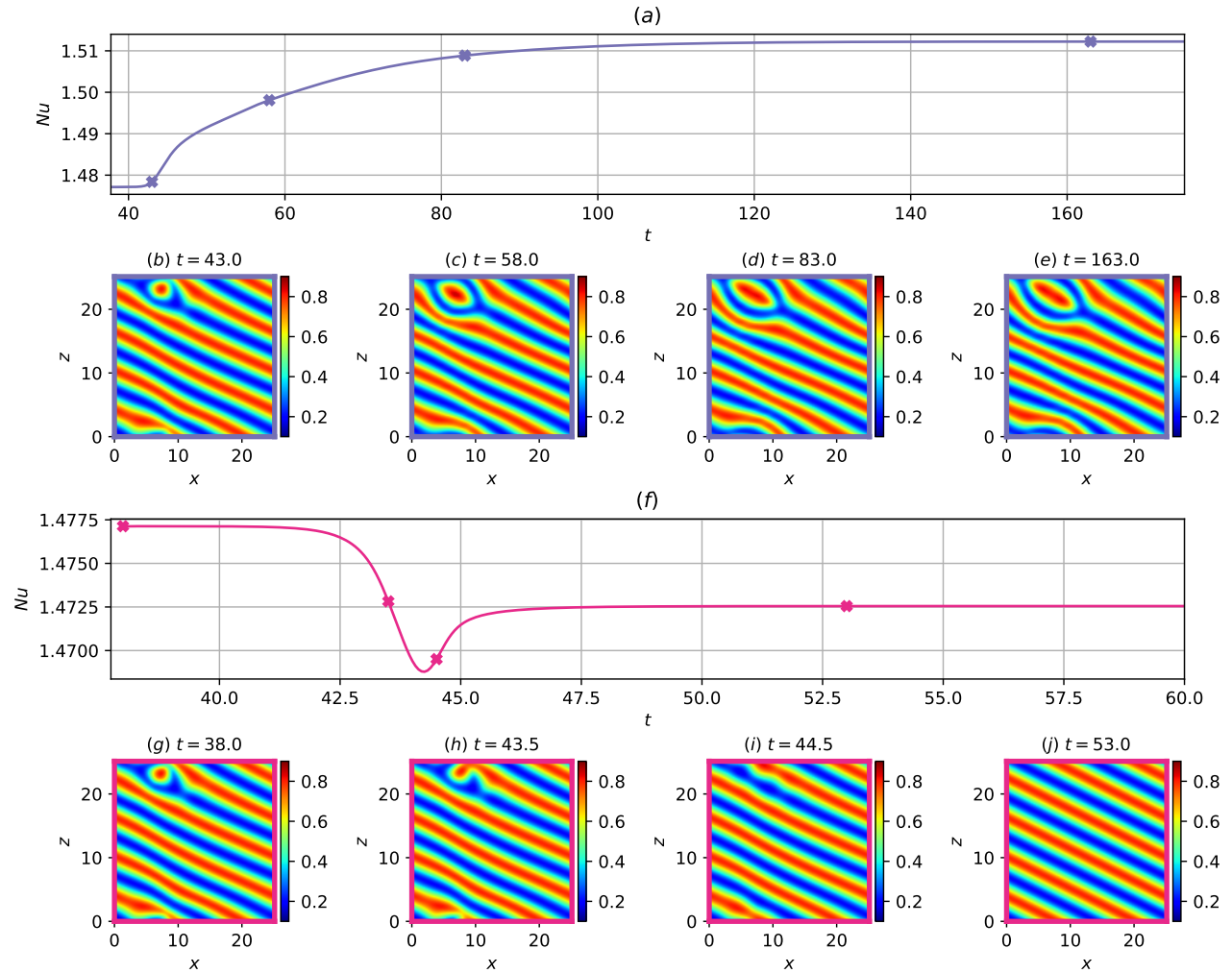


Figure 4.10: Time history of Nu along two opposite directions of the unstable manifold of the *point-defect* edge state: (a) ‘upper’ trajectory leading a stationary elementary state with bubble defect from $t \approx 43 – 163$ and (f) ‘lower’ trajectory decaying to the stable $s_{ISR,q=2.24}$ state. Mid-plane temperature fields are visualised in (b-e) along the upper trajectory at $t = 43.0, 58.0, 83.0, 163.0$, and in (g-j) along the lower trajectory at $t = 38.0, 43.5, 44.5, 53.0$.

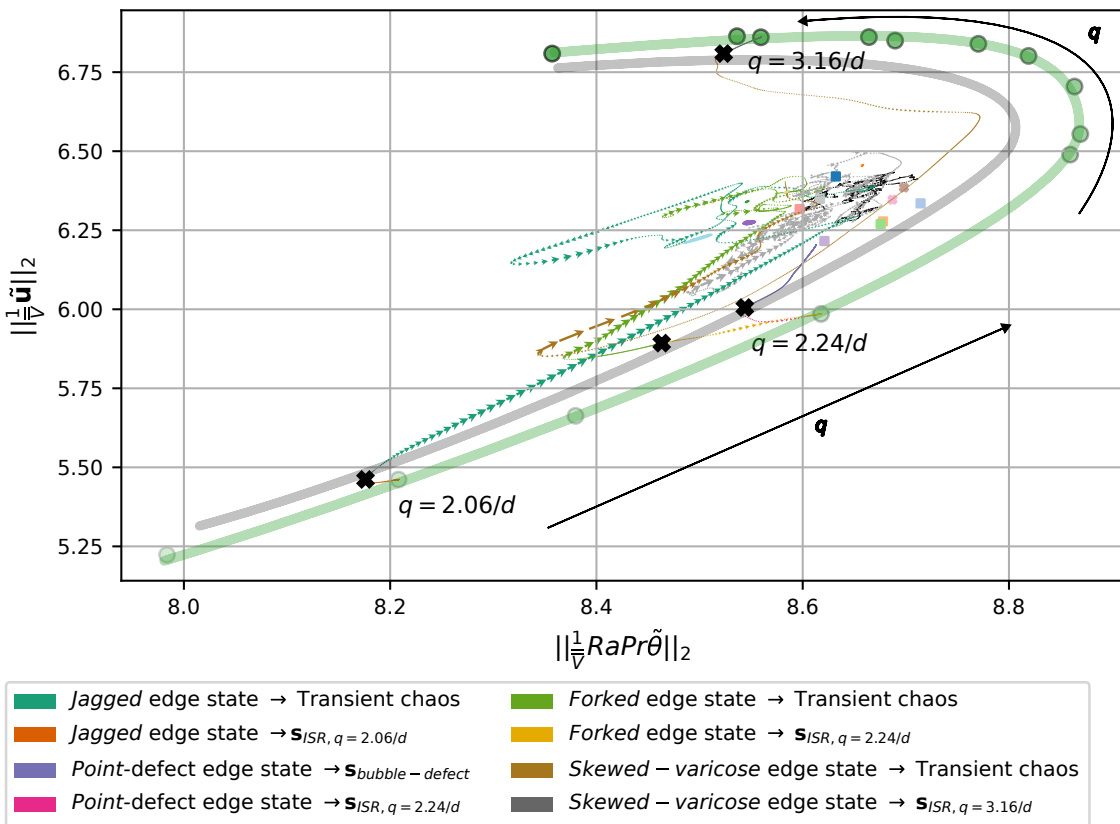


Figure 4.11: Phase portrait of the *jagged*, *point-defect*, *defect* and *skewed-varicose* edge states, along with stable ISRs, elementary states and transient SDC. Green and grey horseshoe lines are the regions, where stable ISRs and edge attractors are expected to be distributed when different sizes of the computational domain are considered.

we expect that there are more edge states, presumably distributed along the (grey) horseshoe-shaped band. It is also worth mentioning that the edge states we found here contain the underlying ISR structure ($s_{q=2.06/d, 2.24/d, 3.16/d}$) modified by spatially localised defects and ‘pinches’ between rolls, supporting its proximity with ISRs in the state space. This feature is also reminiscent of spatially localised edge states identified in boundary layer flows (Khapko et al., 2016). Lastly, we would like to emphasise that we have only considered initial conditions from the states between $s_{ISR,q}$ and $s_{elementary}$ and not strictly between $s_{ISR,q}$ and a transient SDC state. Nevertheless, three of the edge states are found to lie on the boundary separating the stable ISRs from transient SDC, supporting previous findings that the transient chaotic SDC are related to elementary states.

4.5 Unstable ideal straight rolls

Thus far, we have studied the edge and the edge states between some of the stable ISRs and elementary states. The dynamics associated with the unstable ISRs outside of the Busse balloon, however, remain unclear (Busse, 1981). Given that the stable ISRs and SDC form a bistable system, it is expected that some of the unstable ISRs near the Busse balloon would asymptotically reach one of the stable ISRs as the difference between the stable and unstable ISRs would be sufficiently small (Croquette, 1989a; Steinberg & Ahlers, n.d.). On the other hand, the unstable ISRs, which exist far from the boundary of the Busse balloon, may well have a sufficiently large deviation from the stable ISRs, implying that they are possibly associated with a state-space route to the SDC. The purpose of this section is to test this hypothesis by examining the long-term behaviour of the linear instabilities of the unstable ISRs.

We consider the linear instabilities of 3 unstable ISRs on the right side of the Busse balloon, with increasing wavenumber of $q = 3.5/d, 4.0/d, 4.5/d$, as shown in figure 4.12(a). The identification of the linear instability mode (or unstable manifold) with the different spanwise wavenumbers β is considered (see (4.6)). Figure 4.12(b) presents the unstable eigenvalues as a function of β . There are 2, 4 and 7 unstable manifolds ($\Re(\lambda) > 0$) for unstable ISRs of $q = 3.5/d, 4.0/d, 4.5/d$ respectively, forming total 13 unstable manifolds. In general, the growth rate and the number of linear instability modes (i.e. the repelling strength and the number of unstable manifolds) increase as q increases. It is worth mentioning that the solutions of unstable ISRs of $s_{ISR,q}(x, y)$ (required for linear stability analysis) are obtained by restricting the computational domain to the 2D $x-y$ plane which artificially suppresses 3D linear instabilities. We also note that the stability analysis of the unstable ISR, $q = 5.0/d$ was not considered as it quickly evolved into an unstable ISR of $q = 3.5/d$, which will be discussed in section §4.5.1.

To consider the long-term behavior in the direction of the unstable manifolds, an initial condition,

$$\mathbf{s}_0(\mathbf{x}, t = 0) = \mathbf{s}_{ISR,q}(\mathbf{x}) + \hat{\mathbf{s}}_\beta(x, y)e^{i\beta z}, \quad (4.9)$$

is prescribed to equation (4.1). Here, $\hat{\mathbf{s}}_\beta e^{i\beta z}$ is the unstable eigenmode, the amplitude of which was scaled such that its total energy (defined in (4.6)) of $\delta = 10^{-5}, 10^{-4}, 10^{-3}$ were considered. The total energy of the eigenmode, $\delta = 10^{-4}$ was found to be sufficiently small enough to ensure linear growth, while large enough to prevent other eigenmodes from being excited. Next, the initial condition is time

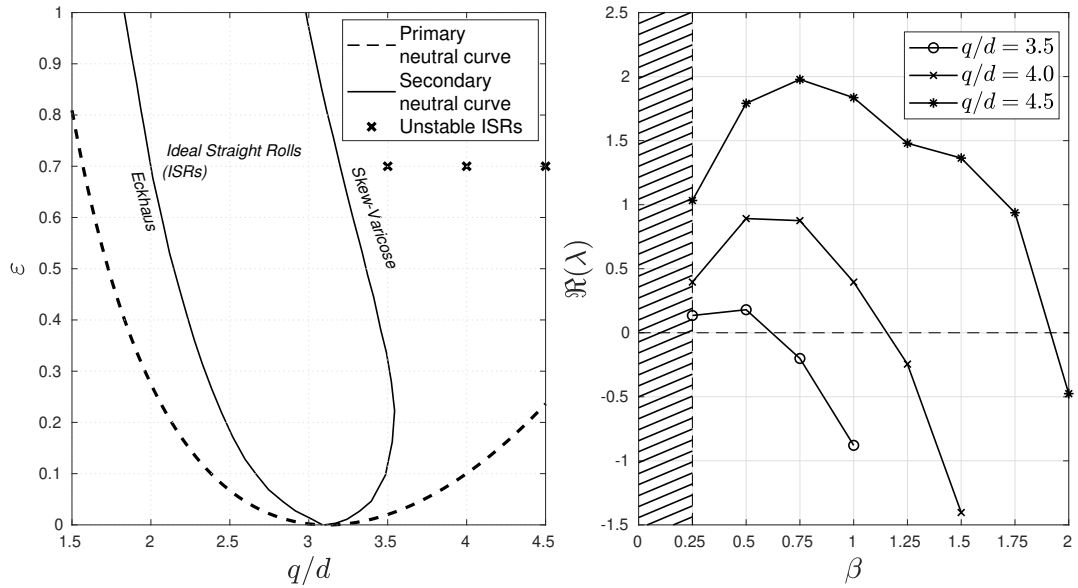


Figure 4.12: (a) Primary and secondary (Busse balloon from figure 1 ([Decker et al., 1994](#))) stability curves and unstable ISRs with $q = 3.5/d, 4.0/d, 4.5/d$; (b) Variation of the growth rate of instabilities of unstable ISRs as a function of spanwise wavenumber β . (Note that there are a total 13 unstable eigenmodes.)

Cases	$\beta = 0.25$	$\beta = 0.50$	$\beta = 0.75$	$\beta = 1.00$	$\beta = 1.25$	$\beta = 1.50$	$\beta = 1.75$
$q = 3.5/d$	ISR _{3.04}	(a) ISR _{2.50}	Stable	Stable	Stable	Stable	Stable
$q = 4.0/d$	ISR _{2.50}	(b) ISR _{3.16}	ISR _{3.00}	ISR _{2.83}	Stable	Stable	Stable
$q = 4.5/d$	ISR _{2.50}	ISR _{2.50}	(c) ISR _{3.00}	ISR _{3.20}	(d) Elementary	ISR _{2.50}	(e) Elementary

Table 4.2: Asymptotic state of secondary linear instabilities of $q = 3.5/d, 4.0/d, 4.5/d$. Subscripts in ISR refer to asymptotic wavenumber q , e.g., ISR_{2.5} refers to ideal straight rolls with wavenumber of $q = 2.5/d$. The asymptotic behaviours of (a-c) and (d,e) are discussed further in §4.5.1 and §4.5.2 respectively.

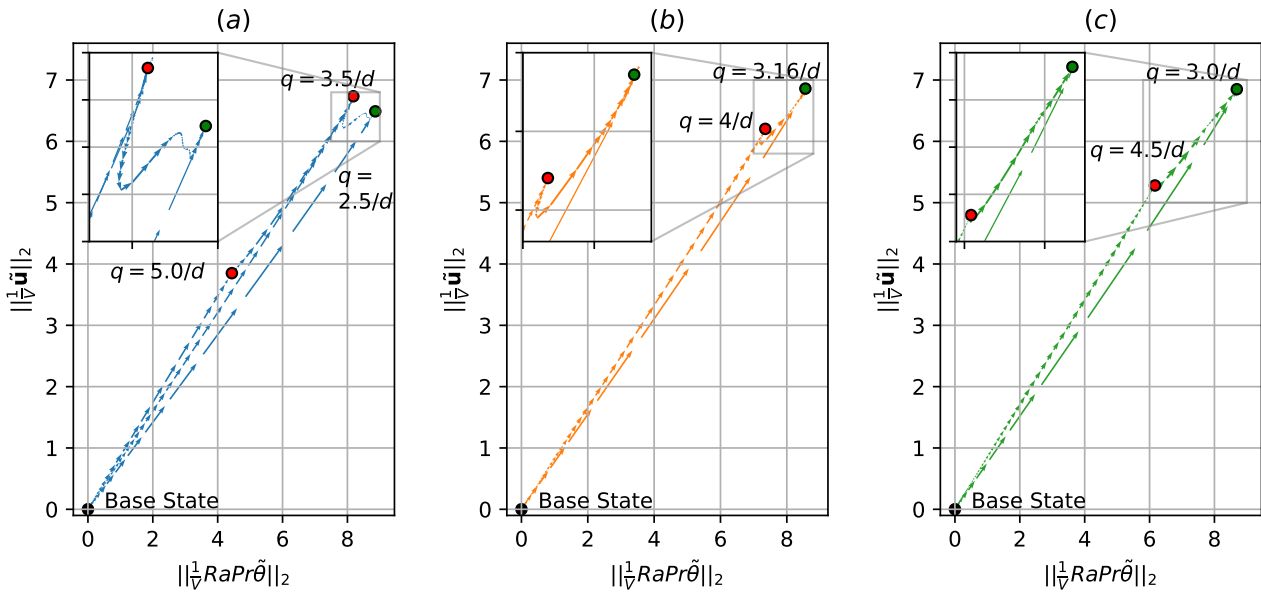


Figure 4.13: The phase-space solution trajectories connecting: (a) unstable base (conductive) state between 10 unstable rolls ($q = 5/d$), 7 unstable rolls ($q = 3.5/d$) and 5 stable rolls ($q = 2.5/d$); (b) unstable base (conductive) state between 8 unstable rolls ($q = 5/d$) and 6 stable rolls ($q = 3.16/d$); (c) unstable base (conductive) state between 9 unstable rolls ($q = 4.5/d$) and 6 stable rolls ($q = 3/d$). Here, the size of the arrows indicates the speed of the solution trajectory (or flow).

integrated over an extended period until an asymptotic state is reached. Table 4.2 shows the asymptotic states of 13 linear instabilities, depicted in figure 4.12(b), of which 11 linear instabilities led to ISRs states, forming a network of heteroclinic orbits which will be discussed in §4.5.1. Only the remaining 2 instabilities led to a transient SDC state before settling into an elementary state discussed further in §4.5.2.

4.5.1 Pathways leading to ISRs - heteroclinic orbits

In this section, the asymptotic behaviour of the most unstable linear modes of ISRs (table 4.2(a-c)) will be discussed. Solution trajectories that connect two invariant states referred to as heteroclinic orbits, are shown in Figure 4.13 which depicts the state space plot of volume normalised L2-norms of velocity and temperature. It reveals a number of heteroclinic orbits, connecting the base state (●), stable (●) and unstable (●) ISRs. Figure 4.13(a) exhibits several solution trajectories linking the base state, stable and unstable ISRs: three orbits connecting the base state to all the stable and unstable ISRs shown, one from the ISR of $q = 3.5/d$ to that of $q = 2.5/d$, and one from the ISR of $q = 5.0/d$ to that of $q = 3.5/d$. Here, caution will need to be taken in interpreting each of the connections as a heteroclinic orbit, because there appears to be an invariant state at which the speed of the solution trajectory nearly vanishes (a sign of the existence of unstable invariant states or ghost states (Strogatz, 2018)): for example, see the solution trajectory between the ISR of $q = 3.5/d$ to that of $q = 2.5/d$ (in the inset of figure 4.13(a)), which will be discussed below with figure 4.14. Starting from the primary base state, the system saturates into an ISR of wavenumber $q = 5.0/d$. Since this ISR is linearly unstable, it evolves into another unstable ISR of $q = 3.5/d$, before ultimately stabilising into

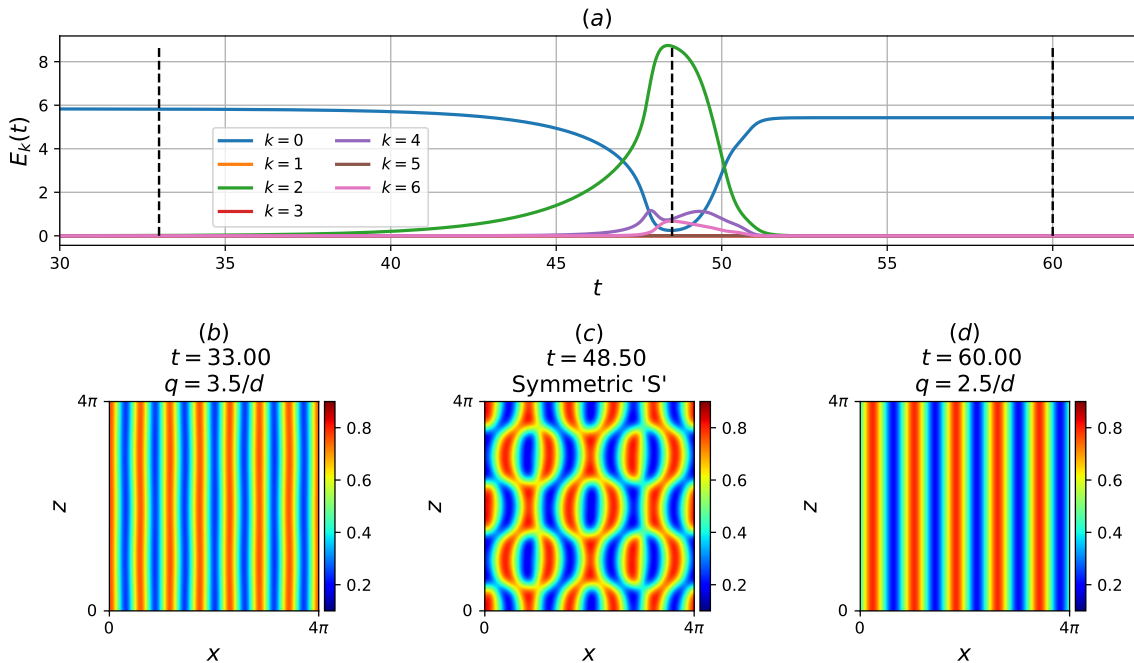


Figure 4.14: Asymptotic behaviour of the linear instability ($\hat{q}_{\beta=0.50}$) about unstable ISR $q = 3.5/d$. (a) Modal energy $E_k(t)$, and temperature snapshots, $\theta(x, z)|_{y=d/2}$ at (b) $t = 33$, (c) $t = 48.5$, (d) $t = 60$.

an ISR of $q = 2.5/d$. Next, figure 4.13(b) shows three solution trajectories connecting the base state, an unstable and stable ISR. Starting from the base state, the system transitions into an unstable ISR of $q = 4/d$ before stabilising into an ISR of $q = 3.16/d$. Lastly, figure 4.13(c) presents three solution trajectories connecting the base state, a stable and unstable ISR. Starting from the base state, it can evolve to an unstable ISR of $q = 4.5/d$ before settling into a stable ISR of $q = 3.0/d$. Figure 4.13 suggests that each of the stable ISRs within the Busse balloon has the basin of attraction, characterised by a web of heteroclinic orbits connecting some of the unstable ISRs outside of the Busse balloon. It is worth emphasising that the connections between the solutions presented here were obtained by time-integrating the dominant unstable manifolds of ISRs. In practice, there are many more unstable manifolds (see table 4.2) which have not been presented, potentially leading to more complex networks of heteroclinic orbits that form the basin of attraction for each stable ISR.

Figure 4.14 describes the asymptotic behaviour with the most unstable eigenmode for $q = 3.5/d$ (table 4.2(a)) in detail, corresponding to the connection between the unstable ISR of $q = 3.5/d$ and the stable ISR of $q = 2.5/d$ in figure 4.13(a). To observe the linear instability defined in Eq. (4.9), we report contribution of modal energy (figure 4.14(a)) as

$$E_k(t) = \frac{1}{2} \int_{\Omega} |\hat{\mathbf{u}}_k(t)|^2 d\Omega, \quad (4.10)$$

where $\hat{\mathbf{u}}_k$ refers to the k -th Fourier coefficient in z -direction. Initially, the simulation starts from the ISR state of 7 rolls ($t = 33$), corresponding to a roll-wavenumber of $q = 3.5/d$. The unstable eigenmode $\hat{s}_{\beta=0.50}$ grows exponentially before peaking at $t = 48.50$, forming an ‘S’-like symmetric state (figure 4.14(c)). Note that, at this point, the time derivative of $E_k(t)$ nearly vanishes, indicating

that the snapshot taken at $t = 48.50$ is potentially close to an unstable invariant state. Finally, the modal energy of $N_z = 2$ decays and the system settles into an ISR state of $q = 2.5/d$ (5 rolls aligned in the x -direction), which is within the Busse balloon. The asymptotic behaviour along the dominant unstable eigenmode for $q = 4.0/d$ and $q = 4.5/d$ is qualitatively similar to figure 4.14, where an unstable ISR stabilises into a stable ISR.

All three cases examined here show that the transition from an unstable ISR to a stable ISR involves an intermediate state, at which $dE_k(t)/dt$ is seen to be relatively small. In the transition pathway from the unstable to stable ISR, it is presumable that there exists an unstable equilibrium (i.e. fixed point/travelling-waves etc.) in the form of the original unstable ISR with its nonlinearly saturated instability, or ghost states (Strogatz, 2018). The existence of such a stationary solution can probably be computed with a typical Newton iteration or variational methods (Parker & Schneider, 2022; Viswanath, 2007), but this is beyond the scope of the present study. In any case, the numerical experiments here suggest that each of the stable ISR has a basin of attraction composed of a network of heteroclinic orbits involving connections between the base state and unstable ISRs.

4.5.2 Pathways leading to elementary states

Now, we discuss the asymptotic behaviour with linear instabilities of $\hat{s}_{\beta=1.75}$ about the unstable ISR of $q = 4.5/d$ (tab 4.2(e)). Contrary to the transitions presented in the previous section, the asymptotic states did not result in ISRs, but transient SDC before settling into an elementary state for case (e) (table 4.2(e))

The asymptotic behavior with $\hat{s}_{\beta=1.75}$ of unstable ISR $q = 4.5/d$ (table 4.2(e)) is presented in figure 4.15. Starting from $t = 1.25$, the unstable ISR state is characterised by 9 convection rolls aligned along the x -axis. The state experiences the linear instability imposed from $t = 1.25$ to $t = 7$, corresponding to an exponential growth in the grey curve ($E_7(t)$ in figure 4.15(a)), marked by cross-convection rolls in figure 4.15(c). Subsequently, the state exhibits a transient SDC behaviour from $t \approx 7$ to $t \approx 80$, characterised by an ‘O’-ring and ‘pac-man’ liked convection pattern illustrated in figure 4.15(d). Following this, the system stabilises into a short-period ($T \approx 1.8$) oscillatory behaviour between $t = 90$ and $t = 110$ (figure 4.15(e)), before transitioning into a long-period time-periodic state from $t = 110$ to $t = 201.75$ (figure 4.15(a) *cont.*), with a period of $T = 51.75$. The convection pattern appears to be travelling diagonally in the negative x - z directions (compare figures 4.15(f,g)), indicating that this state is a relative periodic orbit. Interestingly, the asymptotic behaviour of $\hat{s}_{\beta=1.25}$ about the unstable ISR of $q = 4.5/d$ (table 4.2(d)) also led to an elementary state.

Figure 4.16 presents the state space trajectories of two pathways discussed above, represented by the volume-normalised L2-norms of velocity perturbations, temperature perturbations and Nusselt number. These trajectories are superimposed upon the state space trajectories of SDC and 14 elementary states (figure 4.4). The purple trajectory represents the one along the linear instability direction (i.e. the unstable manifold) of $q = 4.5/d$ with $\beta = 1.25$. Originating from the unstable ISR ($q = 4.5/d$), briefly saturates at $\|\frac{1}{V}\tilde{\mathbf{u}}\| \approx 6.25$ and $\|\frac{1}{V}RaPr\tilde{\theta}\|_2 \approx 8$, before stabilising into a periodic orbit near the *spiral-defect* elementary state (see figure 4.1, represented by the orange trajectory in figure 4.4). The case of $q = 4.5/d$ along the linear instability direction for $\beta = 1.75$ is represented

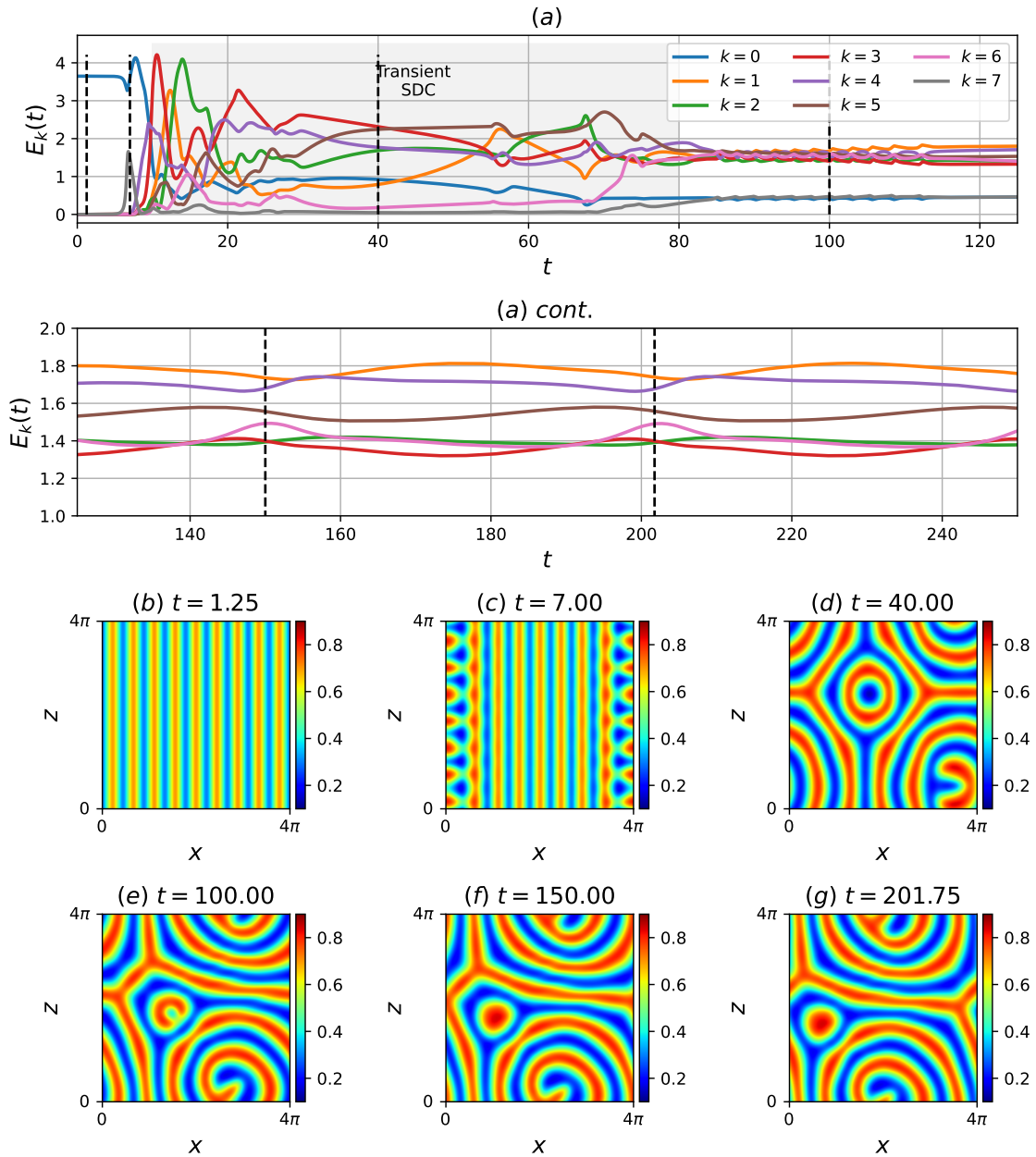


Figure 4.15: Asymptotic behaviour along the linear instability of $\hat{s}_{\beta=1.75}$ about unstable ISR $q = 4.5/d$. (a) Modal energy $E_k(t)$, and temperature snapshots $\theta(x, z)|_{y=d/2}$ at the onset of secondary instability at (b) $t = 1.25$, (c) $t = 7$, following a transient SDC behaviour at (d) $t = 40$, and settling into a elementary state at (e) $t = 100$, (f) $t = 150$ and (g) $t = 201.75$.

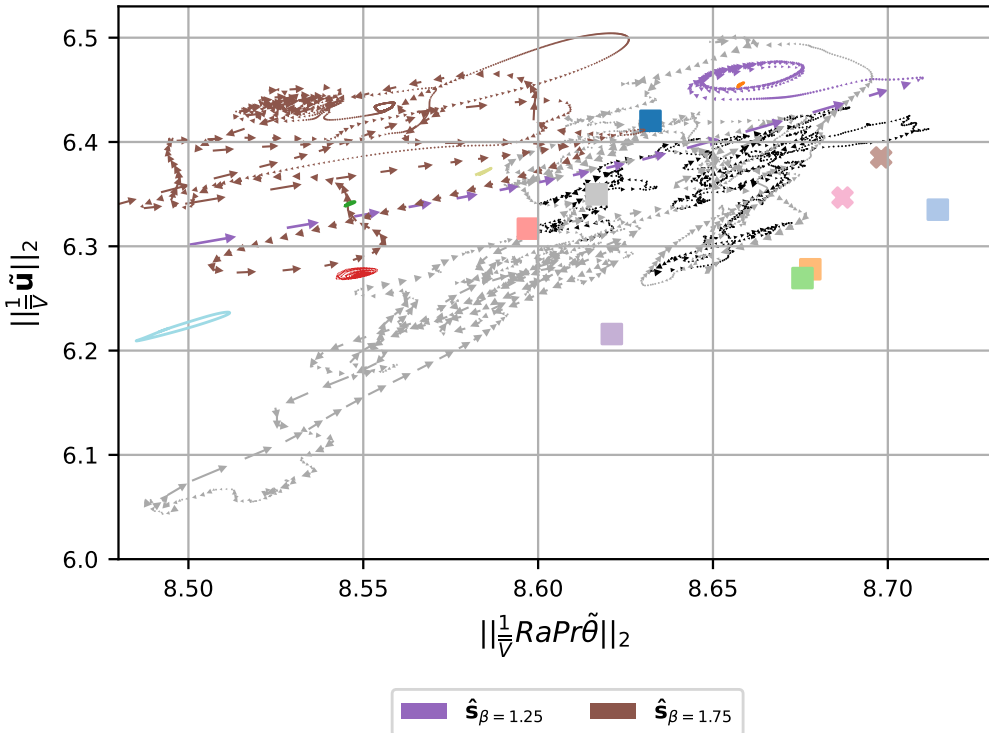


Figure 4.16: State space visualisations using $\|\frac{1}{V}\tilde{u}\|_2$ and $\|\frac{1}{V}RaPr\tilde{\theta}\|_2$, of SDC, and 14 elementary states with colour schemes based upon figure 4.4. The trajectories of two linear instabilities (purple) $\hat{s}_{\beta=1.25}$, (brown) $\hat{s}_{\beta=1.75}$ about an unstable ISR $q = 4.5/d$ leading to elementary states (see figures 4.15) are shown.

by the brown trajectory. Emanating from the unstable ISR ($q = 4.5/d$), the trajectory experiences a period of transient SDC behaviour in the vicinity of elementary states before converging onto a relative periodic orbit, as expected from figure 4.15. It is evident that the two trajectories arising from linear instabilities about the unstable ISR ($q = 4.5/d$) lie within the vicinity of SDC.

4.5.3 A pathway to SDC in an extended domain $\Gamma = 4\pi$

In §4.5.2, we have identified two distinct pathways to elementary states along some unstable manifolds from an unstable ISR. In particular, one of the trajectories evolved into transient SDC before stabilising into an elementary state. This is reminiscent of a chaotic saddle, but with a considerably short lifetime. The transient SDC behaviour observed within the minimal domain implies that if the same initial condition is added in an extended computational domain, it would trigger a chaotic state at least with a longer lifetime. This chaotic state is expected to be SDC in an extended domain, given the analysis in §4.5.2. To examine this hypothesis, we conduct a numerical simulation with an initial condition from the case of table 4.2(e) (i.e. the unstable ISR $q = 4.5/d$ with the instability mode of $\hat{s}_{\beta=1.75}$) in a domain twice larger than each horizontal direction ($\Gamma = 4\pi$).

The solution trajectory along the unstable manifold, $s_{\beta=1.75}$, of ISR $q = 4.5/d$ in an extended domain ($\Gamma = 4\pi$) is presented in figure 4.17. The state, characterised by 18 convection rolls (figure 4.17(b)), experiences the linear instability from $t = 1.25$ to $t = 7$, marked by cross-convection rolls shown in figure 4.17(c). Subsequently, the state exhibits a prolonged period of chaotic behaviour,

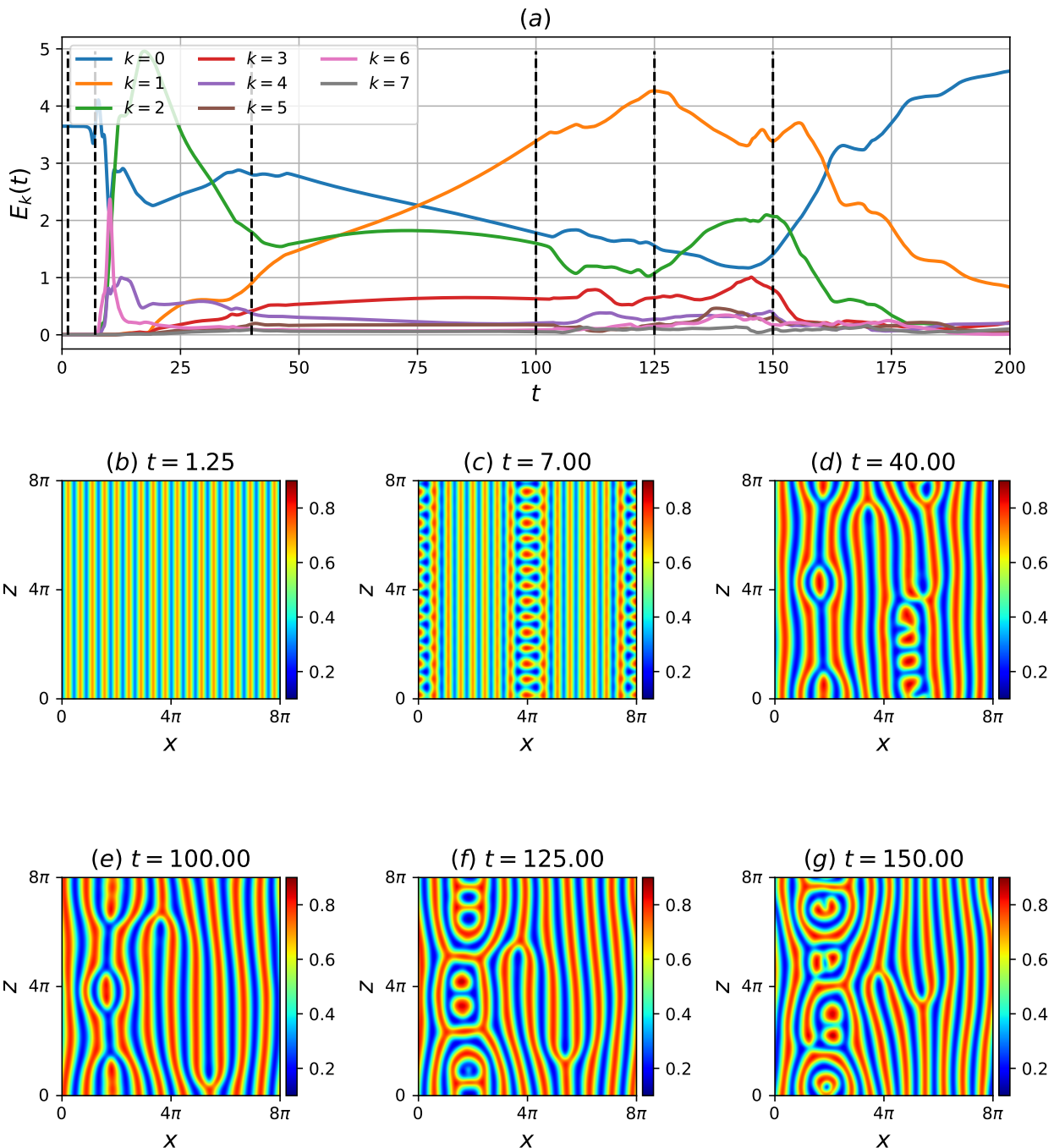


Figure 4.17: Asymptotic behaviour along the linear instability $\hat{s}_{\beta=1.75}$ about unstable ISR $q = 4.50/d$, in an extended domain $\Gamma = 4\pi$. (a) Modal energy $E_k(t)$, and temperature snapshots $\theta(x, z)|_{y=d/2}$, at (b) $t = 1.25$, (c) $t = 7$, (d) $t = 40$, (e) $t = 100$, (f) $t = 125$, (g) $t = 150$.

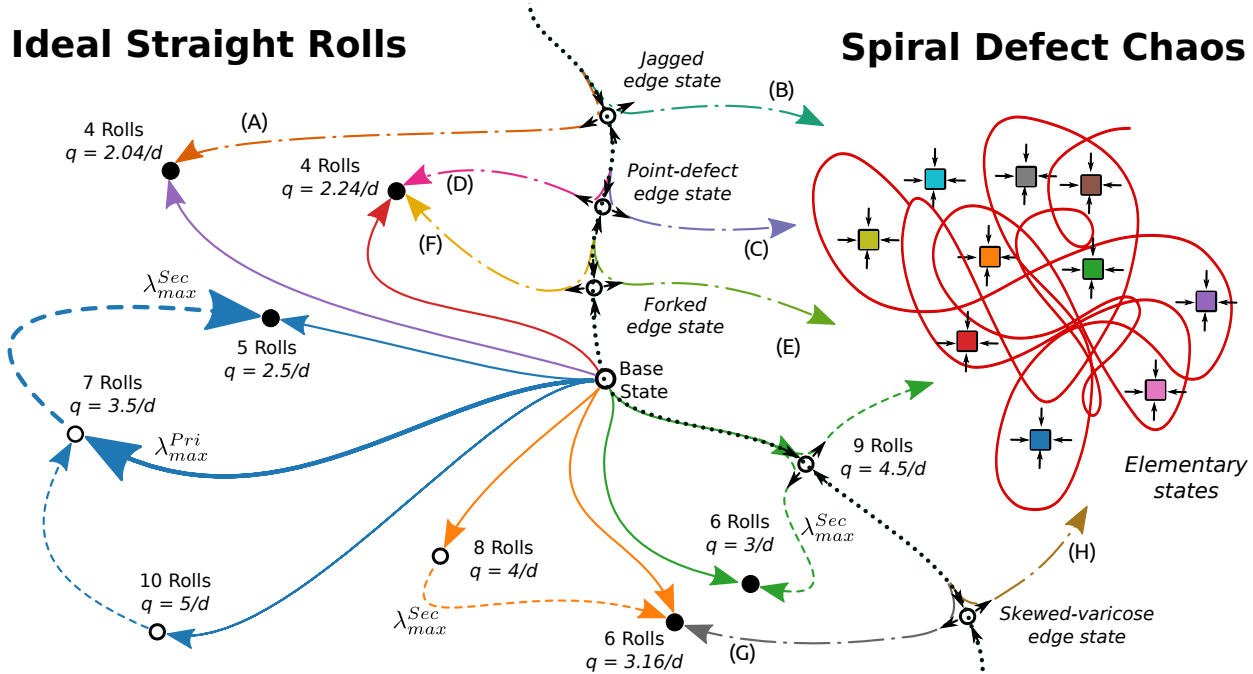


Figure 4.18: State space sketch containing the base, stable and unstable ISRs, edge, elementary states and SDC in a confined domain. Open circles, (\circ) and filled circles/squares (\bullet , \blacksquare) refer to unstable and stable states. Solid ($-$) and dashed lines ($--$) are the solution trajectories along the primary and secondary instabilities respectively, $\lambda_{max}^{Pri,Sec}$ refers to the most unstable primary and secondary linear instability manifolds. Blue, orange and green trajectories denote heteroclinic connections leading toward stable ISRs (trajectories labelled (A-G) and colors adapted from figure 4.13). Dashed-dotted trajectories ($- \cdot -$) refer to solution trajectories emerging from the edge states (color-coded from figure 4.11). The dotted line (\cdots) represents the boundary between ISRs and SDC, consisting of many stable elementary states.

starting from $t = 7$ and lasting beyond $t = 200$. This is in stark contrast to the transient SDC behaviour observed in the minimal domain (figure 4.15), confirming the hypothesis above. Finally, it is interesting to note that the convection patterns of figures 4.17(f,g) contain localised structures that bear resemblance with the stationary *pac-man* (figure 4.1)(c)) and oscillatory *peanut* (figure 4.1(f)) elementary states.

4.6 Summary

Spiral-defect chaos (SDC) has been considered one of the bistable states within a large spatial domain in Rayleigh-Bénard convection. However, existing studies have also shown the presence of multiple stable states in small and large domains, puzzling one's understanding of the bistable system in an extended spatial domain. Starting with numerical simulation in an extended domain ($\Gamma = 16\pi$), we have systematically reduced the computational domain, such that the fundamental patterns of SDC can be isolated.

Through numerical experiments confined within a minimal domain of $\Gamma = 4\pi$, we have identified transient SDC before stabilising in/to stable elementary states of SDC, and 14 different elementary states have been found in this way. From a dynamical system perspective of turbulence in shear

flow, chaotic trajectories (representing turbulence) are typically envisioned to wander among a set of unstable invariant solutions and in some cases, may decay towards the base (laminar) state (see references in §1.2.2). Our results for the chaotic trajectories of SDC in a confined spatial domain reveal a distinct scenario, where chaotic trajectories, once tangled into SDC, stabilise into a non-trivial elementary state instead of returning to the base (ISR) state. This finding is new and challenges the understanding of the transition between the conduction state and spiral defect chaos from a dynamical system viewpoint. Despite this, the elementary states are still situated around the chaotic trajectories of SDC in the state space (figure 4.4), and their statistical properties (figure 4.5) and localised spatial structures (figure 4.1) are similar to those of SDC. This suggests that the computed elementary states may serve as spatially local ‘building block’ structures of SDC that interact with each other to form SDC in an extended domain. Within the minimal domain $\Gamma = 4\pi$, we have identified 14 stable elementary states, with a possibility of additional states yet to be found. Notably, the large number of invariant states seem to be characteristic feature of Rayleigh-Bénard fluid systems such as cylindrical RBC ([Borońska & Tuckerman, 2010a, 2010b](#)) and inclined RBC ([Zheng, Tuckerman, & Schneider, 2024a, 2024b](#)).

To further understand the state space structure of SDC, ISRs and possible gateways toward SDC, we furnish a state space sketch of the solution trajectories connecting the base, stable and unstable ISRs, edge, elementary states and SDC, shown in figure 4.18. Starting from the base state, time-integrating along the unstable manifold guided by primary instabilities leads to either stable or unstable ISRs, denoted by solid trajectories. Notably, the most unstable primary instability leads to a 7 roll ISR ($q = 3.5/d$), before saturating into a stable 5 roll ISR ($q = 2.5/d$), following the most unstable secondary instability, depicted by dashed trajectories. These solution trajectories form a network of heteroclinic orbits, connecting the base state with stable ($q = 2.5/d$) and unstable ($q = 3.5/d, 5/d$) ISRs, represented in blue. Further from the boundaries of the Busse balloon, we have identified two more heteroclinic orbits that form a basin of attractor between the base state, and stable, unstable ISRs, labelled as a group of orange and Green trajectories. These heteroclinic orbits are expected in experimental settings where initial conditions and background noise can be controlled precisely. In practice, where precise controls are inaccessible, it is more likely to observe SDC ($\Gamma = 8\pi, 16\pi$) or stable elementary states ($\Gamma = 4\pi$), which are embedded in the chaotic trajectories of SDC (see coloured ■), supporting the notion that SDC is underpinned by elementary states presumably interacting with each other.

We have identified 4 edge states that lie on the boundary between stable ISRs and transient SDC, where the upper and lower trajectories emerging from their unstable manifold are represented by dash-dotted trajectories. Further from the Busse balloon, we have identified an unstable manifold of a 9 roll ($q = 4.5/d$) ISR, leading to the onset of SDC. Consequently, the unstable base state is also expected to lie on the boundary, as a controlled initial condition could guide the system toward the unstable 9-roll ISR, and subsequently the onset of SDC. Finally, the dotted line represents the boundary between ISRs and SDC, consisting of the base state, edge states and unstable 9 roll ISR ($q = 4.5/d$), illustrating four possible routes toward SDC. Although we have considered the unstable manifolds of ISRs for $\Gamma = 4\pi$, we acknowledge that the dimension of such manifolds depends on the

domain size and that the spatially subharmonic instabilities may arise as the domain size increases. Additionally, there may well be other unstable ISRs and edge states along the boundary. However, the investigation into the existence of such states is challenging due to the daunting computational efforts required. Recent advances, such as the framework proposed in ([Schmid, De Pando, & Peake, 2017](#)), may help to accelerate linear stability analysis and facilitate further investigations.

Chapter 5

Conclusions

In our concluding chapter, we emphasise the main contributions of this thesis and provide recommendations for possible avenues of future work. We explored the transitional regimes of Rayleigh-Bénard Poiseuille (RBP) flows arising from the combination of shear and buoyancy forces in §3. The main findings can be summarised in the following,

1. The existence of the *thermally-assisted sustaining process*, providing an alternative pathway towards turbulence via linearly unstable longitudinal rolls in confined domains.
2. At moderate Reynolds number, a new spatio-temporal regime referred to as intermittent rolls was identified. It is characterised by the quasi-cyclic breakdown and regeneration of longitudinal rolls for moderate Reynolds number in large spatial domains.
3. At low Reynolds number, a buoyancy dominant regime primarily influenced by the magnitude of Rayleigh number and is independent of Reynolds number. In this regime, the convection structures are consistent regimes in Rayleigh-Bénard convection, such as the bistable system between spiral-defect chaos (SDC) and ideal-straight rolls (ISRs), and the presence of oscillatory instabilities. These structures appear to be simply convected along the mean flow.

Next, we provide possible avenues of future work for transitional RBP which may include,

1. Performing a detailed bifurcation analysis of invariant states arising around the thermally-assisted sustaining process (see figure 3.16) in confined domains and minimal band units ([Tuckerman et al., 2020](#)), possibly identifying complex global bifurcations.
2. Conducting bifurcation analysis necessitates the implementation of the Jacobian-free Newton-Krylov (JFNK) methods in Nektar++ ([Knoll & Keyes, 2004](#)). Variants of the JFNK method includes a hook-step modification ([Viswanath, 2007](#)) or the utilisation of preconditioners ([Yan et al., 2021](#)) may accelerate convergence. Apart from JFNK method and its variants, a recent adjoint-based variation method may offer better convergence properties for computing periodic orbits ([Parker & Schneider, 2022](#)).
3. The extension of the *thermally-assisted sustaining process* to other buoyancy and shear driven systems such as the Rayleigh-Bénard Couette (RBC) flow, which may offer the ease of experimental verification in the absence of a mean flow.

4. It may be worth exploring the influence of Reynolds number on the bistable system between spiral-defect chaos (SDC) and ideal straight rolls (ISRs) in detail, and the secondary linear stability of longitudinal rolls. However, we caution that there may be numerous invariant states in the buoyancy driven regime as witness in §4.

In §4, we examined the state space structure of the bistable system between SDC and ISRs in Rayleigh-Bénard convection in various domain sizes. The main contributions of the study is as follows,

1. By systematically minimising the spatial domain to a minimal domain, we have identified stable invariant solutions referred to as *elementary* states. These elementary states are visibly (see figure 4.1) and statistically (see figure 4.5) similar to the spatially localised patterns of SDC, underpinning the pattern formation of SDC.
2. The identification of multiple edge states (and likely a plenty more), forming local attractors along the edge between the basin of attraction of ISRs and elementary states.
3. Multiple networks of heteroclinic orbits (and likely a plenty more) between stable and unstable ISRs.
4. The identification of an unstable ISRs far from the boundaries of the Busse balloon which sit on the boundary between stable ISRs and SDC.

While the newly identified elementary states resembles the localised features of SDC, they remain stable and time independent and therefore do no necessarily capture the temporal dynamics of SDC. As such, possible avenues of future may be dedicated to the following,

1. Computing the unstable invariant solutions of Rayleigh-Bénard convection, such as their equilibria, periodic orbits and heteroclinic connections between them, potential offering descriptions of the temporal dynamics of SDC (necessitating the implementation of bifurcation tools in Nektar++ mentioned above).
2. The onset of sustained spiral defect chaos appears to be linked to a critical domain size, below which, SDC remains transient. Therefore, a bifurcation analysis of elementary states with respect to the spatial domain size could be performed to determine the critical domain size for the onset of sustained chaos.
3. By performing bifurcation analysis in the regime of transient SDC, we may draw similar ideas from transient turbulence (see 1.2.2), perhaps revealing global bifurcations such as crisis bifurcations where the a chaotic attractor becomes leaky or homoclinic tangles in Rayleigh-Bénard convection.

Appendix A

Appendices

A.1 Simulation parameters for Ra - Re sweep

The spectral/ hp quadrilateral element width, heights and polynomial order are kept constant for all simulations, $(\Delta x, \Delta y|_{y=\pm h}, \Delta y|_{y=0}, P) = (0.1\pi, 0.0549, 0.367, 4)$. To resolve the high gradients, the quadrilateral element heights are bunched near the wall, $\Delta y|_{y=\pm h}$, and expanded in the channel center, $\Delta y|_{y=0}$. The basis type employed here consists of the modified Jacobi polynomials, known as the *modified* basis (see §2.3.4). Table A.1 describes the number of Fourier expansions, N_z , and temporal resolution of 52 numerical experiments at $Re = 0, 0.1, 1, 10, 100, 500, 750, 1000, 1050, 2000$, and $Ra = 0, 2000, 3000, 5000, 8000, 10000$ with $Pr = 1$ and a large aspect ratio, $\Gamma = 4\pi$. The initial conditions of all numerical experiments were sampled from a statistically stationary solution based on the time history of the Nusselt number and shear. The laminar solution obtained for $Ra = 0$, $Re \leq 1000$ has been omitted in table A.1.

A.2 First- and second-order statistics of the buoyancy- and shear-driven regime

A.2.1 Buoyancy-driven regime

We present the first- and second-order statistics of the buoyancy-dominated regime (shaded in red), consisting of the (1) SDC & ISRs, and (2) ISRs states in figure A.1, illustrating its temporal and plane-averaged streamwise velocity, $\langle w \rangle_{x,z,t}$, temperature, $\langle \theta \rangle_{x,z,t}$, fluctuating wall-normal velocity squared normalised by thermal velocity scale, $\langle \tilde{v}\tilde{v} \rangle_{x,z,t}/u_\kappa^2$, fluctuating temperature squared, $\langle \tilde{\theta}\tilde{\theta} \rangle_{x,z,t}$ and fluctuating span- and streamwise velocities squared normalised by thermal velocity scale, $\langle \tilde{u}\tilde{u} + \tilde{w}\tilde{w} \rangle_{x,z,t}/u_\kappa^2$. We note that the fluctuating components are defined about a temporal-planar averaged quantity, i.e $\tilde{\mathbf{u}} = \mathbf{u} - \langle \mathbf{u} \rangle_{x,z,t}$. The mean temperature profiles (figure A.1(b)), and the fluctuating span- and streamwise velocities (figure A.1(f)) are visually similar for the same Ra , and are nearly independent of Re . However, we observe the dependence on Re at $Ra = 3000$ in the fluctuating temperature squared (figure A.1(d)), and fluctuating wall-normal velocities (figure A.1(c)), likely due to variations in convection structures, particularly in the convection roll wavenumbers. A detailed

Ra	Re	N_z	dt	T	$\frac{d}{\kappa}$
0	1050	64	0.1	8000	-
0	2000	128	0.02	3000	-
2000	0	64	0.05	50	25
2000	0.1	64	0.005	5	25
2000	1	64	0.01	50	25
2000	10	64	0.05	50	2.5
2000	100	64	0.1	50	0.25
2000	500	64	0.1	50	0.05
2000	750	64	0.1	50	0.033
2000	1000	64	0.1	50	0.025
2000	1050	64	0.1	8000	3.81
2000	2000	128	0.02	2800	0.75
3000	0	64	0.05	3000	1500
3000	0.1	64	0.005	300	1500
3000	1	64	0.05	100	50
3000	10	64	0.05	50	2.5
3000	100	64	0.1	10000	50
3000	500	64	0.1	50	0.05
3000	750	64	0.1	50	0.033
3000	1000	64	0.1	50	0.025
3000	1050	64	0.1	8000	3.81
3000	2000	128	0.02	2800	0.75
5000	0	64	0.005	1200	600
5000	0.1	64	0.001	800	4000
5000	1	64	0.01	2500	1250
5000	10	64	0.05	500	25
5000	100	64	0.1	1000	5
5000	500	64	0.05	8000	8
5000	750	64	0.05	8000	5.33
5000	1000	64	0.02	8000	4
5000	1050	64	0.02	8000	3.81
5000	2000	128	0.02	2800	0.75
8000	0	64	0.0025	600	300
8000	0.1	64	0.0005	600	3000
8000	1	64	0.005	600	300
8000	10	64	0.05	500	25
8000	100	64	0.1	5000	25
8000	500	64	0.05	10000	10
8000	750	64	0.05	8000	5.33
8000	1000	64	0.02	8000	4
8000	1050	64	0.02	8000	3.81
8000	2000	128	0.02	2800	0.75
10000	0	64	0.0025	1000	500
10000	0.1	64	0.00025	800	4000
10000	1	64	0.0025	600	300
10000	10	64	0.05	12000	600
10000	100	64	0.1	8000	40
10000	500	64	0.05	8000	8
10000	750	64	0.05	8000	5.33
10000	1000	64	0.02	8000	4
10000	1050	64	0.02	8000	3.81
10000	2000	128	0.02	2800	0.75

Table A.1: The summary of the spatial and temporal resolution for a given Re , Ra . N_z denotes the number of Fourier expansions in the z -direction. $dt, T, d/\kappa$ denotes the timestep, final time and the final time scaled by the thermal timescale.

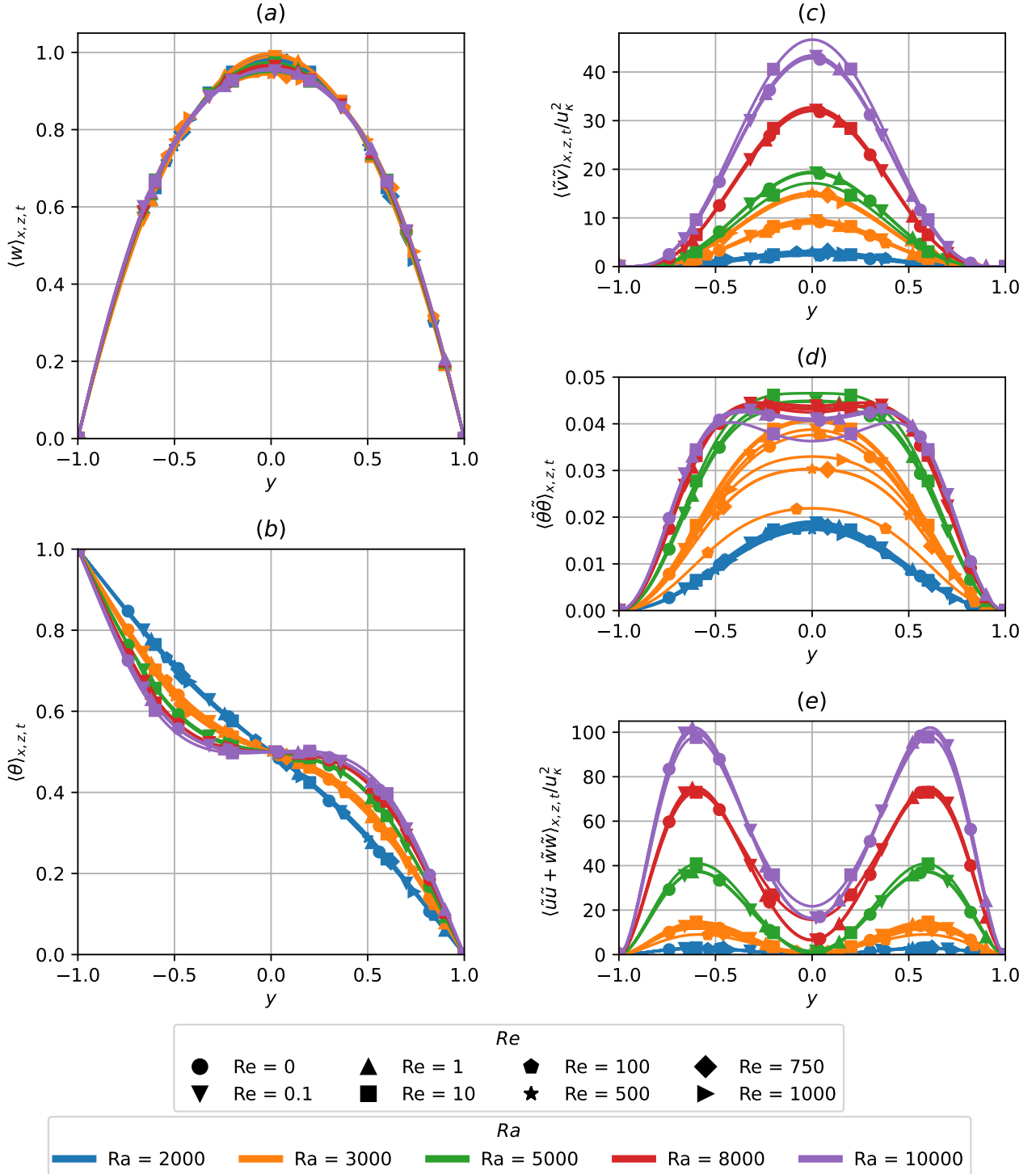


Figure A.1: The wall-normal distribution of temporal and plane- averaged (a) streamwise velocity, (b) temperature, (c) fluctuating wall-normal velocity squared normalised by thermal velocity scale, (d) fluctuating temperature squared and (e) fluctuating span- and streamwise velocities squared normalised by thermal velocity scale of buoyancy-driven regime shaded in red in figure 3.1.

analysis of how the statistical properties vary with roll wavenumber is beyond the scope of this work. We propose that the underlying flow structure, consisting of convection rolls, describes the buoyancy-driven regime, shaded in red in figure 3.1. In this regime, the strength of the convection is primarily controlled by Ra , akin to RBC, and remains independent of Re .

A.2.2 Shear-driven regime

As Re falls within the range of $1050 \leq Re \leq 2000$, shear-driven turbulence dominates, where the impact of Ra on the first- and second-order statistics is weakly dependent on Ra in figure A.2. Figure A.2 describes the temporal and plane-averaged streamwise velocity, $\langle w \rangle_{x,z,t}$, temperature, $\langle \theta \rangle_{x,z,t}$, fluctuating streamwise velocity squared, $\langle \tilde{w}\tilde{w} \rangle_{x,z,t}$, fluctuating wall-normal velocity squared, $\langle \tilde{v}\tilde{v} \rangle_{x,z,t}$, fluctuating spanwise velocities squared, $\langle \tilde{u}\tilde{u} \rangle_{x,z,t}$, fluctuating Reynolds stresses $\langle \tilde{v}\tilde{w} \rangle_{x,z,t}$, and fluctuating temperature squared, $\langle \tilde{\theta}\tilde{\theta} \rangle_{x,z,t}$ at $Re = 2000, 1050$ for $Ra \in [0, 10000]$. The flow structures appear as uniform, featureless turbulence (Tuckerman et al., 2014) at $Re = 2000$, independent of Ra . The spacetime figure of near-wall ($y^+ = 15$), wall-normal and spanwise perturbation kinetic energy, $\mathcal{E}_{u'+v'}$, at $Re = 2000$, $t \in [0, 2800]$, illustrating spatially uniform featureless turbulence, visually distinguishable with $Ra \in [0, 10000]$, corroborating with their Ra -independent first- and second-order statistics in figure A.2. In other words, the dominant physical mechanism is shear-driven turbulence at $Re = 2000$, independent of Ra .

As Re approaches $Re = 1050$, the midplane temperature in figure 3.1 shows regions of spatially localised structures, indicating the presence of turbulent-laminar bands, described in figure 3.5 and 3.6 later. The mean streamwise velocity and temperature gradients at both ends of the wall, and second-order statistics, are enhanced slightly from $Ra = 0$ to $Ra = 10000$. This enhancement could be due to the coexistence of longitudinal rolls with turbulent bands at $Ra = 10000$, discussed in §3.3.3. Notably, we have also included the statistics for a subcritical case ($Ra < Ra_{\parallel}$) at $Ra = 1000$, indicating the presence of subcritical effects as the statistics are slightly enhanced from $Ra = 0$ to $Ra = 1000$, reported by John Soundar Jerome et al. (2012). Nonetheless, there is a distinct change of state between $Re = 1000$ to 1050 (see figure 3.1), marked by the transition from the longitudinal/intermittent roll regime to shear-driven turbulence at $Re \geq 1050$, thus, shaded in blue in figure 3.1.

A.3 Growth rates of primary instabilities

Figure A.4 shows the eigenvalues of the primary instabilities as a function of its spanwise wavenumber αd , leading to the onset of longitudinal rolls at $Re = 1050$. The results are obtained using a Chebyshev-collocation method discretised by 51 Chebyshev polynomials (Driscoll, Hale, & Trefethen, 2014). The crosses denote the spanwise wavenumbers admissible within the domain $\Gamma = \pi/2$, where $\alpha d = 4$ corresponds to the dominant eigenmode.

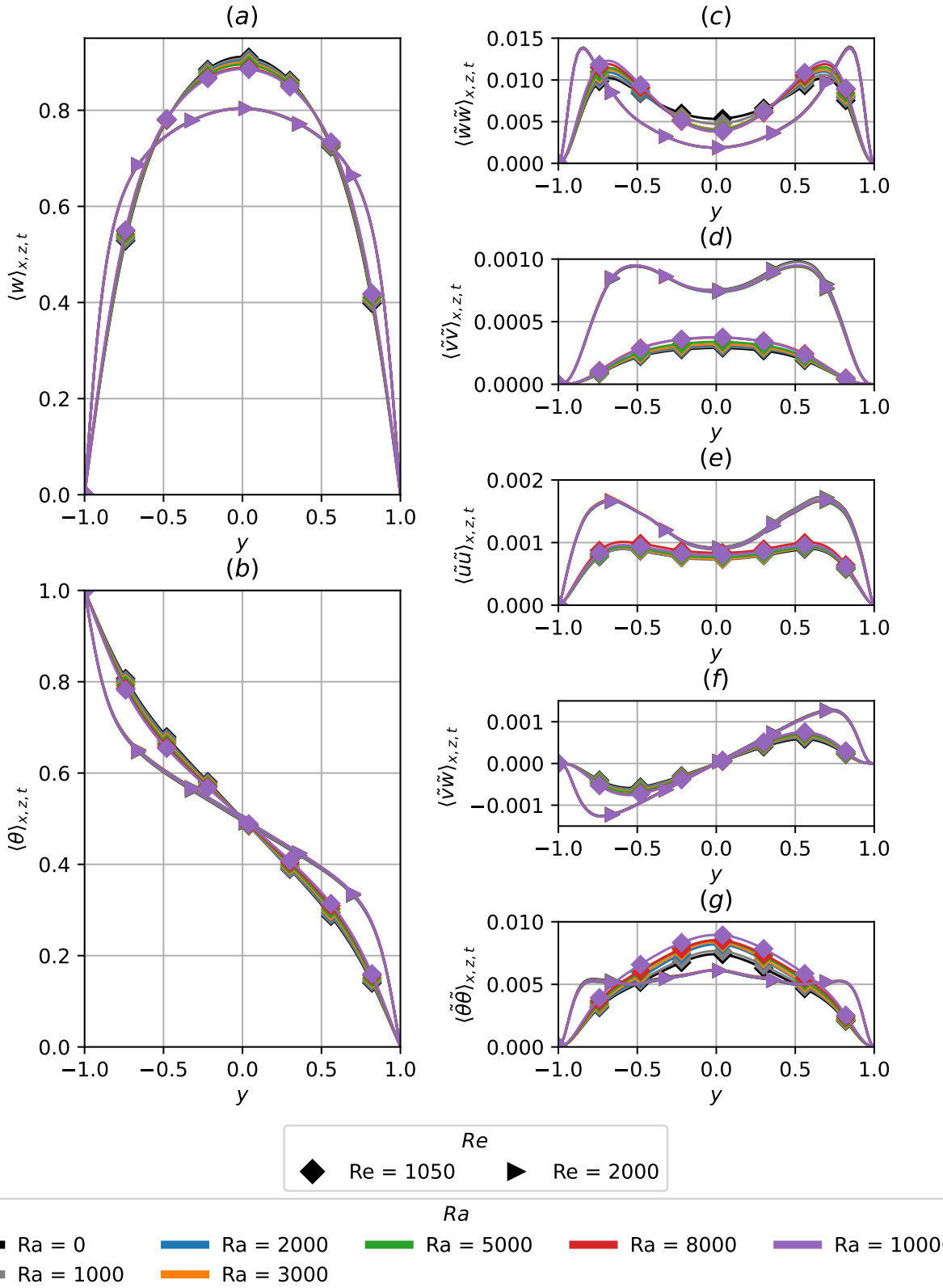


Figure A.2: The wall-normal distribution of temporal and plane- averaged (a) streamwise velocity, (b) temperature, (c) fluctuating streamwise velocity squared, (d) fluctuating wall-normal velocity squared, (e) fluctuating spanwise velocities squared, (f) fluctuating Reynolds stresses and (g) fluctuating temperature squared in the shear-driven regime shaded in blue in figure 3.1.

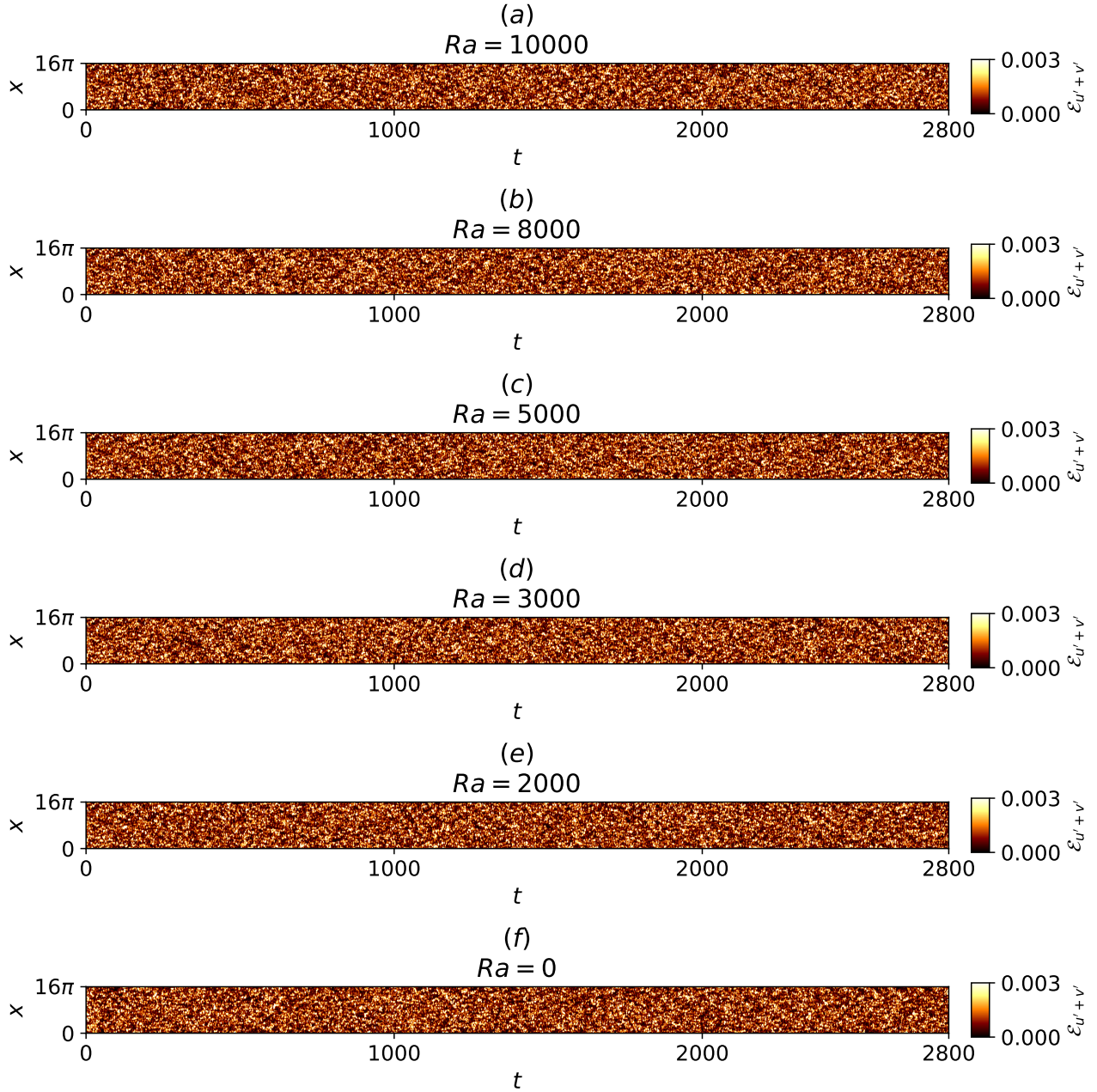


Figure A.3: Spacetime plots of near-wall, wall-normal and spanwise perturbation kinetic energy for $Re = 2000$, $t \in [0, 2800]$, $\Gamma = 4\pi$ at (a) $Ra = 10000$, (b) $Ra = 8000$, (c) $Ra = 5000$, (d) $Ra = 3000$, (e) $Ra = 2000$, (f) $Ra = 0$.

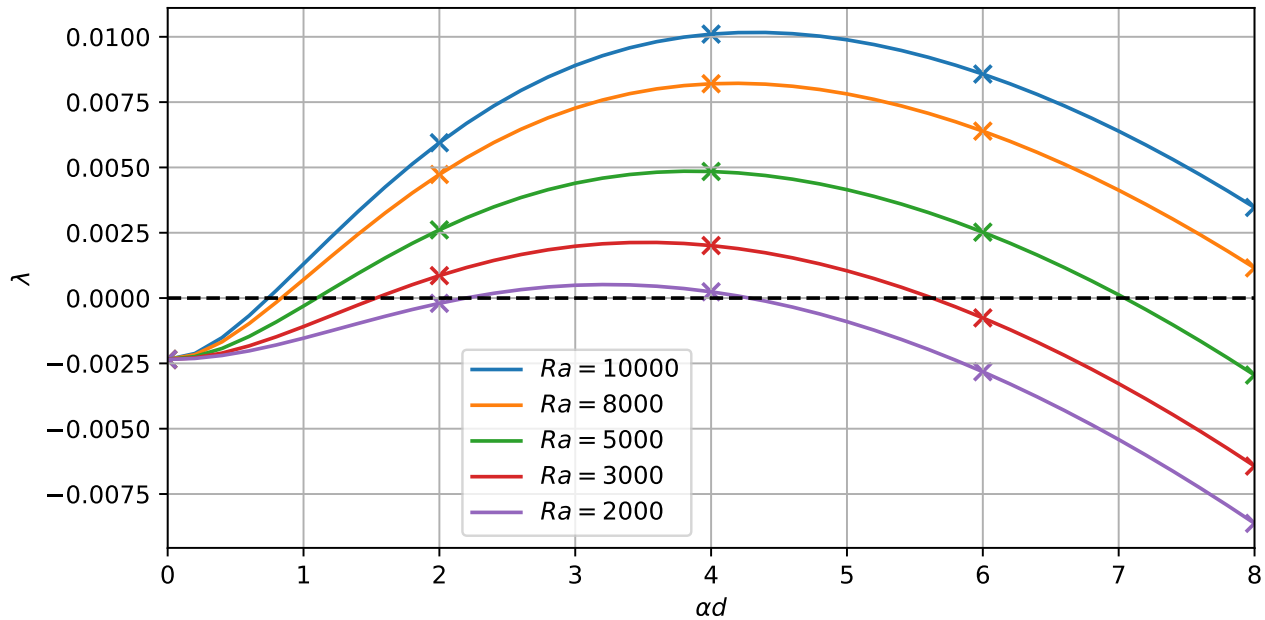


Figure A.4: Growth rates of primary instabilities at $Ra = 10000, 8000, 5000, 3000, 2000$ leading to the onset of longitudinal rolls against spanwise wavenumber of αd at $Re = 1050$.

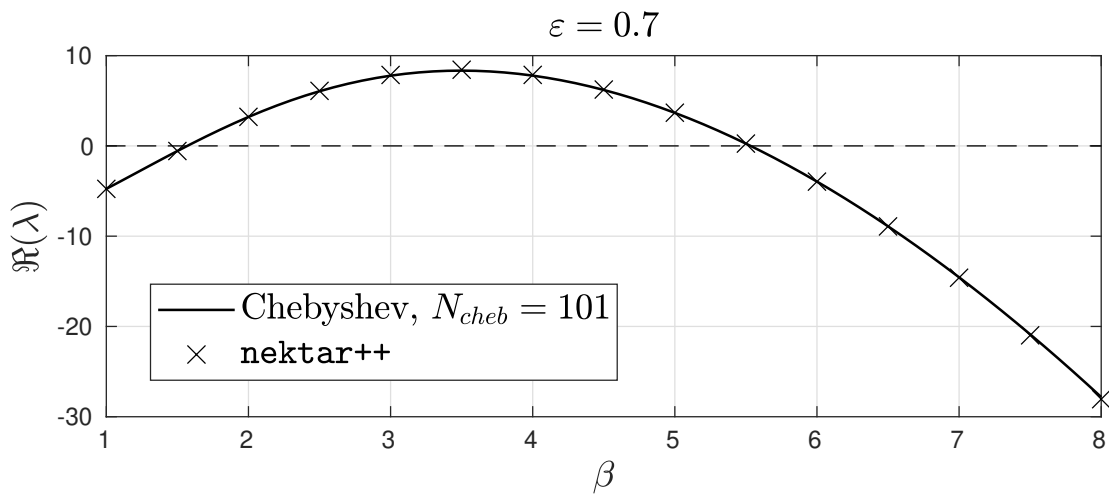


Figure A.5: Eigenvalues of primary instabilities of RBC at $\varepsilon = 0.7$ computed in Nektar++ compared against a Chebyshev-collocation method with 101 Chebyshev expansions.

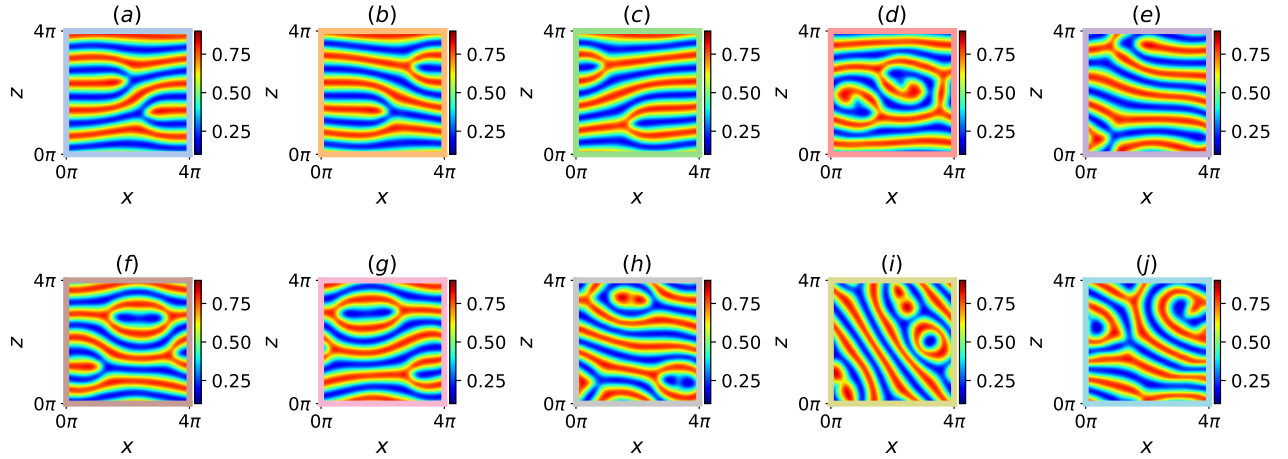


Figure A.6: Temperature snapshots, $\theta(x, z)|_{y=d/2}$, of 10 elementary states confined within a minimal domain $\Gamma = 2\pi$: (a) steady ‘forked-A’ state, (b) steady ‘forked-B’ state, (c) steady ‘forked-c’ state, (d) steady ‘twin-armed’ state, (e) steady ‘tri-rolls’ state, (f) travelling-wave ‘O-a’ state, (g) travelling-wave ‘O-b’ state, (h) steady ‘keyhole’ state, (i) relative periodic orbit ‘eye’ state, (j) relative periodic orbit ‘S’ state

A.4 Verification of linear stability analysis

Figure A.5 shows the eigenvalues as a function of spanwise wavenumber β of RBC at $\varepsilon = 0.7$. The results are obtained using Nektar++ and compared against a Chebyshev-collocation method discretised by 101 Chebyshev polynomials Driscoll et al. (2014).

A.5 Other elementary states and ISRs

Figure A.6 presents snapshots of temperature slices $(\theta(x, z)|_{d/2})$, depicting ten distinct elementary states. These states are obtained within a minimal domain $\Gamma = 2\pi$, consisting of eight stationary states (figures A.6(a-h)) and two travelling-wave states (figures A.6(i,j)). Figure A.7 features a snapshot of fourteen ideal straight rolls (ISRs), and they satisfy rotational symmetry about the y -axis and mirror symmetries about the x - and z -axes due to the horizontal isotropy of the present system. These ISRs represent stable fixed-points in the state space of figures 4.3, 4.4, 4.11, 4.16.

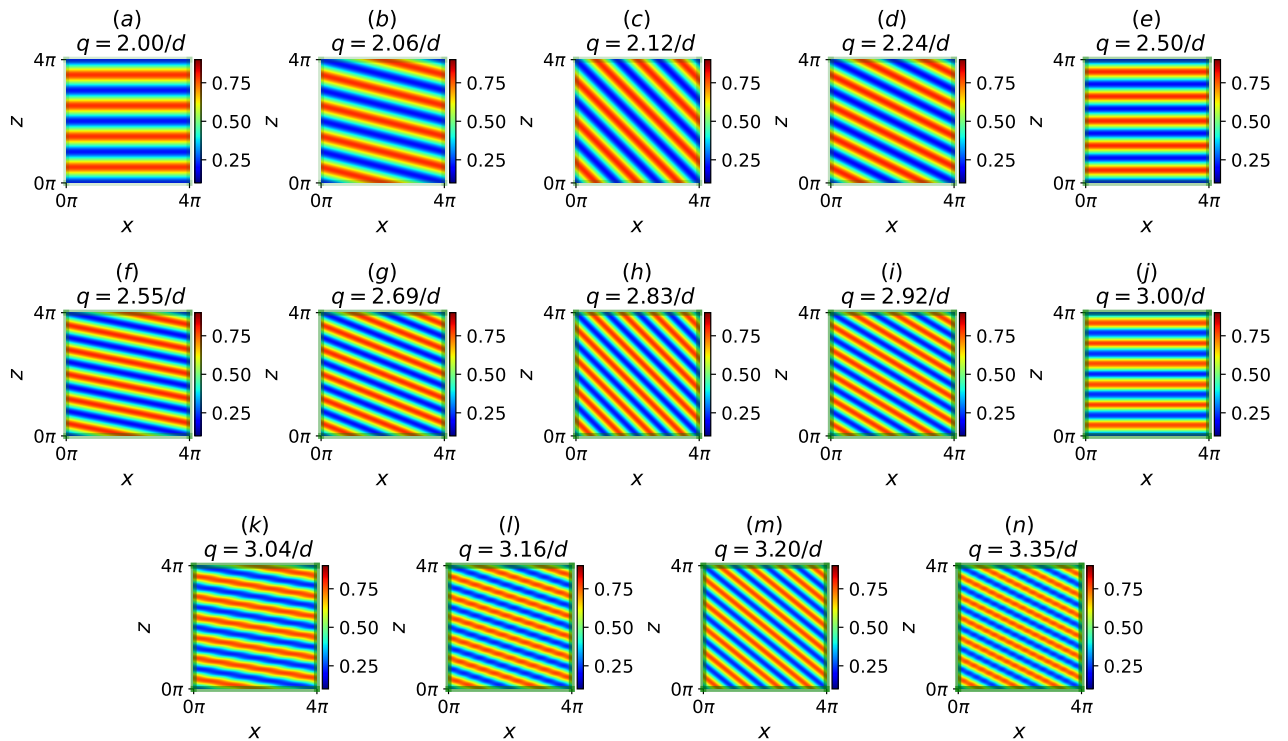


Figure A.7: Temperature snapshots, $\theta(x, z)|_{y=d/2}$, of 14 stable ideal straight rolls (ISRs) confined within a minimal domain, $\Gamma = 6.28$. Plots (a-n) are ordered in increasing wavenumbers, $q \in (2/d, 3.35/d)$.

References

- Affan, H., & Friedrich, R. (2014, June). Spiral defect chaos in an advection-reaction-diffusion system. *Physical Review E*, 89(6), 062920.
- Ahlers, G. (n.d.). Experiments on spatio-temporal chaos.
- Akiyama, M., Hwang, G.-J., & Cheng, K. (1971). Experiments on the onset of longitudinal vortices in laminar forced convection between horizontal plates.
- Anderson, E., Bai, Z., Bischof, C., Blackford, L. S., Demmel, J., Dongarra, J., . . . McKenney, A. (1999). *LAPACK users' guide*. SIAM.
- Arnoldi, W. E. (1951). The principle of minimized iterations in the solution of the matrix eigenvalue problem. *Quarterly of applied mathematics*, 9(1), 17–29.
- Avila, K., Moxey, D., De Lozar, A., Avila, M., Barkley, D., & Hof, B. (2011, July). The Onset of Turbulence in Pipe Flow. *Science*, 333(6039), 192–196. Retrieved 2025-04-01, from <https://www.science.org/doi/10.1126/science.1203223> doi: 10.1126/science.1203223
- Avila, M., Barkley, D., & Hof, B. (2023, January). Transition to Turbulence in Pipe Flow. *Annual Review of Fluid Mechanics*, 55(1), 575–602. Retrieved 2025-04-08, from <https://www.annualreviews.org/doi/10.1146/annurev-fluid-120720-025957> doi: 10.1146/annurev-fluid-120720-025957
- Avila, M., Willis, A. P., & Hof, B. (2010, March). On the transient nature of localized pipe flow turbulence. *Journal of Fluid Mechanics*, 646, 127–136. Retrieved 2025-04-08, from https://www.cambridge.org/core/product/identifier/S0022112009993296/type/journal_article doi: 10.1017/S0022112009993296
- Babuška, I., & Suri, M. (1994, December). The p and $h - p$ Versions of the Finite Element Method, Basic Principles and Properties. *SIAM Review*, 36(4), 578–632. Retrieved 2025-10-18, from <http://pubs.siam.org/doi/10.1137/1036141> doi: 10.1137/1036141
- Bajaj, K. M. S., Cannell, D. S., & Ahlers, G. (1997, May). Competition between spiral-defect chaos and rolls in Rayleigh-Bénard convection. *Physical Review E*, 55(5), R4869–R4872. Retrieved 2025-03-25, from <https://link.aps.org/doi/10.1103/PhysRevE.55.R4869> doi: 10.1103/PhysRevE.55.R4869
- Barkley, D., Blackburn, H. M., & Sherwin, S. J. (2008, July). Direct optimal growth analysis for timesteppers. *International Journal for Numerical Methods in Fluids*, 57(9), 1435–1458. Retrieved 2025-03-25, from <https://onlinelibrary.wiley.com/doi/10.1002/fld.1824> doi: 10.1002/fld.1824
- Barkley, D., & Tuckerman, L. S. (2005, January). Computational Study of Turbulent Laminar

- Patterns in Couette Flow. *Physical Review Letters*, 94(1), 014502. Retrieved from <https://link.aps.org/doi/10.1103/PhysRevLett.94.014502> (Publisher: American Physical Society) doi: 10.1103/PhysRevLett.94.014502
- Barkley, D., & Tuckerman, L. S. (2007). Mean flow of turbulent-laminar patterns in plane Couette flow. *Journal of Fluid Mechanics*, 576, 109–137. (Publisher: Cambridge University Press)
- Block, M. J. (1956, September). Surface Tension as the Cause of Bénard Cells and Surface Deformation in a Liquid Film. *Nature*, 178(4534), 650–651. Retrieved 2025-04-11, from <https://www.nature.com/articles/178650a0> doi: 10.1038/178650a0
- Bodenschatz, E., Cannell, D. S., De Bruyn, J. R., Ecke, R., Hu, Y.-C., Lerman, K., & Ahlers, G. (1992, December). Experiments on three systems with non-variational aspects. *Physica D: Nonlinear Phenomena*, 61(1-4), 77–93. Retrieved 2025-04-11, from <https://linkinghub.elsevier.com/retrieve/pii/016727899290150L> doi: 10.1016/0167-2789(92)90150-L
- Bodenschatz, E., Pesch, W., & Ahlers, G. (2000, January). Recent Developments in Rayleigh-Bénard Convection. *Annual Review of Fluid Mechanics*, 32(1), 709–778. Retrieved 2025-03-25, from <https://www.annualreviews.org/doi/10.1146/annurev.fluid.32.1.709> doi: 10.1146/annurev.fluid.32.1.709
- Borońska, K., & Tuckerman, L. S. (2010a, March). Extreme multiplicity in cylindrical Rayleigh-Bénard convection. II. Bifurcation diagram and symmetry classification. *Physical Review E*, 81(3), 036321. Retrieved 2025-03-25, from <https://link.aps.org/doi/10.1103/PhysRevE.81.036321> doi: 10.1103/PhysRevE.81.036321
- Borońska, K., & Tuckerman, L. S. (2010b, March). Extreme multiplicity in cylindrical Rayleigh-Bénard convection. I. Time dependence and oscillations. *Physical Review E*, 81(3), 036320. Retrieved 2025-03-25, from <https://link.aps.org/doi/10.1103/PhysRevE.81.036320> doi: 10.1103/PhysRevE.81.036320
- Bottin, S., Daviaud, F., Manneville, P., & Dauchot, O. (1998, July). Discontinuous transition to spatiotemporal intermittency in plane Couette flow. *Europhysics Letters (EPL)*, 43(2), 171–176. Retrieved 2025-05-26, from <https://iopscience.iop.org/article/10.1209/epl/i1998-00336-3> doi: 10.1209/epl/i1998-00336-3
- Boullié, N., Dallas, V., & Farrell, P. E. (2022, May). Bifurcation analysis of two-dimensional Rayleigh-Bénard convection using deflation. *Physical Review E*, 105(5), 055106. Retrieved 2025-03-25, from <https://link.aps.org/doi/10.1103/PhysRevE.105.055106> doi: 10.1103/PhysRevE.105.055106
- Busse, F. H. (1972, March). The oscillatory instability of convection rolls in a low Prandtl number fluid. *Journal of Fluid Mechanics*, 52(1), 97–112. Retrieved 2025-03-25, from https://www.cambridge.org/core/product/identifier/S0022112072002988/type/journal_article doi: 10.1017/S0022112072002988
- Busse, F. H. (1978, December). Non-linear properties of thermal convection. *Reports on Progress in Physics*, 41(12), 1929–1967. Retrieved 2025-03-25, from <https://iopscience.iop.org/article/10.1088/0034-4885/41/12/003> doi: 10.1088/0034-4885/41/12/003
- Busse, F. H. (1981). Transition to turbulence in Rayleigh-Bénard convection. In H. L. Swinney

- & J. P. Gollub (Eds.), *Hydrodynamic Instabilities and the Transition to Turbulence* (Vol. 45, pp. 97–137). Berlin, Heidelberg: Springer Berlin Heidelberg. Retrieved 2025-05-29, from http://link.springer.com/10.1007/3-540-13319-4_15 (Series Title: Topics in Applied Physics) doi: 10.1007/3-540-13319-4_15
- Busse, F. H., & Whitehead, J. A. (1971, May). Instabilities of convection rolls in a high Prandtl number fluid. *Journal of Fluid Mechanics*, 47(2), 305–320. Retrieved 2025-04-01, from https://www.cambridge.org/core/product/identifier/S0022112071001071/type/journal_article doi: 10.1017/S0022112071001071
- Butler, K. M., & Farrell, B. F. (1992, August). Three-dimensional optimal perturbations in viscous shear flow. *Physics of Fluids A: Fluid Dynamics*, 4(8), 1637–1650. Retrieved 2025-04-06, from <https://pubs.aip.org/pof/article/4/8/1637/402702/Three-dimensional-optimal-perturbations-in-viscous> doi: 10.1063/1.858386
- Bénard, H. (1901). Les tourbillons cellulaires dans une nappe liquide. - Méthodes optiques d'observation et d'enregistrement. *Journal de Physique Théorique et Appliquée*, 10(1), 254–266. Retrieved 2025-03-25, from <http://www.edpsciences.org/10.1051/jphystap:0190100100025400> doi: 10.1051/jphystap:0190100100025400
- Cakmur, R. V., Egolf, D. A., Plapp, B. B., & Bodenschatz, E. (1997a, September). Bistability and Competition of Spatiotemporal Chaotic and Fixed Point Attractors in Rayleigh-Bénard Convection. *Physical Review Letters*, 79(10), 1853–1856. Retrieved 2025-03-25, from <https://link.aps.org/doi/10.1103/PhysRevLett.79.1853> doi: 10.1103/PhysRevLett.79.1853
- Cakmur, R. V., Egolf, D. A., Plapp, B. B., & Bodenschatz, E. (1997b, February). *Transition from Spatiotemporal Chaos to Ideal Straight Rolls in Rayleigh-Benard Convection*. arXiv. Retrieved 2025-03-25, from <http://arxiv.org/abs/patt-sol/9702003> (arXiv:patt-sol/9702003) doi: 10.48550/arXiv.patt-sol/9702003
- Cantwell, C., Moxey, D., Comerford, A., Bolis, A., Rocco, G., Mengaldo, G., . . . Sherwin, S. (2015, July). Nektar++: An open-source spectral/h p element framework. *Computer Physics Communications*, 192, 205–219. Retrieved 2025-03-25, from <https://linkinghub.elsevier.com/retrieve/pii/S0010465515000533> doi: 10.1016/j.cpc.2015.02.008
- Carrière, P., & Monkewitz, P. A. (1999, April). Convective versus absolute instability in mixed Rayleigh–Bénard–Poiseuille convection. *Journal of Fluid Mechanics*, 384, 243–262. Retrieved 2025-03-25, from https://www.cambridge.org/core/product/identifier/S0022112098004145/type/journal_article doi: 10.1017/S0022112098004145
- Chandrasekhar, S. (1968, May). The stability of spiral flow between rotating cylinders. *Philosophical Transactions of the Royal Society of London. Series A, Mathematical and Physical Sciences*, 263(1135), 57–91. Retrieved 2025-03-25, from <https://royalsocietypublishing.org/doi/10.1098/rsta.1968.0006> doi: 10.1098/rsta.1968.0006
- Chiam, K.-H., Paul, M. R., Cross, M. C., & Greenside, H. S. (2003, May). Mean flow and spiral defect chaos in Rayleigh-Bénard convection. *Physical Review E*, 67(5), 056206. Retrieved 2025-04-15, from <https://link.aps.org/doi/10.1103/PhysRevE.67.056206> doi: 10.1103/PhysRevE.67.056206

- Chorin, A. J. (1967, August). A numerical method for solving incompressible viscous flow problems. *Journal of Computational Physics*, 2(1), 12–26. Retrieved 2025-05-16, from <https://linkinghub.elsevier.com/retrieve/pii/002199916790037X> doi: 10.1016/0021-9991(67)90037-X
- Chu, D. C., & Karniadakis, G. E. (1993, May). A direct numerical simulation of laminar and turbulent flow over riblet-mounted surfaces. *Journal of Fluid Mechanics*, 250, 1–42. Retrieved 2025-05-16, from https://www.cambridge.org/core/product/identifier/S0022112093001363/type/journal_article doi: 10.1017/S0022112093001363
- Clever, R. M., & Busse, F. H. (1974, October). Transition to time-dependent convection. *Journal of Fluid Mechanics*, 65(4), 625–645. Retrieved 2025-03-25, from https://www.cambridge.org/core/product/identifier/S0022112074001571/type/journal_article doi: 10.1017/S0022112074001571
- Clever, R. M., & Busse, F. H. (1991, August). Instabilities of longitudinal rolls in the presence of Poiseuille flow. *Journal of Fluid Mechanics*, 229(-1), 517. Retrieved 2025-03-25, from http://www.journals.cambridge.org/abstract_S0022112091003142 doi: 10.1017/S0022112091003142
- Cloot, A., & Lebon, G. (1984, August). A nonlinear stability analysis of the Bénard–Marangoni problem. *Journal of Fluid Mechanics*, 145(-1), 447. Retrieved 2025-04-13, from http://www.journals.cambridge.org/abstract_S0022112084003013 doi: 10.1017/S0022112084003013
- Cossu, C., & Hwang, Y. (2017, March). Self-sustaining processes at all scales in wall-bounded turbulent shear flows. *Philosophical Transactions of the Royal Society A: Mathematical, Physical and Engineering Sciences*, 375(2089), 20160088. Retrieved 2025-10-31, from <https://royalsocietypublishing.org/doi/10.1098/rsta.2016.0088> doi: 10.1098/rsta.2016.0088
- Croquette, V. (1989a, March). Convective pattern dynamics at low Prandtl number: Part I. *Contemporary Physics*, 30(2), 113–133. Retrieved 2025-03-25, from <http://www.tandfonline.com/doi/abs/10.1080/00107518908225511> doi: 10.1080/00107518908225511
- Croquette, V. (1989b, May). Convective pattern dynamics at low Prandtl number: Part II. *Contemporary Physics*, 30(3), 153–171. Retrieved 2025-03-25, from <http://www.tandfonline.com/doi/abs/10.1080/00107518908222594> doi: 10.1080/00107518908222594
- Cvitanović, P., & Gibson, J. F. (2010, December). Geometry of the turbulence in wall-bounded shear flows: periodic orbits. *Physica Scripta*, T142, 014007. Retrieved 2025-04-23, from <https://iopscience.iop.org/article/10.1088/0031-8949/2010/T142/014007> doi: 10.1088/0031-8949/2010/T142/014007
- Davies, S. J., & White, C. M. (1928, May). An experimental study of the flow of water in pipes of rectangular section. *Proceedings of the Royal Society of London. Series A, Containing Papers of a Mathematical and Physical Character*, 119(781), 92–107. Retrieved 2025-04-25, from <https://royalsocietypublishing.org/doi/10.1098/rspa.1928.0086> doi: 10.1098/rspa.1928.0086

- Dean, R. B. (1978, June). Reynolds Number Dependence of Skin Friction and Other Bulk Flow Variables in Two-Dimensional Rectangular Duct Flow. *Journal of Fluids Engineering*, 100(2), 215–223. Retrieved 2025-04-25, from <https://asmedigitalcollection.asme.org/fluidsengineering/article/100/2/215/409704/Reynolds-Number-Dependence-of-Skin-Friction-and> doi: 10.1115/1.3448633
- Decker, W., Pesch, W., & Weber, A. (1994, August). Spiral defect chaos in Rayleigh-Bénard convection. *Physical Review Letters*, 73(5), 648–651. Retrieved 2025-03-25, from <https://link.aps.org/doi/10.1103/PhysRevLett.73.648> doi: 10.1103/PhysRevLett.73.648
- Del Álamo, J. C., & Jiménez, J. (2006, July). Linear energy amplification in turbulent channels. *Journal of Fluid Mechanics*, 559, 205. Retrieved 2025-04-25, from http://www.journals.cambridge.org/abstract_S0022112006000607 doi: 10.1017/S0022112006000607
- Dong, L., Liu, F., Liu, S., He, Y., & Fan, W. (2005, October). Observation of spiral pattern and spiral defect chaos in dielectric barrier discharge in argon/air at atmospheric pressure. *Physical Review E*, 72(4), 046215. Retrieved 2025-04-15, from <https://link.aps.org/doi/10.1103/PhysRevE.72.046215> doi: 10.1103/PhysRevE.72.046215
- Driscoll, T. A., Hale, N., & Trefethen, L. N. (2014). Chebfun guide. (Publisher: Pafnuty Publications, Oxford)
- Duguet, Y., Schlatter, P., & Henningson, D. S. (2010, May). Formation of turbulent patterns near the onset of transition in plane Couette flow. *Journal of Fluid Mechanics*, 650, 119–129. Retrieved 2025-03-25, from https://www.cambridge.org/core/product/identifier/S0022112010000297/type/journal_article doi: 10.1017/S0022112010000297
- Duguet, Y., Willis, A. P., & Kerswell, R. R. (2008, October). Transition in pipe flow: the saddle structure on the boundary of turbulence. *Journal of Fluid Mechanics*, 613, 255–274. Retrieved 2025-04-23, from https://www.cambridge.org/core/product/identifier/S0022112008003248/type/journal_article doi: 10.1017/S0022112008003248
- Ecke, R. E., Hu, Y., Mainieri, R., & Ahlers, G. (1995, September). Excitation of Spirals and Chiral Symmetry Breaking in Rayleigh-Bénard Convection. *Science*, 269(5231), 1704–1707. Retrieved 2025-03-25, from <https://www.science.org/doi/10.1126/science.269.5231.1704> doi: 10.1126/science.269.5231.1704
- Eckhaus, W. (1965). *Studies in Non-Linear Stability Theory* (Vol. 6; C. Truesdell, L. Collatz, G. Fichera, P. Germain, J. Keller, & A. Seeger, Eds.). Berlin, Heidelberg: Springer Berlin Heidelberg. Retrieved 2025-04-01, from <http://link.springer.com/10.1007/978-3-642-88317-0> doi: 10.1007/978-3-642-88317-0
- Egolf, D. A., Melnikov, I. V., & Bodenschatz, E. (1998, April). Importance of Local Pattern Properties in Spiral Defect Chaos. *Physical Review Letters*, 80(15), 3228–3231. Retrieved 2025-03-25, from <https://link.aps.org/doi/10.1103/PhysRevLett.80.3228> doi: 10.1103/PhysRevLett.80.3228
- Egolf, D. A., Melnikov, I. V., Pesch, W., & Ecke, R. E. (2000, April). Mechanisms of extensive spatiotemporal chaos in Rayleigh-Bénard convection. *Nature*, 404(6779), 733–

736. Retrieved 2025-03-25, from <https://www.nature.com/articles/35008013> doi: 10.1038/35008013
- Ellingsen, T., & Palm, E. (1975, April). Stability of linear flow. *The Physics of Fluids*, 18(4), 487–488. Retrieved 2025-04-07, from <https://pubs.aip.org/pfl/article/18/4/487/459138/Stability-of-linear-flow> doi: 10.1063/1.861156
- Evans, G., & Greif, R. (1991, August). Unsteady three-dimensional mixed convection in a heated horizontal channel with applications to chemical vapor deposition. *International Journal of Heat and Mass Transfer*, 34(8), 2039–2051. Retrieved 2025-03-25, from <https://linkinghub.elsevier.com/retrieve/pii/001793109190215Z> doi: 10.1016/0017-9310(91)90215-Z
- Faisst, H., & Eckhardt, B. (2003, November). Traveling Waves in Pipe Flow. *Physical Review Letters*, 91(22), 224502. Retrieved 2025-04-23, from <https://link.aps.org/doi/10.1103/PhysRevLett.91.224502> doi: 10.1103/PhysRevLett.91.224502
- Faisst, H., & Eckhardt, B. (2004, April). Sensitive dependence on initial conditions in transition to turbulence in pipe flow. *Journal of Fluid Mechanics*, 504, 343–352. Retrieved 2025-05-26, from http://www.journals.cambridge.org/abstract_S0022112004008134 doi: 10.1017/S0022112004008134
- Farrell, B. F. (1988, August). Optimal excitation of perturbations in viscous shear flow. *The Physics of Fluids*, 31(8), 2093–2102. Retrieved 2025-04-07, from <https://pubs.aip.org/pfl/article/31/8/2093/966463/Optimal-excitation-of-perturbations-in-viscous> doi: 10.1063/1.866609
- Feigenbaum, M. J. (1979). The universal metric properties of nonlinear transformations. *Journal of Statistical Physics*, 21, 669–706. (Publisher: Springer)
- Foias, C., Sell, G. R., & Temam, R. (1988, June). Inertial manifolds for nonlinear evolutionary equations. *Journal of Differential Equations*, 73(2), 309–353. Retrieved 2025-04-24, from <https://linkinghub.elsevier.com/retrieve/pii/0022039688901106> doi: 10.1016/0022-0396(88)90110-6
- Fukui, K., Nakajima, M., & Ueda, H. (1983, January). The longitudinal vortex and its effects on the transport processes in combined free and forced laminar convection between horizontal and inclined parallel plates. *International Journal of Heat and Mass Transfer*, 26(1), 109–120. Retrieved 2025-04-15, from <https://linkinghub.elsevier.com/retrieve/pii/S0017931083800131> doi: 10.1016/S0017-9310(83)80013-1
- Gage, K. S., & Reid, W. H. (1968, July). The stability of thermally stratified plane Poiseuille flow. *Journal of Fluid Mechanics*, 33(1), 21–32. Retrieved 2025-03-25, from https://www.cambridge.org/core/product/identifier/S0022112068002326/type/journal_article doi: 10.1017/S0022112068002326
- Geuzaine, C., & Remacle, J. (2009, September). Gmsh: A 3-D finite element mesh generator with built-in pre- and post-processing facilities. *International Journal for Numerical Methods in Engineering*, 79(11), 1309–1331. Retrieved 2025-05-27, from <https://onlinelibrary.wiley.com/doi/10.1002/nme.2579> doi: 10.1002/nme.2579

- Gibson, J. F., Halcrow, J., & Cvitanović, P. (2008, September). Visualizing the geometry of state space in plane Couette flow. *Journal of Fluid Mechanics*, 611, 107–130. Retrieved 2025-04-07, from https://www.cambridge.org/core/product/identifier/S002211200800267X/type/journal_article doi: 10.1017/S002211200800267X
- Gibson, J. F., Halcrow, J., & Cvitanović, P. (2009, November). Equilibrium and travelling-wave solutions of plane Couette flow. *Journal of Fluid Mechanics*, 638, 243–266. Retrieved 2025-04-07, from https://www.cambridge.org/core/product/identifier/S0022112009990863/type/journal_article doi: 10.1017/S0022112009990863
- Gollub, J. P., & Swinney, H. L. (1975, October). Onset of Turbulence in a Rotating Fluid. *Physical Review Letters*, 35(14), 927–930. Retrieved 2025-04-24, from <https://link.aps.org/doi/10.1103/PhysRevLett.35.927> doi: 10.1103/PhysRevLett.35.927
- Golub, G. H., & Van Loan, C. F. (2013). *Matrix computations*. JHU press.
- Gomé, S., Tuckerman, L. S., & Barkley, D. (2020, August). Statistical transition to turbulence in plane channel flow. *Physical Review Fluids*, 5(8), 083905. Retrieved 2025-03-25, from <https://link.aps.org/doi/10.1103/PhysRevFluids.5.083905> doi: 10.1103/PhysRevFluids.5.083905
- Gottlieb, D., & Orszag, S. A. (1977). *Numerical Analysis of Spectral Methods: Theory and Applications*. Society for Industrial and Applied Mathematics. Retrieved 2025-10-18, from <http://epubs.siam.org/doi/book/10.1137/1.9781611970425> doi: 10.1137/1.9781611970425
- Graham, M. D., & Floryan, D. (2021, January). Exact Coherent States and the Nonlinear Dynamics of Wall-Bounded Turbulent Flows. *Annual Review of Fluid Mechanics*, 53(1), 227–253. Retrieved 2025-04-07, from <https://www.annualreviews.org/doi/10.1146/annurev-fluid-051820-020223> doi: 10.1146/annurev-fluid-051820-020223
- Green, M., Kirilov, K., Turner, M., Marcon, J., Eichstädt, J., Laughton, E., . . . Moxey, D. (2024, May). NekMesh: An open-source high-order mesh generation framework. *Computer Physics Communications*, 298, 109089. Retrieved 2025-05-27, from <https://linkinghub.elsevier.com/retrieve/pii/S0010465524000122> doi: 10.1016/j.cpc.2024.109089
- Guermond, J. L., & Shen, J. (2003, January). Velocity-Correction Projection Methods for Incompressible Flows. *SIAM Journal on Numerical Analysis*, 41(1), 112–134. Retrieved 2025-03-25, from <http://epubs.siam.org/doi/10.1137/S0036142901395400> doi: 10.1137/S0036142901395400
- Halcrow, J., Gibson, J. F., Cvitanović, P., & Viswanath, D. (2009, February). Heteroclinic connections in plane Couette flow. *Journal of Fluid Mechanics*, 621, 365–376. Retrieved 2025-04-07, from https://www.cambridge.org/core/product/identifier/S0022112008005065/type/journal_article doi: 10.1017/S0022112008005065
- Hall, P., & Sherwin, S. (2010, October). Streamwise vortices in shear flows: harbingers of transition and the skeleton of coherent structures. *Journal of Fluid Mechanics*, 661, 178–205. Retrieved 2025-10-31, from https://www.cambridge.org/core/product/identifier/S0022112010002892/type/journal_article doi: 10.1017/S0022112010002892

- Hall, P., & Smith, F. T. (1988, June). The nonlinear interaction of Tollmien–Schlichting waves and Taylor-Görtler vortices in curved channel flows. *Proceedings of the Royal Society of London. A. Mathematical and Physical Sciences*, 417(1853), 255–282. Retrieved 2025-10-31, from <https://royalsocietypublishing.org/doi/10.1098/rspa.1988.0060> doi: 10.1098/rspa.1988.0060
- Hall, P., & Smith, F. T. (1990). Near-Planar Ts Waves and Longitudinal Vortices in Channel Flow: Nonlinear Interaction and Focussing. In B. A. Stewart, R. Lal, & B. A. Stewart (Eds.), *Soil Restoration* (Vol. 17, pp. 5–39). New York, NY: Springer New York. Retrieved 2025-10-31, from http://link.springer.com/10.1007/978-1-4612-3432-6_2 (Series Title: Advances in Soil Science) doi: 10.1007/978-1-4612-3432-6_2
- Hall, P., & Smith, F. T. (1991, June). On strongly nonlinear vortex/wave interactions in boundary-layer transition. *Journal of Fluid Mechanics*, 227, 641–666. Retrieved 2025-10-31, from https://www.cambridge.org/core/product/identifier/S0022112091000289/type/journal_article doi: 10.1017/S0022112091000289
- Hamilton, J. M., Kim, J., & Waleffe, F. (1995, March). Regeneration mechanisms of near-wall turbulence structures. *Journal of Fluid Mechanics*, 287, 317–348. Retrieved 2025-04-07, from https://www.cambridge.org/core/product/identifier/S0022112095000978/type/journal_article doi: 10.1017/S0022112095000978
- Henderson, R. D., & Barkley, D. (1996, June). Secondary instability in the wake of a circular cylinder. *Physics of Fluids*, 8(6), 1683–1685. Retrieved 2025-05-20, from <https://pubs.aip.org/pof/article/8/6/1683/260183/Secondary-instability-in-the-wake-of-a-circular> doi: 10.1063/1.868939
- Herbert, T. (1997, January). PARABOLIZED STABILITY EQUATIONS. *Annual Review of Fluid Mechanics*, 29(1), 245–283. Retrieved 2025-05-22, from <https://www.annualreviews.org/doi/10.1146/annurev.fluid.29.1.245> doi: 10.1146/annurev.fluid.29.1.245
- Hoard, C., Robertson, C., & Acrivos, A. (1970, May). Experiments on the cellular structure in bénard convection. *International Journal of Heat and Mass Transfer*, 13(5), 849–856. Retrieved 2025-04-01, from <https://linkinghub.elsevier.com/retrieve/pii/0017931070901304> doi: 10.1016/0017-9310(70)90130-4
- Hof, B., Lucas, P. G. J., & Mullin, T. (1999, October). Flow state multiplicity in convection. *Physics of Fluids*, 11(10), 2815–2817. Retrieved 2025-03-25, from <https://pubs.aip.org/pof/article/11/10/2815/254396/Flow-state-multiplicity-in-convection> doi: 10.1063/1.870178
- Hof, B., Westerweel, J., Schneider, T. M., & Eckhardt, B. (2006, September). Finite lifetime of turbulence in shear flows. *Nature*, 443(7107), 59–62. Retrieved 2025-04-25, from <https://www.nature.com/articles/nature05089> doi: 10.1038/nature05089
- Hopf, E. (1948, December). A mathematical example displaying features of turbulence. *Communications on Pure and Applied Mathematics*, 1(4), 303–322. Retrieved 2025-04-24, from <https://onlinelibrary.wiley.com/doi/10.1002/cpa.3160010401> doi: 10.1002/cpa.3160010401

- Hossain, M. Z., Floryan, D., & Floryan, J. M. (2012, December). Drag reduction due to spatial thermal modulations. *Journal of Fluid Mechanics*, 713, 398–419. Retrieved 2025-03-25, from https://www.cambridge.org/core/product/identifier/S002211201200465X/type/journal_article doi: 10.1017/jfm.2012.465
- Hossain, M. Z., & Floryan, J. M. (2016, March). Drag reduction in a thermally modulated channel. *Journal of Fluid Mechanics*, 791, 122–153. Retrieved 2025-03-25, from https://www.cambridge.org/core/product/identifier/S0022112016000422/type/journal_article doi: 10.1017/jfm.2016.42
- Hossain, M. Z., & Floryan, J. M. (2020, August). On the role of surface grooves in the reduction of pressure losses in heated channels. *Physics of Fluids*, 32(8), 083610. Retrieved 2025-03-25, from <https://pubs.aip.org/pof/article/32/8/083610/1060903/On-the-role-of-surface-grooves-in-the-reduction-of> doi: 10.1063/5.0018416
- Hu, Y., Ecke, R., & Ahlers, G. (1993, December). Convection near threshold for Prandtl numbers near 1. *Physical Review E*, 48(6), 4399–4413. Retrieved 2025-03-25, from <https://link.aps.org/doi/10.1103/PhysRevE.48.4399> doi: 10.1103/PhysRevE.48.4399
- Hu, Y., Ecke, R., & Ahlers, G. (1995, April). Convection for Prandtl numbers near 1: Dynamics of textured patterns. *Physical Review E*, 51(4), 3263–3279. Retrieved 2025-03-25, from <https://link.aps.org/doi/10.1103/PhysRevE.51.3263> doi: 10.1103/PhysRevE.51.3263
- Hu, Y., Ecke, R. E., & Ahlers, G. (1997, June). Convection under rotation for Prandtl numbers near 1: Linear stability, wave-number selection, and pattern dynamics. *Physical Review E*, 55(6), 6928–6949. Retrieved 2025-03-25, from <https://link.aps.org/doi/10.1103/PhysRevE.55.6928> doi: 10.1103/PhysRevE.55.6928
- Huerre, P., & Monkewitz, P. A. (1990). Local and global instabilities in spatially developing flows. *Annual review of fluid mechanics*, 22(1), 473–537.
- Hwang, Y., & Cossu, C. (2010, December). Linear non-normal energy amplification of harmonic and stochastic forcing in the turbulent channel flow. *Journal of Fluid Mechanics*, 664, 51–73. Retrieved 2025-04-25, from https://www.cambridge.org/core/product/identifier/S0022112010003629/type/journal_article doi: 10.1017/S0022112010003629
- Iida, O., & Nagano, Y. (1998). The Relaminarization Mechanisms of Turbulent Channel Flow at Low Reynolds Numbers. *Flow, Turbulence and Combustion*, 60(2), 193–213. Retrieved 2025-04-25, from <http://link.springer.com/10.1023/A:1009999606355> doi: 10.1023/A:1009999606355
- Jeffreys, H. (1928, March). Some cases of instability in fluid motion. *Proceedings of the Royal Society of London. Series A, Containing Papers of a Mathematical and Physical Character*, 118(779), 195–208. Retrieved 2025-04-13, from <https://royalsocietypublishing.org/doi/10.1098/rspa.1928.0045> doi: 10.1098/rspa.1928.0045
- Jensen, K. F., Einset, E. O., & Fotiadis, D. I. (1991, January). Flow Phenomena in Chemical Vapor Deposition of Thin Films. *Annual Review of Fluid Mechanics*, 23(1), 197–232. Retrieved 2025-03-25, from <https://www.annualreviews.org/doi/10.1146/annurev.fl.23.010191.001213> doi: 10.1146/annurev.fl.23.010191.001213

- Jiménez, J., & Moin, P. (1991, April). The minimal flow unit in near-wall turbulence. *Journal of Fluid Mechanics*, 225, 213–240. Retrieved 2025-03-25, from https://www.cambridge.org/core/product/identifier/S0022112091002033/type/journal_article doi: 10.1017/S0022112091002033
- John, A., Gunter, F., & Maria, H. (1993, August). Routes to chaos and turbulence. A computational introduction. *Philosophical Transactions of the Royal Society of London. Series A: Physical and Engineering Sciences*, 344(1671), 207–234. Retrieved 2025-04-24, from <https://royalsocietypublishing.org/doi/10.1098/rsta.1993.0088> doi: 10.1098/rsta.1993.0088
- John Soundar Jerome, J., Chomaz, J.-M., & Huerre, P. (2012, April). Transient growth in Rayleigh-Bénard-Poiseuille/Couette convection. *Physics of Fluids*, 24(4), 044103. Retrieved 2025-03-25, from <https://pubs.aip.org/pof/article/24/4/044103/257562/Transient-growth-in-Rayleigh-Benard-Poiseuille> doi: 10.1063/1.4704642
- Karimi, A., Huang, Z.-F., & Paul, M. R. (2011, October). Exploring spiral defect chaos in generalized Swift-Hohenberg models with mean flow. *Physical Review E*, 84(4), 046215. Retrieved 2025-03-25, from <https://link.aps.org/doi/10.1103/PhysRevE.84.046215> doi: 10.1103/PhysRevE.84.046215
- Karniadakis, G., & Sherwin, S. J. (2005). *Spectral/hp element methods for computational fluid dynamics*. Oxford University Press.
- Karniadakis, G. E., Israeli, M., & Orszag, S. A. (1991, December). High-order splitting methods for the incompressible Navier-Stokes equations. *Journal of Computational Physics*, 97(2), 414–443. Retrieved 2025-03-25, from <https://linkinghub.elsevier.com/retrieve/pii/0021999191900078> doi: 10.1016/0021-9991(91)90007-8
- Kashyap, P. V., Duguet, Y., & Dauchot, O. (2022, December). Linear Instability of Turbulent Channel Flow. *Physical Review Letters*, 129(24), 244501. Retrieved 2025-04-25, from <https://link.aps.org/doi/10.1103/PhysRevLett.129.244501> doi: 10.1103/PhysRevLett.129.244501
- Kawahara, G., & Kida, S. (2001, December). Periodic motion embedded in plane Couette turbulence: regeneration cycle and burst. *Journal of Fluid Mechanics*, 449, 291–300. Retrieved 2025-04-07, from https://www.cambridge.org/core/product/identifier/S0022112001006243/type/journal_article doi: 10.1017/S0022112001006243
- Kelly, R. (1994). The Onset and Development of Thermal Convection in Fully Developed Shear Flows. In *Advances in Applied Mechanics* (Vol. 31, pp. 35–112). Elsevier. Retrieved 2025-03-25, from <https://linkinghub.elsevier.com/retrieve/pii/S0065215608702552> doi: 10.1016/S0065-2156(08)70255-2
- Kennedy, K., & Zebib, A. (1983, March). Combined free and forced convection between horizontal parallel planes: some case studies. *International Journal of Heat and Mass Transfer*, 26(3), 471–474. Retrieved 2025-03-25, from <https://linkinghub.elsevier.com/retrieve/pii/0017931083900522> doi: 10.1016/0017-9310(83)90052-2
- Kerswell, R. R., & Tutty, O. R. (2007, August). Recurrence of travelling waves in tran-

- sitional pipe flow. *Journal of Fluid Mechanics*, 584, 69–102. Retrieved 2025-04-23, from https://www.cambridge.org/core/product/identifier/S0022112007006301/type/journal_article doi: 10.1017/S0022112007006301
- Khapko, T., Kreilos, T., Schlatter, P., Duguet, Y., Eckhardt, B., & Henningson, D. S. (2016, August). Edge states as mediators of bypass transition in boundary-layer flows. *Journal of Fluid Mechanics*, 801, R2. Retrieved 2025-03-25, from https://www.cambridge.org/core/product/identifier/S0022112016004341/type/journal_article doi: 10.1017/jfm.2016.434
- Kim, H. T., Kline, S. J., & Reynolds, W. C. (1971, November). The production of turbulence near a smooth wall in a turbulent boundary layer. *Journal of Fluid Mechanics*, 50(1), 133–160. Retrieved 2025-05-30, from https://www.cambridge.org/core/product/identifier/S0022112071002490/type/journal_article doi: 10.1017/S0022112071002490
- Kim, J., Moin, P., & Moser, R. (1987, April). Turbulence statistics in fully developed channel flow at low Reynolds number. *Journal of Fluid Mechanics*, 177, 133–166. Retrieved 2025-03-25, from https://www.cambridge.org/core/product/identifier/S0022112087000892/type/journal_article doi: 10.1017/S0022112087000892
- Kline, S. J., Reynolds, W. C., Schraub, F. A., & Runstadler, P. W. (1967, December). The structure of turbulent boundary layers. *Journal of Fluid Mechanics*, 30(4), 741–773. Retrieved 2025-03-25, from https://www.cambridge.org/core/product/identifier/S0022112067001740/type/journal_article doi: 10.1017/S0022112067001740
- Knoll, D., & Keyes, D. (2004, January). Jacobian-free Newton–Krylov methods: a survey of approaches and applications. *Journal of Computational Physics*, 193(2), 357–397. Retrieved 2025-11-04, from <https://linkinghub.elsevier.com/retrieve/pii/S0021999103004340> doi: 10.1016/j.jcp.2003.08.010
- Koschmieder, E., & Pallas, S. (1974, September). Heat transfer through a shallow, horizontal convecting fluid layer. *International Journal of Heat and Mass Transfer*, 17(9), 991–1002. Retrieved 2025-04-11, from <https://linkinghub.elsevier.com/retrieve/pii/0017931074901811> doi: 10.1016/0017-9310(74)90181-1
- Kreilos, T., & Eckhardt, B. (2012, December). Periodic orbits near onset of chaos in plane Couette flow. *Chaos: An Interdisciplinary Journal of Nonlinear Science*, 22(4), 047505. Retrieved 2025-04-07, from <https://pubs.aip.org/cha/article/22/4/047505/341745/Periodic-orbits-near-onset-of-chaos-in-plane> doi: 10.1063/1.4757227
- Lai, Y.-C., & Tél, T. (2011). *Transient Chaos* (Vol. 173). New York, NY: Springer New York. Retrieved 2025-05-26, from <http://link.springer.com/10.1007/978-1-4419-6987-3> doi: 10.1007/978-1-4419-6987-3
- Landau, L. D. (1944). On the problem of turbulence. In (Vol. 44, p. 311).
- Lax, P. D., & Milgram, A. N. (1955, December). IX. Parabolic Equations. In *Contributions to the Theory of Partial Differential Equations. (AM-33)* (pp. 167–190). Princeton University Press. Retrieved 2025-05-12, from <https://www.degruyter.com/document/doi/10.1515/9781400882182-010/html> doi: 10.1515/9781400882182-010
- Le Gal, P., Pocheau, A., & Croquette, V. (1985, June). Square versus Roll Pattern at Convective

- Threshold. *Physical Review Letters*, 54(23), 2501–2504. Retrieved 2025-03-25, from <https://link.aps.org/doi/10.1103/PhysRevLett.54.2501> doi: 10.1103/PhysRevLett.54.2501
- Lehoucq, R. B., Sorensen, D. C., & Yang, C. (1998). *ARPACK users' guide: solution of large-scale eigenvalue problems with implicitly restarted Arnoldi methods*. SIAM.
- Liu, J., & Ahlers, G. (1996). Spiral-Defect Chaos in Rayleigh-Bénard Convection with Small Prandtl Numbers. *PHYSICAL REVIEW LETTERS*, 77(15).
- Lowe, M., & Gollub, J. P. (1985, December). Pattern Selection near the Onset of Convection: The Eckhaus Instability. *Physical Review Letters*, 55(23), 2575–2578. Retrieved 2025-04-15, from <https://link.aps.org/doi/10.1103/PhysRevLett.55.2575> doi: 10.1103/PhysRevLett.55.2575
- Luijkh, J.-M., Platten, J. K., & Legros, J. C. (1981). On the existence of thermoconvective rolls, transverse to a superimposed mean Poiseuille flow. *International Journal of Heat and Mass Transfer*, 24(7), 1287–1291. (Publisher: Elsevier)
- Lustro, J. R. T., Kawahara, G., Van Veen, L., Shimizu, M., & Kokubu, H. (2019, March). The onset of transient turbulence in minimal plane Couette flow. *Journal of Fluid Mechanics*, 862, R2. Retrieved 2025-10-30, from https://www.cambridge.org/core/product/identifier/S0022112018009710/type/journal_article doi: 10.1017/jfm.2018.971
- Ma, D.-J., Sun, D.-J., & Yin, X.-Y. (2006, September). Multiplicity of steady states in cylindrical Rayleigh-Bénard convection. *Physical Review E*, 74(3), 037302. Retrieved 2025-03-25, from <https://link.aps.org/doi/10.1103/PhysRevE.74.037302> doi: 10.1103/PhysRevE.74.037302
- Manneville, P. (2006). Rayleigh-Bénard Convection: Thirty Years of Experimental, Theoretical, and Modeling Work. In G. Höhler et al. (Eds.), *Dynamics of Spatio-Temporal Cellular Structures* (Vol. 207, pp. 41–65). New York, NY: Springer New York. Retrieved 2025-03-25, from http://link.springer.com/10.1007/978-0-387-25111-0_3 (Series Title: Springer Tracts in Modern Physics) doi: 10.1007/978-0-387-25111-0_3
- Manneville, P., & Pomeau, Y. (1979). Intermittency and the Lorenz model. *Physics Letters A*, 75(1-2), 1–2. (Publisher: North-Holland)
- Mellibovsky, F., & Eckhardt, B. (2012). From travelling waves to mild chaos: a supercritical bifurcation cascade in pipe flow. *Journal of Fluid Mechanics*, 709, 149–190. Retrieved from <https://www.cambridge.org/core/product/BE84A18A7FCD05488775E46B3C230844> (Edition: 2012/08/29 Publisher: Cambridge University Press) doi: 10.1017/jfm.2012.326
- Meseguer, A., & Trefethen, L. (2003, March). Linearized pipe flow to Reynolds number 107. *Journal of Computational Physics*, 186(1), 178–197. Retrieved 2025-04-03, from <https://linkinghub.elsevier.com/retrieve/pii/S0021999103000299> doi: 10.1016/S0021-9991(03)00029-9
- Morris, S. W., Bodenschatz, E., Cannell, D. S., & Ahlers, G. (1993, September). Spiral defect chaos in large aspect ratio Rayleigh-Bénard convection. *Physical Review Letters*, 71(13), 2026–2029. Retrieved 2025-03-25, from <https://link.aps.org/doi/10.1103/PhysRevLett.71.2026> doi: 10.1103/PhysRevLett.71.2026

- Morris, S. W., Bodenschatz, E., Cannell, D. S., & Ahlers, G. (1996, October). The spatio-temporal structure of spiral-defect chaos. *Physica D: Nonlinear Phenomena*, 97(1-3), 164–179. Retrieved 2025-03-25, from <https://linkinghub.elsevier.com/retrieve/pii/0167278996000966> doi: 10.1016/0167-2789(96)00096-6
- Moxey, D., Cantwell, C. D., Bao, Y., Cassinelli, A., Castiglioni, G., Chun, S., . . . Sherwin, S. J. (2020, April). Nektar++: Enhancing the capability and application of high-fidelity spectral/h p element methods. *Computer Physics Communications*, 249, 107110. Retrieved 2025-03-25, from <https://linkinghub.elsevier.com/retrieve/pii/S0010465519304175> doi: 10.1016/j.cpc.2019.107110
- Müller, H. W., Lücke, M., & Kamps, M. (1992, March). Transversal convection patterns in horizontal shear flow. *Physical Review A*, 45(6), 3714–3726. Retrieved 2025-03-25, from <https://link.aps.org/doi/10.1103/PhysRevA.45.3714> doi: 10.1103/PhysRevA.45.3714
- Nagata, M. (1990, August). Three-dimensional finite-amplitude solutions in plane Couette flow: bifurcation from infinity. *Journal of Fluid Mechanics*, 217, 519–527. Retrieved 2025-04-07, from https://www.cambridge.org/core/product/identifier/S0022112090000829/type/journal_article doi: 10.1017/S0022112090000829
- Nagata, M. (1997, February). Three-dimensional traveling-wave solutions in plane Couette flow. *Physical Review E*, 55(2), 2023–2025. Retrieved 2025-04-07, from <https://link.aps.org/doi/10.1103/PhysRevE.55.2023> doi: 10.1103/PhysRevE.55.2023
- Nicolas, X. (2002, October). Revue bibliographique sur les écoulements de Poiseuille-Rayleigh-Bénard : écoulements de convection mixte en conduites rectangulaires horizontales chauffées par le bas. *International Journal of Thermal Sciences*, 41(10), 961–1016. Retrieved 2025-03-25, from <https://linkinghub.elsevier.com/retrieve/pii/S1290072902013741> doi: 10.1016/S1290-0729(02)01374-1
- Nicolas, X., Luijkh, J.-M., & Platten, J.-K. (2000, February). Linear stability of mixed convection flows in horizontal rectangular channels of finite transversal extension heated from below. *International Journal of Heat and Mass Transfer*, 43(4), 589–610. Retrieved 2025-04-15, from <https://linkinghub.elsevier.com/retrieve/pii/S001793109900099X> doi: 10.1016/S0017-9310(99)00099-X
- Nicolas, X., Mojtabi, A., & Platten, J. K. (1997, February). Two-dimensional numerical analysis of the Poiseuille–Bénard flow in a rectangular channel heated from below. *Physics of Fluids*, 9(2), 337–348. Retrieved 2025-04-01, from <https://pubs.aip.org/pof/article/9/2/337/259822/Two-dimensional-numerical-analysis-of-the> doi: 10.1063/1.869235
- Nicolas, X., Xin, S., & Zoueidi, N. (2010, January). Characterisation of a Wavy Convective Instability in Poiseuille-Rayleigh-Bénard Flows: Linear Stability Analysis and Non Linear Numerical Simulations Under Random Excitations. In *2010 14th International Heat Transfer Conference, Volume 7* (pp. 203–208). Washington, DC, USA: ASMEDC. Retrieved 2025-03-25, from <https://asmedigitalcollection.asme.org/IHTC/proceedings/IHTC14/49422/203/360332> doi: 10.1115/IHTC14-22256
- Nicolas, X., Zoueidi, N., & Xin, S. (2012, August). Influence of a white noise at channel inlet on the

- parallel and wavy convective instabilities of Poiseuille-Rayleigh-Bénard flows. *Physics of Fluids*, 24(8), 084101. Retrieved 2025-04-15, from <https://pubs.aip.org/pof/article/24/8/084101/258132/Influence-of-a-white-noise-at-channel-inlet-on-the> doi: 10.1063/1.4737652
- Orr, W. M. (1907). The Stability or Instability of the Steady Motions of a Perfect Liquid and of a Viscous Liquid. Part II: A Viscous Liquid. *Proceedings of the Royal Irish Academy. Section A: Mathematical and Physical Sciences*, 27, 69–138. Retrieved 2025-04-03, from <http://www.jstor.org/stable/20490591> (Publisher: Royal Irish Academy)
- Orszag, S. A. (1971, December). Accurate solution of the Orr-Sommerfeld stability equation. *Journal of Fluid Mechanics*, 50(4), 689–703. Retrieved 2025-03-25, from https://www.cambridge.org/core/product/identifier/S0022112071002842/type/journal_article doi: 10.1017/S0022112071002842
- Orszag, S. A., Israeli, M., & Deville, M. O. (1986). Boundary conditions for incompressible flows. *Journal of Scientific Computing*, 1(1), 75–111. Retrieved 2025-04-21, from <http://link.springer.com/10.1007/BF01061454> doi: 10.1007/BF01061454
- Orszag, S. A., & Patera, A. T. (1983, March). Secondary instability of wall-bounded shear flows. *Journal of Fluid Mechanics*, 128(-1), 347. Retrieved 2025-03-25, from http://www.journals.cambridge.org/abstract_S0022112083000518 doi: 10.1017/S0022112083000518
- Ostrach, S., & Kamotani, Y. (1975, May). Heat Transfer Augmentation in Laminar Fully Developed Channel Flow by Means of Heating From Below. *Journal of Heat Transfer*, 97(2), 220–225. Retrieved 2025-04-15, from <https://asmedigitalcollection.asme.org/heattransfer/article/97/2/220/416581/Heat-Transfer-Augmentation-in-Laminar-Fully> doi: 10.1115/1.3450344
- Ouazzani, M., Caltagirone, J.-P., Meyer, G., & Mojtabi, A. (1989). Etude numerique et expérimentale de la convection mixte entre deux plans horizontaux à températures différentes. *International journal of heat and mass transfer*, 32(2), 261–269. (Publisher: Elsevier)
- Ouazzani, M., Platten, J. K., & Mojtabi, A. (1990). Etude expérimentale de la convection mixte entre deux plans horizontaux à températures différentes—II. *International journal of heat and mass transfer*, 33(7), 1417–1427. (Publisher: Elsevier)
- Pabiou, H., Mergui, S., & Bénard, C. (2005, October). Wavy secondary instability of longitudinal rolls in RayleighPoiseuille flows. *Journal of Fluid Mechanics*, 542(-1), 175. Retrieved 2025-03-25, from http://www.journals.cambridge.org/abstract_S0022112005006154 doi: 10.1017/S0022112005006154
- Pabiou, H., Nicolas, X., Xin, S., & Mergui, S. (2003). Observations d'une instabilité convective apparaissant sous la forme de rouleaux sinueux dans un écoulement de Poiseuille–Rayleigh–Bénard. *Mécanique & industries*, 4(5), 537–543. (Publisher: Elsevier)
- Paranjape, C. S. (2019). Onset of turbulence in plane Poiseuille flow. (Publisher: IST Austria Klosterneuburg, Austria)
- Paranjape, C. S., Duguet, Y., & Hof, B. (2020, August). Oblique stripe solutions of channel flow. *Journal of Fluid Mechanics*, 897, A7. Retrieved 2025-04-08, from <https://www.cambridge.org>

- .org/core/product/identifier/S0022112020003225/type/journal_article doi: 10.1017/jfm.2020.322
- Paranjape, C. S., Yalnız, G., Duguet, Y., Budanur, N. B., & Hof, B. (2023, July). Direct Path from Turbulence to Time-Periodic Solutions. *Physical Review Letters*, 131(3), 034002. Retrieved 2025-04-08, from <https://link.aps.org/doi/10.1103/PhysRevLett.131.034002> doi: 10.1103/PhysRevLett.131.034002
- Parker, J., & Schneider, T. (2022, June). Variational methods for finding periodic orbits in the incompressible Navier–Stokes equations. *Journal of Fluid Mechanics*, 941, A17. Retrieved 2025-05-29, from https://www.cambridge.org/core/product/identifier/S0022112022002993/type/journal_article doi: 10.1017/jfm.2022.299
- Patel, V. C., & Head, M. R. (1969, August). Some observations on skin friction and velocity profiles in fully developed pipe and channel flows. *Journal of Fluid Mechanics*, 38(1), 181–201. Retrieved 2025-03-25, from https://www.cambridge.org/core/product/identifier/S0022112069000115/type/journal_article doi: 10.1017/S0022112069000115
- Patera, A. T. (1984, June). A spectral element method for fluid dynamics: Laminar flow in a channel expansion. *Journal of Computational Physics*, 54(3), 468–488. Retrieved 2025-03-25, from <https://linkinghub.elsevier.com/retrieve/pii/0021999184901281> doi: 10.1016/0021-9991(84)90128-1
- Paul, M., Chiam, K.-H., Cross, M., Fischer, P., & Greenside, H. (2003, October). Pattern formation and dynamics in Rayleigh–Bénard convection: numerical simulations of experimentally realistic geometries. *Physica D: Nonlinear Phenomena*, 184(1-4), 114–126. Retrieved 2025-03-25, from <https://linkinghub.elsevier.com/retrieve/pii/S0167278903002161> doi: 10.1016/S0167-2789(03)00216-1
- Paul, M. R., Einarsson, M. I., Fischer, P. F., & Cross, M. C. (2007, April). Extensive chaos in Rayleigh–Bénard convection. *Physical Review E*, 75(4), 045203. Retrieved 2025-03-25, from <https://link.aps.org/doi/10.1103/PhysRevE.75.045203> doi: 10.1103/PhysRevE.75.045203
- Pellew, A., & Southwell, R. V. (1940, November). On maintained convective motion in a fluid heated from below. *Proceedings of the Royal Society of London. Series A. Mathematical and Physical Sciences*, 176(966), 312–343. Retrieved 2025-03-25, from <https://royalsocietypublishing.org/doi/10.1098/rspa.1940.0092> doi: 10.1098/rspa.1940.0092
- Pirozzoli, S., Bernardini, M., Verzicco, R., & Orlandi, P. (2017, June). Mixed convection in turbulent channels with unstable stratification. *Journal of Fluid Mechanics*, 821, 482–516. Retrieved 2025-03-25, from https://www.cambridge.org/core/product/identifier/S0022112017002166/type/journal_article doi: 10.1017/jfm.2017.216
- Plapp, B. B. (1997). *Spiral pattern formation in Rayleigh-Benard convection* (Doctoral dissertation). Retrieved 2025-04-01, from <https://ui.adsabs.harvard.edu/abs/1997PhDT.....105P> (Pages: 3118 Publication Title: Ph.D. Thesis ADS Bibcode: 1997PhDT.....105P)
- Plapp, B. B., & Bodenschatz, E. (1996, January). Core dynamics of multi-armed spirals in Rayleigh–Bénard convection. *Physica Scripta*, T67, 111–116. Retrieved 2025-03-25, from <https://>

- iopscience.iop.org/article/10.1088/0031-8949/1996/T67/022 doi: 10.1088/0031-8949/1996/T67/022
- Plapp, B. B., Egolf, D. A., Bodenschatz, E., & Pesch, W. (1998, December). Dynamics and Selection of Giant Spirals in Rayleigh-Bénard Convection. *Physical Review Letters*, 81(24), 5334–5337. Retrieved 2025-03-25, from <https://link.aps.org/doi/10.1103/PhysRevLett.81.5334> doi: 10.1103/PhysRevLett.81.5334
- Prigent, A., & Dauchot, O. (2002, June). "Barber pole turbulence" in large aspect ratio Taylor-Couette flow. *Physical Review Letters*, 89(1), 014501. Retrieved 2025-04-08, from <http://arxiv.org/abs/cond-mat/0009241> (arXiv:cond-mat/0009241) doi: 10.1103/PhysRevLett.89.014501
- Prigent, A., Grégoire, G., Chaté, H., & Dauchot, O. (2003, January). Long-wavelength modulation of turbulent shear flows. *Physica D: Nonlinear Phenomena*, 174(1-4), 100–113. Retrieved 2025-04-08, from <https://linkinghub.elsevier.com/retrieve/pii/S0167278902006851> doi: 10.1016/S0167-2789(02)00685-1
- Pringle, C. C., Duguet, Y., & Kerswell, R. R. (2009, February). Highly symmetric travelling waves in pipe flow. *Philosophical Transactions of the Royal Society A: Mathematical, Physical and Engineering Sciences*, 367(1888), 457–472. Retrieved 2025-04-23, from <https://royalsocietypublishing.org/doi/10.1098/rsta.2008.0236> doi: 10.1098/rsta.2008.0236
- Pujals, G., García-Villalba, M., Cossu, C., & Depardon, S. (2009, January). A note on optimal transient growth in turbulent channel flows. *Physics of Fluids*, 21(1), 015109. Retrieved 2025-04-25, from <https://pubs.aip.org/pof/article/21/1/015109/256743/A-note-on-optimal-transient-growth-in-turbulent> doi: 10.1063/1.3068760
- Ray, S., & Srinivasan, J. (1992, April). Analysis of conjugate laminar mixed convection cooling in a shrouded array of electronic components. *International Journal of Heat and Mass Transfer*, 35(4), 815–822. Retrieved 2025-03-25, from <https://linkinghub.elsevier.com/retrieve/pii/001793109290249R> doi: 10.1016/0017-9310(92)90249-R
- Rayleigh, L. (1916, December). LIX. *On convection currents in a horizontal layer of fluid, when the higher temperature is on the under side.* *The London, Edinburgh, and Dublin Philosophical Magazine and Journal of Science*, 32(192), 529–546. Retrieved 2025-03-25, from <https://www.tandfonline.com/doi/full/10.1080/14786441608635602> doi: 10.1080/14786441608635602
- Reddy, S. C., & Henningson, D. S. (1993, July). Energy growth in viscous channel flows. *Journal of Fluid Mechanics*, 252, 209–238. Retrieved 2025-03-25, from https://www.cambridge.org/core/product/identifier/S0022112093003738/type/journal_article doi: 10.1017/S0022112093003738
- Reddy, S. C., Schmid, P. J., & Henningson, D. S. (1993, February). Pseudospectra of the Orr-Sommerfeld Operator. *SIAM Journal on Applied Mathematics*, 53(1), 15–47. Retrieved 2025-04-07, from <http://epubs.siam.org/doi/10.1137/0153002> doi: 10.1137/0153002

- Reetz, F., Kreilos, T., & Schneider, T. M. (2019, May). Exact invariant solution reveals the origin of self-organized oblique turbulent-laminar stripes. *Nature Communications*, 10(1), 2277. Retrieved from <https://doi.org/10.1038/s41467-019-10208-x> doi: 10.1038/s41467-019-10208-x
- Reetz, F., & Schneider, T. M. (2020, September). Invariant states in inclined layer convection. Part 1. Temporal transitions along dynamical connections between invariant states. *Journal of Fluid Mechanics*, 898, A22. Retrieved 2025-03-25, from https://www.cambridge.org/core/product/identifier/S0022112020003171/type/journal_article doi: 10.1017/jfm.2020.317
- Reetz, F., Subramanian, P., & Schneider, T. M. (2020, September). Invariant states in inclined layer convection. Part 2. Bifurcations and connections between branches of invariant states. *Journal of Fluid Mechanics*, 898, A23. Retrieved 2025-03-25, from https://www.cambridge.org/core/product/identifier/S0022112020003183/type/journal_article doi: 10.1017/jfm.2020.318
- Reynolds, O. (1883, December). An experimental investigation of the circumstances which determine whether the motion of water shall be direct or sinuous, and of the law of resistance in parallel channels. *Philosophical Transactions of the Royal Society of London*, 174, 935–982. Retrieved 2025-04-03, from <https://royalsocietypublishing.org/doi/10.1098/rstl.1883.0029> doi: 10.1098/rstl.1883.0029
- Reynolds, O. (1895, December). On the dynamical theory of incompressible viscous fluids and the determination of the criterion. *Philosophical Transactions of the Royal Society of London*. (A.), 186, 123–164. Retrieved 2025-03-25, from <https://royalsocietypublishing.org/doi/10.1098/rsta.1895.0004> doi: 10.1098/rsta.1895.0004
- Rocco, G. (2014). Advanced Instability Methods using Spectral/hp Discretisations and their Applications to Complex Geometries.
- Rossby, H. T. (1969, April). A study of Bénard convection with and without rotation. *Journal of Fluid Mechanics*, 36(2), 309–335. Retrieved 2025-03-25, from https://www.cambridge.org/core/product/identifier/S0022112069001674/type/journal_article doi: 10.1017/S0022112069001674
- Ruelle, D., & Takens, F. (1971, September). On the nature of turbulence. *Communications in Mathematical Physics*, 20(3), 167–192. Retrieved 2025-04-24, from <http://link.springer.com/10.1007/BF01646553> doi: 10.1007/BF01646553
- Rüdiger, S., & Feudel, F. (2000, October). Pattern formation in Rayleigh-Bénard convection in a cylindrical container. *Physical Review E*, 62(4), 4927–4931. Retrieved 2025-03-25, from <https://link.aps.org/doi/10.1103/PhysRevE.62.4927> doi: 10.1103/PhysRevE.62.4927
- Scagliarini, A., Einarsson, H., Gylfason, Á., & Toschi, F. (2015, October). Law of the wall in an unstably stratified turbulent channel flow. *Journal of Fluid Mechanics*, 781, R5. Retrieved 2025-03-25, from https://www.cambridge.org/core/product/identifier/S002211201500498X/type/journal_article doi: 10.1017/jfm.2015.498

- Scagliarini, A., Gylfason, A., & Toschi, F. (2014, April). Heat flux scaling in turbulent Rayleigh-Bénard convection with an imposed longitudinal wind. *Physical Review E*, 89(4), 043012. Retrieved 2025-03-25, from <http://arxiv.org/abs/1311.4598> (arXiv:1311.4598 [physics]) doi: 10.1103/PhysRevE.89.043012
- Schlichting, H. (1933). Zur Entstehung der Turbulenz bei der Plattenströmung. *Nachrichten von der Gesellschaft der Wissenschaften zu Göttingen, Mathematisch-Physikalische Klasse*, 1933, 181–208. Retrieved from <http://eudml.org/doc/59420>
- Schlichting, H., & Gersten, K. (2017). Onset of Turbulence (Stability Theory). In *Boundary-Layer Theory* (pp. 415–496). Berlin, Heidelberg: Springer Berlin Heidelberg. Retrieved 2025-04-05, from http://link.springer.com/10.1007/978-3-662-52919-5_15 doi: 10.1007/978-3-662-52919-5_15
- Schlüter, A., Lortz, D., & Busse, F. (1965, September). On the stability of steady finite amplitude convection. *Journal of Fluid Mechanics*, 23(01), 129. Retrieved 2025-03-25, from http://www.journals.cambridge.org/abstract_S0022112065001271 doi: 10.1017/S0022112065001271
- Schmid, P. J. (2007, January). Nonmodal Stability Theory. *Annual Review of Fluid Mechanics*, 39(1), 129–162. Retrieved 2025-04-03, from <https://www.annualreviews.org/doi/10.1146/annurev.fluid.38.050304.092139> doi: 10.1146/annurev.fluid.38.050304.092139
- Schmid, P. J., De Pando, M. F., & Peake, N. (2017, November). Stability analysis for n-periodic arrays of fluid systems. *Physical Review Fluids*, 2(11), 113902. Retrieved 2025-03-25, from <https://link.aps.org/doi/10.1103/PhysRevFluids.2.113902> doi: 10.1103/PhysRevFluids.2.113902
- Schmid, P. J., & Henningson, D. S. (2001). *Stability and Transition in Shear Flows* (Vol. 142; J. E. Marsden & L. Sirovich, Eds.). New York, NY: Springer New York. Retrieved 2025-04-03, from <http://link.springer.com/10.1007/978-1-4613-0185-1> doi: 10.1007/978-1-4613-0185-1
- Schmitz, R., Pesch, W., & Zimmermann, W. (2002, March). Spiral-defect chaos: Swift-Hohenberg model versus Boussinesq equations. *Physical Review E*, 65(3), 037302. Retrieved 2025-03-25, from <https://link.aps.org/doi/10.1103/PhysRevE.65.037302> doi: 10.1103/PhysRevE.65.037302
- Schneider, T. M., & Eckhardt, B. (2009, February). Edge states intermediate between laminar and turbulent dynamics in pipe flow. *Philosophical Transactions of the Royal Society A: Mathematical, Physical and Engineering Sciences*, 367(1888), 577–587. Retrieved 2025-04-23, from <https://royalsocietypublishing.org/doi/10.1098/rsta.2008.0216> doi: 10.1098/rsta.2008.0216
- Schneider, T. M., Eckhardt, B., & Yorke, J. A. (2007, July). Turbulence transition and the edge of chaos in pipe flow. *Physical Review Letters*, 99(3), 034502. Retrieved 2025-03-25, from <http://arxiv.org/abs/nlin/0703067> (arXiv:nlin/0703067) doi: 10.1103/PhysRevLett.99.034502
- Shimizu, M., & Manneville, P. (2019, November). Bifurcations to turbulence in transitional channel

- flow. *Physical Review Fluids*, 4(11), 113903. Retrieved from <https://link.aps.org/doi/10.1103/PhysRevFluids.4.113903> (Publisher: American Physical Society) doi: 10.1103/PhysRevFluids.4.113903
- Siggens, J. H. (2003, January). Dynamics of target patterns in low-Prandtl-number convection. *Journal of Fluid Mechanics*, 475, 357–375. Retrieved 2025-03-25, from https://www.cambridge.org/core/product/identifier/S0022112002002896/type/journal_article doi: 10.1017/S0022112002002896
- Skufca, J. D., Yorke, J. A., & Eckhardt, B. (2006, May). Edge of Chaos in a Parallel Shear Flow. *Physical Review Letters*, 96(17), 174101. Retrieved 2025-03-25, from <https://link.aps.org/doi/10.1103/PhysRevLett.96.174101> doi: 10.1103/PhysRevLett.96.174101
- Smith, C. R., & Metzler, S. P. (1983, April). The characteristics of low-speed streaks in the near-wall region of a turbulent boundary layer. *Journal of Fluid Mechanics*, 129(-1), 27. Retrieved 2025-03-25, from http://www.journals.cambridge.org/abstract_S0022112083000634 doi: 10.1017/S0022112083000634
- Sommerfeld, A. (1909). *Ein Beitrag zur hydrodynamischen Erklarung der turbulenten Fluessigkeitsbewegungen*.
- Song, B., Barkley, D., Hof, B., & Avila, M. (2017, February). Speed and structure of turbulent fronts in pipe flow. *Journal of Fluid Mechanics*, 813, 1045–1059. Retrieved 2025-04-08, from https://www.cambridge.org/core/product/identifier/S0022112017000143/type/journal_article doi: 10.1017/jfm.2017.14
- Squire, H. B. (1933, November). On the stability for three-dimensional disturbances of viscous fluid flow between parallel walls. *Proceedings of the Royal Society of London. Series A, Containing Papers of a Mathematical and Physical Character*, 142(847), 621–628. Retrieved 2025-03-25, from <https://royalsocietypublishing.org/doi/10.1098/rspa.1933.0193> doi: 10.1098/rspa.1933.0193
- Steinberg, V., & Ahlers, G. (n.d.). Pattern Formation and Wave-Number Selection by Rayleigh-Benard Convection in a Cylindrical Container. *Physica Scripta T*.
- Strang, G., & Fix, G. J. (2008). *An analysis of the finite element method* (2. ed ed.). Wellesley, Mass: Wellesley-Cambridge Press.
- Strogatz, S. H. (2018). *Nonlinear Dynamics and Chaos* (??th ed.). CRC Press. Retrieved 2025-05-29, from <https://www.taylorfrancis.com/books/9780429961113> doi: 10.1201/9780429492563
- Swift, J., & Hohenberg, P. C. (1977, January). Hydrodynamic fluctuations at the convective instability. *Physical Review A*, 15(1), 319–328. Retrieved 2025-03-25, from <https://link.aps.org/doi/10.1103/PhysRevA.15.319> doi: 10.1103/PhysRevA.15.319
- Swinney, H. L., & Gollub, J. P. (1978). The transition to turbulence. *Physics today*, 31(8), 41–49. (Publisher: American Institute of Physics)
- Tao, J. J., Eckhardt, B., & Xiong, X. M. (2018, January). Extended localized structures and the onset of turbulence in channel flow. *Physical Review Fluids*, 3(1), 011902. Retrieved from <https://link.aps.org/doi/10.1103/PhysRevFluids.3.011902> (Publisher: American Physical

- Society) doi: 10.1103/PhysRevFluids.3.011902
- Theofilis, V. (2003, May). Advances in global linear instability analysis of nonparallel and three-dimensional flows. *Progress in Aerospace Sciences*, 39(4), 249–315. Retrieved 2025-05-20, from <https://linkinghub.elsevier.com/retrieve/pii/S0376042102000301> doi: 10.1016/S0376-0421(02)00030-1
- Toh, S., & Itano, T. (2003, April). A periodic-like solution in channel flow. *Journal of Fluid Mechanics*, 481, 67–76. Retrieved 2025-04-07, from http://www.journals.cambridge.org/abstract_S0022112003003768 doi: 10.1017/S0022112003003768
- Tollmien, W. (1928). Über die Entstehung der Turbulenz. 1. Mitteilung. *Nachrichten von der Gesellschaft der Wissenschaften zu Göttingen, Mathematisch-Physikalische Klasse*, 1929, 21–44. Retrieved from <http://eudml.org/doc/59276>
- Trefethen, L. N. (1997, January). Pseudospectra of Linear Operators. *SIAM Review*, 39(3), 383–406. Retrieved 2025-04-07, from <http://epubs.siam.org/doi/10.1137/S0036144595295284> doi: 10.1137/S0036144595295284
- Tsukahara, T., Iwamoto, K., Kawamura, H., & Takeda, T. (2014, September). *DNS of heat transfer in a transitional channel flow accompanied by a turbulent puff-like structure*. arXiv. Retrieved 2025-03-25, from <http://arxiv.org/abs/1406.0586> (arXiv:1406.0586 [physics]) doi: 10.48550/arXiv.1406.0586
- Tsukahara, T., Kawaguchi, Y., & Kawamura, H. (2014). *An experimental study on turbulent-stripe structure in transitional channel flow*. arXiv. Retrieved 2025-04-09, from <https://arxiv.org/abs/1406.1378> (Version Number: 2) doi: 10.48550/ARXIV.1406.1378
- Tsukahara, T., Seki, Y., Kawamura, H., & Tochio, D. (2014, September). *DNS of turbulent channel flow at very low Reynolds numbers*. arXiv. Retrieved 2025-03-25, from <http://arxiv.org/abs/1406.0248> (arXiv:1406.0248 [physics]) doi: 10.48550/arXiv.1406.0248
- Tuckerman, L. S., & Barkley, D. (1988, July). Global Bifurcation to Traveling Waves in Axisymmetric Convection. *Physical Review Letters*, 61(4), 408–411. Retrieved 2025-03-25, from <https://link.aps.org/doi/10.1103/PhysRevLett.61.408> doi: 10.1103/PhysRevLett.61.408
- Tuckerman, L. S., & Barkley, D. (2000). Bifurcation Analysis for Timesteppers. In *Numerical Methods for Bifurcation Problems and Large-Scale Dynamical Systems* (Vol. 119, pp. 453–466). New York, NY: Springer New York. Retrieved 2025-03-25, from http://link.springer.com/10.1007/978-1-4612-1208-9_20 (Series Title: The IMA Volumes in Mathematics and its Applications) doi: 10.1007/978-1-4612-1208-9_20
- Tuckerman, L. S., & Barkley, D. (2011). Patterns and dynamics in transitional plane Couette flow. *Physics of Fluids*, 23(4). (Publisher: AIP Publishing)
- Tuckerman, L. S., Chantry, M., & Barkley, D. (2020, January). Patterns in Wall-Bounded Shear Flows. *Annual Review of Fluid Mechanics*, 52(1), 343–367. Retrieved 2025-04-08, from <https://www.annualreviews.org/doi/10.1146/annurev-fluid-010719-060221> doi: 10.1146/annurev-fluid-010719-060221
- Tuckerman, L. S., Kreilos, T., Schröbsdorff, H., Schneider, T. M., & Gibson, J. F. (2014, November). Turbulent-laminar patterns in plane Poiseuille flow. *Physics of Fluids*,

- 26(11), 114103. Retrieved 2025-03-25, from <https://pubs.aip.org/pof/article/26/11/114103/315350/Turbulent-laminar-patterns-in-plane-Poiseuille> doi: 10.1063/1.4900874
- Témam, R. (1969, January). Sur l'approximation de la solution des équations de Navier-Stokes par la méthode des pas fractionnaires (II). *Archive for Rational Mechanics and Analysis*, 33(5), 377–385. Retrieved 2025-05-16, from <http://link.springer.com/10.1007/BF00247696> doi: 10.1007/BF00247696
- Vallis, G. K., Parker, D. J., & Tobias, S. M. (2019, March). A simple system for moist convection: the Rainy-Bénard model. *Journal of Fluid Mechanics*, 862, 162–199. Retrieved 2025-04-10, from https://www.cambridge.org/core/product/identifier/S0022112018009540/type/journal_article doi: 10.1017/jfm.2018.954
- Van Dyke, M., & Van Dyke, M. (1982). *An album of fluid motion* (Vol. 176). Parabolic Press Stanford.
- Van Veen, L., & Kawahara, G. (2011, September). Homoclinic Tangle on the Edge of Shear Turbulence. *Physical Review Letters*, 107(11), 114501. Retrieved 2025-10-30, from <https://link.aps.org/doi/10.1103/PhysRevLett.107.114501> doi: 10.1103/PhysRevLett.107.114501
- Viswanath, D. (2007, June). Recurrent motions within plane Couette turbulence. *Journal of Fluid Mechanics*, 580, 339–358. Retrieved 2025-04-08, from https://www.cambridge.org/core/product/identifier/S0022112007005459/type/journal_article doi: 10.1017/S0022112007005459
- Vitral, E., Mukherjee, S., Leo, P. H., Viñals, J., Paul, M. R., & Huang, Z.-F. (2020, September). Spiral defect chaos in Rayleigh-Bénard convection: Asymptotic and numerical studies of azimuthal flows induced by rotating spirals. *Physical Review Fluids*, 5(9), 093501. Retrieved 2025-03-25, from <https://link.aps.org/doi/10.1103/PhysRevFluids.5.093501> doi: 10.1103/PhysRevFluids.5.093501
- Waleffe, F. (1997, April). On a self-sustaining process in shear flows. *Physics of Fluids*, 9(4), 883–900. Retrieved 2025-10-31, from <https://pubs.aip.org/pof/article/9/4/883/260272/On-a-self-sustaining-process-in-shear-flows> doi: 10.1063/1.869185
- Waleffe, F. (2001, May). Exact coherent structures in channel flow. *Journal of Fluid Mechanics*, 435, 93–102. Retrieved 2025-04-07, from https://www.cambridge.org/core/product/identifier/S0022112001004189/type/journal_article doi: 10.1017/S0022112001004189
- Waleffe, F. (2003, June). Homotopy of exact coherent structures in plane shear flows. *Physics of Fluids*, 15(6), 1517–1534. Retrieved 2025-04-07, from <https://pubs.aip.org/pof/article/15/6/1517/448391/Homotopy-of-exact-coherent-structures-in-plane> doi: 10.1063/1.1566753
- Waleffe, F., Kim, J., & Hamilton, J. M. (1993). On the Origin of Streaks in Turbulent Shear Flows. In F. Durst, R. Friedrich, B. E. Launder, F. W. Schmidt, U. Schumann, & J. H. Whitelaw (Eds.), *Turbulent Shear Flows 8* (pp. 37–49). Berlin, Heidelberg: Springer Berlin Heidelberg. Retrieved 2025-10-31, from http://link.springer.com/10.1007/978-3-642-77674-8_4 doi: 10.1007/978-3-642-77674-8_4

- Wang, J., Gibson, J., & Waleffe, F. (2007, May). Lower Branch Coherent States in Shear Flows: Transition and Control. *Physical Review Letters*, 98(20), 204501. Retrieved 2025-04-23, from <https://link.aps.org/doi/10.1103/PhysRevLett.98.204501> doi: 10.1103/PhysRevLett.98.204501
- Wedin, H., & Kerswell, R. R. (2004, June). Exact coherent structures in pipe flow: travelling wave solutions. *Journal of Fluid Mechanics*, 508, 333–371. Retrieved 2025-04-23, from http://www.journals.cambridge.org/abstract_S0022112004009346 doi: 10.1017/S0022112004009346
- Wesfreid, J. E. (2017, June). Henri Bénard: Thermal convection and vortex shedding. *Comptes Rendus. Mécanique*, 345(7), 446–466. Retrieved 2025-04-13, from <https://comptes-rendus.academie-sciences.fr/mecanique/articles/10.1016/j.crme.2017.06.006/> doi: 10.1016/j.crme.2017.06.006
- Willis, G. E., & Deardorff, J. W. (1970, December). The oscillatory motions of Rayleigh convection. *Journal of Fluid Mechanics*, 44(04), 661. Retrieved 2025-03-25, from http://www.journals.cambridge.org/abstract_S0022112070002070 doi: 10.1017/S0022112070002070
- Xi, H., & Gunton, J. D. (1995, November). Spatiotemporal chaos in a model of Rayleigh-Bénard convection. *Physical Review E*, 52(5), 4963–4975. Retrieved 2025-03-25, from <https://link.aps.org/doi/10.1103/PhysRevE.52.4963> doi: 10.1103/PhysRevE.52.4963
- Xi, H.-w., Gunton, J. D., & Viñals, J. (1993, September). Spiral defect chaos in a model of Rayleigh-Bénard convection. *Physical Review Letters*, 71(13), 2030–2033. Retrieved 2025-03-25, from <https://link.aps.org/doi/10.1103/PhysRevLett.71.2030> doi: 10.1103/PhysRevLett.71.2030
- Xiao, X., & Song, B. (2020, January). The growth mechanism of turbulent bands in channel flow at low Reynolds numbers. *Journal of Fluid Mechanics*, 883, R1. Retrieved 2025-04-09, from https://www.cambridge.org/core/product/identifier/S0022112019008991/type/journal_article doi: 10.1017/jfm.2019.899
- Xin, S., Nicolas, X., & Quéré, P. L. (2006, July). Stability analyses of Longitudinal Rolls of Poiseuille-Rayleigh-Bénard Flows in Air-Filled Channels of Finite Transversal Extension. *Numerical Heat Transfer, Part A: Applications*, 50(5), 467–490. Retrieved 2025-03-25, from <http://www.tandfonline.com/doi/abs/10.1080/10407780600620079> doi: 10.1080/10407780600620079
- Xiong, X., Tao, J., Chen, S., & Brandt, L. (2015, April). Turbulent bands in plane-Poiseuille flow at moderate Reynolds numbers. *Physics of Fluids*, 27(4), 041702. Retrieved 2025-04-09, from <https://pubs.aip.org/pof/article/27/4/041702/1019208/Turbulent-bands-in-plane-Poiseuille-flow-at> doi: 10.1063/1.4917173
- Yan, Z.-G., Pan, Y., Castiglioni, G., Hillewaert, K., Peiró, J., Moxey, D., & Sherwin, S. J. (2021, January). Nektar++: Design and implementation of an implicit, spectral/h p element, compressible flow solver using a Jacobian-free Newton Krylov approach. *Computers & Mathematics with Applications*, 81, 351–372. Retrieved 2025-11-04, from <https://linkinghub.elsevier.com/retrieve/pii/S0898122120301073> doi: 10.1016/j.camwa.2020.03.009

- Zammert, S., & Eckhardt, B. (2014, December). Streamwise and doubly-localised periodic orbits in plane Poiseuille flow. *Journal of Fluid Mechanics*, 761, 348–359. Retrieved 2025-04-07, from https://www.cambridge.org/core/product/identifier/S0022112014006338/type/journal_article doi: 10.1017/jfm.2014.633
- Zammert, S., & Eckhardt, B. (2015, April). Crisis bifurcations in plane Poiseuille flow. *Physical Review E*, 91(4), 041003. Retrieved 2025-03-25, from <https://link.aps.org/doi/10.1103/PhysRevE.91.041003> doi: 10.1103/PhysRevE.91.041003
- Zheng, Z., Tuckerman, L. S., & Schneider, T. M. (2024a, December). Natural convection in a vertical channel. Part 1. Wavenumber interaction and Eckhaus instability in a narrow domain. *Journal of Fluid Mechanics*, 1000, A28. Retrieved 2025-11-04, from https://www.cambridge.org/core/product/identifier/S0022112024008425/type/journal_article doi: 10.1017/jfm.2024.842
- Zheng, Z., Tuckerman, L. S., & Schneider, T. M. (2024b, December). Natural convection in a vertical channel. Part 2. Oblique solutions and global bifurcations in a spanwise-extended domain. *Journal of Fluid Mechanics*, 1000, A29. Retrieved 2025-11-04, from https://www.cambridge.org/core/product/identifier/S0022112024008401/type/journal_article doi: 10.1017/jfm.2024.840